Origin of the gamma-ray emission in AGN jets

—

A multi-wavelength photometry and polarimetry data analysis of the quasar 3C 279

INAUGURAL-DISSERTATION

zur
Erlangung des Doktorgrades
der Mathemathisch-Naturwissenschaftlichen Fakultät
der Universität zu Köln

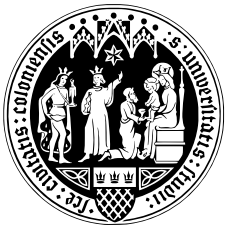

vorgelegt von

Kiehlmann, Sebastian
aus Moers, Deutschland

Köln 2015

Berichterstatter:	Prof. Dr. J. A. Zensus Prof. Dr. A. Eckart
Tag der mündlichen Prüfung:	26. Juni 2015

Abstract

One of the main topics regarding the physics of AGN jets is the origin of the γ-ray emission. The favoured model explaining the production of high energy radiation in blazars is inverse Compton scattering. Though numerically and empirically successfully tested, two major questions remain topics of substantial discussion: First, where is the seed photon field coming from? Does it originate in the jet itself (synchrotron self-Compton (SSC)) or in the accretion disc, the dust torus or the broad line region (external Compton (EC))? And second, where in the jet does the inverse Compton scattering take place?

This thesis aims to locate the γ-ray emission site in the archetypical blazar 3C 279 based on the multi-frequency photometry data provided by the Quasar Movie Project. This data set includes 140 light curves at more than twenty bands, providing dense sampling in frequency and time domain over more than two years. These data allow us to analyse the variability of the light curves and to perform cross-correlation analysis over a large range of frequencies. We estimate the variability power spectra at 26 frequencies. We find similar indices of a power-law spectrum at sub-mm bands and X-rays on the one hand, and at ultraviolet and γ-rays on the other hand. Additionally, we find a strong correlation between X-rays and the 1 mm light curve at short variability time scales. We can infer that the X-ray emission site is located at the mm VLBI core and that X-rays are produced either by synchrotron self-Compton scattering of mm-wavelength synchrotron photons or by external Compton scattering of photons originating from the cosmic microwave background. The correlation between X-rays, γ-rays, and optical bands exhibits complex behaviour. Time lags between the bands change over time, indicating probably different emission sites and different physical conditions. But we find some indication that the γ-ray emission site is located, at least occasionally, at the mm VLBI core. Thus, it is located beyond the broad line region, where infrared photons either from the jet itself or from the dust torus may serve as seed photons for the inverse Compton scattering to GeV energies.

Another major topic of ongoing discussion regards the structure of the magnetic field in the jets. The observed synchrotron radiation in the spectral regime from radio to x-rays and the polarization of the radiation are direct evidence for the existence of magnetic fields in the jets. Furthermore current jet models require magnetic fields to explain the launching and acceleration of jets. But the structure of the magnetic field is unknown. Long, smooth continuous variation of the electric vector position angle (EVPA) and very long baseline interferometry (VLBI) rotation measure studies indicate helical magnetic field structures. Whereas erratic EVPA variation indicates a tangled magnetic field structure and shocks traversing a turbulent medium may temporarily order the tangled magnetic field to produce smooth EVPA changes.

The combined optical polarimetry data provided by the Quasar Movie Project yields an unprecedentedly well sampled polarization curve of 3C 279 which shows

strong variability with rotations of the polarization angle in both directions with different rotation rates and amplitudes. We introduce various, new methods to analyse the polarization variability. We test different classes of stochastic models against the observed data and come to the conclusion that the polarization variability of 3C 279 is following two different processes. During a low brightness state the polarization is consistent with a stochastic process. During a flaring state the variability is dominated by a different process. The preferred model is that of an emission feature on a helical path in a helical magnetic field.

Kurzzusammenfassung

Die Frage nach dem Ursprung der γ-Strahlung ist eines der wesentlichen Themen auf dem Gebiet der Physik aktiver Galaxienkerne. Inverse Compton-Streuung ist das bevorzugte Modell, um die Erzeugung von hochenergetischer Strahlung in Blazaren zu erklären. Obwohl dieses Modell numerisch und empirisch erfolgreich getestet ist, bleiben zwei wesentliche Fragen bislang offen: Erstens, woher stammen die ursprünglichen Photonen, die zu höherer Energie gestreut werden? Werden diese im Jet selbst erzeugt (synchrotron Selbst-Compton (SSC)-Streuung), oder stammen sie aus einer externen Region (externe Compton (EC)-Streuung) wie der Akkretionsscheibe, dem Staubtorus oder der Broad Line Region? Zweitens, wo im Jet findet der Streuprozess statt?

Diese Doktorarbeit versucht das Emissionsgebiet der γ-Strahlung im Blazar 3C 279 anhand von photometrischen Daten, beobachtet bei einer Vielzahl von Frequenzen, zu lokalisieren. Diese Daten werden durch das Quasar Movie Project zur Verfügung gestellt und beinhalten 140 Lichtkurven bei über zwanzig Frequenzen. Damit bietet der Datensatz eine hohe Abtastrate sowohl im Zeit-, wie im Frequenzbereich über einen Zeitraum von über zwei Jahren. Diese Daten ermöglichen es die Variabilität der Lichtkurven zu untersuchen und eine Kreuzkorrelationsanalyse über einen großen Frequenzbereich durchzuführen. Wir schätzen die spektralen Energiedichte der Lichtkurvenvariation in 26 verschienden Frequenzbaïndern ein. Zum Einen finden wir eine vergleichbare Verteilung der Energiedichte für die Röntgen- und die sub-mm-Strahlung, zum Anderen eine vergleichbare Verteilung für die ultraviolette und die γ-Strahlung. Zudem zeigt sich eine starke Korrelation zwischen der Kurzzeitvariabilität der Röntgenstrahlung und der mm-Strahlung. Daraus schließen wir, dass die Röntgenstrahlung in der Nähe des mm-VLBI-Kernes erzeugt wird, entweder durch Selbst-Compton-Streuung von mm-Synchrotronstrahlung oder durch externe Compton-Streuung von Photonen der kosmischen Mikrowellenhintergrundstrahlung. Die Korrelation zwischen γ-Strahlung, Röntgenstrahlung und optischer Strahlung zeigt ein komplexes Verhalten. Die Verzögerungen der Variation zwischen verschiedenen Frequenzbereichen sind zeitlich variable. Dieses Verhalten ist möglicherweise ein Hinweis darauf, dass diese Strahlung an verschiedenen Stellen, unter unterschiedlichen physikalischen Bedingungen erzeugt wird. Dennoch finden wir Anzeichen dafür, dass das Emissionsgebiet der γ-Strahlung, zumindest zeitweilig, mit der Position des mm VLBI Kernes übereinstimmt. Damit liegt das Emissionsgebiet außerhalb der Broad Line Region. Somit kommen als ursprüngliche Photonen für die inverse Compton-Streuung zu höherer Energie lediglich Strahlung im Infrarotbereich in Frage, welche entweder im Jet selbst oder vom Staubtorus emittiert wird.

Ein weiteres Thema andauernder Diskussion betrifft die Struktur des Magnetfeldes im Jet. Die beobachtete Synchrotronstrahlung über das gesamte Spektrum vom Radiobereich bis hin zur Röntgenstrahlung und die kennzeichnende Polarisation dieser Strahlung ist ein direkter Beweis für die Existenz von Magnetfeldern

in Jets. Des Weiteren sind Modelle, die aktuell zur Erklärung des Usprunges und der Beschleunigung von Jets herangezogen werden, wesentlich auf die Existenz von Magnetfeldern angewiesen. Dennoch ist die Struktur der Magnetfelder bislang unbekannt. Lange, kontinuierliche und glatte Verläufe, die die Veränderung des Polarisationswinkels anzeigen sowie Messungen der Faraday-Rotation auf Basis von VLBI-Daten deuten auf eine Helixstruktur des Magnetfeldes hin. Die sprunghafte Variation des Polarisationswinkels wiederum deutet auf ein chaotisches Magnetfeld. Dieses ungeordnete Magnetfeld kann durch eine Schockfront, die das turbulente Medium durchläuft, kurzweilig komprimiert werden und dadurch geordnet erscheinen. Dies kann auch bei einer chaotischen Magnetfeldstruktur zu glatten Verläufen der Polarisationswinkelveränderung führen.

Die kombinierten Polarisationsdaten im optischen Frequenzbereich, die durch das Quasar Movie Project bereitgestellt werden, bilden die Polarisationsvariation von 3C 279 mit sehr hoher zeitlicher Abtastrate ab. Diese Daten zeigen eine hohe Variabilität des Polarisationswinkels. Rotationen in beide Richtungen treten auf mit variierenden Rotationsgeschwindigkeiten und -amplituden. Wir stellen verschiedene, neue Methoden vor, um Polarisationsdaten zu analysieren. Wir testen unterschiedliche Klassen von stochastischen Prozessen gegen die Daten und schlussfolgern, dass 3C 279 zwei verschiedenen Prozessen unterworfen ist, die die Variation der Polarisation erklären. Im Zustand geringer Intensität ist die Polarisationsvariation konsistent mit einem stochastischem Prozess. Wiederum im Zustand starker Intensitätsausbrüche kann die Variation nicht durch einen der hier beschriebenen stochastischen Prozesse beschrieben werden. Das bevorzugte Modell, welches die Variation in diesem Zustand beschrieben kann, ist das eines Emissionsgebietes, welches sich auf einer spiralförmigen Bahn durch ein spiralförmiges Magnetfeld bewegt.

Contents

List of Figures

List of Tables

Chapter 1

Introduction

1.1 Active galactic nuclei

An active galaxy is a special subtype of galaxy which is characterized by its central region, the Active Galactic Nucleus (AGN). Many different classes of extragalactic astrophysical objects are summarized under the term AGN. Those classes, initially interpreted as different kinds of objects but nowadays unified in the model of an AGN, evolved out of various classification schemes and observations at different frequency ranges. Though historically evolved and revised as a single type of object, these classifications are still in use to distinctively characterize subclasses of AGN.

1.1.1 Historical review of AGN observations

Messier 77 (NGC 1068) was the first object, reported in 1909 by Edward Fath, which was later on classified as AGN. The spectrum of this spiral nebula[1] showed emission lines, an unprecedented result at that time (Fath, 1909).

The first systematic study of spectral lines in extragalactic objects was conducted by Seyfert (1943), describing broad and narrow emission lines and absorption lines in various extragalactic nebulae. The fact that not all objects showed broad emission lines led to the first classification into Seyfert 1 galaxies and Seyfert 2 galaxies.

In the 1950s radio astronomy started as a new branch of astronomy and the first systematic radio surveys led to a large number of newly found radio emitting objects listed in the Third Cambridge Catalogue of Radio Sources (3C). Gradually, many of the 3C objects were identified with known astrophysical objects previously observed in optical bands, for instance Cygnus A (3C 405) (Baade and Minkowski, 1954), 3C 273 (Schmidt, 1963), and 3C 48 (Matthews and Sandage, 1963). The spectra of the optical counterparts showed high redshift, indicating that these radio sources were extragalactic objects. Later on the terms *radio galaxy* for extended extragalactic radio sources (e.g. Cynus A) and *quasar* or *quasi-stellar radio source* for point-like sources were established. The class of quasars was generalized to Quasi-Stellar Objects (QSOs) once several point-like optical sources

[1] Nebulous objects, differing from point-like stars, are recorded since the 10th century (*Book of Fixed Stars* by Abd al-Rahman al-Sufi) but first in the early 20th century with spectrographic studies in the 1910s began the discussion that the stars observed were located in a closed system, the Milky Way, and that those nebulae were located far outside of the Milky Way. Within this scientific process, including the *Great Debate* between Harlow Shapley and Heber Curtis and leading up to Edwin Hubble's classification of galaxy morphologies, *spiral nebulae* were first renamed *island universes* and later *galaxies*.

consistent with the optical spectra of quasars but without radio emission were identified. Morphology studies of the extended radio emission from AGN led to the classification into FR-I and FR-II sources (Fanaroff and Riley, 1974).

With the Einstein Observatory (HEAO-2) (1978-1982) and later on ROSAT (1990-1999), RXTE (1995-2012), Chandra (since 1999), XMM-Newton (since 1999), and Swift (since 2004) AGN were also identified as X-ray sources. With the Energetic Gamma Ray Experiment Telescope (EGRET) on the Compton Gamma Ray Observatory satellite operating between 1991 and 2000 some AGN were furthermore identified as γ-ray sources (von Montigny et al., 1995) which are continuously monitored since 2008 with the Large Area Telescope (LAT) on the Fermi satellite. Punch et al. (1992) showed that the emission of Mrk 421 reaches up to TeV-energy, observed with the Whipple 10 m gamma-ray telescope using the the Imaging Atmospheric Cherenkov Technique. With the successors VERITAS and MAGIC more TeV-sources have been identified amongst the AGN.

Antonucci and Miller (1985) showed that the Seyfert 2 galaxy Messier 77 (NGC 1068) showed characteristics of a Seyfert 1 galaxy in polarized light. In the late 1980s to early 1990s the scientific discussion led to the unified model of AGN (Urry and Padovani, 1995, and references therein).

1.1.2 Unified AGN model and radiation processes

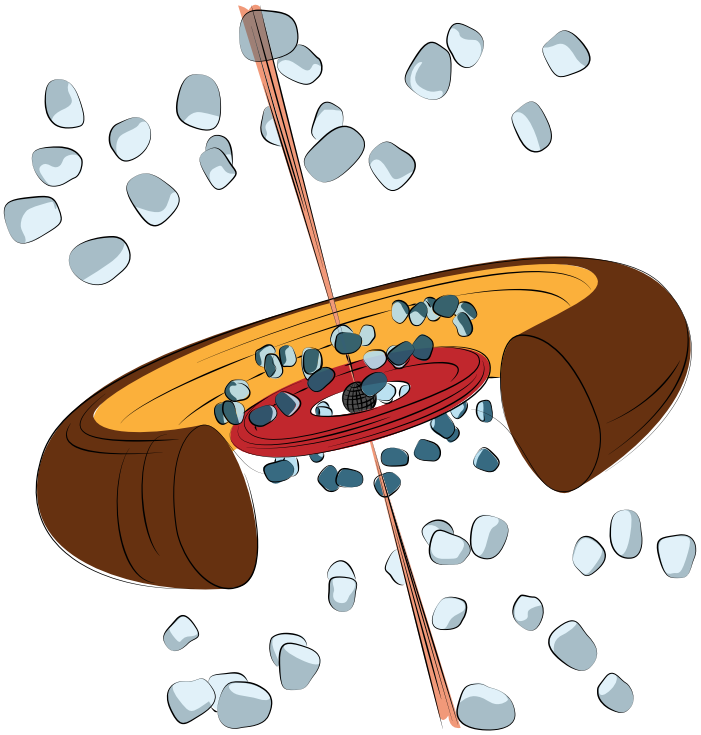

Figure 1.1: Sketch of the unified AGN model with a central SMBH (black) surrounded by an accretion disc (red) and a dust torus (brown). Gas clouds in the BLR (dark blue) are located inside the dust torus, gas clouds in the NLR (pale blue) outside. A jet (orange) does not occur in all AGN (Sketch by S. Kiehlmann, based on Urry and Padovani, 1995).

Figure 1.1 shows a sketch of the unified AGN model containing a SMBH, an accretion disc, a dust torus, gas clouds in the BLR and NLR, and in the case of a radio-loud AGN a jet. The AGN itself is located in the centre of a host galaxy. All components contribute differently to the overall electromagnetic spectrum of the AGN.

The largely accepted model assumes a SMBH at the very centre of the AGN. The order of the central black hole mass typically ranges from 10^6 to 10^{10} solar masses. The SMBH is surrounded by an accretion disc feeding the black hole. This system of SMBH and accretion disc is occasionally referred to as the *central engine*

of an AGN. Due to friction, angular momentum of the gas is transported outward and the gas is moving to lower orbits around the black hole down to the Innermost Stable Circular Orbit (ISCO) below which the gas plunges into the black hole. While moving inward the gas looses potential energy and heats up. Consequentially, the accretion disc produces *thermal radiation*. The temperature of the disc is higher at smaller radii. Thus, the emission of the disc can be modelled as a series of black body radiators integrated over the whole temperature distribution of the disc. The thermal emission from the disc typically ranges from optical to ultraviolet or soft X-rays and peaks at ultraviolet frequencies. This contribution to the overall AGN spectrum is often referred to as the *Big Blue Bump*.

An outflow of disc material may be launched either thermally, radiation pressure driven, or magnetically driven, known as disc *wind*. This material can absorb radiation, appearing as blue shifted Broad Absorption Lines (BAL) if the motion of the wind has a fast component towards the observer.

The accretion disc is surrounded by a dust torus. While it is usually referred to as torus the actual shape and structure is not well determined. The dust torus is emitting thermal radiation peaking at infra-red frequencies, referred to as the IR bump in AGN spectra. The torus is opaque at optical frequencies.

The black hole is additionally surrounded by clouds of gas. This gas is excited by the radiation coming from the disc and then produces emission lines in the optical and ultraviolet range, when the atoms fall back to lower energy levels. As these gas clouds are circulating around the SMBH the emission is Doppler shifted and the integration over the total range of velocity components along the line of sight leads to a broadening of the observed emission lines. The location of those gas clouds producing emission lines is divided into two regions: the broad and the narrow line region. The BLR is close to the central black hole, at ~ 1 parsec distance, within the range of the dust torus. The width of the emission lines, typically measured in velocities corresponding to the circular motion of the gas clouds, ranges from 1000 to 10 000 kilometres per second. Depending on the orientation of the AGN towards the observer the BLR and the accretion disc may be obscured by the dust torus and no broad emission lines are visible in photometric spectra. Nevertheless, these broad lines may be visible in polarized light when scattered off the dust torus towards the observer. The scattering introduces the polarization of the light. The NLR is located beyond the dust torus, at an estimated distance of 10 to 1000 parsecs from the SMBH, and thus is never obscured. Narrow emission lines have a width of < 1000 kilometres per second. The gas density in the NLR is low enough to produce forbidden emission lines (e.g. [O III]). Forbidden lines always appear as narrow, never as broad lines. An observed broad emission line is usually a superposition of a narrow line component from the NLR, a broad line component from the BLR, and potentially a very broad, probably double-peaked component from the accretion disc.

A fraction of AGN produces relativistic jets. These outflows of matter extend far beyond the nucleus and even the host galaxy with sizes up to mega-parsecs. These jets emit synchrotron radiation from radio up to optical, ultraviolet, or even X-rays. The most energetic jets additionally produce X-ray and γ-ray emission, occasionally up to TeV-energy. We discuss the jet emission processes in more detail in section 1.2.

With bolometric luminosities typically about 10^{44} to 10^{48} erg/s, AGN often outshine their host galaxies. Nevertheless, for the less luminous AGN the host galaxy consisting of stars and gas may contribute significantly to the observed

spectrum.

This unified model of AGN can explain all typical characteristics of the many historically evolved sub-classes. The central engine, i.e. the SMBH and the accretion disc, is capable of maintaining the high energy output over long time scales with rapid variability at the same time. The different types of emission lines are explained by the gas clouds in the NLR and BLR, whereas the presence or absence of broad emission lines is related to dust torus which may or may not obscures the BLR and accretion disc depending on the orientation of the AGN with regard to the observer. Radio and γ-ray emission is explained by the presence of a relativistic jet.

1.1.3 AGN classification

The two main classifications of AGN are based on the optical and radio properties. The optical classification differs between *Type 1* AGN, which show broad ($\geq$ 1000 km/s) emission lines in the optical and ultraviolet spectral range, and *Type 2* AGN, which do not show broad emission lines. The radio classification differs between AGN which do and do not show strong radio emission compared to the optical emission. AGN with flux density at $5\,GHz$ at least ten times larger than the flux density at R-band, $f_{5\,\mathrm{GHz}} \geq 10 f_{\mathrm{R}}$, are called *radio-loud*, and *radio-quiet* otherwise. Most of the AGN are radio-quiet (80 % - 85 %, Kellermann et al. (1989)). *Seyfert 1 galaxies* are radio-quiet Type 1 AGN. They show narrow and broad emission lines. *Seyfert 2 galaxies* exhibit only narrow emission lines. In the unified model the system is seen relatively edge-on (regarding to the accretion disc) and the BLR and the accretion disc are hidden behind the dust torus. A broad line component may be visible in polarized light, when the spectral line emission is scattered at the backside of the torus towards the observer (e.g., NGC 1068, Antonucci and Miller (1985)). Generally, Seyfert galaxies have relatively low luminosity. Therefore, only close by Seyfert galaxies are visible and, consequentially, the host galaxy can be resolved. Seyfert are generally hosted in spiral galaxies. D. Osterbrok introduced a more detailed sub-classification of Seyfert galaxies into classes 1.2, 1.5, 1.8, 1.9 based on the relative strength of the narrow and broad components of the Balmer lines.

Radio-quiet QSOs (or *radio-quiet quasars*) are Type 1 AGN more luminous and at further distance than Seyfert 1 galaxies, otherwise there is no clear distinction between the two classes. The host galaxies of radio-quiet QSOs are unresolved and outshone by the nucleus.

LINER galaxies or *LINERs* (Low-ionization nuclear emission-line region) show emission lines from weakly ionized or neutral atoms. In contrast to Seyfert galaxies and QSOs highly ionized emission lines are rare. Consequentially, the power of the exciting source is significantly lower in LINERs. Due to the similarity of showing emission lines LINERs are often regarded to as AGN although it is still under debate if the source of energy is a SMBH with an accretion disc.

AGN with broad absorption lines (BALs) in optical and ultraviolet are classified as *BAL quasars*. Broad absorption lines are probably due to fast disc winds and may occur in Type 1 and Type 2 AGN.

The radio-loud counterpart to Seyfert 2 galaxies are *Narrow Line Radio Galaxies* (NLRG). They show the same optical properties as Seyfert 2 and additionally strong radio emission. Accordingly, *Broad Line Radio Galaxies* (BLRG) are radio-loud Type 1 AGN with the same optical properties as Seyfert 1 galaxies. *Radio-loud*

QSOs or *quasars*[2] are more luminous than BLRG. The luminosity distinction is not clearly defined and there is no further difference between the two classes.

Depending on the radio synchrotron spectrum, which can be described as a power-law function $F_\nu \propto \nu^{-\alpha}$ with spectral index α, the radio-loud quasars are further subdivided into *Flat Spectrum Radio Quasars* (FSRQ) for $\alpha \leq 0.5$ and *Steep Spectrum Radio Quasars* (SSRQ) for $\alpha > 0.5$. Flat Spectrum Radio Quasars (FSRQs) are highly variable throughout the entire spectrum, highly polarized at radio and optical frequencies and the extended radio emission region is dominated by a compact radio core. Thus, classifications as *Optically Violently Variable (OVV)* quasar, *Highly Polarized Quasar* (HPQ), and *Core Dominated Quasar* (CDQ) refer to the same type of object as the term FSRQ and vice versa.

BL Lac objects, named after their prototype BL Lacertae, show similar characteristics as FSRQs, namely high luminosity, strong variability, high polarization. The main observational difference is that BL Lac objects lack strong emission and absorption lines. Therefore, BL Lacs cannot be identified as Type 1 or Type 2 AGN. BL Lacs and FSRQs, collectively, are called *blazars*. In the picture of the unified model they have jets closely aligned with the line of sight and thus differ from other radio-loud AGN only by orientation. Relativistic effects explain the extreme luminosity (Doppler boosting) and fast variability (time compression). The entire spectrum is dominated by emission from the jet, resulting in high polarization in radio and optical bands due to synchrotron emission. BL Lacs are expected to be intrinsically weak, FSRQs intrinsically strong AGN. We describe the physical properties of blazars in more detail in section 1.2.

With radio interferometry an extended radio emitting region can be resolved for many radio-loud AGN, some of which show a two-sided jet. Those sources are additionally classified based on the morphology of the extended emission region (Fanaroff and Riley, 1974). If the separation of the two brightest points – one on each side of the central jet emitting source – is less than half the size the entire radio structure the source is classified as *Fanaroff-Riley Class I* (FR-I) otherwise as *Fanaroff-Riley Class II* (FR-II). FR-II sources are generally more luminous than FR-I sources at radio frequencies and FR-II jets are generally more collimated than FR-I jets.

1.2 Blazars

Blazars are radio-loud AGN with a relativistic jet closely aligned with the line of sight. Blazars include the FSRQs and the intrinsically less powerful BL Lac objects. Blazars typically show strong variability throughout the entire electromagnetic spectrum at time scales from hours to years (e.g. Gupta et al., 2008; Abdo et al., 2010b; Fuhrmann et al., 2014; Hayashida et al., 2015). Blazars are highly polarized in radio and optical (e.g. Agudo et al., 2014; Pavlidou et al., 2014).

1.2.1 Relativistic effects

The extreme luminosity and short time scales of variability can be (partially) attributed to relativistic effects. If an emission region in the jet moves with speed

[2]The terms *QSO* and *quasar* are often used interchangeably. Although quasar initially meant quasi-stellar radio source, equal to the term *radio-loud QSO*, it is also occasionally used in the term *radio-quiet quasar* instead of *radio-quiet QSO*. Therefore, it is recommendable to use the term *radio-loud QSO* or *radio-loud quasar* instead of *quasar* to avoid ambiguity.

v, the normalized speed is given as:

$$\beta = \frac{v}{\mathrm{c}} \leq 1, \tag{1.1}$$

where c is the speed of light. We point out that β is the normalized speed of the bulk motion and not of an individual particle. The corresponding bulk Lorentz factor is:

$$\Gamma = \frac{1}{\sqrt{1-\beta^2}} \geq 1. \tag{1.2}$$

With the angle between the jet flow direction and the line of sight θ the Doppler factor is given as:

$$\delta = \frac{1}{\Gamma(1-\beta\cos\theta)} \geq 1 \tag{1.3}$$

The Lorentz transformation from the rest frame of the emission region to the observer frame introduces various relativistic effects. As a result of time dilation the time scale of an observed event Δt^{obs} is shorter than the time scale Δt^{em} at which the event happens in the rest frame of the emission region:

$$\Delta t^{\mathrm{obs}} = \Delta t^{\mathrm{em}} \delta^{-1}. \tag{1.4}$$

Accordingly, the frequency of emitted and observed radiation changes, light is blue shifted when the jet is directed towards the observer:

$$\nu^{\mathrm{obs}} = \nu^{\mathrm{em}} \delta. \tag{1.5}$$

Due to relativistic aberration light emitted isotropically in the rest frame of the emission region is *beamed* into the direction of the motion. Combining relativistic aberration, blue shift, and time dilation the observed flux density $F^{\mathrm{obs}}_{\nu^{\mathrm{obs}}}$ at an observed frequency ν^{obs} relates to the flux density $F^{\mathrm{em}}_{\nu^{\mathrm{obs}}}$ emitted in the rest frame of the emission region through

$$F^{\mathrm{obs}}_{\nu^{\mathrm{obs}}} = F^{\mathrm{em}}_{\nu^{\mathrm{obs}}} \delta^{3+\alpha}, \tag{1.6}$$

assuming the radiation spectrum follows a power-law $F_\nu \propto \nu^{-\alpha}$ with spectral index α. The observed flux density appears much stronger than the intrinsic flux density. This effect is known as *relativistic beaming*, *Doppler beaming*, or *Doppler boosting*.

Direct observational evidence for relativistic speeds of jets is given by apparent *superluminal motion* (e.g., Gubbay et al., 1969; Pearson et al., 1981; Porcas, 1983; Biretta et al., 1999). Emission features visible in a series of high resolution images (e.g. through Very Long Baseline Interferometry (VLBI) observations) appear to move across the sky faster than the speed of light. This is a projection and light travel time effect. Between two images the emitting region has moved closer to the observer, thus, the light has to move a shorter distance. Consequentially, the

time between the two taken images is shorter than the time of the motion and the velocity is overestimated. The apparent velocity component projected on the sky is given by:

$$\beta_{\mathrm{app}} = \frac{\beta \sin\theta}{1 - \beta \cos\theta}, \tag{1.7}$$

where β is the actual normalized velocity and θ is the angle between the direction of motion and the line of sight.

1.2.2 Jet launching, acceleration and collimation

The relativistic jets of AGN are extremely fast (Lorentz factors up to ~ 50, Lister et al. (2009)) and well collimated outflows. The launching as well as the acceleration and probably the collimation of the jet require a magnetic field. Jet launching models are generally based on one of two mechanisms. Blandford and Znajek (1977) propose an electromagnetic process supported by external, electric currents flowing in the black hole magnetosphere, capable of extracting energy and angular momentum from a rotating black hole. The magnetic field is provided by a magnetized accretion disc. The second mechanism was proposed by Blandford and Payne (1982). Here, energy and angular momentum are extracted from the rotating accretion disc. Again the magnetic field plays a major role. In a very simplistic explanation particles extracted from the accretion disc are slingshot along the magnetic field lines. To collimate a jet either an ordered magnetic field is needed or external gas pressure. The latter could be a disc wind, the BLR gas close to the central engine or the intergalactic medium (IGM) for the large scale jet (e.g., Spruit, 2010).

1.2.3 Spectra and emission processes

The Spectral Energy Distribution (SED) $\nu F_\nu(\nu)$ of blazars[3] is dominated by two main components: the low-energy component typically ranging from radio frequencies to optical, ultraviolet, or X-rays; the high energy component typically ranging from X-rays to GeV or TeV γ-rays (e.g. Abdo et al., 2010c). The low-energy component is produced by synchrotron radiation and self-absorption. The frequency at which the synchrotron component has its maximum is called the *synchrotron peak frequency* ν_{peak}. Blazars are occasionally sub-classified into *Low-Synchrotron-Peaked* (LSP, $\nu_{\mathrm{peak}} < 10^{14}\,\mathrm{Hz}$), *Intermediate-Synchrotron-Peaked* (ISP, $10^{14} \leq \nu_{\mathrm{peak}} \leq 10^{15}\,\mathrm{Hz}$), and *High-Synchrotron-Peaked* (HSP, $\nu_{\mathrm{peak}} < 10^{15}\,\mathrm{Hz}$) blazars. The high energy component can be explained by different processes, including inverse Compton scattering and hadronic particle cascades. Additionally, the *big blue bump*, i.e. thermal radiation from the accretion disc, may contribute significant power in the optical, ultraviolet, X-ray range (c.f. section 1.1.2).

Synchrotron radiation and self-absorption

The low-energy component is produced by synchrotron radiation. Any charged particle moving through a magnetic field follows a spiral trajectory. The continuous

[3]The SED is typically plotted as the logarithmic flux density $\log \nu F_\nu$ [JyHz] over the logarithmic frequency $\log \nu$ $[Hz]$.

change of direction equals an acceleration and, thus, results in the emission of radiation. The synchrotron radiation of a single electron in a magnetic field of strength B peaks at frequency:

$$\nu_{\rm sy} \approx 2.8 \cdot 10^6 \cdot B[\rm G] \cdot \gamma^2 \, \rm Hz. \tag{1.8}$$

At frequencies $\nu \ll \nu_{\rm sy}$ the spectrum[4] follows $F_\nu \propto \nu^{1/3}$. At frequencies $\nu \gg \nu_{\rm sy}$ the spectrum has an exponential cut-off $F_\nu \propto \nu^{1/2} \mathrm{e}^{-\nu}$.

In the case of a population of relativistic particles a broad spectrum of *synchrotron radiation* is emitted. If the energy distribution of the particles follows a power-law

$$n(\gamma) \propto \gamma^{-p}, \tag{1.9}$$

where $n(\gamma)$ is the number density of particles at any Lorentz factor γ with index p, the resulting synchrotron spectrum also follows a power-law

$$F_\nu \propto \nu^{\alpha_{\rm sy}}. \tag{1.10}$$

The spectral index $\alpha_{\rm sy}$ is related to the particle energy distribution through:

$$\alpha_{\rm sy} = \frac{p-1}{2}. \tag{1.11}$$

A power-law particle energy distribution can be produced by the Fermi mechanism (Fermi, 1949). Particles are gradually accelerated, when successively reflected off regions of higher than average magnetic field strength, called *magnetic mirrors*. The Fermi mechanism can occur generally in a turbulent plasma and is particularly efficient at a shock front (Marscher, 2009). A shock wave is typically preceded and followed by magnetic inhomogeneities, reflecting and accelerating particles which pass through the shock front. These particles gain energy with every crossing of the shock. The amount of energy gained is proportional to the velocity of the shock. This process is called *First order Fermi acceleration. Second order Fermi acceleration* occurs in the presence of randomly moving magnetic mirrors in magnetized gas clouds. An alternative to *shock acceleration* is *magnetic reconnection* (Nalewajko et al., 2011).

Typically, in modelling a truncated power-law energy distribution is assumed with a low energy cut-off at $\gamma_{\rm lo}$ and a high energy cut-off at $\gamma_{\rm hi}$. Then, the synchrotron spectrum follows (Böttcher et al., 2012):

$$F_\nu \propto \begin{cases} \nu^{1/3} & \text{for } \nu \ll \nu_{\rm sy}(\gamma_{\rm lo}) \\ \nu^{\alpha_{\rm sy}} & \text{for } \nu_{\rm sy}(\gamma_{\rm lo}) \lesssim \nu \lesssim \nu_{\rm sy}(\gamma_{\rm hi}) \\ \nu^{1/2} \mathrm{e}^{-\nu} & \text{for } \nu \gg \nu_{\rm sy}(\gamma_{\rm hi}). \end{cases} \tag{1.12}$$

At frequencies below $\nu_{\rm SSA}$ the synchrotron radiation is absorbed by the same electron population that produces the radiation. The plasma is optically thick

[4]The spectrum is typically plotted as the logarithmic spectral flux density $\log F_\nu$ [Jy] over the logarithmic frequency $\log \nu$ [Hz].

at $\nu \leq \nu_{\rm SSA}$ and optically thin at $\nu > \nu_{\rm SSA}$. This effect is called Synchrotron Self-Absorption (SSA). In the optically thick part $\nu \leq \nu_{\rm SSA}$ the spectrum follows an inverted power-law with frequency dependence (Böttcher et al., 2012):

$$F_{\nu,\rm SSA} \propto \begin{cases} \nu^{5/2} & \text{if } \nu_{\rm SSA} < \nu_{\rm sy}(\gamma_{\rm lo}) \\ \nu^{2} & \text{otherwise.} \end{cases} \tag{1.13}$$

Leptonic models: Inverse Compton scattering

There are two fundamentally different models to explain the high energy component of the typical blazar SED from X-rays up to TeV γ-rays. The first is the *leptonic model*, in which leptons, i.e. electrons (and maybe positrons) play the major role in the production of high energy photons. Through the Inverse Compton (IC) process these highly relativistic particles can scatter low energy photons to X-ray and γ-ray energies (e.g. Böttcher, 2012; Böttcher et al., 2013). For relativistic electrons with Lorentz factor γ and initial photons in the Thomson scattering limit, i.e. for low initial photon energies, the frequency $\nu_{\rm IC}$ of the up-scattered photon relates to the frequency $\nu_{\rm seed}$ of the initial photon through:

$$\nu_{\rm IC} \sim \gamma^2 \nu_{\rm seed}. \tag{1.14}$$

The initial low energy photons may originate from various *seed photon fields*. If the seed photons come from the synchrotron radiation, i.e. the same electron population produces synchrotron photons and scatters these to higher energies, this process is called Synchrotron Self-Compton (SSC). If the seed photons do not originate from the jet itself but from an external region the process is called External Compton (EC). External photon fields include radiation from the AGN accretion disc (ECD), the dust torus (ECT), the BLR (ECL), and the Cosmic Microwave Background (ECCMB). Böttcher et al. (2012, Fig. 8.5) illustratively sketches the potential contribution of the SSC and various EC contributions to a blazar SED.

Hadronic models: Particle cascades

When the magnetic field strength is high enough (several tens of Gauss) to accelerate protons to relativistic velocity, two processes can produce high energy photons (X-rays and γ-rays). First, the relativistic protons in a strong magnetic field emit synchrotron radiation. Second, the interaction of photons and relativistic protons can lead to particle cascades including various decay processes (Bethe-Heitler pair production, pion decay, $\gamma\gamma$ absorption). In these processes high energy photons are emitted either directly or as synchrotron radiation from the decay products (electrons, positrons, muons, and mesons). As in the leptonic IC model the initial seed photons starting the particle cascades might originate from the jet itself (Synchrotron-Proton Blazar (SPB)), i.e. the electron synchrotron radiation at low energies (radio to optical), or different external components of the AGN (e.g. Böttcher, 2012; Böttcher et al., 2013).

Stationary[5] blazar models with more than 10 model parameters are generally not well constrained by observed SEDs. So far, radio to γ-ray SEDs do not allow

[5]Stationary modelling does not consider the blazar variability. Either a time averaged SED or a single snapshot SED is fit with a stationary model.

to discriminate between leptonic and hadronic models. Even different types of the same model class are not necessarily well constrained. Occasionally, different leptonic models (IC, EC, and combined) fit the same data reasonably well. And different model parameter sets may produce roughly the same result consistent with the data (e.g. Böttcher, 2012; Böttcher et al., 2013; Böttcher et al., 2012).

1.2.4 Polarization

Magnetic fields play a major role in the launching, acceleration, and collimation of jets and in the emission processes. In the presence of a magnetic field, charged particles emit synchrotron radiation. This radiation is polarized perpendicular to the magnetic field lines. The emission from blazars at radio and optical frequencies is highly polarized (e.g. Agudo et al., 2014; Pavlidou et al., 2014). This polarization was the initial direct evidence for the existence of magnetic fields in the jets and for the nowadays largely accepted model that the low-energy part of the blazar spectrum is due to synchrotron radiation.

The polarization fraction, that is the ratio of the polarized light over the total light, is related to the uniformity of the magnetic field. The polarization angle or EVPA is related to the orientation of the magnetic field. Since the first optical polarization measurements (e.g. Kinman, 1967) it is known that blazars exhibit strong variation of the polarization fraction and angle. Large rotations of the optical polarization angle are of special interest (Marscher et al., 2008; Larionov et al., 2008; Abdo et al., 2010a; Marscher et al., 2010). Two main classes of models are attributed to these rotations. On the one hand stochastic variation is considered in a turbulent medium and a turbulent magnetic field (e.g. Jones et al., 1985; D'Arcangelo et al., 2007; Marscher, 2015). On the other hand geometric effects are considered. These include a bending jet trajectory (e.g. Nalewajko, 2010; Abdo et al., 2010a) and the helical motion of an emission feature in a helical magnetic field (e.g. Kikuchi et al., 1988; Marscher et al., 2008, 2010). Also in the class of deterministic, though not geometric, effects is the superposition of two emission regions with different magnetic field orientation (Holmes et al., 1984). The integrated polarization fraction and angle changes when the relative intensity of two emission regions changes. This model can be extended to multiple emission regions and is closely related to the stochastic multi-cell models, when the variation is implemented stochastically. Zhang et al. (2014) and Zhang et al. (2015) introduced a different model, in which a shock compresses the initial helical magnetic field and relativistic aberration and time delay effects lead to an EVPA rotation. The compression of the magnetic field by a passing shock was initially discussed by Laing (1980) in the context of a tangled magnetic field.

The discussion of EVPA rotations is closely related to the magnetic field structure. Whether the magnetic field follows a well behaved, geometric structure (e.g. helical) or is highly tangled, is an open question. Stochastic EVPA swing models generally assume a tangled magnetic field. Magnetic reconnection as an acceleration process for relativistic particles also requires a highly tangled magnetic field. However, Kikuchi et al. (1988), Marscher et al. (2008), Marscher et al. (2010), Zhang et al. (2014), and Zhang et al. (2015) assume a helical magnetic field at the optical emission site. Rotation measure gradients, based on VLBI measurements, are interpreted as direct evidence of helical magnetic fields (e.g., Gabuzda et al., 2004). Yet, the magnetic field structure and the origin of large EVPA rotations remain an open discussion.

1.3 The Quasar Movie Project

As discussed in the previous section, two of the main questions in blazar physics regard the origin of the γ-ray emission and the structure of the magnetic field. Yet, no conclusive answer has been found whether leptonic or hadronic models correctly explain the production of high energy photons in blazars. This question is closely related to the matter content of the jets, whether it is electrons with or without positrons, protons, ions, or a mixture. Even under the assumption of a leptonic jet, the seed photon field participating in the IC scattering is not conclusively determined. The question whether a SSC process or an EC process is responsible for the high energy radiation is directly related to the question where this process takes place.

The main aim of the Quasar Movie Project is to understand and to locate the origin of the γ-ray emission in blazars using multi-wavelength monitoring and high-resolution VLBI observations of two archetypical gamma-ray bright quasars, 3C 273 and 3C 279. An unprecedented densely-sampled VLBI monitoring campaign was carried out between 2010 and 2012, observing 3C 273 and 3C 279 roughly every 20 days with the Very Long Baseline Array (VLBA) at six frequencies from 5 to 86 GHz. At the same time a broad-band monitoring campaign incorporated dozens of ground-based radio, millimetre, infrared and optical telescopes together with X-ray and gamma-ray satellites. The analysis of the variability at various frequencies and cross-correlation analysis will reveal physical connections between the emission processes at different bands. The reduced VLBI data will yield information about structural, spectral and polarization changes in the parsec-scale radio jets during the campaign period. Correlations between structural changes and the variability at different frequencies may hint to the emission sites in the jets. In addition, the dense sampling in time and frequency allows to produce a time series of spectra. These data offer an excellent opportunity to test various stationary and time dependent blazar models.

Furthermore, the Quasar Movie Project data set includes multiple polarization curves at optical, millimetre, and radio frequencies. The optical data combined offers an unprecedented densely-sampled polarization curve, allowing to test different models of EVPA swing mechanisms against it.

This PhD project deals with the processing and the analysis of the multi-wavelength photometry and polarimetry data of 3C 279.

1.4 3C 279

3C 279, also designated PKS 1253-05 and J1256.1-0547 in the 2FGL catalogue[6], is one of the brightest and most studied blazars. It was the very first object for which superluminal motion ($\beta_{\rm app} = 21 \pm 4$) was observed (Whitney et al., 1971; Cotton et al., 1979). It is located in the southern sky at right ascension $12^{\rm h}56^{\rm m}11.1^{\rm s}$ and declination $-05^{\rm d}47'22''$ in J2000.0 equatorial coordinates, at redshift $z = 0.5362 \pm 0.0004$ (Marziani et al., 1996).

3C 279 shows narrow and broad emission lines and is, thus, classified as quasar (Marziani et al., 1996). Based on the optical variability it is classified as OVV quasar (Webb et al., 1990), based on the radio-spectrum as FSRQ (Healey et al., 2007). In 1991, 3C 279 was detected with the Energetic Gamma Ray Experiment

[6] 2nd year Fermi Gamma-ray LAT Point Source Catalogue

Telescope (EGRET) on the Compton Gamma Ray Observatory (Hartman et al., 1992). In 2008, emission at TeV energies was detected from 3C 279 with the Major Atmospheric Gamma-Ray Imaging Cherenkov (MAGIC) telescopes (Errando et al., 2008). The AGN has a SMBH mass of $M_{\mathrm{SMBH}} = 10^{8.9\pm0.5}\,M_{\odot}$ and is located in a bright host galaxy ($M_{\mathrm{R}} = -23.8$) (Nilsson et al., 2009).

3C 279 has been extensively monitored with VLBI over more than four decades (e.g. Whitney et al., 1971; Cotton et al., 1979; Jorstad et al., 2005; Chatterjee et al., 2008; Homan et al., 2009; Lister et al., 2009; Agudo et al., 2010; Lu et al., 2013). The projected jet structure at VLBI scales extends to south-west. The jet is closely aligned with the line of sight (viewing angle $2.1 \pm 1.1\,^{\circ}$), well collimated (half opening angle 0.4 ± 0.2), and relativistic (average Lorentz factor $\langle\Gamma\rangle = 15.5 \pm 2.5$ (Jorstad et al., 2005). Different components of the jet flow show a variety of speeds (Jorstad et al., 2005; Chatterjee et al., 2008) and may be accelerating (Bloom et al., 2013). The jet is linearly and circularly polarized (Wardle et al., 1998; Homan et al., 2009) and the observation of circular polarization has led to different interpretations about the matter content of 3C 279: pair plasma (Wardle et al., 1998) or proton-electron plasma (Homan et al., 2009).

Various broadband variability studies have been performed to analyse the variability at different bands through Power Spectral Density (PSD) estimations (e.g., Chatterjee et al., 2008; Hayashida et al., 2012; Park and Trippe, 2014), to understand the physical connection between the emission processes at different frequencies though cross-correlation analysis (e.g., Wehrle et al., 1998; Chatterjee et al., 2008; Larionov et al., 2008; Hayashida et al., 2012), and to test different blazar models against the observed SEDs (same references as before). Whereas the radio and mm light curves generally appear to lag behind the variability at higher frequencies in 3C 279 (Chatterjee et al., 2008) and probably generally in blazars (Fuhrmann et al., 2014), the correlation between γ-rays, X-rays, and optical frequencies appears to change over time. Zero time lag between optical and γ-ray indicating a co-spatial emission region (Wehrle et al., 1998; Abdo et al., 2010a) and γ-rays leading the optical variation attributed to „different profiles of the decreasing magnetic and radiation energy densities along the jet“ (Hayashida et al., 2012) have been reported. Chatterjee et al. (2008) pointed out time-dependent changes of the time lags between X-rays and optical bands, interpreted as the presence of two independent processes connecting these bands. In Abdo et al. (2010a) and Hayashida et al. (2012) an X-ray *orphan flare* without counterpart in γ-rays or optical has been reported. And most recently, Aleksić et al. (2014) do not find any correlation between γ-rays, X-rays, and optical arguing for three different emission regions for the γ- and X-ray, the optical bands, and the radio emission.

A special interest has been shown in optical EVPA rotation events coinciding with optical and γ-ray flaring epochs. Larionov et al. (2008) reported a simultaneous counter-clockwise EVPA swing of $\sim 300\,^{\circ}$ in ~ 100 days at optical and 43 GHz between January 2007 and July 2007 interpreted as an emission feature on a helical trajectory tracing different parts of a helical magnetic field. γ-ray data was not yet available at that time. End of February 2009 a clockwise rotation of the optical EVPA was observed of $208\,^{\circ}$ in 18 days coinciding with a γ-ray flare. Hayashida et al. (2012) interpret the simultaneous occurrence of the optical polarization swing and the γ-ray flare as indicator for a co-spatial emission region and the polarization swing as bending jet. Aleksić et al. (2014) report a new optical polarization rotation and coinciding γ-ray flaring event happening between May and June 2011. This counter-clockwise rotation of $140\,^{\circ}$ in ~ 30 days, again, is interpreted as a bending

jet, despite the opposite rotation sense with regard to the rotation in 2008.

All flaring events between September 2007 and August 2012, and EVPA rotation events between November 2008 and August 2012 are captured by the data set of the Quasar Movie Project. We introduce the photometry data in the following chapter.

Chapter 2

Photometry data

The Quasar Movie Project (QMP) has acquired a large photometry data set including light curves at radio frequencies, mm, sub-mm, infrared, optical and ultraviolet bands, X-rays and γ-rays. All telescopes contributing photometry data to the QMP are listed in table 2.1. We describe the collected light curves and further processing of the data in sections 2.2 to 2.5. In the next section we introduce different methods we use to process the data. Especially, we introduce a new method of cross-calibrating light curves and a new, iterative method of averaging data.

2.1 Data processing methods:

In the following sections we introduce our cross-calibration method (section 2.1.1) and averaging algorithm (section 2.1.2) and discuss the extinction correction (section 2.1.3) and the magnitude-to-flux density conversion (section 2.1.4).

2.1.1 Cross-calibration

At various bands we have gathered data from multiple observatories as shown in table 2.1. The goal is to combine all data sets within the same band to achieve a much better time sampling than usually is possible with a single telescope. Differences in the instrumentation and in the data reduction schemes can lead to different flux values for data points gathered at the same time but with different instruments. When different light curves are combined these differences add noise to the intrinsic variation, potentially at all time scales, which may affect the light curve analysis like, for instance, the power spectral density estimation. We correct for these instrumental differences by cross-calibrating the individual data sets within one band. The cross-calibration algorithm consists of three parts, the *pair-wise cross-calibration*, the *successive cross-calibration*, and the *randomized cross-calibration*, which are described in the following. Generally the cross-calibration algorithm operates in magnitude scale, where calibration differences show up as offsets; flux density values are first converted to a logarithmic scale $f_i \rightarrow \log_{10}(f_i)$.

Pair-wise cross-calibration: We consider two light curves consisting of triplets of time values, flux values, and flux uncertainties (t_i, f_i, σ_i). One light curve $(t_{\mathrm{cal},i}, f_{\mathrm{cal},i}, \sigma_{\mathrm{cal},i})$ is calibrated regarding to a reference light curve $(t_{\mathrm{ref},j}, f_{\mathrm{ref},j}, \sigma_{\mathrm{ref},j})$. For each time $t_{\mathrm{cal},i}$ the closest data point $t_{\mathrm{ref},j}$ is identified selecting j such that $|t_{\mathrm{cal},i} - t_{\mathrm{ref},j}|$ is minimized. Only quasi-simultaneous pairs $[i, j]$ of data points are considered for which $|t_{\mathrm{cal},i} - t_{\mathrm{ref},j}| \leq \Delta t_{\mathrm{qs}}$ where Δt_{qs} denotes the maximum allowed

Table 2.1: Observatories contributing photometry data to the Quasar Movie Project.

Observatory/Observer	Tel. diam.	Filter
	cm, mm, sub-mm	
UMRAO, USA	26 m	5, 8, 15 GHz
OVRO, USA	40 m	15 GHz
Metsähovi, Finland	14 m	37 GHz
Effelsberg[1], Germany	100 m	2.7, 5, 8.3, 11, 15, 23, 33 GHz
IRAM[1], Spain	30 m	86, 142, 229 GHz
SMA, Hawaii	8× 6 m	229, 345 GHz
APEX[1], Chile	12 m	345 GHz
	infrared	
Campo Imperatore, Italy	1.1 m	K, H, J
Kanata, Japan	1.5 m	Ks, J
OAGH, Mexico	2.12 m	Ks, H, J
REM, Chile	0.6 m	K, H, J
SMARTS, Chile	0.9-1.5 m	K, J
	optical	
AAVSO, USA	var.	I, R, V, B
Abastumani, Georgia	0.7 m	R
Calar Alto, Spain	2.2 m	R
CrAO, Ukraine	0.7 m	I, R, V, B
Kanata, Japan	1.5 m	V
T. Krajci[2], USA	0.36 m	I, R, V
NMS T11, USA	0.5 m	R, V
Perkins, USA	1.83 m	I, R, V, B
ROVOR, USA	0.4 m	R, V
SAAO, South Africa	0.76 m	I, V, B
SAO RAS, Russia	1.0 m	I, R, V, B
R.D. Schwartz, USA	0.41 m	I, R, V, B
SMARTS, Chile	0.9-1.5 m	R, V, B
OAN-SPM, Mexico	0.84 m	R
St. Petersburg, Russia	0.4 m	I, R, V, B
Steward, USA	1.52 m, 2.3 m	V, 4609 Å
Swift-UVOT, space	0.3 m	V, B, U
	ultraviolet	
Swift-UVOT, space	0.3 m	W1, M2, W2
	X-ray	
RXTE, space		2.4-10 keV
Swift-XRT, space		0.3-10 keV
	γ-ray	
Fermi-LAT, space		0.1-300 GeV

[1] Data from these observatories contain observations performed in the framework of the F-Gamma project.

[2] Observing as member of the Center for Backyard Astrophysics.

time difference. On the one hand $\Delta t_{\rm qs}$ should be chosen as small as possible to avoid intrinsic variation at time scales shorter than $\Delta t_{\rm qs}$ contaminating the cross-calibration. On the other hand $\Delta t_{\rm qs}$ has to be large enough to obtain a significant amount of data pairs. Even if some intrinsic variation can be expected at shorter time scales, this is less critical for non-periodic and unevenly sampled light curves. The intrinsic contribution should average out if a sufficient number of data pairs has been identified, but it cannot be guaranteed for any number data pairs as it depends on the intrinsic variation and the exact sampling.

Over all pairs i, j the error-weighted mean of the point-wise flux offsets is calculated:

$$f_{\rm cal} = \frac{\sum\limits_{i,j} w_{i,j} \cdot (f_{{\rm ref},j} - f_{{\rm cal},i})}{\sum\limits_{i,j} w_{i,j}} \text{ with} \tag{2.1}$$

$$w_{i,j} = \begin{cases} \left(\sigma^2_{{\rm cal},i} + \sigma^2_{{\rm ref},j}\right)^{-1} & \text{if} \quad |t_{{\rm cal},i} - t_{{\rm ref},j}| \leq \Delta t_{\rm qs} \\ 0 & \text{otherwise,} \end{cases} \tag{2.2}$$

with the uncertainty:

$$\sigma_{\rm cal} = \left(\sum_{i,j} w_{i,j} \right)^{-1/2}. \tag{2.3}$$

The calibration-offset is applied to the magnitudes as an additional term

$$f_{{\rm calibrated},i} = f_{{\rm cal},i} + f_{\rm cal}, \tag{2.4}$$

or as a factor to flux densities

$$f_{{\rm calibrated},i} = 10^{f_{\rm cal}} \cdot f_{{\rm cal},i}. \tag{2.5}$$

Successive cross-calibration: The single cross-calibration algorithm fails, when no quasi-simultaneous data points in the reference and the calibration light curve can be found. To enhance the reference basis, all light curves within the same band are calibrated successively. The first light curve is calibrated regarding to a reference using the *pair-wise cross-calibration*, the calibration is applied and both light curves are combined as the new reference curve. Subsequently the next light curves are calibrated and added to the reference curve. Light curves which cannot be calibrated because there are no quasi-simultaneous data points with the reference curve are queued and calibrated as soon as possible. This process allows to cross-calibrate all light curves if each light curve overlaps - has quasi-simultaneous data points - with another light curve successively back to the reference data. Light curves which do not overlap with any other light curve - remaining in the queue - cannot be cross-calibrated.

Randomized cross-calibration: The calibration-offsets determined by the *successive cross-calibration* may depend on the order in which the data sets are calibrated and added to the reference data. This can be the case when multiple light curves overlap in the same time interval. Then the choice of the quasi-simultaneous

data pairs may differ depending on the data that is already part of the reference light curve. To get a better estimate of the appropriate calibration offsets independent of the calibration order we repeat the *successive cross-calibration* with different orders. We implement two options for randomization. In the first one a reference light curve is preselected and always kept as the initial reference, while the order of the successive calibration is varied. In the second one no reference curve is preselected and the order of all light curves is varied. For up to six light curves, $N \leq 6$ (not including the optional reference data), we iterate through all $N!$ combinations of possible orders. For more than six light curves 1 000 random permutations are chosen. For each iteration the calibration offsets for all light curves are stored, with zero offset for the first light curve - the initial reference. The final calibration offset for each light curve is calculated as the average over all iterations. This average may optionally be weighted (a) by the offset uncertainties σ_{cal} (eq. (2.3)) or (b) by the inverse of the number of data points of the initial reference data in each iteration (if no reference data is preselected) trusting longer data sets more than shorter ones as reference data.

2.1.2 Iterative averaging

Most of the professionally observed data has one data point per night at maximum, while some of the amateur data sets from the AAVSO campaign contain several, up to 50 short exposures per night, but with much larger uncertainties. We need to average data within very short time intervals to remove noise at the order of the uncertainties, which otherwise affects the further data processing (e.g. the cross-calibration) and the data analysis (e.g. the power spectral density estimation and cross-correlation analysis). One scheme often applied is to bin the data in an even time grid with a bin width equal to the averaging time interval. Multiple data points in one bin are then averaged. This scheme is problematic, when two close data points, which should be averaged, fall into two adjacent bins. To avoid this case we implement an algorithm that iteratively selects data ranges which fall into the averaging time scale. We describe this algorithm in the following.

The time series consists of a series of sorted time steps t_i, $i = 1, \ldots, N$ with a measured observable and a corresponding uncertainty at each t_i. Here, we consider only the time steps t_i to explain how the data ranges, which should be averaged, are selected. The averaging time interval is Δt_{avg}. We illustrate some steps of the algorithm in fig. 2.1 with $\Delta t_{\mathrm{avg}} = 10$.

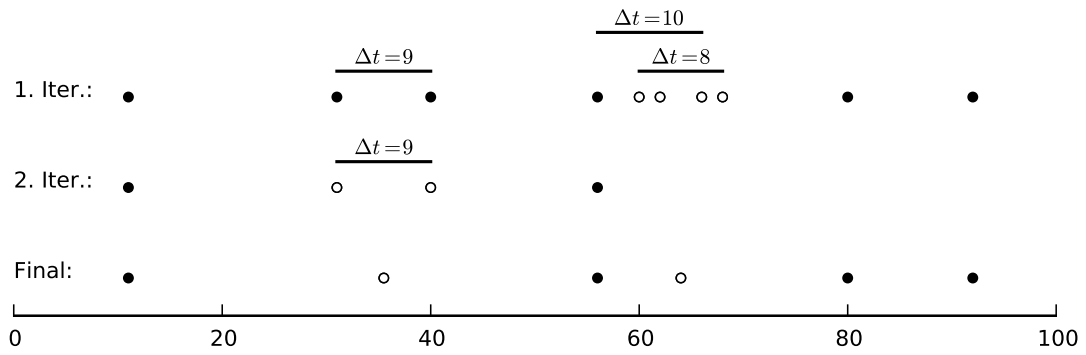

Figure 2.1: Exemplary illustration of the averaging time range selection.

Step 1: find all averaging data ranges. The algorithm iterates through all time

steps. For each t_i the data points are selected which fall into the time interval $[t_i - \Delta t, t_i]$. If multiple data point lie in this interval, the data range is stored. If this data range is an extension of the previously stored range, then no new range is stored but the latest is updated. This step is illustrated in the first row of fig. 2.1 marked as iteration 1. The first data range is found at the third data point ranging over the second and third data point. The second range is found at the fourth data point which is successively extended up to the seventh data point. A third range is identified from the fifth to the eighth data point. After iterating through all data points the algorithm has obtained a list of identified ranges, in the example figure the three ranges are marked by horizontal bars.

Step 2: optimal range selection. Of all identified data ranges the shortest is selected for averaging. In the example we have two ranges overlapping. Choosing the shortest range ensures that the algorithm averages over the data points which are the closest. In fig. 2.1 the selected range is marked by open circles.

Step 3: recursion. Steps 1 and 2 are repeated recursively over all data points before and after the data range selected in the prior recursion step. The recursion stops once no further averaging ranges are found. The second iteration in fig. 2.1 shows the identification of potential averaging ranges for data points one to four. Splitting the data and performing steps 1 and 2 recursively ensures that no data points are averaged multiple times. In the example the mean over data points five to eight is closer to data point four than Δt_{avg}. Performing steps 1 and 2 iteratively over the full data would successively average data point four to eight although the time range is larger than Δt_{avg}. This is avoided by the splitting and recursion.

The next iterations in the example would select the fourth data point and then the last two data points, which should not be averaged. As shown in the final row of fig. 2.1, two ranges of data points get averaged in the example. The algorithm ensures that for each data point t_i no others data point are in the range $[t_i - \Delta t_{\mathrm{avg}}/2, t_i + \Delta t_{\mathrm{avg}}/2]$. The time difference between any two data points is $\geq \Delta t_{\mathrm{avg}}/2$. For each averaging range we use the arithmetic mean to calculate the averaged time. For the corresponding data values any other type of average (e.g. weighted mean) may be chosen.

2.1.3 Extinction correction

All observations in infrared, optical and ultraviolet bands are affected by galactic extinction due to dust in the Galaxy. A fraction of the light that was emitted by the extragalactic source gets absorbed by galactic dust it passes through. The absorption depends on the wavelength of the light and the total amount of dust along the line of sight. An extinction correction term A_λ can be calculated following Cardelli et al. (1989):

$$\left\langle \frac{A_\lambda}{A_V} \right\rangle = \frac{a(\lambda) + b(\lambda)}{R_V}, \tag{2.6}$$

where A_V is the extinction at V-band, R_V is the ration of the V-band extinction and B-V colour excess $R_V = A_V / E_{B-V}$ and $a(\lambda)$ and $b(\lambda)$ are empirical relations described by Cardelli et al. (1989), eq. 2a-5b. We assume $R_V = 3.1$ (e.g. Cardelli et al., 1989; Schlegel et al., 1998) and use $A_V = 0.0886$ attained from the NASA/IPAC Infrared Science Archive (`http://irsa.ipac.caltech.edu/applications/DUST/`). We have calculated extinctions corrections for 3C 279 for all relevant filters in infrared, optical, and ultraviolet. The filter properties and the extinction corrections

are listed in tables 2.2 and 2.3. The extinction correction is subtracted from the light curves in magnitude scale.

Table 2.2: Optical/infrared filters: extinction correction, effective wavelength, zero points and reference.

filter	A_λ [mag]	λ_{eff} [μm]	ZP [Jy]	reference
B	0.1173	0.44	4260	[1]
4609 Å	0.1106	0.46		
V	0.0885	0.55	3640	[1]
R	0.0747	0.64	3080	[1]
I	0.0542	0.79	2530	[1]
J	0.0247	1.26	1603	[2]
H	0.0168	1.60	1075	[2]
K_s	0.0104	2.159	666.7	[3]

[1] λ_{eff} and ZP taken from Bessell (1979), table 4.
[2] λ_{eff} and ZP taken from Campins et al. (1985), tables 1, 4.
[3] λ_{eff} and ZP taken from Cohen et al. (2003), table 2.

Table 2.3: UVOT-filters: extinction correction, effective wavelength, zero points and conversion factor.

filter	A_λ [mag]	λ_{eff}[1] [μm]	ZP[1] [counts]	f_0[1] [erg/s/cm^2/Å]
W2	0.2599	0.2030	17.35	$6.2 \cdot 10^{-16}$
M2	0.2730	0.2231	16.82	$8.50 \cdot 10^{-16}$
W1	0.1869	0.2634	17.49	$4.00 \cdot 10^{-16}$
U	0.1410	0.3501	18.34	$1.63 \cdot 10^{-16}$

[1] Taken from Poole et al. (2008), table 6, 8, 10.

2.1.4 Flux scale conversion

The infrared, optical and ultraviolet light curves are calibrated in the magnitude scale, which is an inverse, logarithmic scale of the spectral flux density. For the cross-correlation analysis and the production of SED[1] it is necessary to transform magnitudes into flux densities. UVOT-magnitudes m are converted to spectral flux densities F_ν following Poole et al. (2008):

$$F_\nu = \frac{\lambda_{\text{eff}}^2}{\text{c}} \cdot f_0 \cdot 10^{(ZP-m)/2.5}, \tag{2.7}$$

with λ_{eff}, ZP and f_0 listed in table 2.3 and c the speed of light. All other magnitudes are converted to F_ν by:

$$F_\nu = ZP \cdot 10^{-m/2.5}, \tag{2.8}$$

with the corresponding ZP given in table 2.2.

[1] We have produced a time series of SEDs but not yet analysed the SEDs. Therefore we will not discuss them in this thesis.

2.2 Radio, mm and sub-mm data

Radio, mm and sub-mm light curves were acquired from different observatories and blazar monitoring campaigns. The F-Gamma project provides 2.7, 5, 8.3, 11, 15, 23, 33, 43, 86, and 142 GHz observations between October 2010 and March 2012 made at the Effelsberg 100 m telescope in Germany operated by the Max Planck Institute for Radioastronomy and the 30 m telescope on Pico Valeta in Spain operated by the Institut de Radioastronomie Millimétrique (IRAM) (Fuhrmann et al., 2014; Angelakis et al., 2015). The 37 GHz light curve from January 2009 to May 2012 was observed at the 14 m Metsähovi Radio Observatory operated by the Aalto University in Finland (Teräsranta et al., 1998, 2004). Observations at 15 GHz were performed at the 40 m telescope of the Owens Valley Radio Observatory (OVRO) in California, USA as part of the OVRO 40 M Telescope Fermi Blazar Monitoring Program (Richards et al., 2011). The light curve ranges from January 2008 to March 2012. The University of Michigan Radio Astronomy Observatory (UMRAO) provides data at 5, 8, and 15 GHz observed between October 2010 and February 2012 with the 26 m telescope (Aller et al., 1985).

The light curves in mm and sub-mm bands are provided by IRAM, SMA and APEX. At the IRAM 30 m telescope observations at 86 GHz and 229 GHz were performed between April 2010 and January 2012 (Agudo et al., 2010, 2014) additional to the F-Gamma 86 and 142 GHz observations. Further 229 GHz data and 345 GHz data is provided by the Submillimeter Array (SMA), a radio interferometer consisting of eight 6 m telescopes located on Mauna Kea in Hawaii. The data starts in January 2003 and continues to March 2013 (Gurwell et al., 2007). Additional 345 GHz data was observed with the 12 m Atacama Pathfinder Experiment (APEX) telescope between May 2007 and June 2011 (Larsson et al., 2012).

We carefully remove outliers from the light curves. The identified outliers deviate by more than 10 % from the enclosing data points and no corresponding variation is seen in close-by bands. All light curves are averaged within 0.5 days. We cross-calibrate the following sets of light curves using the method described in section 2.1.1 (*ref* marks the calibration reference) and combine them: APEX 870 μm (ref) and SMA 870 μm; IRAM 1.3 mm (ref) and SMA 1.3 mm; F-Gamma 3.5 mm (ref) and IRAM 3.5 mm; F-Gamma 21 mm (ref), OVRO 20 mm and UMRAO 21 mm; F-Gamma 36 mm (ref) and UMRAO 36 mm; F-Gamma 62 mm (ref) and UMRAO 62 mm. The chosen maximum time interval of quasi-simultaneous data points is $\Delta t_{\rm qs} = 10$ d. The cross-calibration factors are listed in table 2.4. No extinction correction is applied at (sub-)mm- and cm-bands.

2.3 Infra-red, optical, and ultraviolet data

We have gathered data of 3C 279 in infrared, optical, and ultraviolet bands observed at various telescopes. Some of these data have been observed as part of several monitoring campaigns. We briefly introduce the observatories and campaigns which contributed data to the Quasar Movie project. Details about the data reduction for each telescope are given in the corresponding references.

The QMP collaboration organized a multi-wavelength observation campaign of 3C 279 (and 3C 273) between October 2010 and March 2012 which includes observations from the AAVSO, CrAO, T. Krajci, NMS T11, OAGH, REM, ROVOR,

Table 2.4: Cross-calibration offsets at sub-mm, mm, and cm bands.

Filter	Obs.	Cal. factor
345 GHz	APEX	reference
345 GHz	SMA	0.889 ± 0.014
229 GHz	IRAM	reference
229 GHz	SMA	0.985 ± 0.011
86 GHz	IRAM[1]	reference
86 GHz	IRAM[2]	0.95 ± 0.017

[1] F-Gamma
[2] Agudo

Filter	Obs.	Cal. factor
15 GHz	Effelsberg	reference
15 GHz	OVRO	0.975 ± 0.004
15 GHz	UMRAO	0.968 ± 0.003
8 GHz	Effelsberg	reference
8 GHz	UMRAO	0.98 ± 0.004
5 GHz	Effelsberg	reference
5 GHz	UMRAO	0.987 ± 0.004

SAAO, SAO RAS, R.D. Schwartz, SPM, and Swift. The American Association of Variable Star Observes (AAVSO)[2] contributed observations in I, R, V, and B-band between November 2003 and June 2012. Observations with the 1 m Zeiss-1000 telescope at the Special Astrophysical Observatory of the Russian Academy of Science (SAO RAS), additional observations with the 70 cm AZT-8 telescope at CrAO, and by T. Krajci, A. Sadun (including the observations with the Remote Observatory for Variable Object Research (ROVOR) 40 cm telescope and the 50 cm New Mexico Skies (NMS) telescope 11) and R. D. Schwartz employed various software implementations of the differential aperture photometry technique to measure brightness of 3C 279 on CCD images obtained through colour filters intended to implement the spectral response curve close to the one of Cousins (1976) R_C system. An appropriate circular aperture size was chosen by each observer based on seeing conditions. An attempt was made to standardize the list of comparison stars used in the campaign by suggesting the observers to use the list maintained at LSW Heidelberg[3], but it was not always possible to follow this in practice. Some observers used ensemble photometry while others employed a single comparison star. In particular, the SAO RAS and the AZT-8 CrAO telescope images were reduced (see Doroshenko et al., 2005) using the star N9 from González-Pérez et al. (2001). The observations started in January 2011 and ended in May 2012. I_c, V, and B-band light curves were obtained between January 2011 and January 2012 at the South African Astronomical Observatory (SAAO) At the 84 cm telescope of the Observatorio Astronómico Nacional - San Pedro Mártir (OAN-SPM) R-band data was gathered between January 2011 and April 2012 (Sorcia et al., 2013).

Near-infrared observations in K_s, H, J-band are obtained from the Observatorio Astrofísico Guillermo Haro (OAGH) 2.12 m telescope which is operated in Sonora, Mexico by the Instituto Nacional de Astrofísica, Optica y Electronica (INAOE) (Carraminana et al., 2010; Abdo et al., 2011). We have acquired data between February 2008 and July 2011. Between March 2011 and June 2011 near infrared observations in K, H, and J-band were conducted at the 60 cm Rapid Eye Mount (REM) telescope in Chile, operated by the Italian Istituto Nazionale di Astrofisica (INAF), using the REMIR infrared camera (Dolcini et al., 2005)

The Ultraviolet/Optical Telescope (UVOT) is an instrument mounted

[2] http://www.aavso.org/
[3] http://www.lsw.uni-heidelberg.de/projects/extragalactic/charts/1253-055

on the Swift satellite (Roming et al., 2005). The UVOT is equipped with three optical filters U, B, V and three ultraviolet filters W1, M2, W2 (Poole et al., 2008). We have acquired data in all six bands from January 2006 until May 2012.

During its 96 minute orbit, Swift switches between multiple targets. Each target is often observed during a few consecutive revolutions, so a typical Swift/UVOT observation consists of a series of sub-exposures (typically from 10 to 1500 seconds long) which are often stacked during the post-processing to get a daily-average measurement with improved SNR and magnitude limit (Sokolovsky, 2009). However, in this work we follow Sokolovsky (2009) and process the sub-exposures individually to improve time resolution. Custom-made routines based on CFITSIO library[4] are used to split multi-image daily data files provided by the Swift Archive into FITS-images containing individual sub-exposures and extract middle-of-exposure times associated with them.

Aperture photometry of 3C 279 was performed by K. Sokolovsky[5] using the standard Swift tool `uvotsource` from the HEASoft package[6] It sums-up all the counts within the source region (5" diameter circular aperture centred on the source position) and divides this number by the exposure time to obtain count rate. The background count rate (estimated in an annulus with the inner radius of 10" and the outer radius of 23") is subtracted and the magnitude is computed from the coincidence-corrected net count rate following Poole et al. (2008). The magnitudes used in this work are in the Vega system.

The Boston University Blazar Research Group[7] provided additional data from CrAO, Perkins, St. Petersburg, and Calar Alto. I, R, V, B-band light curves were observed at the 70 cm telescope of the Crimean Astrophysical Observatory (CrAO) located in the Ukraine starting in June 2005 until June 2012 (Larionov et al., 2008; Jorstad et al., 2010). The 1.8 m Perkins telescope of Lowell Observatory in Arizona, USA observed in I, V, B-band from April 2011 to June 2012, and R-band from March 2006 to June 2012 (Jorstad et al., 2010). Additional I, R, V, B-band data was observed with the 40 cm telescope of St. Petersburg State University in St. Petersburg, Russia between January 2001 and May 2012 (Jorstad et al., 2010). Observations in R-band at the 2.2 m of the Calar Alto Astronomical Observatory in Spain were conducted as part of the Monitoring AGN with Polarimetry at the Calar Alto Telescopes (MAPCAT)[8] project (Jorstad et al., 2010; Agudo et al., 2012). We have obtained data between July 2007 and February 2012.

The Calar Alto observatory, CrAO, SAAO, and SPM are also participating in the WEBT-collaboration[9] (e.g. Böttcher et al., 2007; Larionov et al., 2008). We have obtained further data observed within the WEBT-collaboration from Abastumani and Campo Imperatore. The Abastumani Astrophysical Observatory in Georgia provided R-band data observed with the 70 cm Maksutov Meniscus telescope between November 2010 and July 2012 (Kurtanidze and Nikolashvili, 1999, 2002). K, H, J-band data was observed at the 1.1 m AZT-24 telescope at

[4] `http://heasarc.gsfc.nasa.gov/fitsio/fitsio.html`

[5] Affiliation: (1) Astro Space Center of Lebedev Physical Institute, Profsoyuznaya 84/32, 117997, Moscow, Russia, (2) Sternberg Astronomical Institute, M.V.Lomonosov Moscow State University, Universiteskij prosp. 13, Moscow 119991, Russia

[6] For more details see the Swift-UVOT Software Guide `https://archive.stsci.edu/swiftuvot/UVOT_swguide_v2_2.pdf`

[7] `https://www.bu.edu/blazars/`

[8] `http://www.iaa.es/~iagudo/_iagudo/MAPCAT.html`

[9] `http://www.oato.inaf.it/blazars/webt/`

Campo Imperatore, Italy between March 2008 and May 2012 (Larionov et al., 2008; Jorstad et al., 2010).

The Higashi-Hiroshima Observatory provided V, K_s, and J-band data observed at the 1.5 m Kanata telescope between December 2009 and June 2011. Observations before February 2010 were performed with the TRISPEC instrument (Watanabe et al., 2005), later observations with HOWPol (Kawabata et al., 2008; Hayashida et al., 2015).

The Small & Moderate Aperture Research Telescope System (SMARTS) consortium organized by Yale University operates four telescopes with aperture sizes 0.9 m, 1.0 m, 1.3 m, and 1.5 m at Cerro Tololo in Chile. We have attained K, J, R, V, B-band light curves from the SMARTS blazar campaign between February 2008 and May 2012 (Bonning et al., 2012; Chatterjee et al., 2012).

The Steward Observatory spectropolarimetric monitoring project of the University of Arizona maintains an open access data base of LAT-monitored blazars[10]. We are using the V-band light curve observed between November 2008 and July 2012 with the Bok 2.3 m telescope located on Kitt Peak in Arizona, USA and the 1.54 m Kuiper telescope located on Mt. Bigelow in Arizona, USA (Smith et al., 2009). Additionally, Patiño-Álvarez et al. (2015) provide observations of continuum emission at 4609 Å wavelength, which corresponds to redshift-corrected 3000 Å, measured from spectra observed at the Steward Observatory between November 2008 and July 2011.

We apply the cross-calibration method introduced in section 2.1.1 to all light curves observed within the same filter to correct for instrumental and calibration differences. We set the maximum time difference of quasi-simultaneous data points to $\Delta t_{\mathrm{qs}} = 3$ d.We select the following fixed reference light curves: SMARTS (B, V, R, J), St. Petersburg (I), OAGH (H, K_s). We cross-calibrate K-band and K_s-band combined to the OAGH K_s-band light curve and treat all light curves as K_s-band light curves afterwards. Cross-calibration between light curves in slightly different bands strictly is only possible if the colour does not change over time. In fig. 2.2 the colour indices $B - V$, $V - R$, and $R - J$ are plotted over time. These indices are calculated from coinciding SMARTS data. The colour indices exhibit significant variation with standard deviations between 0.12 and 0.14 but do not show continuous trends on time scales larger than $\gtrsim 500$ days. The K and K_s-band light curves are long enough such than the cross-calibration will not to be affected by a continuous colour change.

After the applied cross-calibration we notice a systematic offset of the SAO RAS light curves regarding to other calibrated light curvs in the same band. The offset changes its sign at JD 2455800 systematically through all bands. Therefore, we split the SAO RAS light curves at JD 2455800 and cross-calibrate data before and after this data separately. The origin of this systematic difference is unknown. No changes to the telescope or instrument are reported at that time. The calibration offsets before and after JD 2455800 differ by ~ 0.07 magnitude.

We carefully remove outliers comparing inter- and cross-band light curves. We remove data points that deviate from the combined ultraviolet, optical and infrared light curves by $\gtrsim 0.5$ mag if no comparable variation is seen in the neighbouring bands.

To reduce the observational noise we average data points within 0.5 days. The variation at smaller time scales is at the order of the uncertainties, therefore we

[10] http://james.as.arizona.edu/~psmith/Fermi/

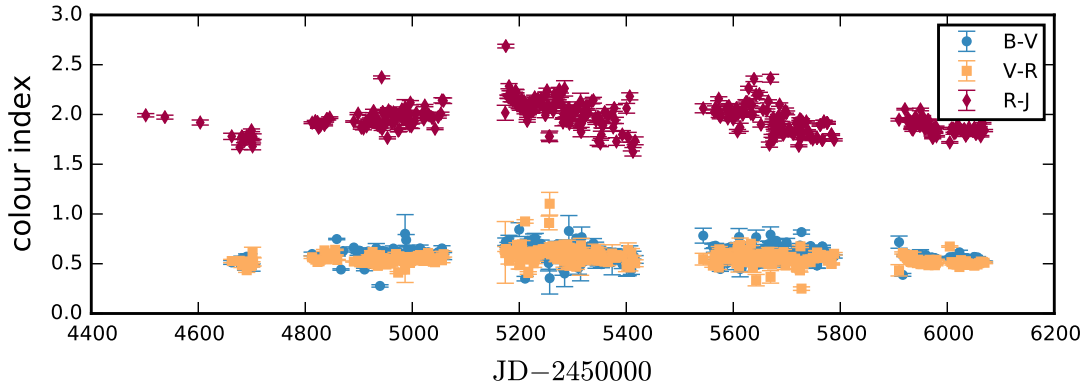

Figure 2.2: Colour indices of 3C 279 based on simultaneous SMARTS data.

do not remove significant real variation. We use the iterative averaging scheme introduced in section 2.1.2. For each identified data range of half a day, which contains multiple data points, we calculate the uncertainty weighted magnitude. After the removal of outliers and averaging we determine the cross-calibration offsets anew, apply them to the original, non-averaged data and re-check the data for outliers. We repeat the steps of removing outliers, averaging and cross-calibration until all outlying data points have been reliably identified and removed. The final cross-calibration offsets are determined and applied after averaging the individual light curves.

In table 2.5 all light curves and the corresponding cross-calibration offsets are listed, which are included in the combined light curves at B, V, R, I, J, H, and K_s-band. The calibration offsets are at the order of 0.1 mag or lower. Observatories which contributed just a single data point are excluded. We combine all light curves of the same band into a single data set. We also combine the K and K_s band data. Slight magnitude offsets are adjusted by the cross-calibration and the whole data set is treated as K_s-band light curve in the following. All combined light curves are averaged again within 0.5 days.

We apply the corresponding extinction correction A_λ given in tables 2.2 and 2.3 to each light curve and convert magnitudes to spectral flux densities F_ν [mJy] following eqs. (2.7) and (2.8).

2.4 X-ray data

We have attained three X-ray light curves from data acquired with Swift-XRT and RXTE-PCA. The Rossi X-Ray Timing Explorer (RXTE) is a spaceborne X-ray telescope equipped with three instruments: the All-Sky Monitor (ASM, Levine et al. (1996)) operating at 2-12 keV, the Proportional Counter Array (PCA, Glasser et al. (1994)) with an energy range of 2-60 keV, and the High Energy X-ray Timing Experiment (HEXTE, Rothschild et al. (1998)) operating at 15-250 keV. The Boston University Blazar Group provides a reduced X-ray light curve to the Quasar Movie Project based on RXTE-PCA data observed between January 1996 and December 2011, modelled and integrated over the energy range 2.4-10 keV. Details about the data reduction are presented in Chatterjee et al. (2008).

The Swift satellite (Gehrels, 2004; Nousek, 2004) is equipped with three instruments: the Burst Alert Telescope (BAT), the Wolter Type I X-ray

Table 2.5: Cross-calibration offsets at optical and infrared bands.

Filter	Obs.	Cal. offset [mag]
B	SMARTS	reference
B	AavsoFJQ	0.048 ± 0.001
B	AavsoMGW	0.07 ± 0.002
B	AavsoSGOR	0.02 ± 0.001
B	AavsoSRIC	-0.085 ± 0.002
B	CrAO[1]	0.044 ± 0.001
B	CrAO[2]	0.158 ± 0.001
B	Perkins	0.117 ± 0.001
B	SAAO	-0.021 ± 0.001
B	SAO RAS[3]	0.023 ± 0.001
B	SAO RAS[4]	0.1 ± 0.001
B	St. Pet.	0.082 ± 0.002
B	SwiftUVOT	0.11 ± 0.001
V	SMARTS	reference
V	AavsoBHU	0.0802 ± 0.001
V	AavsoBRAC	0.0743 ± 0.001
V	AavsoCTX	-0.0274 ± 0.002
V	AavsoDKS	0.1332 ± 0.001
V	AavsoFJQ	0.1175 ± 0.001
V	AavsoFJY	1.0427 ± 0.002
V	AavsoGCO	-0.0233 ± 0.002
V	AavsoJM	0.0301 ± 0.001
V	AavsoKKQ	-0.0053 ± 0.001
V	AavsoKSF	0.0801 ± 0.001
V	AavsoMGW	0.0402 ± 0.001
V	AavsoMZK	0.0924 ± 0.001
V	AavsoSGOR	0.0311 ± 0.001
V	AavsoSRIC	-0.2609 ± 0.004
V	AavsoTRF	0.0535 ± 0.001
V	AavsoWDZ	0.055 ± 0.004
V	CrAO[1]	0.0367 ± 0.001
V	CrAO[2]	0.0599 ± 0.001
V	Irkutsk	0.0219 ± 0.001
V	Kanata	-0.0741 ± 0.001
V	Krajci	0.0077 ± 0.001
V	Perkins	0.0216 ± 0.001
V	SAAO	0.0607 ± 0.001
V	SAO RAS[3]	0.0139 ± 0.001
V	SAO RAS[4]	0.0884 ± 0.001
V	NMS T11	0.0879 ± 0.001
V	St. Pet.	0.0831 ± 0.001
V	Steward	0.118 ± 0.001
V	SwiftUVOT	0.0074 ± 0.001

[1] Data from the Boston University Blazar group.
[2] Data from the dedicated Quasar Movie Project campaign.
[3] Before JD2455800.
[4] After JD2455800.

Filter	Obs.	Cal. offset [mag]
R	SMARTS	reference
R	AavsoBHU	0.123 ± 0.001
R	AavsoKSF	0.044 ± 0.001
R	AavsoMGW	-0.018 ± 0.001
R	AavsoSGOR	0.007 ± 0.001
R	AavsoSRIC	-0.155 ± 0.002
R	Abastumani	0.036 ± 0.001
R	CalarAlto	0.064 ± 0.001
R	CrAO (phot)[1]	0.004 ± 0.001
R	CrAO (pol)[1]	0.026 ± 0.001
R	CrAO (phot)[2]	0.769 ± 0.001
R	KVA	0.023 ± 0.001
R	Krajci	0.037 ± 0.001
R	Liverpool	-0.015 ± 0.001
R	Perkins (phot)	-0.045 ± 0.001
R	Perkins (pol)	0.066 ± 0.001
R	SAO RAS[3]	-0.013 ± 0.001
R	SAO RAS[4]	0.03 ± 0.001
R	SPM	0.022 ± 0.001
R	NMS T11	0.058 ± 0.001
R	St. Pet. (phot)	0.019 ± 0.001
R	St. Pet. (pol)	0.024 ± 0.001
I	St. Pet.	reference
I	AavsoMGW	-0.01 ± 0.001
I	AavsoSGOR	-0.016 ± 0.001
I	AavsoSRIC	-0.203 ± 0.004
I	CrAO[1]	0 ± 0.001
I	CrAO[2]	0.059 ± 0.001
I	Krajci	0.002 ± 0.001
I	Perkins	-0.058 ± 0.001
I	SAAO	-0.031 ± 0.001
I	SAO RAS[3]	-0.001 ± 0.001
I	SAO RAS[4]	-0.029 ± 0.002
J	SMARTS	reference
J	Campo Imp.	0.123 ± 0.001
J	Kanata	0.172 ± 0.001
J	OAGH	0.089 ± 0.002
J	REM	0.130 ± 0.001
H	OAGH	reference
H	Campo Imp.	0.04 ± 0.01
H	REM	0.06 ± 0.03
K_s	OAGH	reference
K	Campo Imp.	0.138 ± 0.003
K_s	Kanata	-0.030 ± 0.005
K	REM	-0.306 ± 0.007
K	SMARTS	0.475 ± 0.001

TELESCOPE (XRT, Burrows et al. (2004)), and the ULTRAVIOLET/OPTICAL TELESCOPE (UVOT, Roming et al. (2005)). The XRT has an energy range of 0.3-10 keV. The XRT data were processed by F. Schinzel[11] with standard procedures using the `xrtpipeline v0.12.6` to calibrate the observations and the HEASoft package version 6.11.1. Details about the data reduction can be found in Schinzel et al. (2011). We have obtained two energy flux density curves integrated over the energy ranges 0.3-10 keV and 2.4-10 keV from January 2010 to August 2011. The adopted energy range for spectral fitting in both cases is 0.3−10 keV. A fixed neutral hydrogen column density[12] of $n_{\mathrm{H}} = 2.1 \cdot 10^{20}\,\mathrm{cm}^{-2}$ was used for the Galactic absorption.

In fig. 2.3 we show the RXTE-PCA and Swift-XRT energy index and energy flux density over the over-lapping time after November 2009. The light curves show insignificant differences at the order of the uncertainties. Nevertheless, we do not combine both light curves to avoid introducing noise due to instrumental differences.

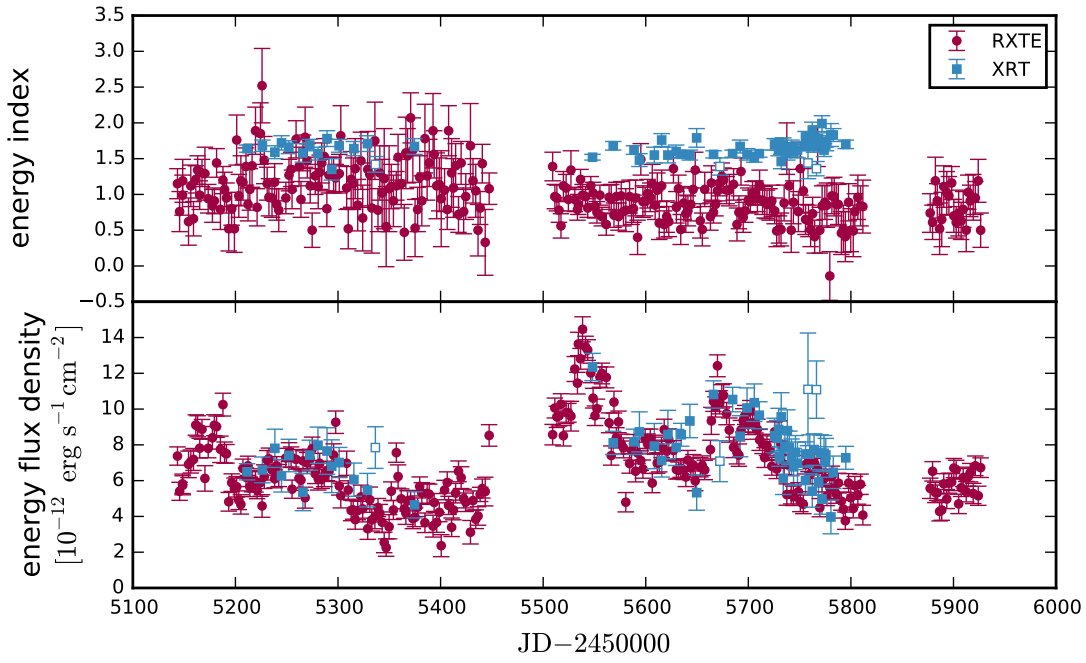

Figure 2.3: RXTE-PCA and Swift-XRT X-ray energy indices (upper panel) and light curves (lower panel) of 3C 279 starting November 2009. Open data points are flaged as outliers.

2.5 Gamma-ray data

The FERMI GAMMA-RAY SPACE TELESCOPE, launched in 2008 and formerly operated under the name GAMMA-RAY LARGE AREA SPACE TELESCOPE (GLAST) consists of two instruments: the GLAST BURST MONITOR (GBM) and the LARGE AREA TELESCOPE (LAT, Atwood et al. (2009)). The LAT operates at energies between 20 MeV and 300 GeV. We have reduced two photon flux density curves integrated over 0.1-300 GeV with daily and weekly binning from

[11] Affiliation: Department of Physics and Astronomy, University of New Mexico, Albuquerque NM, 87131, USA

[12] `https://www.astro.uni-bonn.de/hisurvey/`

August 2008 to September 2012 from the Pass 7 Dataset. We analysed LAT data for the sky region in which 3C 279 (2FGL J1256.1-0547) is located following the standard procedure[13], using the LAT analysis software `ScienceTools v9r27p1`. The photons were extracted from a region of interest (ROI) centered on the radio position of 3C 279 within a radius of 10 °. The *source* event class was applied to ensure that the collected events considered in this analysis have a high probability of being photons. Events above the zenith angle 100 ° were removed to avoid a significant contamination by γ-rays produced from cosmic-ray interactions in Earth's atmosphere. The P7SOURCE_V6 instrument response functions (IRF) were used. The background component of Galactic diffuse emission `gal_2yearp7v6_v0.fits` was added. Upper Limits for a test statistic $1 < \mathrm{TS} < 10$ were calculated using the profile method, for $\mathrm{TS} < 1$ the Bayesian method was used. Further details about the data reduction are given in Schinzel et al. (2011).

Additionally, we have two adaptively binned photon flux density curves in the same energy range 0.1-300 GeV with constant uncertainties of 15 % and 25 % between August 2008 and March 2012 reduced with the method presented by Lott et al. (2012).

2.6 The final multi-wavelength data set

Table 2.6 gives an overview over the final QMP photometry data set and the time sampling. The full data set covers 26 frequency bands. The light curves range from 1.3 years to 16 years in duration. Data throughout all bands is available from approximately JD 2454400. The median time sampling ranges from daily sampling at optical frequencies and γ-rays to roughly monthly sampling at radio frequencies. Especially at optical and infrared bands and at several cm and mm-bands we have achieved high sampling rates by combining data from up to 37 individual light curves.

[13] `http://fermi.gsfc.nasa.gov/ssc/data/analysis/`

Table 2.6: Time sampling of the light curves. The first column shows the band, columns 2-5 the total time and the minimum, maximum and median time step in days and column 6 the number of data points. The last column notes if a light curve is combined from different instruments.

Band	T	$\Delta t_{\rm min}$	$\Delta t_{\rm max}$	$\widetilde{\Delta t}$	N	
			radio			
114 mm	504	12.0	57.0	17.4	23	
62 mm	523	0.9	57.0	3.7	58	comb.
36 mm	523	0.7	57.0	3.0	67	comb.
29 mm	523	12.0	57.0	17.9	23	
21 mm	1536	0.6	54.8	2.3	371	comb.
13 mm	466	11.8	69.7	17.1	21	
			(sub-)mm			
9 mm	466	12.0	69.7	18.4	19	
8 mm	1247	0.9	50.9	2.0	297	
3 mm	703	0.7	70.0	13.7	46	comb.
2 mm	526	13.9	82.9	35.9	15	
1 mm	3709	0.6	202.1	4.1	380	comb.
870 μm	3906	0.7	311.0	10.2	130	comb.
			infrared			
Ks	1562	0.5	159.5	2.0	352	comb.
H	1550	0.6	299.7	4.2	73	comb.
J	1568	0.5	127.4	2.0	411	comb.
			optical			
I	2551	0.4	922.6	1.6	247	comb.
R	2335	0.5	319.8	1.1	645	comb.
V	3159	0.4	152.3	1.1	1056	comb.
B	2349	0.4	183.3	1.2	564	comb.
U	2311	0.5	383.1	2.2	171	
4609 Å	950	0.9	198.3	1.0	104	
			ultraviolet			
W1	2311	0.5	383.1	2.2	168	
M2	2311	0.5	383.1	2.0	131	
W2	2311	0.5	359.4	3.1	141	
			x-ray			
RXTE	5821	0.01	426.0	2.2	1850	
XRT	584	0.07	173.6	6.1	62	
			Fermi-LAT γ-ray			
1 d bin	1504	1.0	7.0	1.0	1383	
7 d bin	1498	7.0	7.0	7.0	215	
adbin 15unc	1300	0.5	33.3	3.2	252	
adbin 25unc	1314	0.1	15.6	1.2	663	

Chapter 3

Multi-wavelength flux variability

In this chapter, we show the photometry light curves throughout the entire frequency spectrum and briefly describe the observed variability. Furthermore, we estimate the PDF of the light curves.

3.1 3C 279 light curves

Figure 3.1 shows the combined Quasar Movie Project light curves of 3C 279 between Oct. 2007 and June 2012. We mark those time periods which have been discussed in the literature at the top of the figure.

We observe several flaring periods in these data. Two major flares in γ-rays around JD 2454800 and JD 2454880 are accompanied by a flux increase towards the first γ-ray flare and a flux decrease after the second γ-ray flare throughout all bands from X-rays to infrared. The whole flaring period lasts ~ 280 days. This flaring period is followed by two strong X-ray flares, which roughly have the same time separation as the previous γ-ray flares but are delayed by ~ 160 days. The first X-ray flare around JD 2454945 has no γ-ray counterpart and is accompanied only by a minor flux increase in infrared, optical and ultraviolet bands. After this first X-ray flare a second general flux increase starts in γ-rays and infrared to ultraviolet bands that lasts roughly 200 days and peaks at JD 2455045 in all bands from γ-rays to infrared, including the second prominent X-ray flare. All flares throughout late 2008 and 2009 occur during a continuous flux decrease in cm and mm bands.

In contrast, all the following flares between 2010 and mid-2012 occur during a continuous flux increase in the mm and radio bands, which starts in the 8 mm band roughly around the JD 2455045 flare. The radio flux increase continues for more than 2.5 years until the end of the data set and probably further. The 8 mm flux increase happens in several steps: the flux is increasing by a few Janskies within time scales at the order of 100 days, followed by roughly constant flux for a similar amount of time. Comparable behaviour can be seen in the other mm and cm bands. General non-flaring periods ($\sim$ JD $2455200-5400$ and $\sim$ JD $2455600-5660$) appear to coincide with periods of roughly constant flux in the 8 mm band. Between JD 2455200 and JD 2455400 3C 279 shows little variability at 8 mm to ultraviolet bands and generally low flux values at infrared to ultraviolet bands, compared to other periods. Between JD 2455300 and JD 2455400 also γ-rays do not show significant variability.

The strong γ-rays flare around JD 2455465 coincides with a flux increase at 8 mm. Unfortunately, X-rays to infrared bands have an observation gap, but the

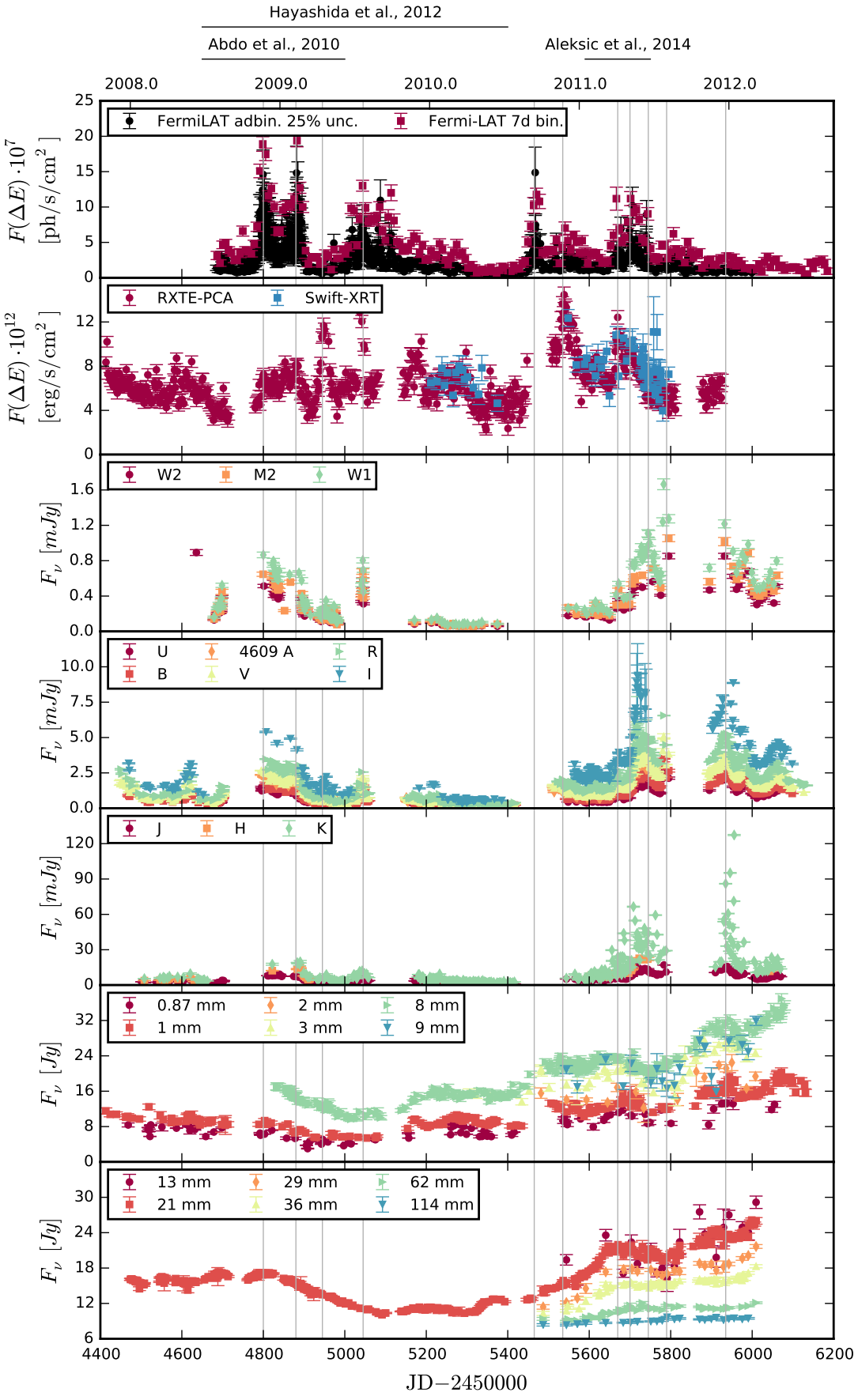

Figure 3.1: Light curves of 3C 279 between Oct. 2007 and June 2012. Top to bottom panel: Fermi-LAT γ-rays (0.1-300 GeV), X-rays (2.4-10 keV), ultraviolet, optical, infrared, sub-mm and mm bands, cm bands. Horizontal lines mark prominent peaks in different bands.

4609 Å light curve indicates a coinciding optical flare. 70 days later follows a strong X-ray flare accompanied by only weak variability in γ-rays compared to the previous γ-ray flare.

Around JD 2455670 a series of multiple flares in infrared, optical, ultraviolet begins. Before JD 2455800 this flaring epoch is coinciding with variability in X-rays and γ-rays. Several of the flare peaks in γ-rays, X-rays, and the optical range coincide but not all have counterparts in each other bands. The optical flaring period after $\sim$ JD 2455900 differs from the previous flaring periods as it is not accompanied by strong variability in the γ-rays.

In summary, we observe various combinations of events throughout the multi-wavelength data: optical, X-ray, and γ-ray flaring periods during a general radio flux rise and decrease; coinciding flares from γ-rays to infrared; an X-ray flare without γ-ray counterpart; and optical flares without γ-ray counterparts. Coincident flare peaks as in 2009 may indicate a co-spacial emission region of the infrared to ultraviolet and the X-ray and γ-ray bands, whereas time lags between flare peaks as possibly seen in 2011 may indicate different emission regions or different sizes of the emission region. If the optical frequency range is correlated with the γ-rays during the flaring period between JD 2455600 and JD 2455800 and the optical flaring period after the observation gap is a continuation of the same event, the lack of γ-rays during the continued optical flaring period could indicate a change in the ambient photon field. We discuss the correlation between different light curves in detail in chapter 5.

In the γ-ray, X-ray and optical light curves we see a spiky structure with flux increases by a factor up to ~ 6 times at time scales shorter than 20 days, whereas at mm to cm bands the peaks gradually become less pronounced and the variability is more dominated by variability on longer time scales. We estimate and discuss the power spectrum of the light curve variability throughout all bands in detail in chapter 4.

In the following section we estimate the probability density function of the light curves.

3.2 Estimation of the light curve probability density functions

In figs. 3.2 to 3.5 we show the adaptively binned Fermi-LAT light curve (25% unc.), the RXTE X-ray light curve, the V-band and 1 mm light curve and estimates of the corresponding Probability Density Function (PDF) and Cumulative Distribution Function (CDF). The direct estimate of the PDF and CDF (shown by black solid lines) depend on the sampling of the light curve. For example, reduced sampling, i.e. fewer observations during a quiescent state and better sampling during a flaring epoch reduces the estimated probability density at low flux values.

A better estimate of the intrinsic PDF and CDF is obtained, when the light curve is first interpolated to a regular time grid. We choose a time step of 0.1 days and interpolate linearly between data points. Long observation gaps > 50 days, which are expected to show significant variation deviating from a linear trend, are ignored in the interpolation. We show the estimated PDF and CDF based on the interpolated light curves as purple lines.

Figure 3.2 shows a large difference between the direct estimate and the interpolation based estimate of the distribution function. The reason is the adaptive binning.

The integration time of photon counts is shorter for higher flux values. Thus, the light curve is best sampled, i.e. has the most data points, during flares. Low flux requires longer integration time and results in fewer data points. Therefore, the direct PDF estimate is biased towards higher flux values.

We test the interpolation based distribution functions against Gaussian distributions with the Kolmogorov–Smirnov test (KS test). The hypothesis of Gaussian distributed light curves is rejected at 3σ significance for all four light curves. We perform this test for all light curves. For all well sampled light curves (21 mm, 1 mm, optical, infra-red, RXTE X-rays, and Fermi-LAT γ-rays) the hypothesis of Gaussian distributed light curves is rejected at 3σ significance, at least. For the less well sampled light curves the Gaussian distribution cannot be rejected. However, these bands show variation similar to close bands which are not normally distributed. For these cases we suppose that we have too few data points to characterize the distribution properly and assume the PDF is better characterized by the PDF estimate of a close band, which is better sampled. Therefore, we conclude that all light curves are not Gaussian distributed. This result affects the light curve simulation in chapters 4 and 5.

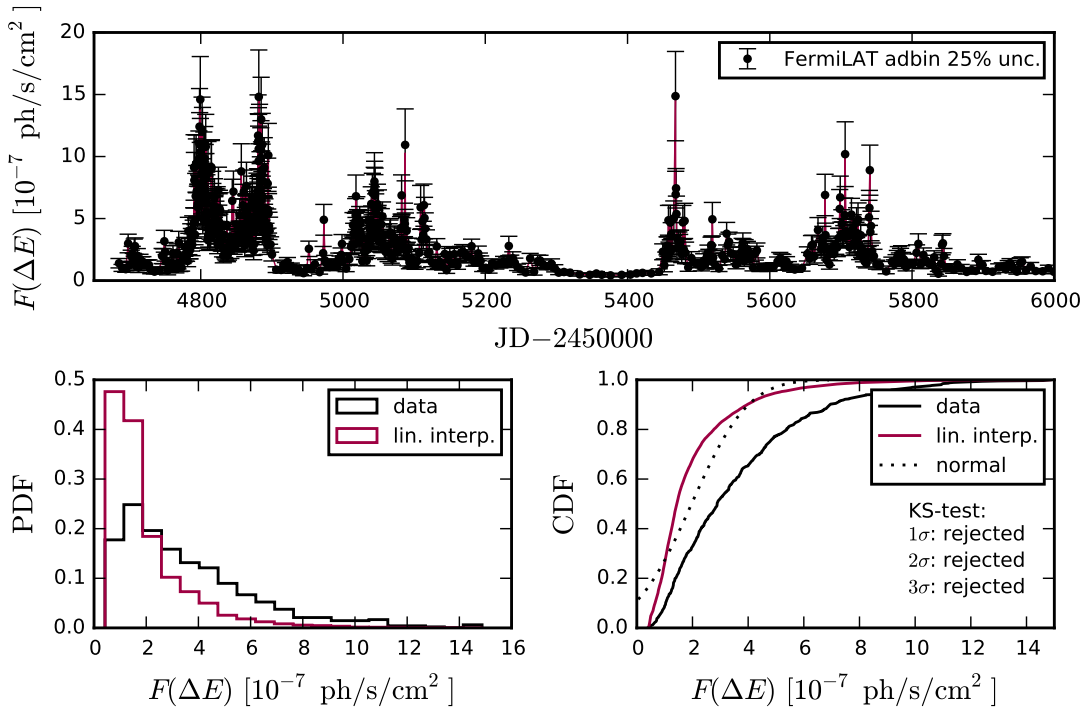

Figure 3.2: Estimation of the PDF of the adaptively binned (25 % unc.) Fermi-LAT γ-ray light curve. Upper panel: observed (black dots) and linear interpolated light curve (coloured lines). Lower left panel: PDF based on the data (black) and the linear interpolation (purple). Lower right panel: CDF based on the data (solid black) and the linear interpolation (solid purple) and the best fit Gaussian distribution.

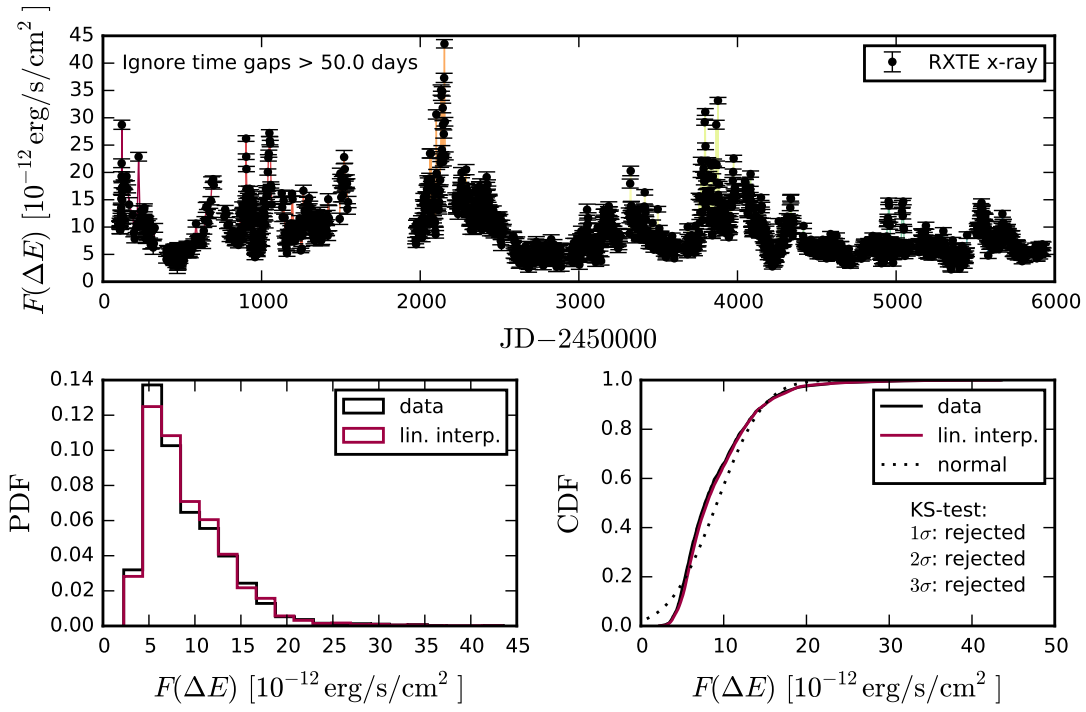

Figure 3.3: Estimation of the PDF of the RXTE X-ray light curve. Upper panel: observed (black dots) and linear interpolated light curve (coloured lines). Lower left panel: PDF based on the data (black) and the linear interpolation (purple). Lower right panel: CDF based on the data (solid black) and the linear interpolation (solid purple) and the best fit Gaussian distribution.

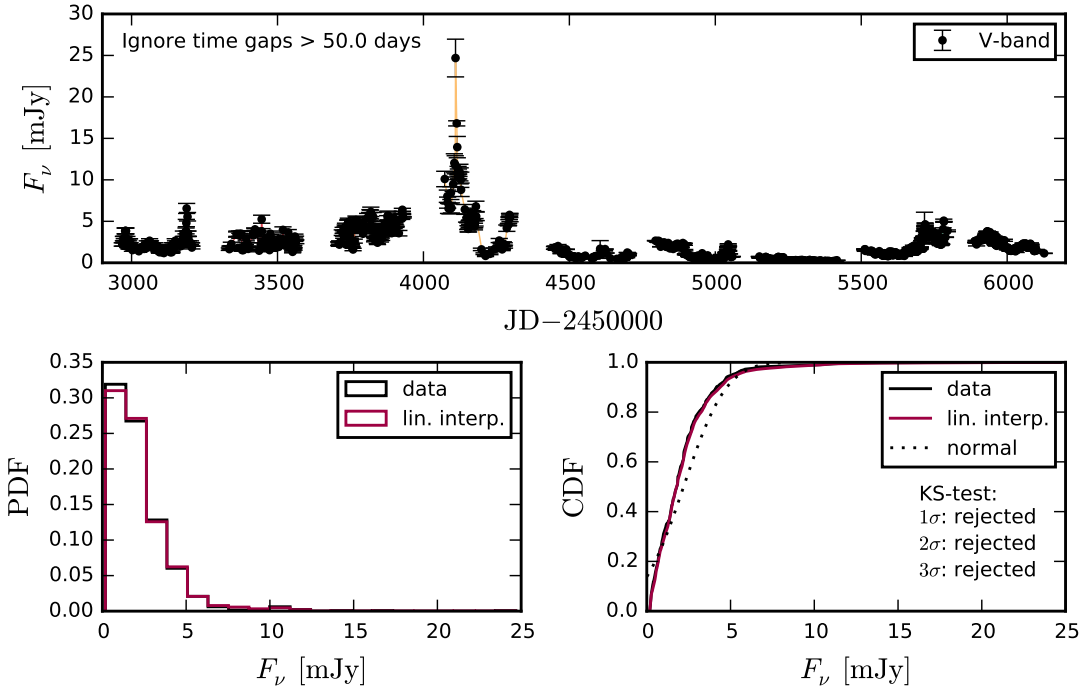

Figure 3.4: Estimation of the PDF of the V-band light curve. Upper panel: observed (black dots) and linear interpolated light curve (coloured lines). Lower left panel: PDF based on the data (black) and the linear interpolation (purple). Lower right panel: CDF based on the data (solid black) and the linear interpolation (solid purple) and the best fit Gaussian distribution.

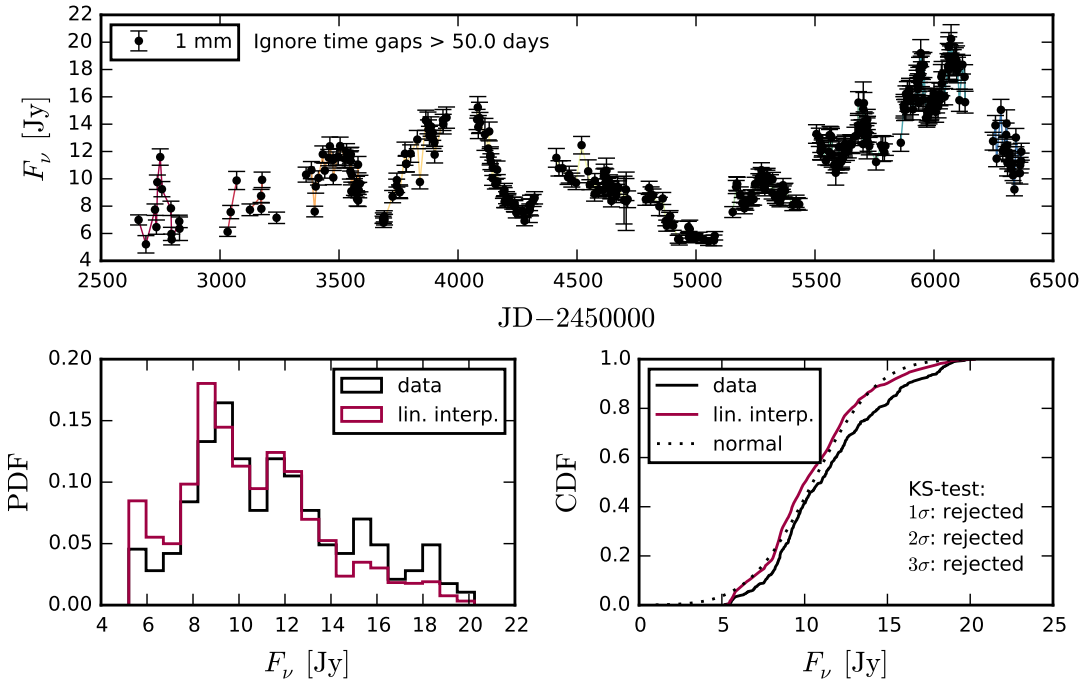

Figure 3.5: Estimation of the PDF of the 1 mm light curve. Upper panel: observed (black dots) and linear interpolated light curve (coloured lines). Lower left panel: PDF based on the data (black) and the linear interpolation (purple). Lower right panel: CDF based on the data (solid black) and the linear interpolation (solid purple) and the best fit Gaussian distribution.

Chapter 4

Power spectral densities

The Power Spectral Density (PSD) of a light curve allows to estimate the contribution of different time scales to the total variability. Periodicity of a signal at a certain time scale is seen as a peak in the power spectrum at the corresponding frequency, whereas a continuum power spectrum corresponds to non-periodic signals. Typical examples of continuum power spectra are the following. Constant power at all frequencies corresponds to a *white noise* process. The power spectrum of a *red noise* process follows a power-law, typically the power is decreasing with increasing frequency. A broken power-law (eq. (4.7)) indicates a characteristic time scale at the break frequency. Differences and similarities in the PSDs between different bands allow to judge whether or not the processes producing the variability at those bands are the same or not.

The PSDs of 3C 279 light curves have been estimated in γ-rays (Abdo et al., 2010b; Max-Moerbeck et al., 2014b), X-rays (Chatterjee et al., 2008), R-band (Chatterjee et al., 2008, 2012), and at 14.5 Ghz and 15 GHz (Chatterjee et al., 2008; Max-Moerbeck et al., 2014b). We estimate the power spectral indices over the full frequency range covered by the Quasar Movie Project. First, we want to test if the variability at all frequencies is consistent with a red noise process. Second, we test if and how the power spectral index changes depending on the emission frequency, potentially indicating different time scales of variability. Third, we use the estimated power spectra for the light curve simulation in chapter 5.

We discuss problems of the PSD estimation arising from finite and uneven data sampling and observational errors in section 4.1. In section 4.2 we explain various methods to simulate light curves which we apply in this and the following chapter. We discuss the method of estimating the intrinsic power spectrum which was originally introduced by Uttley et al. (2002), further developed and applied by Chatterjee et al. (2008), Abdo et al. (2010b), Max-Moerbeck et al. (2014b), and our own implementation in section 4.3. We apply this method to our light curves and discuss the results in sections 4.4 and 4.5. In section 4.6 we briefly discuss whether we can assume stationarity for our light curves or not. We note, that the term *spectrum* in this chapter refers to the power spectrum of the light curve variability, not to be confused with the emission spectrum.

4.1 Estimation of the raw power spectrum

A light curve, or in more general terms a *time series*, is a sequence of N triplets (t_i, f_i, e_i), ordered such that $t_{i+1} > t_i$, where t_i is the time of observation, $f_i = f(t_i)$ is the observed signal, e.g. spectral flux density, energy flux density or photon flux,

as a function of time and e_i is the estimated uncertainty of each data point, with $i = 1, \ldots, N$.

The PSD of a signal $f(t)$ is a function of frequency ν describing how the variance of $f(t)$ is distributed over each contributing frequency ν, decomposing the signal into superposed periodic components. For a distcrete, evenly sampled[1] time series the PSD can be estimated by the *periodogram*, the squared modulus of the discrete Fourier transform

$$P(\nu_k) = \frac{2T}{N}\left(\left[\sum_{i=1}^{N} f_i \cos(2\pi\nu_k t_i)\right]^2 + \left[\sum_{i=1}^{N} f_i \sin(2\pi\nu_k t_i)\right]^2\right) \tag{4.1}$$

evaluated at the *natural frequencies* $\nu_k = \frac{k}{T}$ and

$$k = \begin{cases} 1, \ldots, N/2 & \text{for } N \text{ even} \\ 1, \ldots, (N-1)/2 & \text{for } N \text{ odd} \end{cases} \tag{4.2}$$

$$T = \frac{N}{N-1}(t_N - t_1), \tag{4.3}$$

where $\nu_{\min} = \frac{1}{T}$ is the lowest frequency and $\nu_{\mathrm{Nyq}} = \frac{N}{2T}$ is the Nyquist frequency. The normalization $\frac{2T}{N}$ is a matter of convention and differs in various implementations.

For unevenly sampled data the Lomb-Scargle periodogram (LSP) (Scargle, 1982) can be used. Scargle (1982) shows that the LSP can reliably detect a periodic signal in white noise background, observed at unevenly distributed time steps. Our simulations, though, show that the LSP cannot be used to discriminate different spectral indices of continuous red noise spectra. We simulate light curves with an underlying power-law spectrum with spectral index β_{intr}, a total time $T = 1000$ and sampling $\Delta t = 0.5$ (in arbitrary units) using the algorithm presented by Timmer and Koenig (1995, herafter TK), which is described in detail in section 4.2.1. For six different spectral indices we simulate 100 light curves each, calculate the regular periodogram and the LSP and estimate the spectral index with a linear regression of the log-log periodogram. The estimated indices are shown in fig. 4.1. Whereas the regular periodogram allows a good estimation of the intrinsic spectral index, the estimation based on the LSP generally has a higher uncertainty, is biased towards flatter spectra and cannot discriminate indices $\gtrsim 2$.

The LSP is not applicable to estimate the spectral index of a red noise process. In order to use the regular periodogram, we have to re-sample the unevenly sampled light curves to a regular grid. We discuss the re-sampling scheme in section 4.1.4. First, we discuss the effects of finite sampling, red noise leakage and aliasing on the spectral index estimation in sections 4.1.1 to 4.1.3.

4.1.1 The necessity of a window function

As discussed by Max-Moerbeck et al. (2014a) accounting for the effects of the finite length of light curves is critical for the estimation of the spectral index. Power at frequencies below $\nu_{\min} = T^{-1}$, where T is the total time of the light curve, cannot be estimated by the periodogram, which is limited to the frequency range

[1] $t_{i+1} - t_i = \mathrm{const}\ \forall\ i$

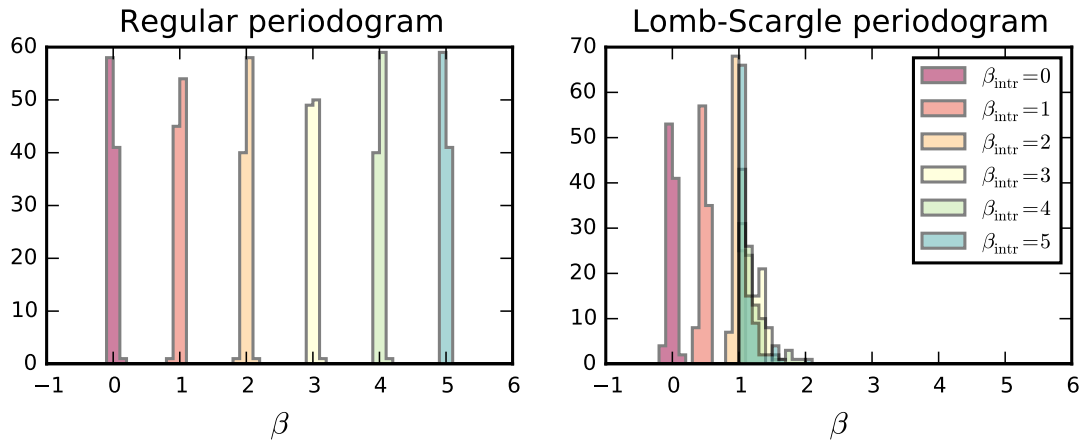

Figure 4.1: Estimates of the spectral index β for various intrinsic indices $\beta_{\rm intr}$ based on the regular (left panel) and the Lomb-Scargle periodogram (right panel).

$[\nu_{\rm min}, \nu_{\rm Nyq}]$. But if power at lower frequencies contributes to the variation of the light curve, some power leaks into the frequency range of the periodogram. This effect is known as *red noise leakage*. Intrinsically steep spectra are flattened by the leaked power, which affects strongest the high frequencies where the intrinsic power is low comparable to lower frequencies. This flattening is shown in the right panel of fig. 4.2. For six different intrinsic spectral indices each histogram is based on 100 simulated light curves of total time $T = 1000$ at a sampling of $\Delta t = 0.5$ (in arbitrary units) including power down to a frequency $\frac{1}{10}\nu_{\rm min}$. The spectral index is estimated by a linear regression of the log-log periodogram. Intrinsic spectral indices $\beta_{\rm intr} > 2$ cannot be discriminated. For comparison, in fig. 4.1 (left panel) no low frequency power is included.

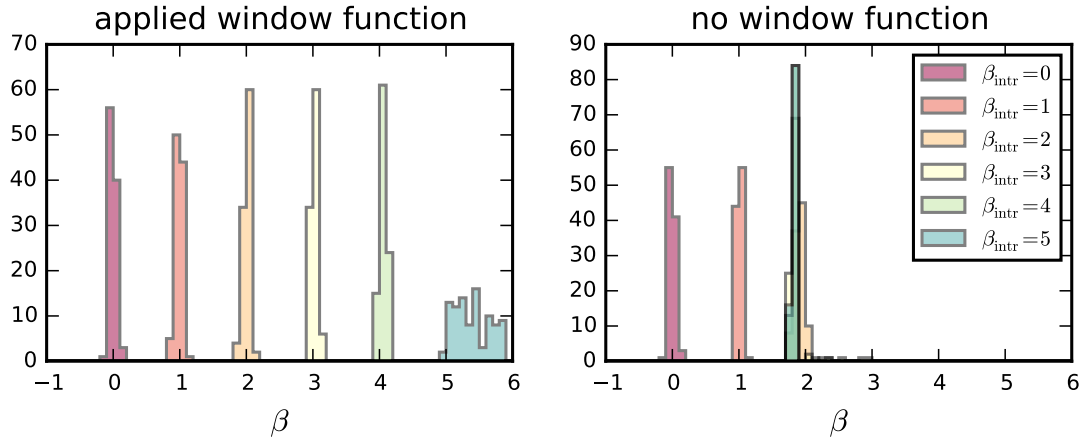

Figure 4.2: Estimates of the spectral index β for various intrinsic indices $\beta_{\rm intr}$ based on the regular periodogram influenced by red noise leakage with (left panel) and without (right panel) applying a Hann window function to the light curve.

The spectral index can be estimated up to much higher intrinsic indices, when the light curve is multiplied with an appropriate window function before the periodogram is calculated. In the left panel of fig. 4.2 we show the distributions of estimated spectral indices of the same simulations as for the right panel, but multiplied with a Hann window function before the calculation of the periodogram.

The Hann window function is defined as:

$$w_{\text{Hann}}(t) = \begin{cases} \sin^2\left(\frac{\pi t}{T}\right) & \text{for } 0 \leq t \leq T \\ 0 & \text{otherwise.} \end{cases} \tag{4.4}$$

For the intrinsic index $\beta_{\text{intr}} = 5$ the distribution of the estimated index is biased towards steeper spectra and has a large spread. We discuss the bias due to red noise leakage in detail in the following section.

4.1.2 Red noise leakage and linear de-trending

To test the effect of red noise leakage we simulate 1 000 light curves with a total time $T = 1000$ and sampling $\Delta t = 1$ (in arbitrary units) using the TK algorithm (described in section 4.2.1). The underlying power spectrum follows a power-law (eq. (4.5)) with spectral index β_{intr}.To include lower frequency power we simulate light curves with a total time $N \cdot T$, including variation down to frequencies N^{-1} times the lowest frequency measured with a periodogram, setting $N = 1, 4, 10, 49, 100, 499, 999$.[2] We estimate the periodograms from light curve sections of duration T. Before calculating the periodogram the mean flux is subtracted from the light curves (following Uttley et al. (2002)) and the light curves are multiplied with a Hann window function (eq. (4.4)). We estimate the spectral slope $-\beta$ by linear regression of the periodogram in log-log space. We test different spectral indices $\beta_{\text{intr}} = 1, 2, 3, 4, 5$.

Figure 4.3 shows histograms of the measured spectral indices β for different intrinsic β_{intr} (columns) and different amounts of included low frequency power N (rows). Each histogram is based on 1 000 simulations. For each parameter combination we also print the average bias $\Delta\beta = \beta_{\text{intr}} - \langle\beta\rangle$ and the distribution standard deviation σ in fig. 4.3.

The estimation of the spectral index is biased, when no lower frequency power ($N = 1$) is included in the light curve simulation. The estimated spectral index is less steep than the intrinsic. The bias is larger for steeper spectra. When low frequency power is included ($N > 1$) the tested β_{intr}-N parameter space has a threshold. For β_{intr} and N (> 1) below this threshold (a) the standard deviation of the β distribution is constant and (b) the index estimation is not biased. Beyond that threshold (a) the standard deviation increases, indicating less accurate index estimation, and (b) the estimation is biased towards steeper spectra. For fixed N and increasing intrinsic index the measured index is unbiased within the threshold, beyond the threshold the bias towards steeper spectra increases gradually. Accordingly, the same happens for fixed β_{intr} and increasing N. The higher β_{intr} the lower is the N-threshold and vice versa.

For $N > 4$ the contribution of low frequencies, which are below the accessible range of the periodogram, appear as a quasi linear trend in the light curves, as illustrated in the left panel of fig. 4.4. The right panel shows the deviation from a linear trend, estimated through the standard error of a linear regression, decreasing for higher N. The discussed threshold and the bias beyond that threshold originate in the amount of the relative low frequency contribution. The stronger

[2]Those numbers are chosen to minimize the calculation time. The numbers 5, 50, 500, 1000 would yield high prime numbers in the factorization of the Fast Fourier Transform (FFT), drastically increasing the calculation time.

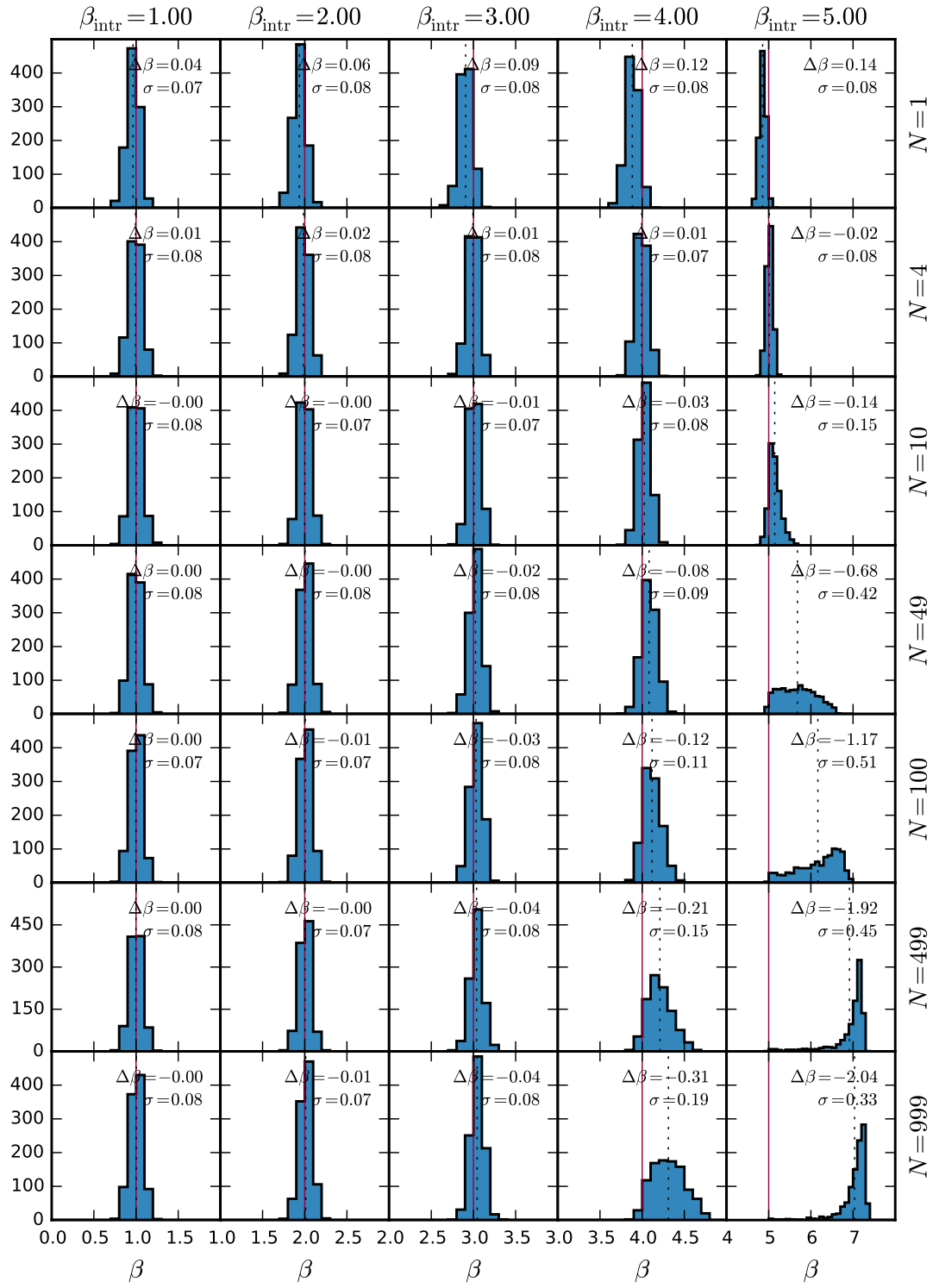

Figure 4.3: Distribution of measured spectral indices β based on TK-simulated light curves for different intrinsic spectral indices β_{intr} (columns) and different amounts of included low frequency power N (rows). Solid red lines indicate β_{intr}, dotted black lines indicate the distribution mean.

the quasi linear trend (high N) and the stronger the contribution of low frequencies (high β_{intr}) the less accurately can the higher frequency contributions be measured.

Additionally, the β_{intr}-N-threshold depends on the total light curve time T. The shorter T the smaller are the threshold values. The longer the total time T the lower are the frequency contributions captured by the periodogram. Thus, the

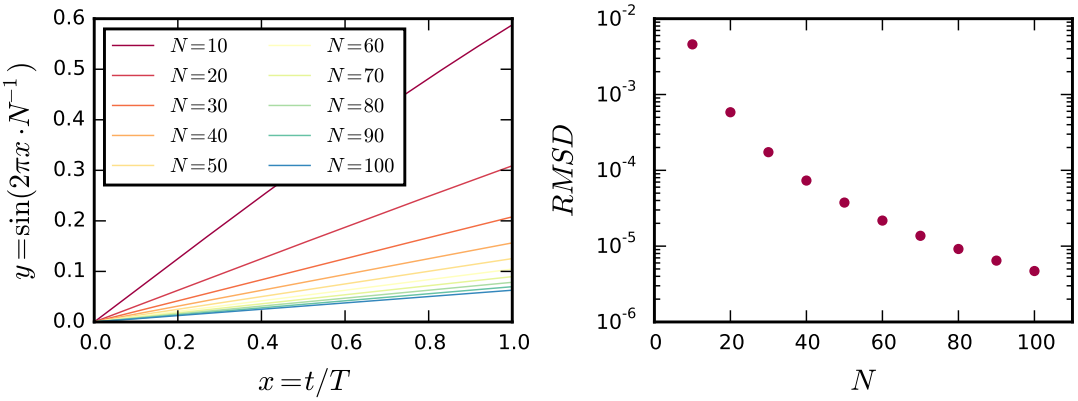

Figure 4.4: The left panel shows sinusoid functions for various frequencies, where $N = 1$ corresponds to a full cycle in the function range $x = 0 \ldots 1$ and, thus, to the lowest frequency $\nu_{\min} = 1/T$ which can be measured in the periodogram of the signal $y(x)$. The function curvature decreases with increasing N converging to a linear trend. The right panel shows the root mean square deviation from a linear curve.

β_{intr}-N-threshold is increased.

We run the same simulations as before and linearly de-trend the light curves before applying the window function and calculating the periodogram. The results are shown in fig. 4.5. Linear de-trending resolves the problem of less accurate spectral index estimation in the case of included low frequency power ($N > 1$). The distribution spread σ is now constant for all tested N and β_{intr}. There is no systematic offset between intrinsic index and measured index for spectral indices $\beta_{\text{intr}} \lesssim 3$ independent of the choice of $N \gtrsim 10$. Therefore, linear de-trending increases the reliability of the periodogram. The estimation of intrinsically steep spectral indices $\beta_{\text{intr}} \gtrsim 3$ is still biased depending on β_{intr} and the total time T and N. We come to the conclusion that, when low frequency contribution to observed light curves is to be expected, linear de-trending of the light curves allows a more reliable estimation of the spectral index and is recommended. The uncertainty of the spectral index estimation in the unbiased limit is given by the distribution spread $\sigma \approx 0.08$.

4.1.3 Aliasing

Aliasing happens when a signal is under-sampled. Some of the power at frequencies $> \nu_{\text{Nyq}}$ is shifted into the frequency range of the periodogram, introducing a difference between the intrinsic and the estimated spectrum. To test the effect of aliasing we simulate 1 000 light curves with a total time $T = 1000$ and sampling $\Delta T = 1$ (in arbitrary units) using the TK algorithm (c.f. section 4.2.1). We include low frequency power simulating initial light curves of total duration $10 \cdot T$, extracting short light curve of duration T and measure the periodogram after linear de-trending the light curves to avoid contamination by a truncated power-law spectrum (c.f. section 4.1.2). We include high frequency power by simulating light curves with an initial sampling $N^{-1}\Delta T$. We re-sample the simulated light curves to ΔT and measure the periodograms after linear de-trending and windowing the light curves.

Figure 4.6 shows the distribution of measured spectral indices β based on TK-simulated light curves for various intrinsic spectral indices β_{intr} and various

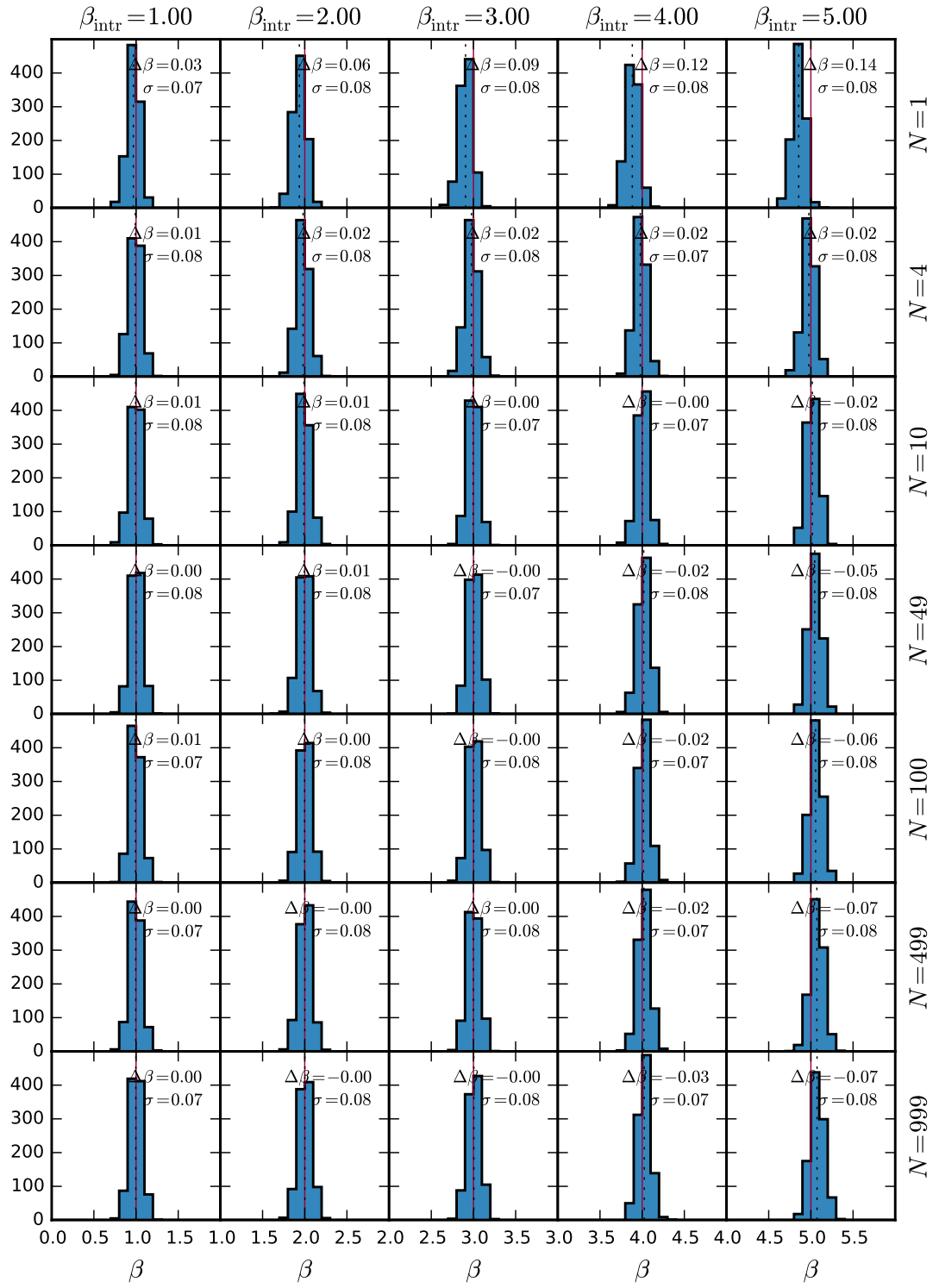

Figure 4.5: Same as fig. 4.3 with linear de-trending before measuring β.

amounts of included high frequency power N, where $N = 1$ means no power at frequencies higher than captured by the periodogram frequency range and otherwise power included at frequencies N times higher than captured by the periodogram.

When no high frequency power is included in the simulated light curves ($N = 1$) the estimated spectral index is consistent with the intrinsic index within the uncertainty described in section 4.1.2. Aliasing moves power from under-sampled high frequencies to lower frequencies. The highest frequencies measured with a periodogram, which have the lowest intrinsic power when the spectrum follows a

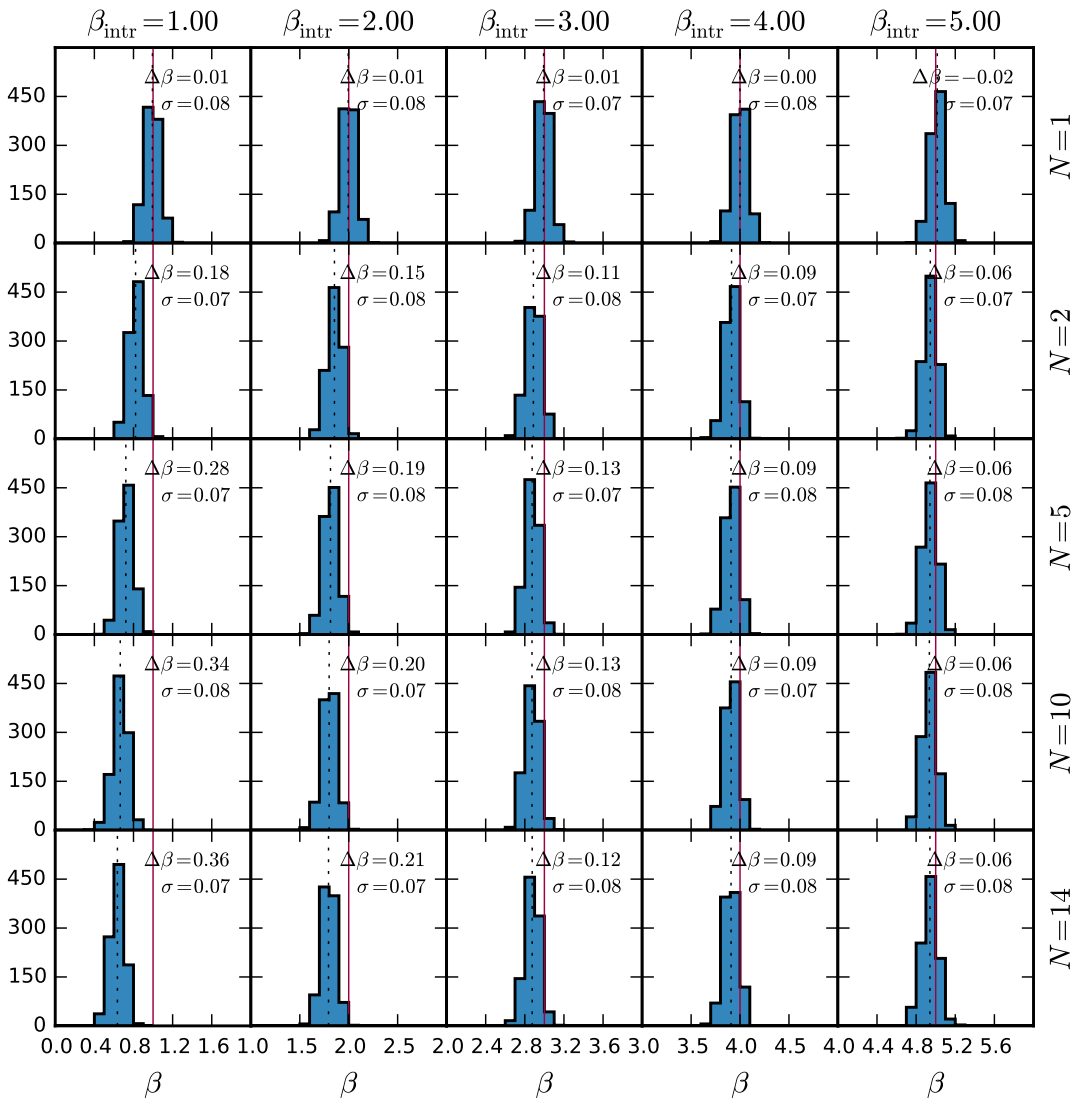

Figure 4.6: Distribution of measured spectral indices β based on TK-simulated light curves for different intrinsic spectral indices $\beta_{\rm intr}$ (columns) and different amounts of included high frequency power N (rows). Solid red lines indicate $\beta_{\rm intr}$, dotted black lines indicate the distribution mean. β is measured after linear de-trending and windowing the light curves.

power-law, are affected the most. Consequentially, aliasing flattens the spectrum. When the intrinsic spectrum get steeper, i.e. $\beta_{\rm intr}$ increases, the under-sampled frequencies contribute less power. The aliasing bias decreases for higher $\beta_{\rm intr}$, observable along the rows of fig. 4.6. For higher N more under-sampled frequencies affect the simulated light curve, more power is aliased into the periodogram and the aliasing bias $\Delta\beta$ increases, as shown in the columns of fig. 4.6. The increase of the bias with N asymptotically saturates. The saturation point $N_{\rm sat}(\beta_{\rm intr})$ depends on the intrinsic spectrum. Therefore, the bias can be estimated from the measured spectral index if N is chosen large enough such that the bias is saturated $N > N_{\rm sat}$. Accordingly, for observed light curves the bias can be estimated under the assumption that the intrinsic spectrum continues beyond the saturation frequency which corresponds to $0.5N_{\rm sat} \cdot \Delta t^{-1}$.

4.1.4 Splitting and re-sampling the data

In general we have observed light curves that are of finite length and unevenly sampled, including some observation gaps of much longer duration than the average time step. Before calculating the regular periodogram (eqs. (4.1) to (4.3)) we have to re-sample the light curve to an even grid. The choice of the re-sampling time step is critical. Using the largest time step of the original data comes at the cost of loosing information at higher frequencies. Choosing a smaller time step on the other hand means to invent interpolated data points in observation gaps. This becomes most critical for long gaps, where multiple, adjacent data points would be invented.

Therefore we split the data at long observations gaps maintaining the total light curve $f_{\mathrm{full}}(t_i)$ and yielding N_{split} split light curves $f_{\mathrm{split},n}$, $n = 1 \ldots N_{\mathrm{split}}$ for $N_{\mathrm{split}} - 1$ observation gaps. We re-sample the total light curve to an even grid with the new constant time step equal to the largest original time step: $\Delta t_{\mathrm{tot}} = \max(t_i - t_{i-1})$, maintaining the information at frequencies lower than $\Delta t_{\mathrm{tot}}^{-1}$. We re-sample each split light curve to a constant time step equal to the median of the original time steps $\Delta t_{\mathrm{split},n} = \mathrm{median}(t_i - t_{i-1})$, maintaining information at higher frequencies than given by the longest time step, but contaminated by occasional invented data points. All re-sampled data points are linearly interpolated from the two closest data points of the original light curve.

To estimate the effect of linear interpolation on the periodogram, we re-sample each light curve M times at various time zero points $t_0 \rightarrow t_0 + \frac{i}{\Delta t}$, $i = 0 \ldots M-1$, yielding M re-sampled total light curves and $M \cdot N_{\mathrm{split}}$ re-sampled split light curves. Each re-sampled total and split light curve is linearly de-trended to minimize the red noise leakage bias (c.f. section 4.1.2) and multiplied with a Hann window function (eq. (4.4), section 4.1.1) before the periodogram is calculated.

This process yields $M \cdot (N_{\mathrm{split}} + 1)$ periodograms at different frequency ranges depending on the sampling and total time of each light curve. We set a regular binning in the logarithmic frequency space covered by all periodograms. We calculate the final raw power spectrum by averaging the logarithmic power in each bin as suggested by Papadakis and Lawrence (1993). Accordingly, the standard deviation of each frequency bin normalized with the number of data points in the bin gives an estimate of the uncertainty. These uncertainties reflect errors due to the re-sampling using M realizations and differences between different parts of the split light curve which contribute to the same frequency bins. We do not interpolate empty bins.

In the following we summarize the steps taken to estimate the raw power spectrum of an unevenly sampled light curve:

1. Re-sample full light curve $f(t_i)$ to largest time step $\Delta t_{\mathrm{tot}} = \max(t_i - t_{i-1})$, M times with different zero points.

2. Split full light curve $f(t_i)$ at $N_{\mathrm{split}} - 1$ observation gaps $\rightarrow f_{\mathrm{split},n}(t_i)$, $n = 1 \ldots N_{\mathrm{split}}$.

3. Re-sample each split light curve at corresponding median time steps $\Delta t_{\mathrm{split},n} = \mathrm{median}(t_i - t_{i-1})$, M times with different zero points.

4. Linearly de-trend each extracted light curve.

5. Multiply each extracted light curve with a Hann window function.

6. Calculate periodograms for all re-sampled full and split, de-trended, windowed light curves.

7. Calculate logarithmically averaged power, over logarithmic frequency bins.

Although we reduce the effects of finite and uneven sampling and red noise leakage with our re-sampling scheme, linear de-trending and the application of a window function, their imprints cannot be fully removed from the estimated raw power spectrum. Additionally, aliasing probably affects the periodogram. Therefore it is inevitable to use a Monte Carlo base method, comparing the periodograms of simulated light curves with known intrinsic spectrum against the periodograms of the observed data. In section 4.2 we explain how we simulate light curves and in section 4.3 we discuss the method of estimating the intrinsic power spectrum of our light curves.

4.2 Light curve simulation

In the previous section we have discussed the measurement of the raw power spectrum of a light curve. In section 4.3 we discuss a method to estimate the intrinsic spectrum based on the comparison of the raw power spectrum of data and simulated light curves with known properties. In this section we report how light curves following a model Power Spectral Density (PSD) are simulated using the algorithm of Timmer and Koenig (1995) (TK). We discuss various methods to fix the spectral model amplitude, including a recent improvement of the TK-algorithm introduced by Emmanoulopoulos et al. (2013) which allows to simulate light curves following both a model PSD and Probability Density Function (PDF). Furthermore, different approaches of simulating observational errors are discussed.

We will use simulated light curves to estimate the intrinsic power spectrum of the observed light curves in section 4.3 and to estimate the significance of cross-correlation functions in chapter 5.

4.2.1 Generating Gaussian noise

Uttley et al. (2002) suggest three different spectral models. The simple *power-law model* with the spectral index β and the power A at frequency ν_0:

$$S(\nu) = A \left(\frac{\nu}{\nu_0} \right)^{-\beta}. \tag{4.5}$$

The *knee model* has a constant power A below the bend frequency ν_{knee} and follows a power-law with spectral index β at frequencies above ν_{knee}:

$$S(\nu) = \frac{A}{\left[1 + \left(\frac{\nu}{\nu_{\mathrm{knee}}} \right)^2 \right]^{\frac{\beta}{2}}}. \tag{4.6}$$

The *broken power-law model* follows a power-law with spectral index β_{lo} at frequencies below ν_{break} and a power-law with index $\beta_{\mathrm{hi}} > \beta_{\mathrm{lo}}$ at lower frequencies. The power at the break frequency is given by A:

$$S(\nu) = \begin{cases} A \left(\frac{\nu}{\nu_{\text{break}}}\right)^{-\beta_{\text{lo}}} & \text{if } \nu < \nu_{\text{break}} \\ A \left(\frac{\nu}{\nu_{\text{break}}}\right)^{-\beta_{\text{hi}}} & \text{otherwise.} \end{cases} \tag{4.7}$$

We use the method by Timmer and Koenig (1995) (TK) to produce noise $f(t)$ that follows an underlying power spectrum $S(\nu)$, given e.g. by eqs. (4.5) to (4.7). The steps of the TK algorithm are:

1. Choose a spectral model $S(\nu)$.
2. Set up the Fourier frequencies $\nu_1, \ldots \nu_N$ corresponding to the wanted sampling rate Δt and total time T of the simulated light curve, with $\nu_2 = 2 \cdot \nu_1, \ldots \nu_N = N \cdot \nu_1 = \nu_{\text{Nyq}}$ where ν_{Nyq} is the Nyquist frequency.
3. Draw two random numbers $\hat{a}_{r,j}, \hat{a}_{i,j}$ from a Gaussian distribution for each Fourier frequency ν_j, $j = 1, \ldots, N$, as the real and imaginary part of the Fourier coefficients $\hat{a}_j = \hat{a}_{r,j} + i\hat{a}_{i,j}$. If N is even the Fourier coefficient of the Nyquist frequency has to be real $\hat{a}_N = \hat{a}_{r,N} + i \cdot 0$.
4. In order to produce a real valued light curve the Fourier coefficients of the negative Fourier frequencies $\nu_{-j} = -\nu_j$ are given by the complex conjugates of the positive frequency coefficients: $\hat{a}_{-j} = \hat{a}_j* = \hat{a}_{r,j} - i\hat{a}_{i,j}$.
5. Each Fourier component is scaled by a factor based on the model spectrum: $\hat{a}_j \to \hat{a}_j \cdot \sqrt{\frac{1}{2} S(\nu_j)}$.
6. The light curve is given by the (real valued) inverse discrete Fourier transform (riDFT) a_k, $k = 1, \ldots, N$ of the Fourier coefficients $\hat{a}_j$.

In section 4.1.2 we have shown that it is mandatory to include power at frequencies lower than $\nu_{\text{min}} = T^{-1}$, where T is the total time of the simulated light curve. Using a model spectrum $S(\nu)$ truncated at ν_{min}, produces a light curve with a spectrum flatter than targeted $\beta_{\text{intr}} < \beta_{\text{model}}$ (c.f. fig. 4.5). Furthermore, periodograms of the observed light curves are expected to be affected by red noise leakage. Therefore, simulated light curves should include low frequency power as well, to be subjected to the same effects. In order to include power at lower frequencies we simulate light curves with a total time $10 \cdot T$. These long light curves are then split into 10 light curves of the targeted duration T. We chose a factor of 10 compromising between including as much low frequency power as relevant and reducing the computational time. Up to a factor of 4 longer light curves the contribution adds a modulation to the light curve, for factors > 4 longer light curves a secular trend is added. This trend converges for increasing factors to a linear trend, which we remove from the light curves before calculating the periodogram. Our simulations show that for a factor of 10 longer light curves the index estimation is unbiased for intrinsic indices $\beta_{\text{intr}} < 3$. Higher factors do not add significant variation (c.f fig. 4.4 right panel), reduces the reliability of the index estimation for steep spectra and increases the computational time of the TK algorithm.[3]

[3]The calculation time of the TK algorithm is mainly given by the $\mathcal{O}(n \log n)$ dependence of the inverse FFT on the number of data points n.

As discussed in section 4.1.3, aliasing affects the estimation of the power spectral index. Spectra appear flatter than they intrinsically are. Since the observed data probably is affected by high frequency variation, high frequency power has to be included in the simulations as well. It is problematic though that the index estimation depends on the amount of high frequency power, i.e. the frequency range which is included in the simulation. Assuming the observed data follows a power-law spectrum without truncation, the high frequency cut off of the model spectrum should be chosen as high as possible. On the other hand this increases the number of light curve data points and consequentially the computational time of the TK algorithm. In fig. 4.6 we could show that the aliasing bias saturates at a factor $N_{\mathrm{sat}}(\beta_{\mathrm{intr}})$. Therefore it would be sufficient to simulate initial light curves at a sampling rate $N_{\mathrm{sat}}^{-1}(\beta_{\mathrm{intr}}) \cdot \Delta t$. Then both data and simulation are affected by aliasing by the same amount.

We initially simulate the light curves at a sampling rate $0.1 \cdot \mathrm{median}(t_i - t_{i-1})$, where t_i are the time steps of the final simulated light curve. Under the assumption of a pure, non-truncated power-law spectrum for the observed data the bias $\Delta\beta_{\mathrm{obs}}$ can be estimated from fig. 4.6. For an intrinsic spectral index $\beta_{\mathrm{intr}} = 1$ the bias is $\Delta\beta = 0.36$, which is the saturated bias at this intrinsic index. Choosing a sampling rate factor of 0.1 (corresponding to $N = 10$ in fig. 4.6) the bias is 0.34. Comparing simulated light curves against the observed data the final bias at $\beta_{\mathrm{intr}} = 1$ is at the order of 0.01 and decreasing for steeper intrinsic spectra, which we can neglect.

With the dense initial sampling rate of $0.1 \cdot \mathrm{median}(t_i - t_{i-1})$ we account also for the necessity of re-sampling the simulated light curve. The re-sampling is discussed in section 4.2.6

4.2.2 Fitting the spectral amplitude

The variance $\sigma^2(f(t_i))$ of a light curve $f(t_i)$ is equal to the corresponding PSD $\mathrm{PSD}_f(\nu)$ integrated over the full frequency range:

$$\sigma^2(f(t_i)) = \int \mathrm{PSD}_f(\nu)\,\mathrm{d}\nu. \tag{4.8}$$

Consequentially, the amplitude A in the spectral model (e.g. eqs. (4.5) to (4.7)) is not a free parameter but fixed by the amplitudes of the observed light curve, which we want to resemble with the simulations. Uttley et al. (2002) set an initially arbitrary model amplitude to simulate the light curves. They calculate the periodogram of the simulations and the observed light curve and then use a least square fitting method to determine the correct amplitude.

The least square fitting reduces to calculating the y-offset of the observed and simulated power spectrum in log-space, if the observed light curve is not affected by observational errors and no errors are simulated. The assumption of no measurement noise is not applicable and consequentially errors should also be simulated.

In the simplest case of homoscedastic errors the measurement noise adds a constant term to the power spectrum (c.f. section 4.2.7). When changing the amplitude the power spectrum will not only be shifted, but it changes its shape, if the intrinsic power is below the noise level at high frequencies. The frequency range which is noise dominated depends on the intrinsic spectrum.

Considering measurement noise in the observed light curve and including error simulation in the least square fitting is not trivial, but requires varying the amplitude

and performing a minimization. An alternative approach to adjust the spectral amplitude is explained in the following.

4.2.3 Matching the light curve variance

Max-Moerbeck et al. (2014a) suggest to use eq. (4.8) to scale the simulated light curve amplitude to match the observed light curve amplitude. Instead of scaling the spectral model amplitude A in the Fourier domain, Max-Moerbeck et al. (2014a) scale the light curve variance in the time domain. The intrinsic variance $\sigma^2_{\rm signal}$ of the observed light curve is estimated through

$$\sigma^2_{\rm data} = \sigma^2_{\rm signal} + \sigma^2_{\rm noise}, \tag{4.9}$$

where $\sigma^2_{\rm data}$ is calculated from the observed light curve and $\sigma^2_{\rm noise}$ is estimated from the 1σ observational uncertainties e_i as $\sigma^2_{\rm noise} \approx \overline{e_i^2}$.

Light curves are simulated with an initial arbitrary spectral amplitude A and re-scaled by a factor a to $f_{\rm sim} \rightarrow a^{-1} f_{\rm sim}$. The scaling factor a is determined as:

$$a^2 = \frac{\sigma^2_{\rm data} - \overline{e_i^2}}{\sigma^2_{\rm sim}} \tag{4.10}$$

The corresponding spectral amplitude of the scaled light curve is $a^{-2}A$.

Equation (4.8) implies that both methods, fitting the spectral amplitude and matching the light curve variance, to adjust the simulated light curve amplitude to the observed one are equivalent. We have tested both approaches for the simple case of no observational errors, where the spectral amplitude fitting is easily possible. We have found that the two methods lead to a different scaling of the simulated light curve. Reasons are that, first, the PSD estimation is affected by aliasing and red noise leakage. Second, it is only evaluated at specific frequencies and, third, limited to a certain frequency range given by the sampling rate and the total light curve time. Therefore, summing over the discrete PSD estimation is only an approximation of the light curve variance.

Matching the light curve variance is a more direct approach in the simulation of light curves, which is easier to handle and computationally less expensive than fitting the spectral amplitude, when measurement noise affects the observed light curve and is considered in the simulation. In the next section we discuss an extension of the TK algorithm, which allows to adjust the PDF of the simulated light curves, and thus automatically matches the light curve variance.

4.2.4 Generating noise following both the desired PSD and PDF

The TK algorithm (section 4.2.1) produces Gaussian noise following an underlying power spectrum $S(\nu)$. As we have shown in section 3.2 the observed light curves f_i are not Gaussian distributed. Emmanoulopoulos et al. (2013, hereafter EMP) introduce an algorithm that iteratively adjusts the Probability Density Function (PDF) of a TK-simulated light curve. We briefly summarize the algorithm steps.

(1.1) A normally distributed signal $f_{\rm norm}(t_i)$ of N data points, $i = 1, \ldots, N$, with an underlying model power spectrum $S(\nu)$ is produced using the TK algorithm.

Low and high frequency power contribution is included at this stage. The Discrete Fourier Transform (DFT)[4] $DFT_{\rm norm}(\nu_j)$ of $f_{\rm norm}(t_i)$ is calculated at the natural frequencies ν_j and from the DFT the corresponding amplitudes $\mathcal{A}_{\rm norm}(\nu_j)$.

(1.2) N random numbers are drawn either from a model PDF or from the Empirical Cumulative Distribution Function (ECDF) of an observed light curve, yielding the first iteration of the simulated light curve $f_{{\rm sim},k=1}(t_i)$, where k is the iteration step. $f_{{\rm sim},k=1}(t_i)$ follows a white noise process.

(2) The DFT $DFT_{{\rm sim},k}$ of $f_{{\rm sim},k}(t_i)$ is calculated and the corresponding amplitudes $\mathcal{A}_{{\rm sim},k}(\nu_j)$.

(3) *Spectral adjustment:* A new adjusted DFT is created, which has the amplitudes of $DFT_{\rm norm}(\nu_j)$ and the phases of $DFT_{{\rm sim},k}$, calculating

$$DFT_{{\rm sim,adj.},k}(\nu_j) = DFT_{{\rm sim},k}(\nu_j) \cdot \frac{\mathcal{A}_{{\rm sim},k}(\nu_j)}{\mathcal{A}_{\rm norm}(\nu_j)} \tag{4.11}$$

at each frequency ν_j. This adjusted DFT is then back transformed to $f_{{\rm sim,adj.},k}(t_i)$ using the inverse Discrete Fourier Transform (iDFT). This light curve follows the model spectrum $S(\nu)$ but does not have the target PDF.

(4) *Amplitude adjustment:* A new light curve $f_{{\rm sim},k+1}(t_i)$ is created from $f_{{\rm sim,adj.},k}(t_i)$ and $f_{{\rm sim},k=1}(t_i)$ such that the highest value of $f_{{\rm sim,adj.},k}(t_i)$ is replaced by the highest value of $f_{{\rm sim},k=1}(t_i)$ and so on, following the ranking of the flux values. The resulting light curve has the target PDF but a different spectrum.

Steps 2-4 are repeated iteratively until the simulated light curve converges: $f_{{\rm sim},k+1}(t_i) \equiv f_{{\rm sim},k}(t_i)$. Emmanoulopoulos et al. (2013) show that this algorithm is capable of producing simulated light curves which have both the target PSD and PDF.

In sections 4.2.2 and 4.2.3 we have discussed two methods how to adjust the spectral amplitude A such that the simulated light curves have the same variance as the observed light curve. When the EMP algorithm is used to adjust the PDF of a simulated light curve the variance is automatically adjusted. In this case the choice of the initial spectral amplitude A is arbitrary.

We discuss the performance of the EMP algorithm in more detail in the following section.

4.2.5 Stability of the spectral index

In the previous section we have summarized the algorithm by Emmanoulopoulos et al. (2013) which allows to adjust the PDF of a simulated Gaussian light curve. Now, we test if the algorithm maintains the model spectrum the Gaussian light curve is based on.

For each model spectrum (power-law with various spectral indices) we produce 1 000 Gaussian noise light curves with the TK algorithm including low frequency power down to a 10th of the lowest measured frequency. We do not include high frequency power to avoid aliasing bias in this test. Based on each TK light curve we produce a second light curve with the EMP algorithm, adjusting the PDF to

[4]Since the light curve consists only of real values, a real-valued implementation of the DFT can be used, which considers that the negative frequency terms are just the complex conjugates of the corresponding positive frequency terms. Accordingly, a real-valued implementation of the iDFT can be used for the back transformation.

a log-normal distribution[5]. We linearly de-trend all simulated light curves, apply the Hann window function, calculate the periodogram and estimate the spectral index with a linear regression of the log-log periodogram. The distributions of the estimated spectral indices based on the TK and EMP light curves for various intrinsic spectral indices are shown in fig. 4.7.

The TK algorithm produces light curves with a spectral index β distributed around the target index β_{intr} with a constant distribution spread (when lower frequency power is included and higher frequency power is not included; c.f.sections 4.1.2 and 4.1.3). The EMP algorithm does not preserve the spectral index in general. For intrinsic indices up to $\beta_{\mathrm{intr}} \approx 1.8$ the spectrum is preserved. For intrinsically steeper spectra, the algorithm does not maintain the spectral index but flattens the spectrum. Independent of the initial spectral index the resulting index is distributed around $\beta = 1.7 \pm 0.3$.

Emmanoulopoulos et al. (2013) test their algorithm with a detailed model of the PSD and the PDF fitted to a reference data set. They show that all model parameters estimated from the simulated light curve converge over the iteration steps close to the target parameters. They do not claim that the algorithm works for arbitrary combinations of PSDs and PDFs, which is what we tried here.

Our interpretation is, that the EMP algorithm works only for realistic combinations of PSD and PDF. The PDF is not independent of the power spectrum as the light curve amplitudes are encoded in the power spectrum. Thus, for incompatible spectrum and PDF the algorithm cannot converge at the targeted power spectrum parameters.

To test the raw power spectrum of observed light curves against that of simulated light curves, we need to cover a large range of spectral indices. The EMP algorithm cannot maintain steep spectra. Furthermore, the estimation of the PDF, which is influenced by uneven sampling, observation gaps and observational uncertainties, introduces additional uncertainties in the power spectral density estimation. Therefore, we do not use the EMP algorithm in the context of the intrinsic power spectrum estimation, but variance adjusted (c.f. section 4.2.3) TK-simulated light curves to estimate the intrinsic power spectra (sections 4.3 to 4.5). We will use EMP adjusted simulated light curves to estimate the significance of the cross-correlation functions in chapter 5.

4.2.6 Re-sampling and re-binning to uneven grid

The TK algorithm produces simulated light curves with even sampling steps. Those light curves are either re-sampled or re-binned to match the uneven sampling of the observed light curve. Re-sampling is based on a simple linear interpolation. The interpolated values do not reflect the intrinsic variation. Thus, the re-sampling changes the power spectrum of the simulated light curve. This effect can be reduced by choosing a denser initial time grid. But increasing the number of data points significantly increases the computational time of the TK algorithm. We choose an initial time sampling step of $0.1 \cdot \mathrm{median}(t_i - t_{i-1})$, where $t_i - t_{i-1}$ are the time steps of the re-sampled and accordingly the observed light curve.

To simulate γ-ray light curves we use re-binning instead of re-sampling. Each data point of the observed γ-ray light curve is the average of the integrated flux over a certain time span. Those time intervals range from 0.1 days to 8.6 days.

[5]The choice of a log-normal distribution for the light curve PDF here is arbitrary, but it is reasonably close to most observed data.

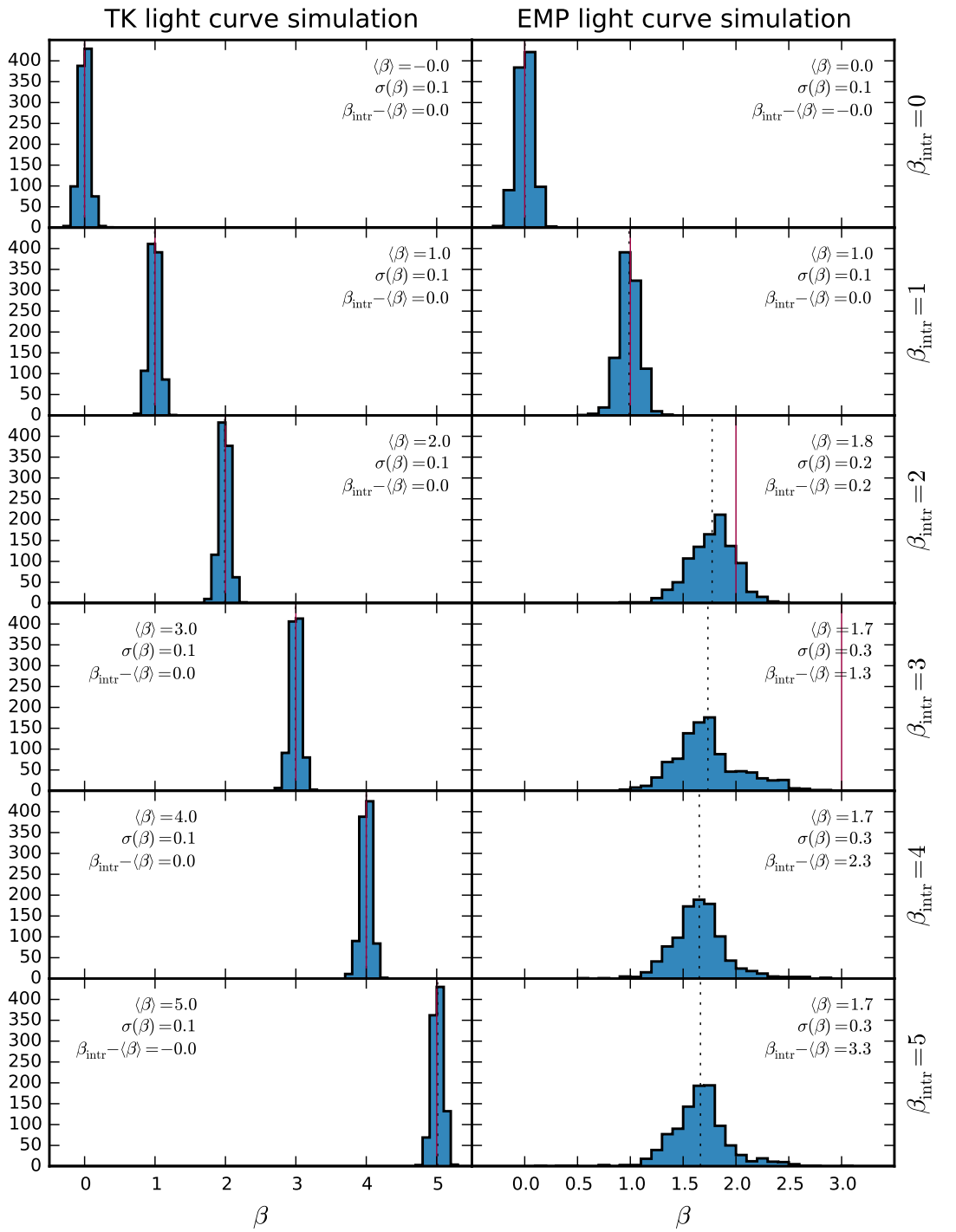

Figure 4.7: Distribution of measured spectral indices β based on TK-simulated (left column) and EMP-simulated (right column) light curves for different intrinsic spectral indices β_{intr} (rows). Solid red lines indicate β_{intr}, dotted black lines indicate the distribution mean. β is measured after linear de-trending and windowing the light curves.

To resemble the same averaging pattern in the simulated light curves we re-bin the simulated curves using the same binning as for the observed data. We note that this approach has its limitations since the binning is decoupled from the flux. For actual observed data it is usually necessary to integrate over long time spans when the flux is low to get reasonable statistics, while integration steps are short during flaring epochs. Here we apply the exact same sampling as for the data, independent of the simulated flux.

4.2.7 Error simulation

Observational uncertainties show up as additional power at each frequency in the periodogram. There are two options to implement the measurement noise. First, Uttley et al. (2002) add a constant noise term to the spectral model (e.g. eqs. (4.5) to (4.7)). This approach assumes a constant noise scale at all frequencies, thus, constant, i.e.homoscedastic errors for all light curve data points.

Secondly, Max-Moerbeck et al. (2014a) apply simulated errors to the final light curve – the intrinsic signal – when it is "observed". This method allows (a) to apply different error scales to the data points and (b) to choose a proper distribution for the errors (e.g. Gaussian or Poisson). We use the method of Max-Moerbeck et al. (2014a) to add heteroscedastic Gaussian errors to each light curve data point:

$$f_{\mathrm{sim,data}}(t_i) = f_{\mathrm{sim,intr}}(t_i) + \mathcal{N}(0, e_i), \tag{4.12}$$

where e_i are the 1σ uncertainties of the observed light curve in randomized order. If the number of data points of the simulated light curve should not match the observed data points, the error scales e_i could be drawn randomly from the cumulative distribution function of the observed uncertainties. Since we apply the errors after the re-sampling, the number of simulated data points matches the number of observed data points and we can directly apply the observational uncertainties.

We add Gaussian noise even in the case of simulated γ-ray light curves. Since the observed light curve is adaptively binned, it is reasonable to assume Gaussian instead of Poisson noise.

4.2.8 Light curve simulation for PSD estimation

We briefly summarize the steps of the light curve simulation used in the following section to estimate the intrinsic power spectrum of light curves:

1. Choose a spectral model $S(\nu)$.

2. With the TK algorithm produce an evenly sampled light curve at a sampling rate $0.1 \cdot \mathrm{median}(t_i - t_{i-1})$ for a total time $10 \cdot T$, where t_i are the (unevenly sampled) target time steps and T is the targeted total light curve time (section 4.2.1).

3. Split the full light curve into 10 curves of total time T, yielding 10 simulations in one iteration, and perform the following steps on each attained light curve.

4. Match the light curve variance (section 4.2.3).

5. Re-sample or re-bin (in the case of simulated γ-ray light curve) the simulated light curve (section 4.2.6) to match the sampling of the observed light curve.

6. Add simulated measurement noise (section 4.2.7).

In the following section we describe how these simulated light curves are used to estimate the intrinsic power spectral index of our observed light curves.

4.3 Estimation of the intrinsic power spectrum

The raw power spectrum estimation as described in section 4.1 is influenced by the uneven and finite sampling, observational errors, red noise leakage and aliasing. Uttley et al. (2002) introduce a Monte Carlo based method to estimate the *intrinsic* power spectrum of a light curve. A large number of artificial light curves is simulated with known model power spectra, resembling the same uncertainties and sampling as the observed light curve. The periodograms of the simulated and the observed light curves are tested against each other, varying through the spectral model parameters. This method was recently revised by Max-Moerbeck et al. (2014a). In the following we describe our implementation of the method and point out differences to Uttley et al. (2002) and Max-Moerbeck et al. (2014a).

We simulate light curves as described in section 4.2. We follow Max-Moerbeck et al. (2014a) in matching the light curve variance and the simulation of errors differing from Uttley et al. (2002). For each simulated light curve we estimate the raw power spectrum as described in section 4.1 following the method of Max-Moerbeck et al. (2014a) but including an estimation of the uncertainty introduced due to the re-sampling (c.f. section 4.1.4).

After calculating a large data base of simulated periodograms we roughly follow the methods of Uttley et al. (2002) and Max-Moerbeck et al. (2014a) to find the optimal model parameters. In section 4.3.1 we describe the minimization process leading to the best model parameter, in section 4.3.2 we explain how we derive p-values and confidence intervals for the estimated model parameter, and in section 4.3.3 we introduce a method to estimate the reliability of the parameter estimation.

We restrict the estimation of the intrinsic power spectrum to a simple power-law spectrum (eq. (4.5)), which has only one model parameter, limiting the minimization explained in the following section to a one-dimensional problem of estimating the spectral index.

4.3.1 Best model parameter

We iterate through a range of spectral indices β_j, j=1 ... M. For each β_j we simulate N light curves and measure the raw power spectrum $P_{\mathrm{sim},j,i}(\nu)$, i=1 ... N as described in section 4.1. The resulting power spectra are stored in a data base. We calculate the average model spectrum

$$\overline{P_{\mathrm{sim},j}}(\nu) = \frac{1}{N}\sum_{i=1}^{N} P_{\mathrm{sim},j,i}(\nu), \tag{4.13}$$

the root mean square spread of all simulations regarding to the average model for each sampled frequency

$$\Delta\overline{P_{\mathrm{sim},j}}(\nu) = \sqrt{\frac{1}{N}\sum_{i=1}^{N}\left(P_{\mathrm{sim},j,i}(\nu) - \overline{P_{\mathrm{sim},j}}(\nu)\right)^2}, \tag{4.14}$$

and the test statistic

$$\chi^2_{\mathrm{obs}}(\beta_j) = \sum_{\nu=\nu_{\min}}^{\nu_{\max}} \frac{\left[P_{\mathrm{obs}}(\nu) - \overline{P_{\mathrm{sim},j}}(\nu)\right]^2}{\Delta\overline{P_{\mathrm{sim},j}}(\nu)^2}. \tag{4.15}$$

as introduced by Uttley et al. (2002). We minimize $\chi^2_{\mathrm{obs}}(\beta_j) \to \chi^2_{\min}$ to find an estimator of the intrinsic spectral index:

$$\hat{\beta}_{\mathrm{intr}} = \underset{j}{\operatorname{argmin}}\, \chi^2_{\mathrm{obs}}(\beta_j). \tag{4.16}$$

We use a polynomial p_n of order n fitted to $\chi^2_{\mathrm{obs}}(\beta_j)$. Instead of arbitrarily choosing an order we increase n iteratively, starting with $n = 3$, and determine for each iteration the minimum value and the position of the minimum. The iteration stops when the position of the minimum converges (to an accuracy of 0.01) or the highest order is reached, which is given by $n = M - 1$ where M is the number of tested spectral indices. We use the lowest order, converged fit to estimate $\chi^2_{\min}$ and $\hat{\beta}_{\mathrm{intr}}$.

$\chi^2_{\mathrm{obs}}(\beta_j)$ may cover several orders of magnitude. We select only the lowest values for the actual fit based on the criterion $\chi^2(\beta_j) < 10^m \cdot \min\left(\chi^2(\beta_j)\right)$ with m selected such that at least five data points are fitted. Instead of analytically calculating the minimum of the polynomial of a priori unknown order, we evaluate the fitted polynomial at a step size of 0.001 and linearly interpolate the minimum value and minimum position from the two lowest values.

4.3.2 p-value and confidence interval

We select the tested model with spectral index closest to the optimal index $\beta \approx \hat{\beta}_{\mathrm{intr}}$ as the optimal model, yielding the average best model power spectrum $\overline{P_{\mathrm{opt}}}(\nu)$ and best model spread $\Delta\overline{P_{\mathrm{opt}}}(\nu)$ as calculated by eqs. (4.13) and (4.14). For all simulation $i = 1 \ldots N$ per tested spectral index β_j we calculate the test statistic

$$\chi^2_{\mathrm{sim},i}(\beta_j) = \sum_{\nu=\nu_{\min}}^{\nu_{\max}} \frac{\left[P_{\mathrm{sim},j,i}(\nu) - \overline{P_{\mathrm{opt}}}(\nu)\right]^2}{\Delta\overline{P_{\mathrm{opt}}}(\nu)^2}. \tag{4.17}$$

For each tested β_j the number n of simulations with $\chi^2_{\mathrm{sim},i}(\beta_j) > \chi^2_{\min}$ to calculate the probability

$$P(\chi^2_{\mathrm{sim},i}(\beta_j) > \chi^2_{\min} | H_0) = \frac{n}{N} \tag{4.18}$$

with the Null hypothesis H_0 that the observed data follows a power-law spectrum with the corresponding index β_j. For $\beta_j = \hat{\beta}_{\mathrm{intr}}$ eq. (4.18) gives the model p-value.

Iterating through all β_j yields p-values as a function of the spectral index $P(\chi^2_{\mathrm{sim},i}(\beta_j) > \chi^2_{\min} | H_0)(\beta_j)$. We smooth this function to reduce the noise by convolving it with a Hann window function of a window length of 11 data points. We fit a cubic spline to the smoothed function and estimate where the cubic spline fit is equal to $1-\alpha$ for a given significance level α. The two corresponding spectral indices define the *confidence interval*. If $P(\chi^2_{\mathrm{sim},i}(\beta_j) > \chi^2_{\min} | H_0)(\beta_j)$ does not reach $1-\alpha$ at $\beta_j < \beta_{\mathrm{opt}}$ or $\beta_j > \beta_{\mathrm{opt}}$ the corresponding confidence interval limit does not

lie within the tested range of spectral indices and the lowest or highest index merely give an upper or lower limit. If $\chi^2_{\rm min}$ does not lie within the confidence interval, the confidence interval is not defined and the model result is not reliable as the p-value minimum does not agree with the χ^2-minimization. If $P(\chi^2_{{\rm sim},i}(\beta_j)>\chi^2_{\rm min}|H_0)(\beta_j)$ is larger than $1-\alpha$ for all β_j, i.e. the observed data is closer to the average model than most or any simulation, the confidence interval is not defined at this significance level α.

4.3.3 Reliability test

In this section we discuss a method to test the reliability of the intrinsic spectral index estimation presented in sections 4.3.1 and 4.3.2. We use every simulated power spectrum with known spectral index as "observed" spectrum and test it against the models to estimate the accuracy of the spectral index estimation, the accuracy of the confidence interval and the rate of false negatives.

In practice we calculate the average model $\overline{P_{{\rm sim},\beta_j}}(\nu)$ and RMS $\Delta\overline{P_{{\rm sim},\beta_j}}(\nu)$ for each tested spectral index β_j as in section 4.3.1, eqs. (4.13) and (4.14). We then calculate the test statistic (eq. (4.15))

$$\chi^2_{{\rm sim},i} = \sum_{\nu=\nu_{\rm min}}^{\nu_{\rm max}} \frac{\left[P_{{\rm sim},i}(\nu) - \overline{P_{{\rm sim},\beta}}(\nu)\right]^2}{\Delta\overline{P_{{\rm sim},\beta_j}}(\nu)^2}. \tag{4.19}$$

for every simulation tested against every model, yielding a $N \cdot M$-matrix of χ^2-values for a total number of simulations N and M models, i.e. different spectral indices.

We minimize χ^2 for all N simulations and obtain a distribution of estimated $\hat{\beta}_{\rm intr}$ for every intrinsic spectral index $\beta_{\rm intr}$. The distribution mean, spread and shape allow to estimate the *index estimation accuracy* and allow to check whether there is a systematic offset between the average estimated $\hat{\beta}_{\rm intr}$ and the true $\beta_{\rm intr}$.

For every simulation we select the best model based on the χ^2-minimization and calculate the p-value for each β_j. For $\beta_j \approx \hat{\beta}_{\rm intr}$ we decide whether the model is rejected at a significance level α or not. As any rejection is a false negative, this allows to estimate the *rate of false negatives* depending on the intrinsic $\beta_{\rm intr}$.

For every simulation we calculate the confidence interval as described in section 4.3.2 and check whether or not the intrinsic spectral index lies within the derived confidence limit at significance level α. This provides a *sanity check of the confidence interval*, which states that if the experiment is repeated N times the true spectral index lies $(1-\alpha)N$-times within the derived confidence interval.

The tests are performed over the full range of the tested spectral indices. We point out, that the method cannot be reliable at the lowest and at the highest spectral indices as the χ^2-minimization requires simulations at even lower and higher spectral indices, respectively. The reliability tests are only meaningful for the middle range of tested spectral indices and the range of tested spectral indices should be adjusted accordingly.

We discuss a detailed example of the spectral index estimation, the calculation of the model p-value and the confidence interval, and the reliability tests in the following section.

4.4 B-band and 9 mm-band power spectral analysis

In this section we discuss the power spectral analysis of the 3C 279 B-band and 9 mm light curves as exemplary application of the method described in section 4.3. The two light curves are shown in fig. 4.8.

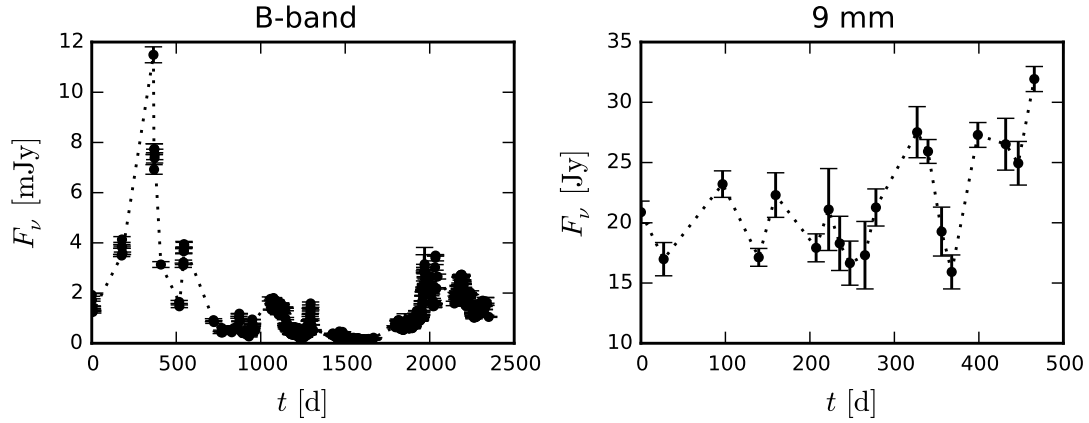

Figure 4.8: Light curves of 3C 279 in B-band (left panel) and 9 mm (right panel).

We simulated light curves as described in section 4.2.8 following a power-law spectrum (eq. (4.5)) with spectral indices initially selected at a step size of 0.1:

$$\beta \in [0.00, 0.1, 0.2, \ldots, 5.0].$$

After a first analysis of the results we decrease the step width of the tested spectral indices to 0.02 in the range of $1.0 - 5.0$ for the B-band data and $0.0 - 5.0$ for the 9 mm data in order to increase the accuracy of the spectral index estimation. All figures shown in the following are based on the denser sampling of the tested spectral index range.

For each spectral index β we create 100 B-band light curves and 500 9 mm light curves[6], calculate the raw power spectra as summarized in section 4.1.4 and store the resulting estimated PSDs.

The average model power spectra calculated with eq. (4.13) and the raw power spectrum of the observed light curves are shown in fig. 4.9. The B-band model spectra clearly show how the sampling pattern of the light curve and the measurement noise affect the estimation of the spectrum. Although the intrinsic spectrum is a power-law the measured periodograms deviate from a linear function in the log-log plot, especially at the lowest frequencies the power is lower than intrinsically. The intrinsically very steep models ($\beta \gtrsim 3$) appear flatter at high frequencies. Here the intrinsic power is below the measurement noise contribution. The 9 mm power spectra show a gap. This gap contains an empty frequency bin, where no power can be measured due to the sampling of the light curve. We do not interpolate empty bins.

[6]The number of simulations we regularly use for each observed light curve and each tested spectral index is N_{500} with two exceptions: for V-band and B-band we have limited the number of simulations to N_{100}. Those are the two best sampled and longest light curves, requiring a dense initial time grid, which drastically increases the computational time for those simulations.

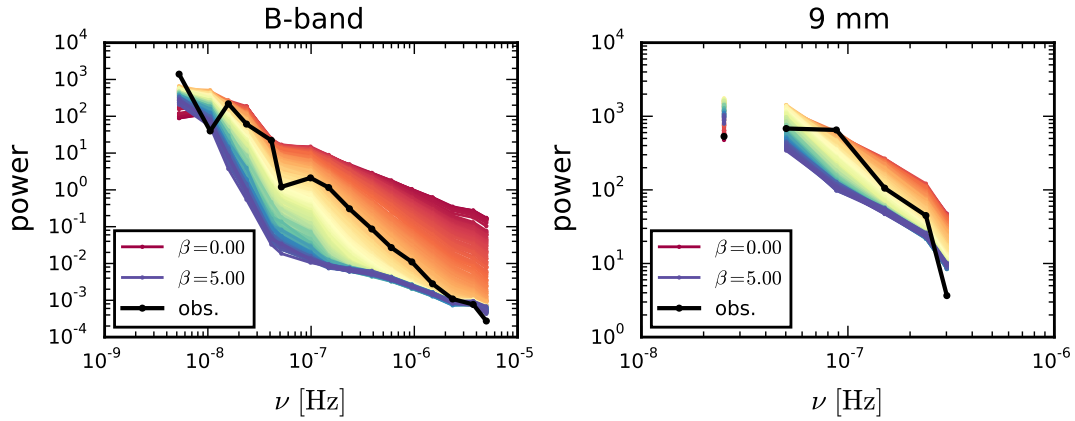

Figure 4.9: The black lines show the raw power spectra of the B-band (left panel) and 9 mm (right panel) light curves with power in arbitrary units. Coloured lines show the average PSD models for spectral indices between one and five.

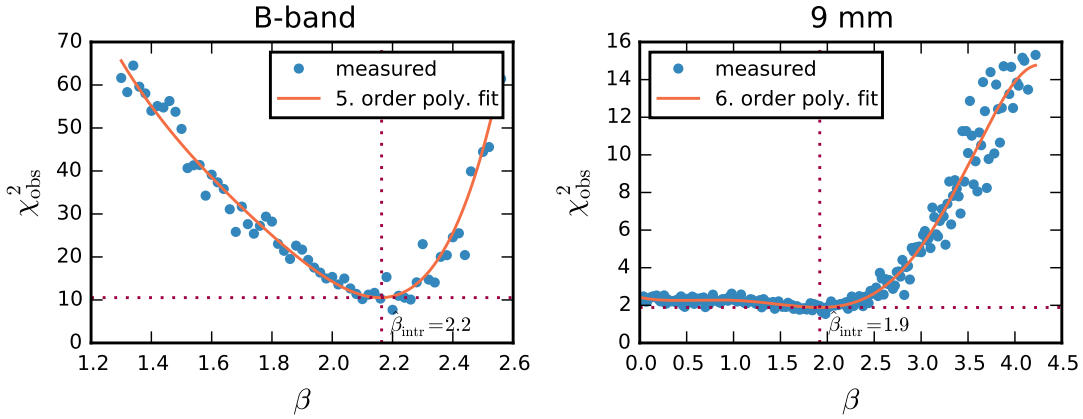

Figure 4.10: χ^2-minimization for the power spectral index estimation at B-band (left panel) and 9 mm (right panel). Blue dots are the model χ^2 estimates, orange lines show a polynomial fit.

In fig. 4.10 we show the χ^2-minimization. Each data point gives the test statistic $\chi^2_{\rm obs}(\beta)$ (eq. (4.15)) based on 100 or 500 simulated light curves for the B-band and the 9 mm, respectively. The orange lines indicate the polynomial fits to the data. The orders at which the minima of the polynomials converged are printed in the figure. $\chi^2_{\rm obs}(\beta)$ shows a clear minimum for the B-band data allowing a reliable estimation of the spectral index. For the 9 mm data $\chi^2_{\rm obs}(\beta)$ is almost flat for spectral indices $\beta < 2$, indicating that this range of indices is indistinguishable given the data sampling. The estimated intrinsic spectral indices are $\hat{\beta}_{\rm intr} = 2.2$ for B-band and $\hat{\beta}_{\rm intr} = 1.9$ for 9 mm.

We show the distributions of $\chi^2_{\rm sim}$ (eq. (4.17)) for the optimal model spectra $\beta \approx \hat{\beta}_{\rm intr}$ in fig. 4.11. The p-values are 46 % for the B-band data, 85 % for the 9 mm data. The hypothesis of a power-law spectrum with a spectral index $\hat{\beta}_{\rm intr} = 2.2$ for B-band and $\hat{\beta}_{\rm intr} = 1.9$ for 9 mm cannot be rejected at any reasonable significance level.

Figure 4.12 shows the fractions of rejected model simulations at each tested spectral index. The curves are smoothed with a Hann window over 11 data points and then fitted with a cubic spline. The confidence interval limits are estimated at

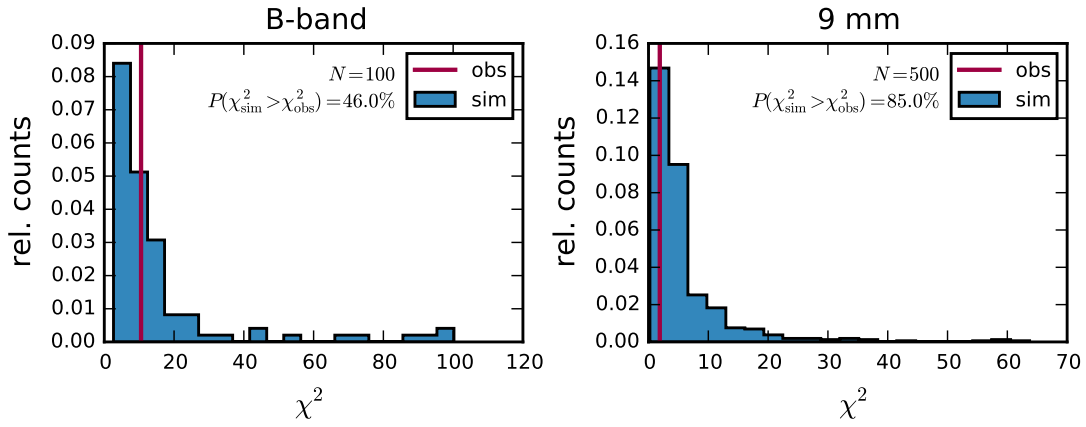

Figure 4.11: Distributions of $\chi^2_{\rm sim}$ at the optimal models $\beta \approx \hat{\beta}_{\rm intr}$ for B-band (left panel) and 9 mm (right panel). Red lines indicate the minimized $\chi^2_{\rm min}$ of the observed data.

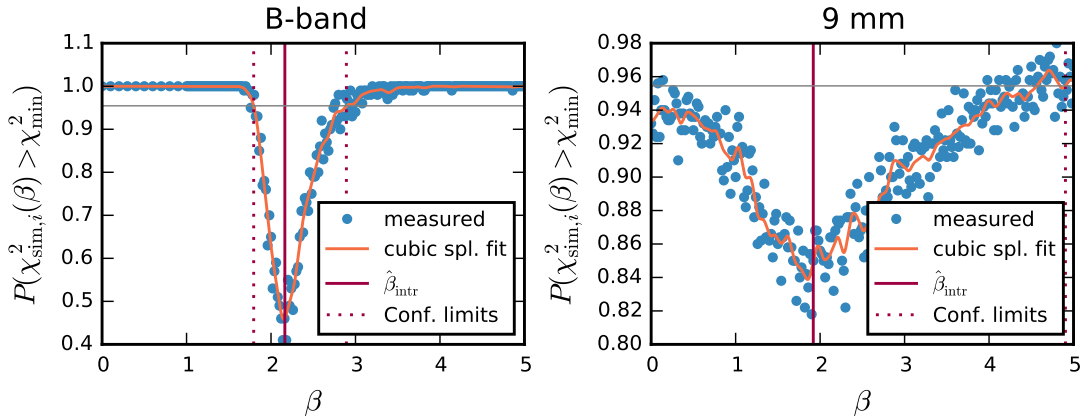

Figure 4.12: Fraction of rejected model simulations at each tested spectral index for B-band (left panel) and 9 mm (right panel). Solid orange lines show a smoothed cubic spline fit. Solid red lines mark $\chi^2_{\rm min}$. Dotted red lines mark the limits of the the confidence interval at 2σ significance (indicated as thin grey line.

2σ significance $\alpha \approx 5\,\%$, where the fit has a value of $1-\alpha$. If the fit has multiple intersections with the $1-\alpha$-line at spectral indices below or above $\hat{\beta}_{\rm intr}$, as it is the case for the 9 mm data at $\beta > \hat{\beta}_{\rm intr}$, we use the most conservative limit which gives the largest confidence interval. The lower limit of the confidence interval for the 9 mm data is not defined at 2σ significance within the tested range of spectral indices.

In the following we discuss the reliability of the method used to derive the previous results. Therefore, we apply the reliability tests introduced in section 4.3.3. For all N simulated power spectra with a model spectral index $\beta_{\rm intr} = 2.2$ (B-band) and $\beta_{\rm intr} = 1.9$ (9 mm), corresponding to the optimal indices derived above, we have estimated the spectral index $\beta_{\rm intr}$. In fig. 4.13 we show the distributions of the differences between the intrinsic and the estimated spectral indices $\beta_{\rm intr} - \hat{\beta}_{\rm intr}$ for the B-band and the 9 mm data. These distributions characterize the accuracy of the spectral index estimation. For the B-band the estimation is unbiased at the order of the step size 0.02 of tested spectral indices. The distribution is not Gaussian but has elevated wings, indicating not an optimal estimation of the spectral index.

We report the distribution standard deviation as standard error for the estimated spectral index. The distribution of the 9 mm data is biased, skewed, broad in comparison to the B-band distribution and shows strong peaks at the lowest and highest values. These distribution properties indicate an unreliable estimation of the spectral index for the 9 mm data.

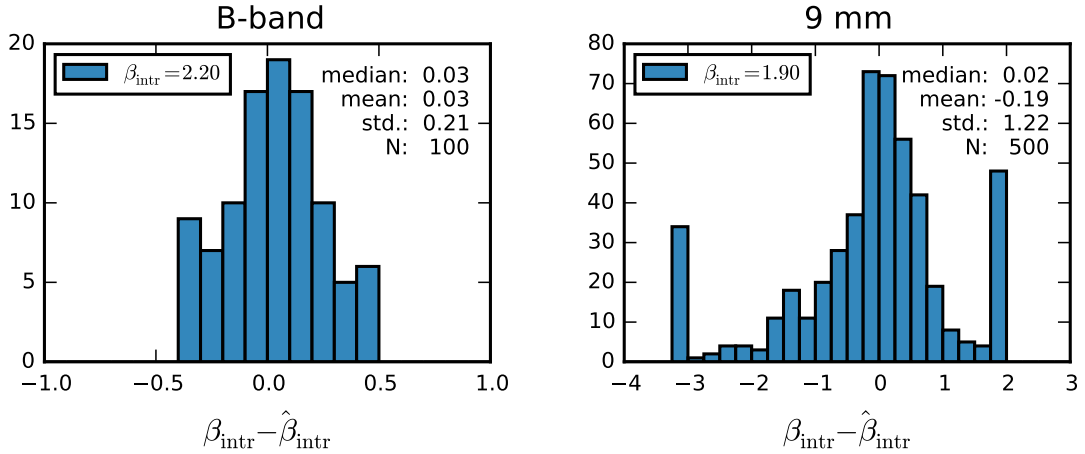

Figure 4.13: Distributions of the spectral index estimation accuracy based on N light curves simulations with the B-band (left pane) and 9 mm (right panel) data sampling.

In fig. 4.14 the rate of *false negatives* are shown for all tested spectral indices. For each simulated light curve we have estimated the spectral index, calculated the p-value and either rejected or accepted the model at 2σ significance. The fraction of rejections over all simulated light curves at each tested index equals the rate of false negatives. For the B-band and 9 mm data we can expect less than two percent of false rejections at the estimated intrinsic spectral index. For both light curves the power-law spectral model is not rejected.

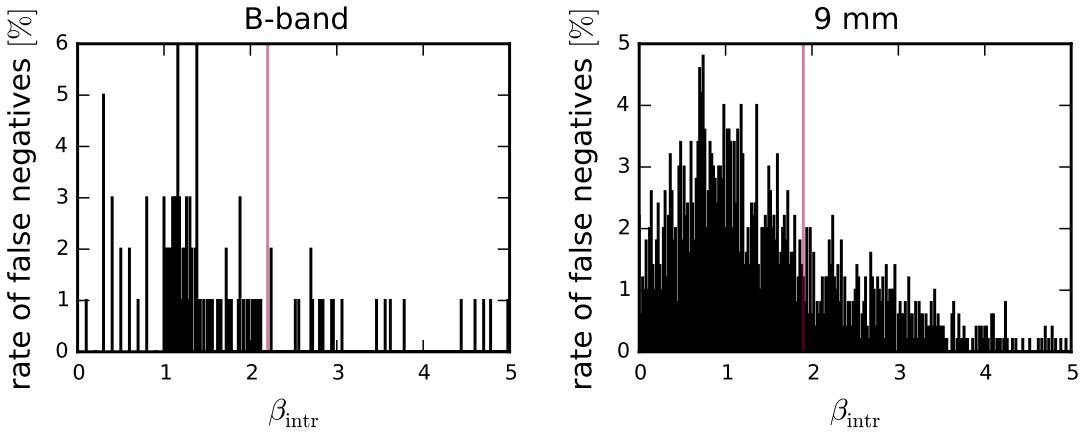

Figure 4.14: Expected rates of false model rejections at each tested spectral index based on simulated light curves with the B-band (left pane) and 9 mm (right panel) data sampling.

Finally, we test if the confidence intervals are estimated reliably. If a confidence interval is estimated correctly at a significance level α, the definition states that when repeating a measurement N times, each time calculating a confidence interval, $N \cdot (1-\alpha)$ of the confidence intervals contain the actual value of interest. We

calculate confidence intervals at 2σ significance for the estimated spectral index based on all light curve simulations at each test model index. The result is shown in fig. 4.15. At each model index the green bar indicates the fraction of simulations for which the derived confidence interval contained the intrinsic spectral index. The stacked yellow bars shows the fraction of simulations for which the confidence interval could not be determined at 2σ significance. This is the case if the function $P(\chi^2_{\mathrm{sim},i}(\beta_j)>\chi^2_{\mathrm{min}})$ does not intersect with the significance level. An example is shown in fig. 4.12. The confidence interval may be defined at a higher significance level. We do not check if the intrinsic spectral index is included in the confidence interval at higher significance levels. The remaining red bar indicates the fraction of simulation, where the model index is not in the confidence interval. We indicate the 2σ significance level as a grey line. For most of the tested spectral indices the red bar starts below the significance line. This shows that the derived confidence intervals do not follow the definition. The confidence intervals are probably underestimated.

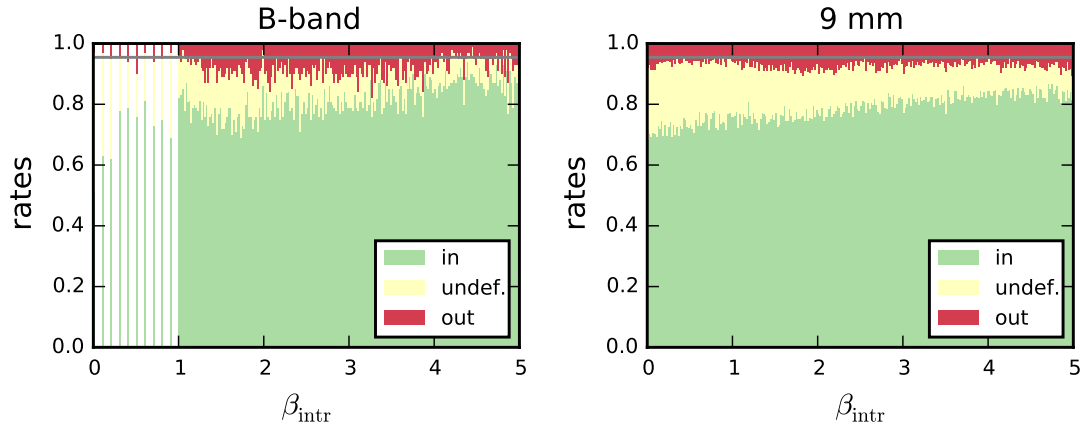

Figure 4.15: Ratios of confidence intervals which do (green) and which do not (red) contain the value of interest based on light curve simulations with the B-band (left pane) and 9 mm (right panel) data sampling at different intrinsic spectral indices. Yellow parts indicate the fraction of simulations for which the confidence interval is not defined at 2σ significance.

We have discussed the power spectral analysis of the B-band and the 9 mm light curve in detail as examples of a reliable and a non-reliable estimation of the power spectral index, respectively. The B-band data show a distinct and consistent minimum in the χ^2-minimization and the p-values (figs. 4.10 and 4.12), the distribution of the spectral index estimation accuracy (fig. 4.13) is unbiased, not skewed and has a comparably small spread regarding to the 9 mm distribution. The 9 mm data does not show a clear minimum in the χ^2-minimization, the confidence interval covers the whole tested range of spectral indices, and the distribution of the spectral index estimation accuracy shows a bias towards steeper spectra, is skewed, broad and multi-modal. We define three qualitative criteria to characterize the reliability of a spectral index estimation:

χ^2-fit: A clear dip in the $\chi^2_{\mathrm{obs}}(\beta)$ plot indicates a good parameter estimation. The lower the polynomial order used to fit this function, the better is the minimum localized, i.e. the more reliable is the parameter estimation.

Confidence interval: A clear dip in the p-values over the tested spectral indices indicates a good parameter estimation. The smoother the function and the

cubic spline fit the more reliable the estimation.

Direct reliability estimation: The simulation based distribution of $\beta_{\rm intr} - \hat{\beta}_{\rm intr}$ provides a direct estimation of the accuracy. A single-peaked, Gaussian-like distribution with zero mean indicates a reliable, unbiased estimation of the spectral index with an uncertainty given by the distribution spread. A mean deviating from zero and a skewed distribution indicate a bias. A multi-modal distribution points out an unreliable estimation of the spectral index. We accept single-peaked, unbiased, non-skewed distributions as high reliability criteria.

The first and second criterion are independent. One may indicate a good estimation while the other does not. The third criterion is probably the best as it directly measures the reliability and it usually reflects the first and second criterion. For instance, when the first and second criterion indicate a good estimation the third shows a narrow unbiased distribution, on the other hand if the confidence interval is asymmetrical the distribution is asymmetrical, both indicating a possible bias towards lower or higher spectral indices. We use these three criteria to rate the quality of the power spectral analysis in the following section.

4.5 Multi-wavelength power spectral analysis

In fig. 4.16 we show the estimated power spectral densities for all tested light curves. Raw PSDs are shown as red points. Grey error bars indicate the standard deviation in each frequency bin. We choose a frequency binning of 5 logarithmic bins per order. The power-law models based on the estimated intrinsic spectral indices are shown as blue lines. In the γ-ray panel open squares additionally show the direct periodogram of the weekly-binned light curve and the dashed blue line the corresponding linear regression. All PSDs can be described as power-law. For the infrared, optical, and ultraviolet light curves the simulation based spectral indices do not differ significantly from direct linear regressions of the raw periodograms. At cm, mm, and sub-mm frequencies the simulation based and direct estimates of the spectral index differ. Direct estimates can be over-estimated (e.g. 870 μm) or under-estimated (e.g. 8 mm).

The X-ray PSD shows a bend over the whole frequency range which cannot be easily attributed to a characteristic frequency. We have not tested other spectral models (e.g. broken power-law) against the X-ray data, since the simple power-law model with a p-value of 37 % cannot be rejected at a reasonable significance level. But Chatterjee et al. (2008) point out they cannot reject a spectral break at a frequency $\leq 10^{-8}$ either. Further model testing is necessary to answer whether the X-ray power spectrum has a break. We point out that the gap in the estimated PSD is critical as it might contain the potential break frequency. We note further, that a drop of power at the lowest measured frequency does not necessarily indicate a break. We observe this reduced power at the lowest measured frequency in almost all bands, independent of the frequency. Thus, we suspect it originates in the finite sampling of the light curves and is not an intrinsic feature. The same argument holds for the direct periodogram of the γ light curve. A potential spectral break at $\nu \sim 10^{-8}$ Hz has to be investigated by testing different models against the data.

We plot the estimated power spectral indices of all bands over the logarithmic frequency in fig. 4.17. Grey error bars indicate the confidence intervals at 2σ

significance. Arrows mark the upper or lower limits of the tested spectral index range, when the confidence interval limit does not lie within that range. Coloured error bars display the uncertainties estimated from the distribution of the spectral index estimation accuracy (e.g. fig. 4.13). The spectral indices, uncertainties, confidence intervals and p-values are also listed in table 4.1. We have estimated the reliability of theses parameters based on the three criteria discussed in the previous section. We use the following colour-coding in fig. 4.17 to indicate the reliability of the data points:

Green circles (Yes) The estimation is reliable, when all three criteria are fulfilled.

Red diamonds (No) The estimation is not reliable when the third criterion is not fulfilled (biased or multi-modal distribution) and at least one of the other two criteria.

Orange squares (Maybe) The estimation reliability is not clear when one or two criteria are not heavily violated and the others are fulfilled.

We have derived estimates of the γ-ray power spectral index based on the 7d-binned and the adaptively binned (25 % unc.) light curve The results are given in table 4.1. The confidence interval at 2σ significance is not defined for the spectral index based on the 7d-binned data, therefore we calculate the 3σ confidence interval. The adaptively binned light curves does not result in a reliable estimate. The estimate based on the 7d-binned light curve is reliable and it is consistent with the average spectral index for FSRQs 1.4 ± 0.1 reported by Abdo et al. (2010b), consistent within the uncertainties with the index 1.6 ± 0.2 reported by Abdo et al. (2010b) for 3C 279 based on data from August 2008 to July 2009, and the index 1.6 ± 0.4 reported by Max-Moerbeck et al. (2014b) based on data from August 2008 to from August 2011. We are using this value based on the 7d-binned data in all following analysis and discussion.

For X-rays Chatterjee et al. (2008) report a power spectral index of 2.3 ± 0.3 based on RXTE observations between January 1996 and June 2007. Our light curve includes the same data but extends to December 2011. We find a significantly flatter power spectral index of 1.5 ± 0.1 indicating a stronger contribution of short term variability than found by Chatterjee et al. (2008). In fig. 4.18 we show the RXTE light curve between January 1996 and December 2011. The black dotted line marks the end of June 2007, the data range of Chatterjee et al. (2008). The light curve exhibits more flaring activity before June 2007. Red points show a smoothed curve, the original data convolved with a Hann window of 1000 days width. The standard deviation of the smoothed light after June 2007 is only 20 % of the standard deviation before June 2007, whereas the standard deviation of the residual curve is 50 % after June 2007 with respect to before. The long term variation is reduced more than the short term variation, resulting in a less steep power spectrum when the data after June 2007 is included in the analysis.

The power spectral indices at ultraviolet, optical, and infrared bands range between 1.7 and 2.3. They do not show significant differences. The frequency range from optical to ultraviolet shows a trend towards flatter spectra, indicating more short time scale variability at ultraviolet frequencies. Inversely, the range from infrared to optical shows a trend towards steeper spectra. The differences in both frequency ranges are not significant and an uncertainty weighted linear regression over the infrared to ultraviolet range yields a slope consistent with zero.

Table 4.1: Results of the power spectral analysis of the QMP light curves: bands (col.1), logarithmic frequencies (col.2), estimated spectral indices (col.3) and the corresponding uncertainties (col.4) and confidence intervals (col.5,6), p-values (col.7) and qualitative estimations of the reliability (col.8).

Band	$\log \nu\,\mathrm{Hz}^{-1}$	$\hat{\beta}$	$\sigma_{\hat{\beta}}$	conf. int.		p-value	Reliable
114 mm	9.4	3.4	1.7	1.7	>6.0	80 %	No
62 mm	9.7	2.4	0.6	1.8	3.9	88 %	Yes
36 mm	9.9	3.6	1.1	<0.0	>5.0	100 %	No
29 mm	10.0	3.7	1.0	2.2	>5.0	75 %	No
21 mm	10.2	3.0	0.6	2.0	>5.0	18 %	Maybe
13 mm	10.4	1.6	0.9	<0.0	2.5	92 %	No
9 mm	10.5	1.9	1.2	<0.0	5.0	85 %	No
8 mm	10.6	2.8	0.4	2.2	5.0	84 %	Yes
3 mm	11.0	2.3	0.9	1.2	>5.0	50 %	No
2 mm	11.2	1.6	1.7	<0.0	3.4	92 %	No
1 mm	11.4	1.9	0.2	1.5	3.1	42 %	Yes
0.87 mm	11.5	1.6	0.2	1.3	1.9	86 %	Yes
Ks	14.1	1.8	0.1	1.5	2.2	35 %	Yes
H	14.3	2.0	0.3	1.7	2.4	77 %	Yes
J	14.4	1.8	0.1	1.5	2.3	42 %	Yes
I	14.6	2.2	0.3	1.7	2.7	80 %	Yes
R	14.7	2.1	0.2	<0.0	>5.0	100 %	Yes
V	14.7	1.9	0.1	1.5	>5.0	7 %	Yes
4609 A	14.8	2.3	0.2	2.0	2.6	82 %	Yes
B	14.8	2.2	0.2	1.8	2.9	46 %	Yes
U	14.9	1.9	0.2	<0.0	>5.0	96 %	Yes
W1	15.1	1.8	0.2	1.5	2.1	71 %	Yes
M2	15.1	1.7	0.4	1.4	1.9	80 %	Maybe
W2	15.2	1.8	0.2	1.5	2.1	71 %	Yes
X-ray	18.1	1.5	0.1	1.2	1.7	37 %	Yes
γ-ray (7d bin)	23.0	1.4	0.2	0.9	1.8	98 %	Yes
γ-ray (adbin 25unc)	23.0	2.6	1.0	1.5	>5.0	98 %	Yes

The uncertainty weighted average is 1.9 ± 0.1. This value is indicated in fig. 4.17 as dashed, black line. The averaged index is consistent with the values 1.7 ± 0.3 reported in Chatterjee et al. (2008) for R-band data between January 1996 and June 2007 and $2.3^{+0.2}_{-0.5}$ reported in Chatterjee et al. (2012) for R-band data in 2008-2010.

At 870 μm and 1 mm the power spectral index is the same as in the ultraviolet, optical, infrared frequency range with in the uncertainties. We note that, on the other hand, the 870 μm power spectral index is also consistent with the X-ray index within the uncertainties, which is significantly flatter than the average optical power spectrum. Towards lower frequencies the power spectral index appears to gradually increase, yielding steeper power spectra. The uncertainty weighted linear regression gives a slope of -0.7 ± 0.3. The slope does not change significantly when we exclude the data points rated as unreliable (red points in fig. 4.17) from the regression. The slope clearly differs from zero but estimates of the power spectral indices have too large uncertainties to evaluate whether the relation $\beta(\nu)$ follows a

power-law. The power spectral index 3.0 ± 0.6 at 21 mm is consistent within the uncertainties with the result of 2.3 ± 0.5 reported by Chatterjee et al. (2008) and index $2.4^{+0.3}_{-0.6}$ reported by Max-Moerbeck et al. (2014b).

Throughout all bands from radio to γ-rays we find PSDs consistent with a red noise process, meaning that variability amplitudes are larger on longer than on shorter time scales. Radio frequencies are dominated by longer time scale variability than the infrared to γ-rays frequency range.

At cm, mm, and sub-mm frequencies the power spectrum steepens gradually towards lower frequencies, the contribution of short time scale variability decreases. This change in the variability time scales can be explained by different sizes of the emission regions. When the volume of the emitting region gets larger only large scale variation on longer time scales changes the total flux significantly, whereas more localized perturbations on shorter time scales do not affect the intensity integrated over the full volume significantly: the lower the frequency, the larger the volume, the less variability on short time scales. Two effects can increase the size of the emission region towards lower frequencies. The first is explained by the Marscher and Gear (1985) model. Particles accelerated to high energies by a shock fill a smaller region than particles accelerated to lower energies. The reason is that the distance a particle can travel from the shock front depends on the *cooling time*, i.e. the time scale at which the particle looses its energy either through the emission of synchrotron radiation or through IC scattering. The cooling time scales with the particle Lorentz factor γ as $t_{\rm cool} \sim \gamma^{-1}$. Particles of lower energy loose their energy less fast, travel further and, thus, fill a larger volume than particles of higher energy. The second effect is related to the opacity of the emission region. The region becomes optically thin to low frequency radiation only if the particle density is low enough, i.e. the initial volume has expanded sufficiently. Both effects also lead to a time delay in the emission at different frequencies, which is discussed in chapter 5.

At 870 μm and 1 mm the power spectral index is consistent with the infrared to ultraviolet range, indicating that these frequency ranges of radiation are probably produced by the same electron population. The trend over the cm to mm frequency range and the spectral index at 870 μm also indicate that the spectral index at sub-mm frequencies could be as flat as at X-rays, implying that both frequency ranges are produced by the same electron population consistent with the leptonic IC model. With eqs. (1.8) and (1.14) we estimate the frequency $\nu_{\rm seed}$ of the seed photons:

$$\nu_{\rm seed} \sim 2.8 \cdot 10^6 \cdot B[\mathrm{G}] \frac{\nu_{\rm IC}}{\nu_{\rm sy}}. \tag{4.20}$$

Assuming a magnetic field strength $B{\sim}1$ G (Hartman et al., 2001) and $\nu_{\rm sy}{\sim}10^{12}$ Hz, $\nu_{\rm IC}{\sim}10^{18}$ Hz, the seed photon frequency is at the order of $\nu_{\rm seed}{\sim}10^{12}$ Hz, the same order as the synchrotron photons. The Cosmic Microwave Background (CMB) peak frequency at $\nu_{\rm CMB}$=160 GHz corresponds to $\nu'_{\rm CMB} = (z+1)\nu_{\rm CMB} \approx$ 246 GHz at redshift z=0.5362 (Marziani et al., 1996) of 3C 279. Assuming a Lorentz factor Γ=15.5 (Jorstad et al., 2005), the Doppler shifted frequency of the CMB photons in the comoving frame of the emission region is at $\nu^{\rm em}_{\rm CMB} = \nu'_{\rm CMB}\Gamma^{-1}(1-\beta)^{-1} \sim 10^{12}$ Hz. Thus, the synchrotron photons (SSC) and the CMB photons (EC) are potential seed photons for the IC scattering to keV energies.

We find a significant difference in the power spectral index at γ-rays and infrared, optical frequencies, comparable to the result of Chatterjee et al. (2008).

Table 4.2: Results of the power spectral analysis of the V-band light curve parts (col.1): time ranges of the extracted light curve (col.2), estimated spectral indices (col.3) and the corresponding uncertainties (col.4).

Part	JD − 2450000	$\hat{\beta}$	$\sigma_{\hat{\beta}}$
IV	4073-4296	2.4	0.7
VI	4795-5058	2.0	0.2
VII	5151-5416	2.1	0.4
VIII	5512-5795	2.5	0.5
I-III	2968-3930	1.4	0.1
VII-IX	5151-6126	1.8	0.3

The short term variability contribution is stronger at γ-rays. In the context of the leptonic models this difference in the variability time scales could imply that the electron population producing the infrared and optical synchrotron radiation and the electron population up-scattering seed photons to GeV-energies through IC scattering are not the same, but the population responsible for the IC scattering is more energetic (Chatterjee et al., 2008). A flattening of the power spectrum from optical to ultraviolet frequencies is visible in fig. 4.17, although not significant given the uncertainties. If this gradual change of the power spectral index is real, this would imply a consistent power spectrum at far-ultraviolet and γ-rays, suggesting that electrons IC scattering photons to GeV-energies are the same emitting the high energy end of the synchrotron spectrum. With eq. (4.20), $B{\sim}1\,\mathrm{G}$ (Hartman et al., 2001) and $\nu_{\mathrm{sy}}{\sim}10^{15}\,\mathrm{Hz}$, $\nu_{\mathrm{IC}}{\sim}10^{23}\,\mathrm{Hz}$ the estimated frequency of the seed photons is at the order of $\nu_{\mathrm{IC}}{\sim}10^{14}\,\mathrm{Hz}$, i.e. infrared in the observers reference frame. These photons could originate from the dusty torus.

4.6 Stationarity

The fact that the estimated power spectral index of the X-ray data differs between our result and the result of Chatterjee et al. (2008) and that this difference is not necessarily method related, but introduced by different time ranges for the observed light curves raises the question if we can reliably estimate the typical variability behaviour of a source when the light curves are not stationary. We test our longest and best sampled optical light curve, V-band, for stationarity. We want to know if the power spectral index changes when we choose different parts of the light curve. We select 9 parts of the light curve marked in fig. 4.19 (I to IX) based on the observational periods and three longer parts (I-III, IV-VI, VII-IX). We estimate the spectral index for each part with the same method as used for the full light curves. We get reliable results for six periods, which are listed in table 4.2.

The estimated spectral indices range from $1.4{\pm}0.1$ to $2.5{\pm}0.5$. The uncertainties are generally larger than for the full light curve and except for part I-III all values are consistent with the index estimated from the full light curve within the uncertainties. Therefore, we cannot clearly determine if the power spectrum changes over time or if the estimation is simply not reliable enough for short periods. The shorter the extracted light curves the smaller is the tested frequency range and long time scale variation is neglected.

Generally, the assumption of stationarity is in conflict with the very fact of sporadic flaring activity that blazars typically exhibit over the whole frequency

range. Flaring epochs and non-flaring epochs are usually too short to estimate the underlying power spectrum reliably and inevitably not representative for long term variation. Therefore, we have to estimate the power spectrum from long data sets under the assumption that the studied light curve represents all states of the jet to estimate a representative average PSD. For the γ-rays, optical and 21 mm light curves this seems to be the case as we get consistent results with other values reported in the literature, which are based on light curves at different times. For the X-rays the RXTE light curve of Chatterjee et al. (2008) had not yet covered all states as the continued light curve shows different variation from the previous part. Unfortunately, we cannot know if the light curve until December 2011 is a well enough representation of the average behaviour. Only longer monitoring can reveal at what time scale quasi-stationarity can be assumed, in that sense that most likely all states are captured in a representative distribution within a long term light curve.

4.7 Summary of the PSD analysis

In this chapter we have thoroughly investigated the effects of finite and uneven sampling and observational noise on the estimation of the variability power spectrum of light curves. We have suggested a few advancements over the methods presented by Uttley et al. (2002) and Max-Moerbeck et al. (2014a). These include de-trending the light curves to minimize red noise leakage and multiple re-sampling to estimate the uncertainties due to unevenly sampled data.

We apply our method to all light curves of the Quasar Movie Project and estimate the power spectral indices over a frequency range from 5 GHz to γ-rays. Generally, the power spectrum is consistent with a red noise process at all frequencies. At cm and mm bands we find a gradual steepening of the power spectral index, consistent with lower frequency radiation originating from a larger emission region. We find indications for similar power spectra at sub-mm frequencies and X-rays on the one hand and ultraviolet to far-ultraviolet and γ-rays on the other hand. We interpret these results such that the same electron population is producing the synchrotron sub-mm radiation and up-scattering photons to keV energies. The seed photons are in the mm to sub-mm regime and could be provided either by the local synchrotron emission or the CMB indicating SSC-scattering or EC-CMB scattering, respectively. The γ-ray emission is produced by the electrons responsible for the high energy end of the synchrotron spectrum, in the ultraviolet to far-ultraviolet range. The seed photons are in the infrared frequency range and could originate from the local synchrotron emission (SSC) or the dusty torus (EC-T).

In chapter 5 we discuss the cross-correlation between all light curves and investigate whether the variability differences found and discussed here are also reflected in the correlation of the different light curves. We will use the power spectral models derived in this chapter to simulate light curves with the same variability as the observed data, in order to estimate the significance of the cross-correlation .

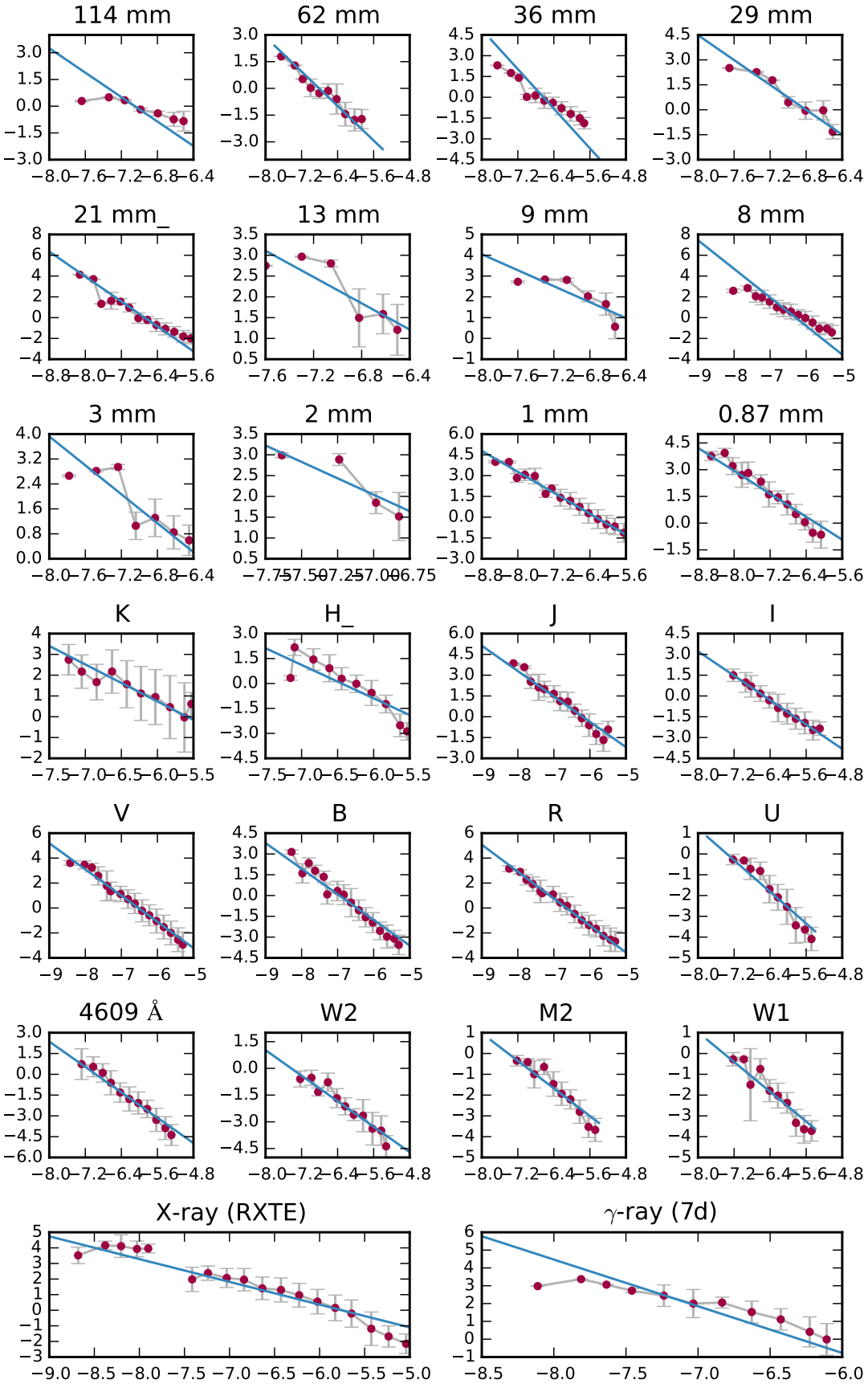

Figure 4.16: Raw power spectral densities. X-axis are $\log_{10}$ of the frequency in Hertz, y-axis are $\log_{10}$ of the power in arbitrary units. Blue lines indicate the estimated intrinsic power spectrum. The γ-ray PSD is based on the 7d-binned light curve.

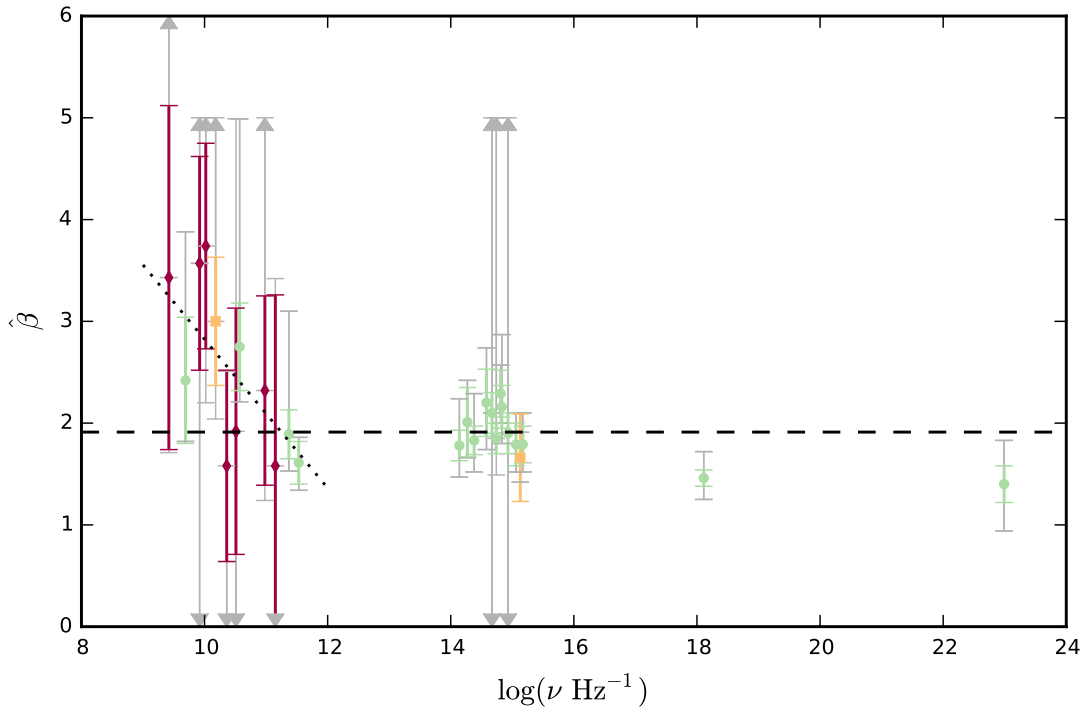

Figure 4.17: Estimated power spectral indices over the logarithmic frequency. Green data points are reliable estimates, red are non-trusted, for yellow data point the reliability is uncertain. Coloured error bars indicate the simulation based uncertainties, grey error bars the 2σ confidence intervals, grey arrows mark the tested parameter range, when no limit for the confidence interval is available. The dashed black line marks the weighted average index of the infrared, optical, ultra-violet frequency range. The dotted black line indicates a weighted linear regression of the cm, mm, sub-mm frequency range. The γ-ray spectral index is based on the 7d-binned light curve.

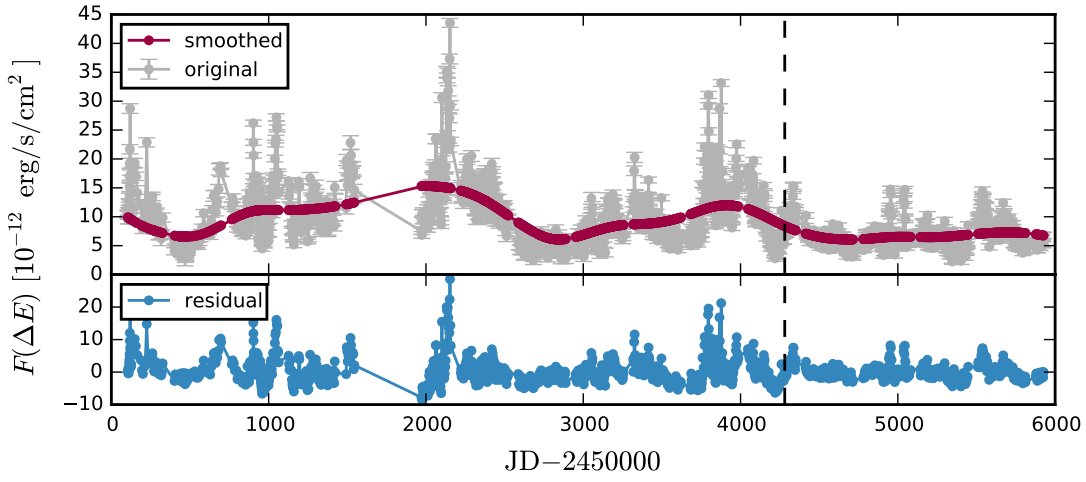

Figure 4.18: RXTE X-ray light curve of 3C 279. Grey points show the observed data, red points a smoothed curve, and blue points the residual curve. The dotted black line marks the end of the data of Chatterjee et al. (2008).

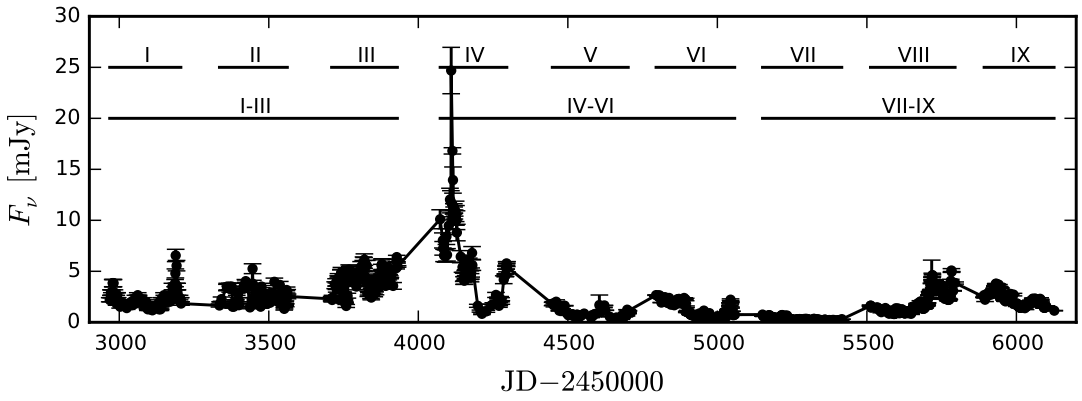

Figure 4.19: V-band light curve of 3C 279. Different parts are marked which are used to test the light curve for stationarity.

Chapter 5

Cross-correlation analysis

In this chapter we discuss the cross-correlation of the light curves. The main goal is to find correlated bands, indicating a physical connection of the emission processes, and to estimate the time lags of the correlation allowing to understand the emission process and to pinpoint the emission region. In section 5.1 we introduce the methods of estimating the cross-correlation function, the significance of the correlation, and the confidence interval of the time lag corresponding to the correlation peak. We discuss the cross-correlation between radio bands, between the optical bands, and between the best sampled cm, mm, optical bands, X-rays and γ-rays in section 5.2. The results are summarized in section 5.3.

5.1 Methods of the cross-correlation analysis

In this section, the methods are introduced which we use later on to estimate the strength of correlation and typical time lags between light curves of different bands. In section 5.1.1, we discuss the estimation of the cross-correlation function given unevenly sampled light curves. In section 5.1.2 we describe a method to estimate the significance of correlations, and in section 5.1.3 we describe the automatic identification of correlation peaks and the estimation of time lag uncertainties.

5.1.1 Estimation of the cross-correlation function

The cross-correlation function $R_{xy}(\tau)$ of two signals $x(t)$ and $y(t)$ describes the correlation, i.e. the similarity of the signals as a function of a relative time delay τ between the signals. It is defined as:

$$R_{xy}(\tau) = \int_{-\infty}^{\infty} x^*(t)y(t+\tau)\mathrm{d}t, \tag{5.1}$$

where $x^*(t)$ is the complex conjugate of $x(t)$. The cross-correlation function is defined in the interval $[-1, 1]$, where a value of 0 denotes no correlation, 1 perfect correlation, and -1 perfect anti-correlation.

For discrete unevenly sampled time series different methods have been proposed to estimate the cross-correlation. Edelson and Krolik (1988) introduced the Discrete Correlation Function (DCF), which is regularly used in correlation studies (e.g. Fuhrmann et al., 2014; Rani et al., 2014). For two discrete time series $x_i = x(t_i)$

and $y_j = y(t_j)$, first, the unbinned discrete correlations for all measured pairs i, j are calculated

$$\mathrm{UDCF}_{ij} = \frac{(x_i - \overline{x})(y_i - \overline{y})}{\sigma_x \sigma_y} \tag{5.2}$$

and the associated time lags

$$\Delta t_{ij} = t_j - t_i, \tag{5.3}$$

where $\overline{x}$ is the mean of the time series x_i and σ_x the standard deviation, for y respectively. The individual time lags Δt_{ij} are re-binned to an even grid of bin width $\Delta\tau$ and the DCF is then calculated by averaging all values of UDCF_{ij} associated with on time lag bin

$$\mathrm{DCF}(\tau) = \frac{1}{N} \sum \mathrm{UCDF}_{ij}, \tag{5.4}$$

where for each τ the sum is over all N pairs i, j with $\tau - \frac{\Delta\tau}{2} \leq \Delta t_{ij} < \tau + \frac{\Delta\tau}{2}$. Accordingly, the uncertainty of the DCF is given by the standard deviation of the UDCF_{ij} associated with each bin:

$$\sigma_{\mathrm{DCF}}(\tau) = \frac{1}{N-1} \left[\sum \left(\mathrm{UCDF}_{ij} - \mathrm{DCF}(\tau) \right)^2 \right] \tag{5.5}$$

The choice of the time lag binning $\Delta\tau$ is arbitrary, but $\Delta\tau$ should be large enough to average over multiple values $N > 2$ of UDCF_{ij}.

The DCF is not properly normalized when the time series (t_i, x_i, e_i), (t_j, y_i, e_j) are affected by uncertainties e_i, e_j. Correlating observational noise affected light curves, may result in DCF values larger than one, which makes the direct interpretation of the DCF impossible. For homoscedastic errors, the DCF can be normalized properly by reformulating eq. (5.2):

$$\mathrm{UDCF}_{ij} = \frac{(x_i - \overline{x})(y_i - \overline{y})}{\sqrt{(\sigma_x^2 - e_x^2)(\sigma_y^2 - e_y^2)}}, \tag{5.6}$$

where e_x and e_y are the uniform uncertainties of the time series x and y, respectively. For heteroscedastic errors, the DCF cannot be properly normalized.

The Local Cross-Correlation Function (LCCF) introduced by Welsh (1999) maintains the normalization to the $[-1, 1]$-interval. It is defined as:

$$\mathrm{LCCF}(\tau) = \frac{1}{N} \frac{\sum (x_i - \overline{x}_\tau)(y_j - \overline{y}_\tau)}{\sigma_{x\tau} \sigma_{y\tau}}, \tag{5.7}$$

where the sum is over the N pairs of indices (i, j) such that $\tau \leq \Delta t_{ij} < \tau + \Delta\tau$. In contrast to the DCF the mean values $\overline{x}_\tau$, $\overline{y}_\tau$ and the standard deviations $\sigma_{x\tau}$, $\sigma_{y\tau}$ are calculated over the data pairs (i, j) associated with each time lag bin instead of the full time series.

Max-Moerbeck et al. (2014a) show through a series of tests that the LCCF performs more accurate and more reliably than the DCF in the estimation of a correlation time lag. Therefore, we are using the LCCF in the following to estimate the correlation function of two light curves.

5.1.2 Significance of the cross-correlation function

As discussed in the previous section the DCF is not properly normalized, when the light curves are affected by observational noise, and the estimated correlation function can exceed values of ± 1. Thus, the DCF alone does not carry useful information, but it is necessary to estimate the significance of the correlation coefficients at each time lag. Even when using the LCCF, which avoids the normalization problem, it is necessary to estimate the significance of correlations. When two signals, each containing an arbitrary flaring peak, are cross-correlated the resulting correlation function has a peak at the corresponding time lag. It is required to test whether the correlation is significant.

Two methods are commonly used to estimate the significance of the cross-correlation function. Either a large data base of observed light curves for multiple objects is available. Then random pairs of light curves can be correlated to estimate the probability of correlations by chance. This method is known as *mixed source correlation* (e.g., Larsson et al., 2012; Fuhrmann et al., 2014). Alternatively, light curves with the same underlying power-spectrum as the observed light curves are simulated and correlated. Various implementations of this Monte Carlo method are reported in the literature, e.g. Chatterjee et al. (2008), Larsson et al. (2012), Rani et al. (2014), Max-Moerbeck et al. (2014a), and Max-Moerbeck et al. (2014b). In the following we describe our own implementation of the light curve simulation and the Monte Carlo method.

For each observed light curve we simulate 200 light curves with the same underlying power spectrum as the observed light curve. We use a power-law spectral model and the Timmer and Koenig (1995) (TK) algorithm to produce a Gaussian light curve. We use the power-law indices estimated in chapter 4, table 4.1. The initial sampling rate is $0.1 \cdot \mathrm{median}(t_i - t_{i-1})$ and the initial total time $10 \cdot T$, where t_i are the (unevenly sampled) target time steps and T is the targeted total light curve time, thus including low and high frequency power. The long light curve is split into 10 parts of the targeted duration T and the following steps are applied to each part individually. We test two approaches adjusting the light curve amplitude: (a) matching the light curve variance (section 4.2.3) and (b) adjusting the light curve PDF (section 4.2.4). The adjusted light curve is re-sampled of re-binned (binning in the case of γ-ray light curves) and simulated observational noise is added. The light curve simulation is describe in detail in section 4.2. In the following paragraph we discuss the impact of the simulation type on the significance estimation.

With 200 simulated light curves per observed band, we can calculate up to 40 000 simulated correlation functions. We use the same type of correlation function, the LCCF, and the same time lag binning $\Delta\tau$ as for the observed data. At each time lag bin the distribution of correlation coefficients allows to calculate *significance levels*. Additionally, at each time lag bin we calculate the *significance* of the correlation as the fraction of simulated correlation functions with a correlation coefficient lower than the coefficient based on the observed light curves. A significance of one indicates that no simulation resulted in a correlation coefficient at least as high as observed[1] and that the observed correlation coefficient is unlikely to occur by chance. In the numerator and denominator of the number fraction of simulations we consider only those simulated correlation functions which have same sign of the correlation coefficient as the observation based coefficient. With a bootstrap

[1] One minus the significance would be the typical definition of a p-value.

method, selecting only a varying fraction of the simulated correlation functions in multiple iterations, it is possible to calculate uncertainties for the significance levels and the significance.

Light curve simulation: In figs. 5.1 to 5.3 examples of simulated light curves are shown for the adaptively binned γ-ray, V-band, and 21 mm light curves. The left panels show simulated Gaussian light curves based on the Timmer and Koenig (1995) algorithm with variance adjusted scaling. The right panels show simulated light curves with adjusted PDF based on the Emmanoulopoulos et al. (2013) (EMP) algorithm. Black open dots show the corresponding observed light curve for comparison.

Throughout all bands the simulated Gaussian light curves (left panels in the exemplary figures) do not show the flaring behaviour observed. The reason is that the light curve PDF is not Gaussian as we have shown in section 3.2. The PDF adjusted simulations (right panels) resemble the observed flaring behaviour. In section 4.2.5 we have discussed that the EMP algorithm does not work for inconsistent combinations of model PSD and PDF. We point out that here we combine the optimal estimated power spectral model and the estimated probability density function. Therefore, the EMP algorithm is applicable.

In figs. 5.4 to 5.6 we compare the estimation of the significance of the correlation function, when the estimation is based on TK simulated light curves and EMP simulated light curves. At γ-rays the significance of the correlation is lower, when estimated through EMP simulated light curves. The correlation function of two light curves is more likely to show a strong correlation at a certain time lag, when these light curves show flaring peaks rather than Gaussian noise with a flat power spectrum. Thus the average correlation coefficients at arbitrary time lags are increased by the PDF adjustment of the simulated light curves and consequentially the significance of the data correlation peaks are lowered. At V-band we do not find a significant difference in the correlation significance estimation based on the two light curve simulation methods. In the 21 mm band, the correlation significance is generally higher when estimated through the EMP simulated light curves regarding to the TK simulated light curves, in contrast to the γ-rays auto-correlation significance estimation. The variation of the simulated Gaussian light curves is dominated by the low frequency power contribution, whereas the observed light curves and the EMP simulated light curves show some more substructure at shorter time scales (fig. 5.3). This substructure generally decreases the correlation between two signals in comparison to the correlation of two fairly smooth Gaussian light curves. Thus, the significance levels based on the EMP simulated light curves are lower in fig. 5.6 and the data auto-correlation is estimated to be more significant.

We have shown that the choice of the light curve simulation algorithm affects the significance estimation of the correlation function. Depending on the intrinsic power spectrum of the light curve variation the choice of one or another simulation algorithm may lead to over- or under-estimate the significance. We have argued that the PDF adjusted, simulated light curves produced by the Emmanoulopoulos et al. (2013) algorithm resemble the variation of the observed light curves better than simulated Gaussian light curves. Therefore, in the following we use simulated, PDF adjusted light curves for the significance estimation of the cross-correlation function.

In the next section, we explain how the peaks in a correlation function are identified and how the uncertainty of the corresponding time lags is estimated.

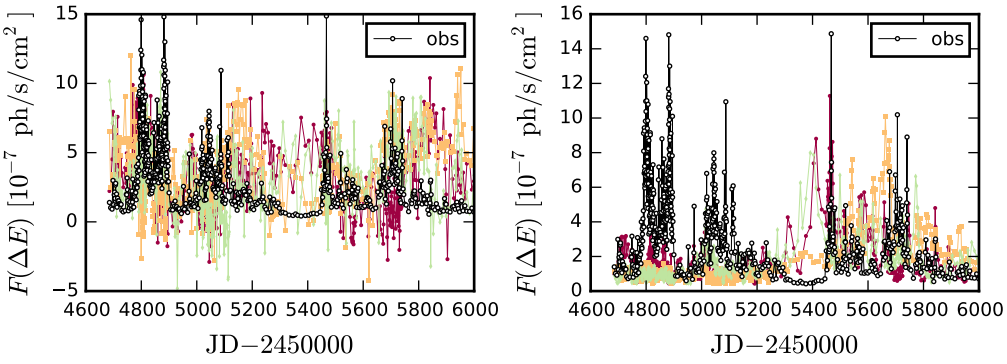

Figure 5.1: Observed (black dots) and simulated (colored dots) γ-ray light curves. Left panel: Simulations based on the TK algorithm. Right panel: Simulations based on the EMP algorithm.

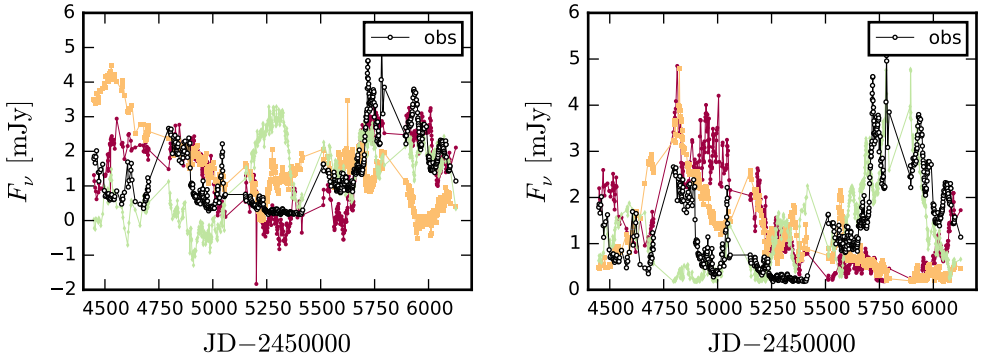

Figure 5.2: Observed (black dots) and simulated (colored dots) V-band light curves. Left panel: Simulations based on the TK algorithm. Right panel: Simulations based on the EMP algorithm.

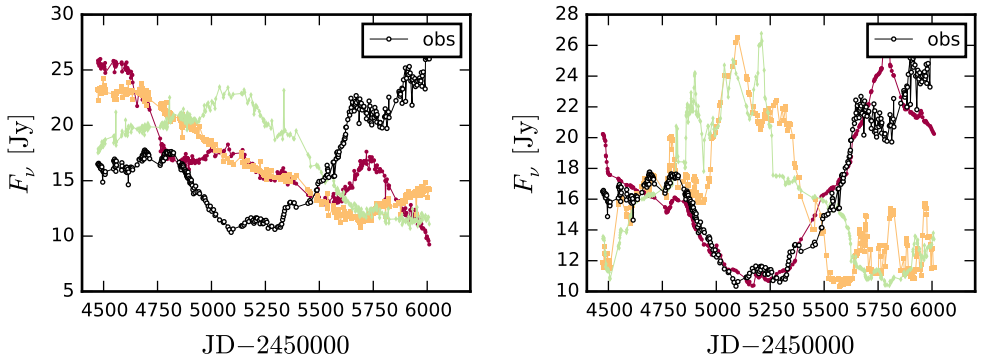

Figure 5.3: Observed (black dots) and simulated (colored dots) 21mm light curves. Left panel: Simulations based on the TK algorithm. Right panel: Simulations based on the EMP algorithm.

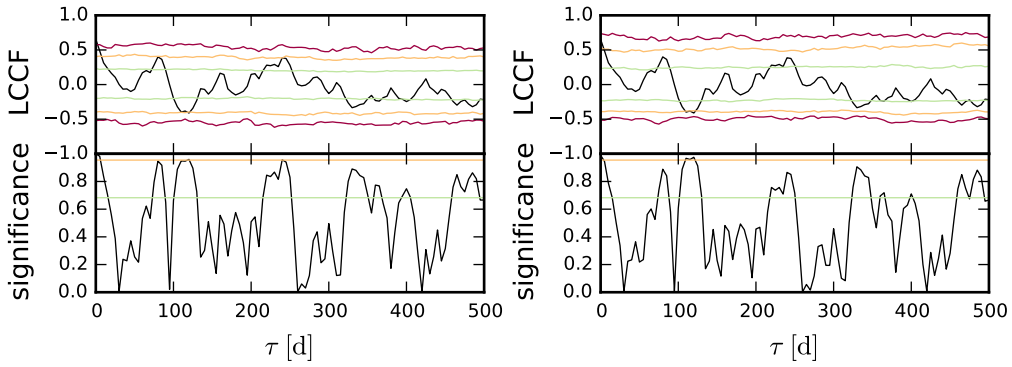

Figure 5.4: Auto-correlation function of the γ-ray (adbin. 25% unc.) light curve (upper panels, black solid) with 1σ, 2σ, 3σ significance levels (green, orange, red lines) and corresponding significance (lower panels) based on TK simulated light curves(left panels) and EMP simulated light curves (right panels).

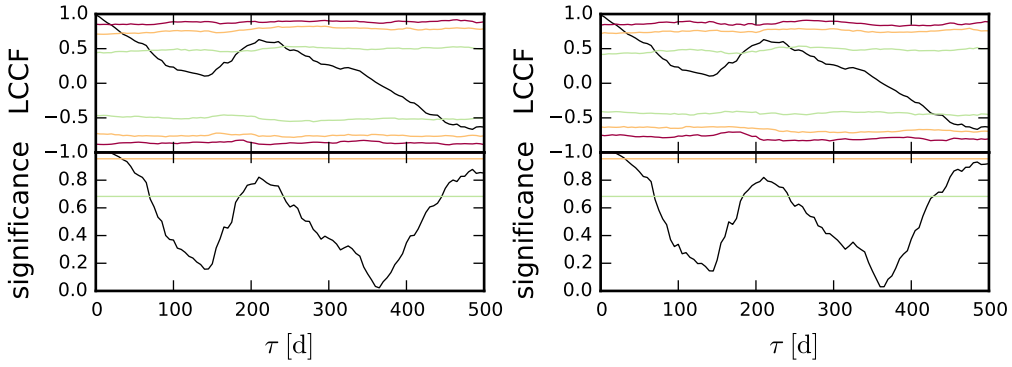

Figure 5.5: Auto-correlation function of the V-band light curve (upper panels, black solid) with 1σ, 2σ, 3σ significance levels (green, orange, red lines) and corresponding significance (lower panels) based on TK simulated light curves (left panels) and EMP simulated light curves (right panels).

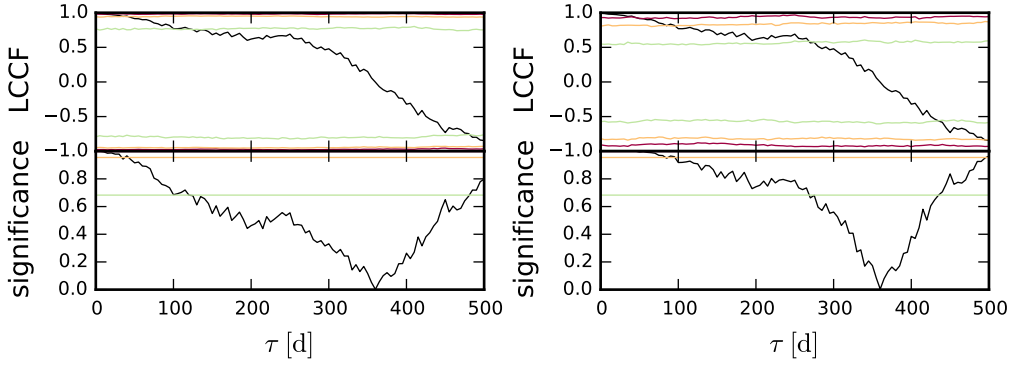

Figure 5.6: Auto-correlation function of the 21 mm light curve (upper panels, black solid) with 1σ, 2σ, 3σ significance levels (green, orange, red lines) and corresponding significance (lower panels) based on TK simulated light curves (left panels) and EMP simulated light curves (right panels).

5.1.3 Time lag uncertainty

A peak in the cross-correlation function indicates a correlation between two signals at the corresponding time lag. We need to identify the peaks in the correlation function to find typical time lags between different bands and to estimate the significance of the correlation at that time lag. With observed light curves at 26 different bands we can test 325 different cross-correlations[2]. Therefore, we implement an automation to identify peaks in the cross-correlation functions. The LCCF generally shows multiple peaks (e.g. fig. 5.4). We do not want to identity just the highest valued peak or the most significant peak, which are not necessarily the same, but all positive correlation peaks, for comparison. The time sampling pattern and the observational noise introduce noise in the LCCF. It is not feasible to identify all local maxima in the LCCF. Therefore, we use the following scheme to identify peaks in the correlation function. The LCCF is smoothed by convolution with a Hann window function of width $\Delta\tau_{\mathrm{sm}}$. We choose the window width accordingly to remove the noise pattern but to keep the intrinsic extrema of the correlation function. Local maxima in the smoothed function with positive function values are identified. Then, within a smoothing window width centred around each identified peak the maximum of the original, un-smoothed LCCF is used as the actual peak value. The LCCF peak values and corresponding time lags and significance are stored. We limit the analysis of the correlation function to a time lag range, such that at least half of each light curve overlaps.

In the upper panels of figs. 5.7 and 5.8 we show two examples of the peak identification. We show the estimated auto-correlation functions of the V-band and the 21 mm light curve with a time lag binning of $\Delta\tau = 1\,\mathrm{d}$. The blue curves show the smoothed correlation functions, the result of convolving the measured function with a Hann window over 51 data points, corresponding to a window size of 51 days. In both examples, three local maxima with positive correlation coefficients are identified, marked by red vertical lines.

The time lags corresponding to the identified correlation function peaks are affected by the time sampling and the observational errors of the two correlated light curves. To estimate the uncertainty of the time lags we implement the *random subset selection* and *flux randomization* methods described by Peterson et al. (1998), Max-Moerbeck et al. (2014a). In multiple iterations the following two steps are performed. First, the data points of both light curves are modified by adding a random number to each data point drawn from a Gaussian distribution with zero mean and standard deviation according to the uncertainty of the data point. This *flux randomization* allows to estimate the time lag uncertainty due to observational noise. Second, a random subset of data points of each light curve is selected. If one light curve has N data points, we draw N integers from a uniform distribution $\mathcal{U}_{\mathrm{int}}(1, N)$, remove the duplicates and sort the numbers. We select the corresponding data points of the light curve, leaving approximately $1 - \mathrm{e}^{-1} \approx 0.63\,\%$ of the data and do the same for the other light curve. This *random subset selection* allows to estimate the time lag uncertainty due to the time sampling of the two light curves. Then, the flux randomized subsets of the two light curve are correlated and we use the method previously described to find the peaks of the correlation function and the corresponding time lags. Over multiple iterations the Cross-Correlation Peak Distribution (CCPD) is established, which is the distribution of time lags

[2] 26 light curves give 26^2 correlation functions, 26 are auto-correlation functions and 650 are cross-correlation functions, half of which are reversed functions of a corresponding cross-correlation.

corresponding to the identified peaks of the correlation functions build with the bootstrap method. In the lower panels of figs. 5.7 and 5.8 we show examples of the CCPD for the auto-correlation of the V-band and the 21 mm light curves, each based on 100 bootstrap iterations.

The example CCPD of the V-band auto-correlation shows distinct distributions around each identified peak time lag. To characterize the distribution of time lags around an identified correlation peak, we have to identify the local distribution. Therefore, we define a threshold time lag $\Delta\tau_{\mathrm{CCPD}}$. For each identified peak, marked by a vertical line in the example figures, we iterate through all time lags in the CCPD towards lower and higher values, the local distribution is limited by gaps in the CCPD larger than the threshold. In the example figures the pale, red regions mark the local distributions. The identification of the local distribution is relatively distinct for the V-band auto-correlation (fig. 5.7). For the 21 mm auto-correlation (fig. 5.8), on the other hand, the local distribution identification is less clear. Generally the identification depends on the choice of the threshold $\Delta\tau_{\mathrm{CCPD}}$. The larger the range of $\Delta\tau_{\mathrm{CCPD}}$ for which the local distribution identification is independent of $\Delta\tau_{\mathrm{CCPD}}$ the more distinct is the distribution.

Once the local distributions are identified, the confidence interval at a given significance level can be calculated for time lag. Additionally, we estimate the mode of the local CCPD. If the mode is consistent with the time lag identified from the original data, this indicates a reliable estimation. Whereas a difference between the identified time lag and the local CCPD mode indicates a strong uncertainty due to the time sampling and the uncertainties of the observed light curves.

We note again, that the identification of the local CCPD and thus the confidence interval of the correlation time lags depend on the choice of the distribution threshold $\Delta\tau_{\mathrm{CCPD}}$. We choose $\Delta\tau_{\mathrm{CCPD}}$ later on based on a few tests with different cross-correlations.

5.2 DCF analysis

With light curves at 26 different bands, we can produce 26 autocorrelation functions and 650 cross-correlation functions. In the following sections we discuss the correlation between specifically selected bands.

5.2.1 Cross-correlation of the radio bands

We cross-correlate all light curves at cm, mm, and sub-mm bands with a time lag binning, $\Delta\tau = 10\,\mathrm{d}$. A shorter binning interval is not feasible given the time sampling of the radio light curves ranging between 2 and 36 days. For the automatic correlation peak identification, we use a smoothing window over 11 data points, corresponding to a window size of 110 days. We run 1000 bootstrap iterations and use a time lag threshold $\Delta\tau_{\mathrm{CCPD}} = 20\,\mathrm{d}$ to estimate 3σ confidence intervals for the correlation time lags.

For most of the light curve pairs, the corresponding CCPD does not show a clear peak and we cannot identify a typical time lag between those light curves. These are especially combinations of the less well sampled light curves. In table 5.1 we list the estimated time lags between those pairs of bands for which the estimation was possible. The first row and first column give the combination of all light curve pairs. The second row lists the corresponding frequencies in GHz. In the upper part of the table (above the double horizontal line) the measured time lags corresponding to

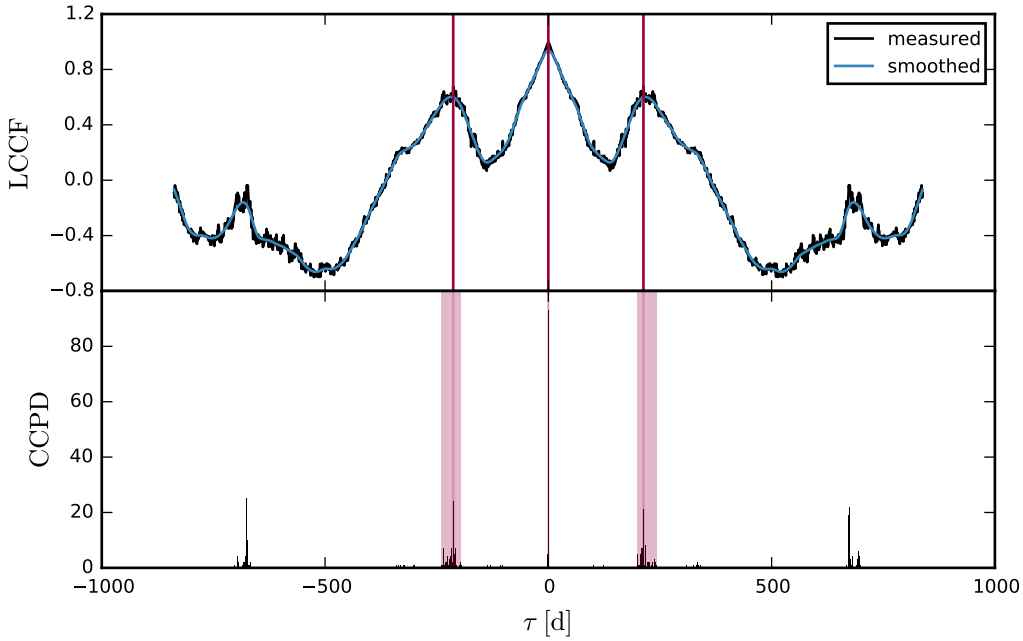

Figure 5.7: Measured and smoothed auto-correlation function of the V-band light curve (upper panel). Cross-Correlation Peak Distribution (CCPD) based on 100 bootstrap iterations (lower panel). Vertical black lines mark the identified correlation peaks. Pale, red regions mark the corresponding 3σ confidence intervals.

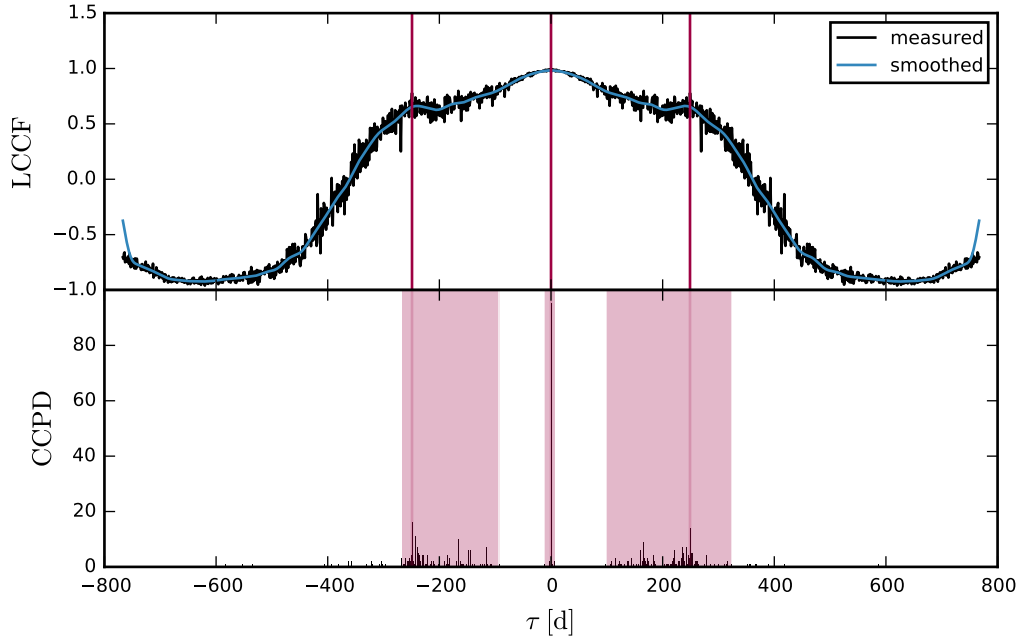

Figure 5.8: Measured and smoothed auto-correlation function of the 21 mm light curve (upper panel). Cross-Correlation Peak Distribution (CCPD) based on 100 bootstrap iterations (lower panel). Vertical black lines mark the identified correlation peaks. Pale, red regions mark the corresponding 3σ confidence intervals.

each light curve combination are given in units of days. A positive time lag means the corresponding light curve listed on top is leading the light curve listed on the left side of the table, for a negative sign vice versa. Only for the two best sampled light curves at 21 mm and 8 mm we have obtained correlation time lags regarding to all other bands. Generally, the CCPD is multi-modal and does not show distinct gaps. Therefore, we cannot identify the local peak distribution centred around identified correlation peaks and cannot reliably estimate the confidence intervals of the time lags. Furthermore, the multi-modal structure of the CCPD complicates the identification of the most significant cross-correlation time lag. Generally, we have selected the strongest peak in the CCPD and the identified time lag with the highest significance. Usually, both criteria give a consistent result. In a few cases we have not selected the most significant direct estimate of the time lag, but the mode of the CCPD. In these cases, the distribution mode was located one time lag bin lower or higher than the direct estimate of the time lag, indicating that the direct estimate is biased by the time sampling or the observational errors of the two light curves. The significance corresponding to the time lags given in table 5.1 ranges between 90 % and 100 %.

In the lower part of table 5.1 (below the double horizontal line) we have subtracted the corresponding time lag in the 8 mm column from each row. All time lags in this part of the table are calculated relative to the 8 mm band. We show the time lags along each row plotted over the corresponding frequencies in fig. 5.9. The open black data points and corresponding error bars show the average time lag at each frequency and the standard deviation. We use the time lag bin of 10 days as minimum error, where the scatter is lower than 10 days.

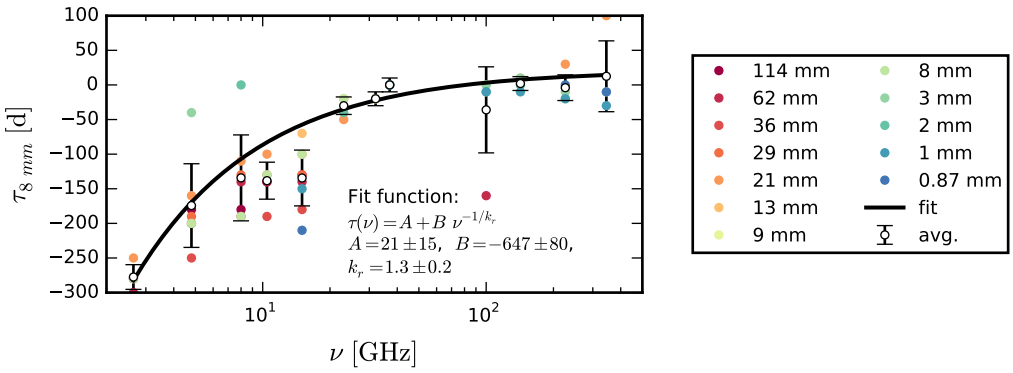

Figure 5.9: Estimated time lags regarding to the 8 mm band depending on the frequency (coloured points). Black open points: averaged time lag at each frequency with corresponding uncertainty. Solid black line: least square fit to the averaged curve.

We observe a general increasing trend in the average time delay depending on the frequency and test this dependency is consistent with an opacity effect. Due to Synchrotron Self-Absorption (SSA) the innermost region of a jet is optically thick, i.e. the optical depth[3] is $\tau_s > 1$. Assuming a conical jet geometry, the size r of that region depends on the frequency of the emission ν through

$$r \propto \nu^{-1/k_r}, \tag{5.8}$$

[3]We note, that we use the conventional symbol τ_s for the optical depth. We use τ for the time lag in the cross-correlation analysis.

Table 5.1: Cross-correlation time lags at cm, mm, sub-mm bands. For a detailed description see text.

Band:	114 mm	62 mm	36 mm	29 mm	21 mm	13 mm	9 mm	8 mm	3 mm	2 mm	1 mm	0.87 mm
Freq. [GHz]:	2.64	4.80	8.00	10.45	15.00	23.05	32.00	37.00	100.00	142.33	226.00	345.00
114 mm	0	100	100	140	150			280				
62 mm	-100	0	60	60	60			200	40			
36 mm		-60	0	0	10			190				
29 mm		-60	0	0	0			130				
21 mm	-150	-60	-10	0	0	50		100			130	200
13 mm					-50	0	0	20		30		
9 mm						0	0	20				
8 mm	-280	-200	-190	-130	-100	-20	-20	0	0	0	-20	-10
3 mm		-40						0	0	10	-10	
2 mm			0			-40		0	-10	0		
1 mm					-130			20	10	10	0	-10
0.87 mm					-200			10			10	0
114 mm	-280	-180	-180	-140	-130			0				
62 mm	-300	-200	-140	-140	-140			0	-160			
36 mm		-250	-190	-190	-180			0				
29 mm		-190	-130	-130	-130			0				
21 mm	-250	-160	-110	-100	-100	-50		0			30	100
13 mm					-70	-20	-20	0		10		
9 mm						-20	-20	0				
8 mm	-280	-200	-190	-130	-100	-20	-20	0	0	0	-20	-10
3 mm		-40						0	0	10	-10	
2 mm			0			-40		0	-10	0		
1 mm					-150			0	-10	-10	-20	-30
0.87 mm					-210			0			0	-10

where the coefficient

$$k_r = \frac{(3-2\alpha)m + 2n - 2}{5 - 2\alpha} \tag{5.9}$$

relates to the radius dependence of the magnetic field $B(r) \propto r^{-m}$ and the electron density $N(r) \propto r^{-n}$ and the spectral index α of the optically thin emission[4] (Konigl, 1981). A value of $k_r = 1$ relates to equipartition of the magnetic and electron energy density, which is achieved for instance for $m = 1$ and $n = 2$, where k_r becomes independent of α (Konigl, 1981; Lobanov, 1998). Accordingly, the distance from the jet base at which the jet becomes optically thin, that is at the surface of optical depth $\tau_s = 1$, depends on the frequency ν through

$$r_{\mathrm{core}} \propto \nu^{-1/k_r}. \tag{5.10}$$

When this "τ_s=1"-surface is identified with the VLBI-core, the relation eq. (5.10) can be observed with multi-frequency VLBI observations[5], known as *core shift* (Lobanov, 1998).

Assuming the jet plasma moves with a constant velocity v in the region that emits the cm to sub-mm radiation, then the time delay delay between a frequency ν and a reference frequency ν_0 is given by

$$\tau = t - t_0 - \Delta t_{\mathrm{rel}} = \frac{r_{\mathrm{core}}(\nu) - r_{\mathrm{core}}(\nu_0)}{v} - \Delta t_{\mathrm{rel}}, \tag{5.11}$$

where Δt_{rel} is a relativistic shortening of the duration, since the emission region at t is closer to the observer than at t_0

$$\Delta t_{\mathrm{rel}} = \frac{r_{\mathrm{core}}(\nu) - r_{\mathrm{core}}(\nu_0)}{\mathrm{c}} \cos\theta, \tag{5.12}$$

with the speed of light c, and the viewing angle θ. Thus, the observed time delay is with $\beta = v/\mathrm{c}$

$$\begin{aligned} \tau(\nu) &= \frac{r_{\mathrm{core}}(\nu) - r_{\mathrm{core}}(\nu_0)}{\mathrm{c}} \cdot (\beta^{-1} - \cos\theta) \\ &\propto r_{\mathrm{core}}(\nu) \\ &\propto \nu^{-1/k_r}. \end{aligned} \tag{5.13}$$

We fit a function of the form $\tau(\nu) = A + B\,\nu^{-1/k_r}$ to the averaged data shown in fig. 5.9 using a least square minimization based on the Levenberg–Marquardt algorithm weighing the measured data with the corresponding uncertainties. The best fit parameters are $A = 21 \pm 15$, $B = -647 \pm 80$, and

$$k_r = 1.3 \pm 0.2.$$

[4]Konigl (1981) used a different sign convention for the spectral index.

[5]To get absolute positions of the VLBI core at different frequencies the phase-referencing technique (Beasley and Conway, 1995) is necessary.

We note, (a) that we could not give reasonable uncertainty estimates for the individual time lag measurements, and (b) that all time lag estimates referring to the 8 mm data are additionally affected by the (unknown) uncertainties of the 8 mm time lags. Therefore the uncertainties of the averaged time lag data are likely underestimated and consequentially the uncertainties of the fit parameters are also underestimated.

The observed time lags in the cm to sub-mm bands are consistent with Synchrotron Self-Absorption (SSA) in a conical jet in equipartition. This result is consistent with the stacked correlation analysis of Fuhrmann et al. (2014).

Close inspection of the mm and sub-mm time lags in fig. 5.9 shows a potential change of sign in the derivative of the time lag frequency-dependence around the 2 mm band, if we neglect the time lag estimates of the correlation with the 21 mm band (orange data points). This time lag inversion cannot be fit with the fit function. We note, that the 21 mm to 0.87 mm time lag of 200 days may be largely overestimated. The corresponding local CCPD is strongly skewed towards shorter time lags. The accuracy of the time lag estimation does not allow to verify if the 1 mm and 0.87 mm band lag behind the 2 mm light curve. 1 mm and 870 μm lagging behind 2 mm could not be explained by the opacity effect discussed above. One possible explanation is the gradual acceleration of particles. If the time scale of accelerating particles to sufficiently high energy to produce synchrotron radiation at 1 mm or shorter wavelengths is longer than for higher wavelength synchrotron radiation, there would be an increasing time lag with higher frequencies lagging behind lower frequencies (e.g., Böttcher et al., 2007; Chatterjee et al., 2008). The opacity effect has an inverse frequency dependence and both effects could explain a maximum in the time lag function, as it is indicated around 3 mm in fig. 5.9.

5.2.2 Cross-correlation of the ultraviolet, optical, infrared bands

We cross-correlate all ultraviolet, optical, and infrared light curves with a time lag binning of one day. We estimate the correlation significance with 1000 simulated correlation-functions per light curve pair. The found correlation peaks generally have a significance of 1, indicating that the correlation is unlikely to occur by chance. For a few exceptions the significance is at 0.98 or higher.

We found that 58 % of the correlations are at zero time lag. The direct estimate of the time lag and the mode of the CCPD based on 1000 bootstrap iterations per light curve pair are consistent, indicating a reliable result. Cross-correlations with the K-band, I-band, and 3000 Å light curve show correlation time lags up to $\pm$19 days. For all other bands the correlation time lags range between -3 and 3 days. The lower and upper time lag confidence limits are at the order of -10 days and $+10$ days, respectively, and all confidence intervals are consistent with zero time lag. The time lags deviating from zero do not show any frequency dependent trend. We conclude that strong deviations from zero are results of the time sampling of the corresponding light curves and observational noise. All time lags are consistent with zero and a potentially frequency dependent time lag at the order of a day or lower cannot be measured significantly.

5.2.3 Cross-correlation of best sampled light curves

We cross-correlate the best sampled light curves: 21 mm, 8 mm, 1 mm, 0.87 mm, V-band, X-rays (RXTE), γ-ray (adaptive binning with 25 % uncertainty). In the previous section we have shown that all ultraviolet, optical, and infrared light curves are consistent with zero time lag. Therefore we select only the best sampled light curve in this frequency range, the V-band, for the correlation analysis with other frequencies. we choose three different time lag bin sizes: 1, 5, and 10 days. For each pair of light curves we cross-correlate 1000 pairs of simulated light curves for the significance estimation and we use 1000 bootstrap iterations to estimate the time lag uncertainties. For the automatic correlation peak identification we set a window size of 101, 21, and 11 data points corresponding to 101 days, 105 days, and 110 days for the time lag bin sizes 1, 5, and 10 days, respectively.

X-ray vs. low frequencies

Figure 5.10 shows the correlation function of the X-ray light curve and the 1 mm light curve with 1 day binning of the LCCF. We do not find any significant correlation at the 2σ confidence level. However, the inspection of the two light curves in the upper panel of fig. 5.10 shows that the variability is quite similar for different periods of time. The largest difference appears during the two X-ray flares shortly before and after JD 2455000. The sampling of the 1 mm light curves leaves it unclear if the first X-ray flare is also appearing in the 1 mm band. The second X-ray flare has clearly no counterpart in the 1 mm curve.

In the following we test how the variation time scale affects the correlation between the two bands. First, we take the observed and simulated light curves as before and convolve them with a Hann window function of width $\Delta t_{\rm sm}$, producing smoothed light curves with damped variation at time scales shorter than $\Delta t_{\rm sm}$. Second, we produce de-trended (residual) light curves, subtracting the smoothed light curve from each original observed and simulated light curve, thus dampening variation at time scales larger than $\Delta t_{\rm sm}$. Then, we perform the same cross-correlation analysis on the smoothed and de-trended light curves as before.

In fig. 5.11 we show the 1 day binned correlation function of the X-ray and 1 mm light curve after de-trending both curves with a window size of $\Delta t_{\rm sm} = 300$ days. The corresponding smoothed light curves are shown in fig. 5.12. The short term variability of X-rays and 1 mm is significantly correlated (significance: 1) with a time lag of -6 ± 11 days. The sign indicates X-rays leading, but within the uncertainties the time lag is consistent with zero. De-trending the light curves with window sizes of $\Delta t_{\rm sm} = 100, 200, \ldots, 500$ days result in the same time lag and significance. The long term variability of the smoothed light curves is not significantly correlated.

In table 5.3 the time lags and corresponding significance between short time scale ($\Delta t_{\rm sm} = 300$ days) X-rays and 1, 8, and 21 mm bands are listed. The 870 μm light curve is not sampled well enough for proper smoothing and de-trending and we do not find reliable time lags between the short term variability in X-rays and 870 μm. The time lags in 1, 8, and 21 mm are generally consistent with zero time lag within the confidence intervals. But the time lags show a frequency dependent trend, indicating that the short term variability in X-rays is correlated with zero time lag with the emission at a wavelength between 1 mm and 8 mm.

The strong correlation (significance: 1) of the short term variability of X-rays and mm bands indicates a physical connection between the two emission

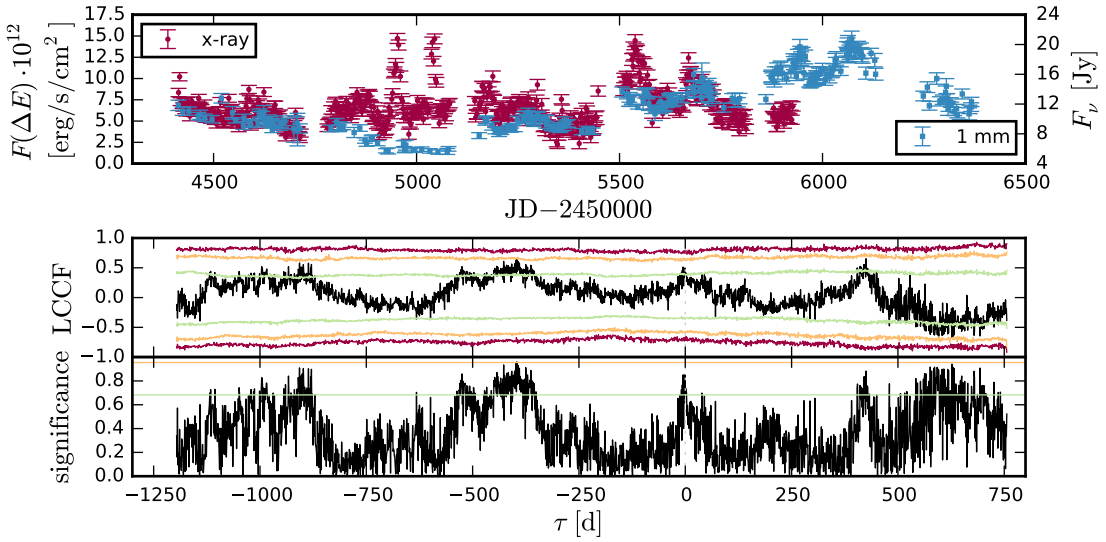

Figure 5.10: Correlation of X-rays and 1 mm band. Upper panel: X-ray light curve (red) and 1 mm light curve (blue). Mid panel: cross-correlation function (black) and significance levels 1σ (green), 2σ (orange), 3σ (red). Lower panel: significance of the correlation coefficients.

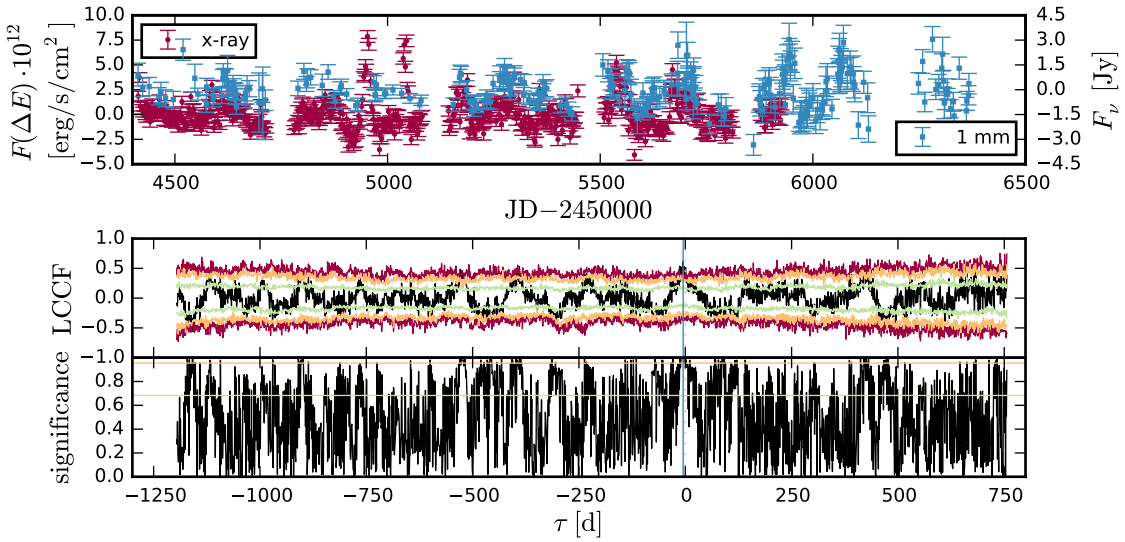

Figure 5.11: Correlation of the de-trended X-ray and 1 mm light curves. Upper panel: X-ray light curve (red) and 1 mm light curve (blue) de-trended with a window size $\Delta t_{\rm sm} = 300$ d. Mid panel: cross-correlation function (black) and significance levels 1σ (green), 2σ (orange), 3σ (red). Lower panel: significance of the correlation coefficients. The vertical, blue line marks the strongest correlation peak.

Table 5.2: Cross-correlation time lags and corresponding p-values between X-rays and mm, cm bands after de-trending the light curves with a Hann window of 300 days width. Uncertainties correspond to 3σ confidence interval estimated from the CCPD.

	1 mm	8 mm	21 mm
Time delay:	-6^{+11}_{-11} d	$+6^{+24}_{-20}$ d	10^{+15}_{-15} d
p-values:	1	0.98	0.98

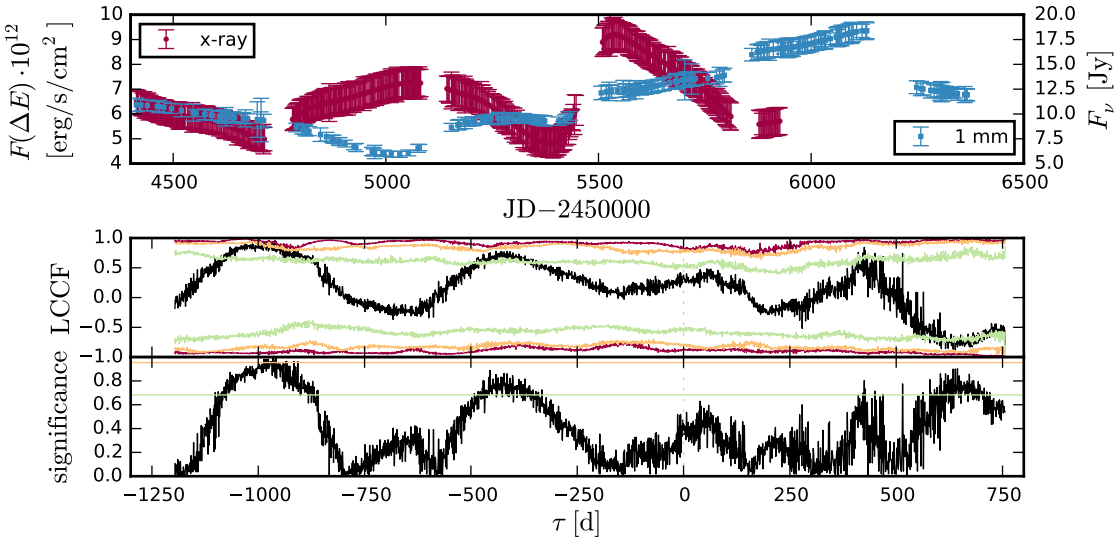

Figure 5.12: Correlation of the smoothed X-ray and 1 mm light curves. Upper panel: X-ray light curve (red) and 1 mm light curve (blue) smoothed with a window size $\Delta t_{\rm sm} = 300$ d. Mid panel: cross-correlation function (black) and significance levels 1σ (green), 2σ (orange), 3σ (red). Lower panel: significance of the correlation coefficients.

processes. The time lag is consistent with zero within the uncertainties for all tested correlations. Zero time lag indicates that the radiation X-rays and mm, cm wavelength is produced in the same emission region. Thus, the same electron population produces the mm, cm synchrotron radiation and scatters photons to X-ray energy. The correlation is strongest at 1 mm and decreases towards longer wavelengths as the short term variability becomes less dominant at longer wavelengths. This result is consistent with the similar power spectral indices at 870 μm and X-rays.

The difference in the short term and long term correlation indicates that two processes affect the correlation between X-rays and mm, cm bands. Whereas the short term variability is due to changes in the electron population affecting both bands at the same time, the long term variability of the X-rays may be affected by changes in the seed photon field.

V-band vs. low frequencies and X-rays

For the cross-correlation analysis between V-band and the mm, cm bands we use a time binning of 5 days in the calculation of the LCCF. The 21 mm, 8 mm, 1 mm, and 870 μm cross-correlations time lags based on the 5 day binned LCCFs are consistent with the 10 day binned results discussed in section 5.2.1. One day binning does not allow a reliable time lag estimation.

Figures 5.13 to 5.16 show the cross-correlation analysis of the V-band light curve after JD 2454400 with the four cm to sub-mm bands. The upper panels show the two light curves in comparison. Mid panels show the cross-correlation function with 5 day time lag binning as a black line and the 1σ, 2σ, and 3σ significance levels as green, orange, and red line, respectively. In the lower panels the corresponding significance is shown. A dotted grey line marks the zero time lag and two blue solid lines mark the most probable positive and negative time lag. These time lags and the corresponding significance are listed in table 5.3. The upper and lower limits correspond to the 3σ confidence interval.

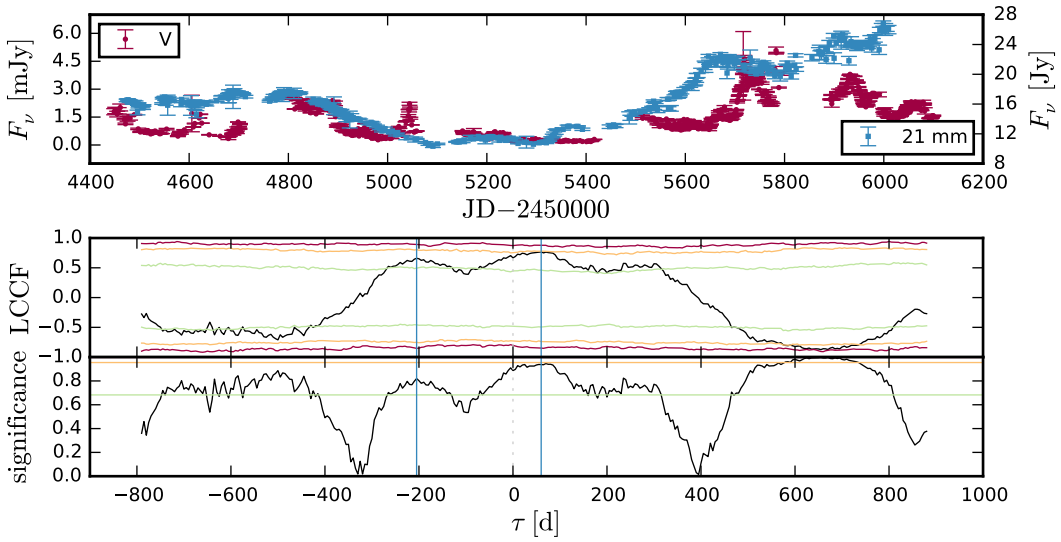

Figure 5.13: Correlation of V-band and 21 mm band. Upper panel: V-band light curve (red) and 21 mm light curve (blue). Mid panel: cross-correlation function (black) and significance levels 1σ (green), 2σ (orange), 3σ (red). Lower panel: significance of the correlation coefficients. Vertical, blue lines mark the strongest positive and negative correlation peak.

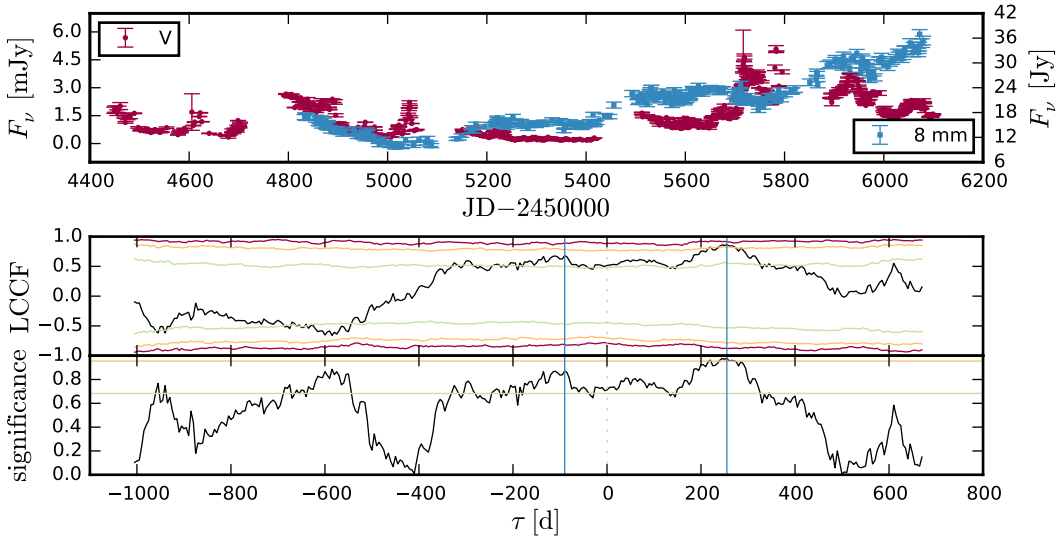

Figure 5.14: Correlation of V-band and 8 mm band. Upper panel: V-band light curve (red) and 8 mm light curve (blue). Mid panel: cross-correlation function (black) and significance levels 1σ (green), 2σ (orange), 3σ (red). Lower panel: significance of the correlation coefficients. Vertical, blue lines mark the strongest positive and negative correlation peak.

We identify a positive and a negative time lag in all correlation functions. Negative time lags correspond to V-band leading the radio bands, positive lags to lagging behind. The leading (negative) peaks have a significance below 2σ. If V-band is leading the radio bands the absolute time lag has to increase from sub-mm to cm bands to be consistent with the time lags between the radio bands. The direct estimates of the V-band to radio time lags are contradicting the intra radio time lags, but given the high uncertainties are potentially consistent.

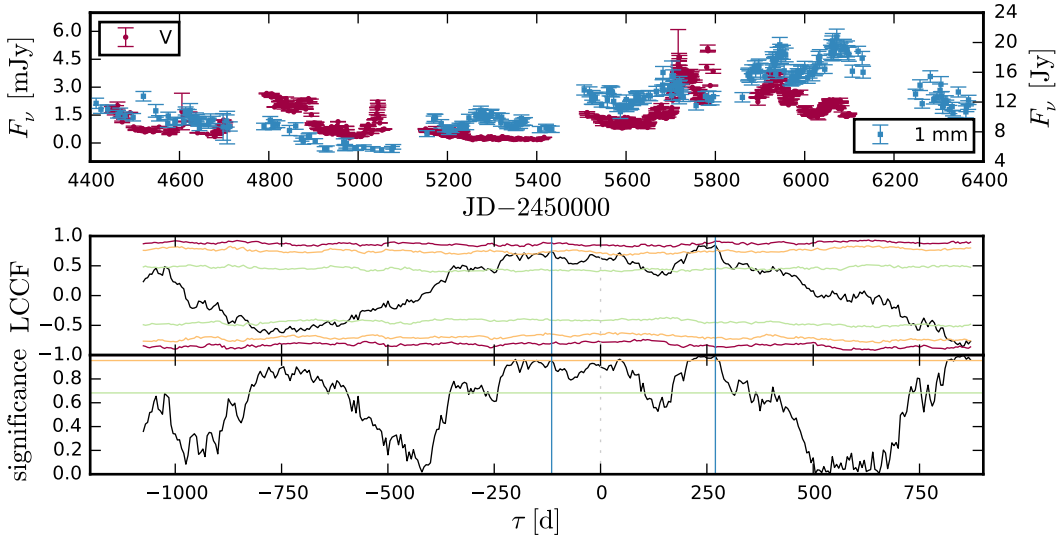

Figure 5.15: Correlation of V-band and 1 mm band. Upper panel: V-band light curve (red) and 1 mm light curve (blue). Mid panel: cross-correlation function (black) and significance levels 1σ (green), 2σ (orange), 3σ (red). Lower panel: significance of the correlation coefficients. Vertical, blue lines mark the strongest positive and negative correlation peak.

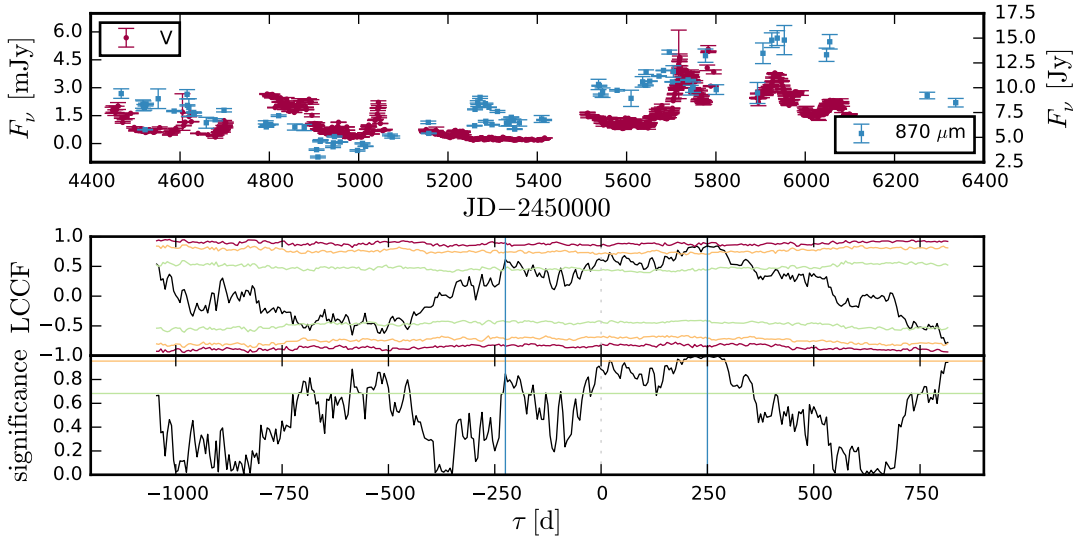

Figure 5.16: Correlation of V-band and 870 μm band. Upper panel: V-band light curve (red) and 870 μm light curve (blue). Mid panel: cross-correlation function (black) and significance levels 1σ (green), 2σ (orange), 3σ (red). Lower panel: significance of the correlation coefficients. Vertical, blue lines mark the strongest positive and negative correlation peak.

The lagging (positive) correlation peaks are more significant $> 2\sigma$. And the confidence intervals are smaller, indicating a more reliable estimation and a less broad correlation peak. For all bands the positive correlation peak is more likely to be a real, non-coincidental correlation than the negative correlation peak. The V-band to radio time lags are consistent with the intra radio time lags, such that the 21 mm light curve is leading less than the mm and sub-mm bands. Relative time lags between the mm and sub-mm bands are consistent with the relative

lags regarding to the V-band within the uncertainties. But the time lag between V-band and 21 mm of 60^{+28}_{-61} days is too low. From the intra radio time lags we would expect ≈ 120 days time delay between V-band and 21 mm.

Table 5.3: Time lags and p-values of the most significant lagging (positive time lag) and leading (negative time lag) correlation between V-band and the 21 mm, 8 mm, 1 mm, and 870 μm bands. The time lag uncertainties correspond to the 3σ confidence intervals.

	21 mm	8 mm	1 mm	0.87 mm
V (lagging)	60^{+28}_{-61} d	255^{+30}_{-47} d	270^{+30}_{-63} d	250^{+45}_{-100} d
p-values:	0.94	0.98	0.99	0.99
V (leading)	-205^{+68}_{-35} d	-90^{+5}_{-155} d	-115^{+30}_{-125} d	-225^{+160}_{-10} d
p-values:	0.82	0.87	0.96	0.85

We further test how the variation time scale affects the correlation between two bands. We use the same method discussed before to produce smoothed and de-trended (residual) light curves, thus dampening variation at time scales larger or shorter than $\Delta t_{\rm sm}$, respectively. In figs. 5.17 and 5.18 we show the cross-correlation of the smoothed and de-trended V-band and 21 mm light curves with a smoothing window width of 300 days. The de-trended light curves correlate significantly (significance: 1) at a time lag of 70 days, V-band lagging, consistent with the positive time lag estimated from the original light curves. The correlation significance decreases with increasing and decreasing window sizes, indicating the two light curves correlate the most at time scales at the order of ≈ 300 days. The potential negative time lag discussed previously is at no time scale as significant as the positive lag. The correlation function of the smoothed light curves shows a broad peak centred at 20 days time lag. For increasing window sizes $100, 200, \ldots, 500$ days the peak centre shifts from 50^{+30}_{-45} days to -10^{+70}_{-60} days. This result implies that the long term variability on time scales larger than 500 days of the optical bands and the 21 mm radio band is correlated with zero time lag within the uncertainties. We note, though, that two light curves of 1800 days length are probably not long enough to estimate the correlation on long time scales larger than 500 days reliably. On the other hand, the short term variability on time scales shorter than 500 days has a time lag with V-band lagging behind the radio variability. this time lag increases towards shorter time scale variability. At time scales shorter than 100 days we do not find any significant cross-correlation.

We perform the same smoothing and de-trending analysis for the correlation between V-band and 8 mm, 1 mm, and 870 μm. For all bands, smoothed and de-trended with window sizes $100, 200, \ldots, 500$ days we find significant correlation (significance: $0.98 - 1$) between V-band and the low frequency band at positive time lags consistent with the time lags estimated from the original light curves within the uncertainties. A decrease of the time lag for longer variability time scales cannot be confirmed given the uncertainties of the time lags.

X-rays leading the 1 mm band by 6 ± 11 days in the short term variability and V-band potentially lagging behind the 1 mm band by 270^{+30}_{-63} days implies a correlation between X-rays and V-band with V lagging behind X-rays by 264^{+41}_{-74} days. The upper panel of fig. 5.19 shows the X-ray and V-band light curve. In the lower panel we shift the V-band light curve by -250 days. This plot reveals a complex situation. Up to JD 2455150 the two observed light curves (upper panel) roughly match with zero time lag including two small optical flares accompanying the prominent X-ray

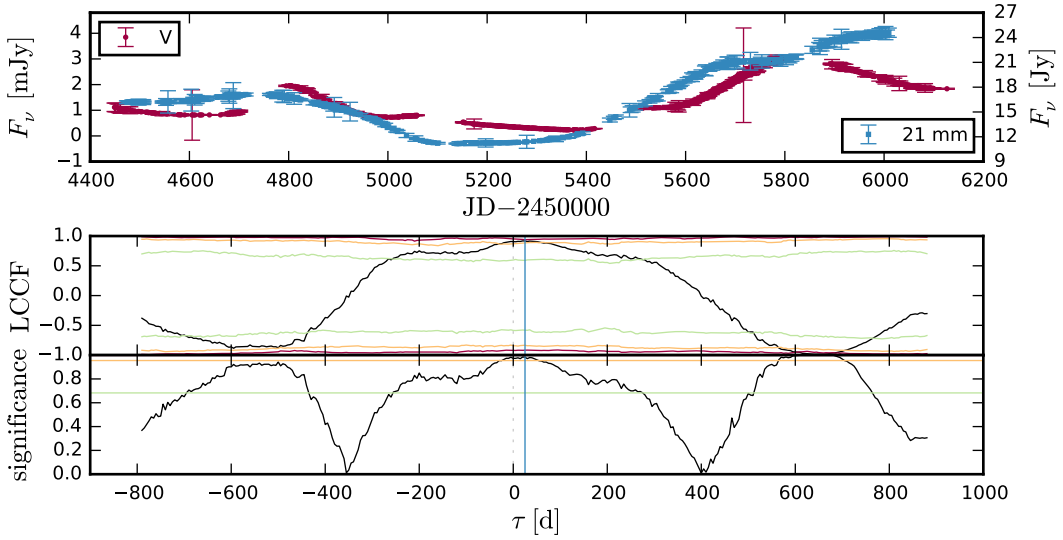

Figure 5.17: Correlation of the smoothed V-band and 21 mm band. Upper panel: V-band light curve (red) and 21 mm light curve (blue) smoothed with a window size $\Delta t_{\rm sm} = 300$ d. Mid panel: cross-correlation function (black) and significance levels 1σ (green), 2σ (orange), 3σ (red). Lower panel: significance of the correlation coefficients. The vertical, blue line marks the strongest correlation peak.

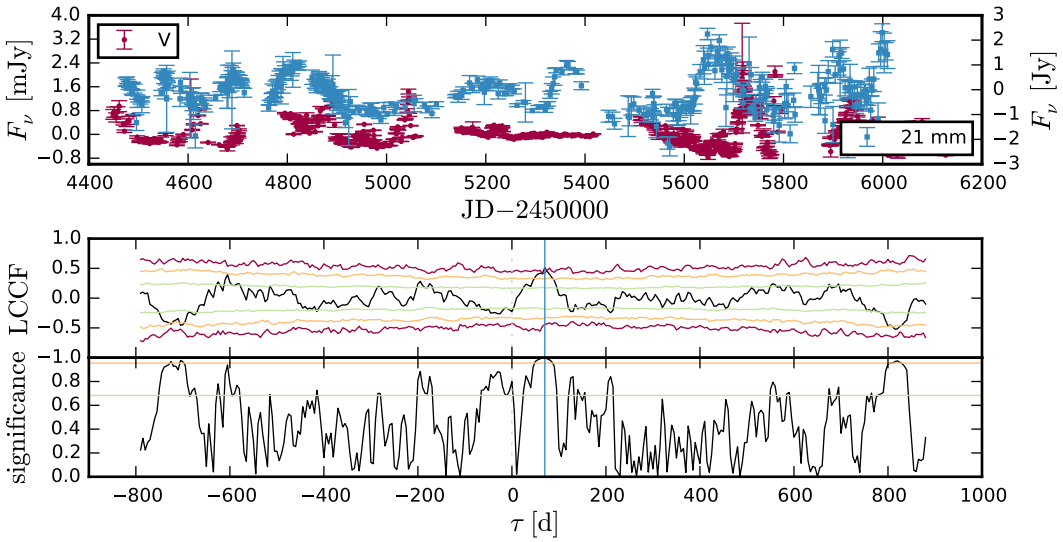

Figure 5.18: Correlation of the de-trended V-band and 21 mm band. Upper panel: V-band light curve (red) and 21 mm light curve (blue) de-trended with a window size $\Delta t_{\rm sm} = 300$ d. Mid panel: cross-correlation function (black) and significance levels 1σ (green), 2σ (orange), 3σ (red). Lower panel: significance of the correlation coefficients. The vertical, blue line marks the strongest correlation peak.

flares at $\sim$ JD 2454953 and $\sim$ JD 2455041, respectively. In the lower panel, V-band shifted by -250 days, the two light curves match after $\sim$ JD 2455250. This time lag is consistent with the expected value. If this time lag is real, both light curves miss a prominent flare in the observation gap. Consequentially, the LCCF does not show significant correlation between the two bands. After de-trending both light curves with a window size of the strongest correlation (significance: 1) is found in the confidence interval [-258, -180] but it is dominated by the correlation

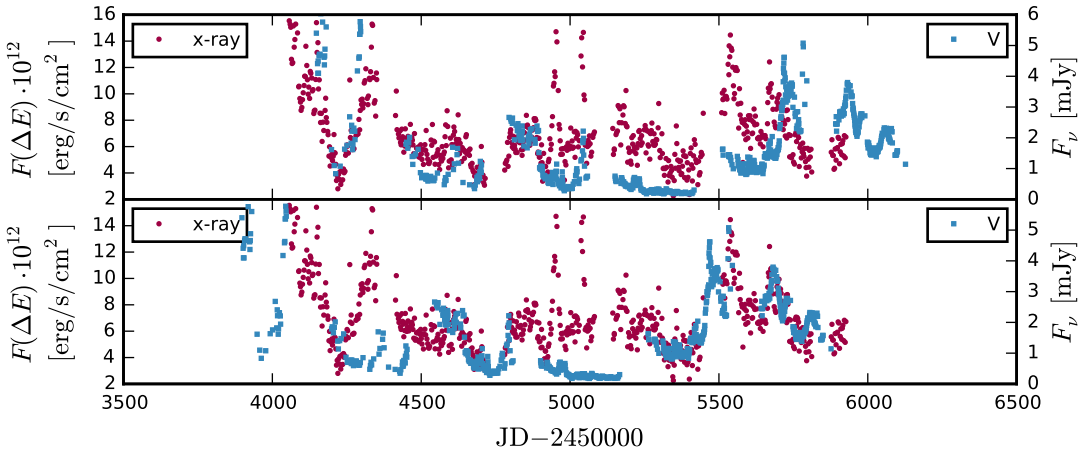

Figure 5.19: X-ray (red) and V-band (blue) light curve. Upper panel: actual light curves. Lower panel: V-band shifted by -250 days.

of the x-ray flare at $\sim$ JD 2455538 and the optical flare at $\sim$ JD 2455719 and not time lag indicated by our manual shift. The Swift data does not fill the X-ray observation gap. Therefore, we cannot confirm if there has been an X-ray flare around $\sim$ JD 2455500. At zero time lag the LCCF of the de-trended light curves shows a small peak with significance 0.73.

In summary, we find three different correlation scenarios for V-band regarding to the lower frequencies and X-rays: first, V-band leading X-rays, mm, and cm bands; second, V-band lagging X-rays, mm, and cm bands; third, a time dependent correlation with zero time lag before JD 2455150 and V-band lagging after JD 2455150. The first scenario, V-band leading, is not significant. The correlation coefficients of V-band against mm, cm bands do not exceed 2σ significance and the time lags are not consistent with the relative time lags in the mm, cm bands. Therefore, we conclude that the leading V-band correlations are by chance and not indicating a real physical connection.

The second scenario is more likely given the significance and consistency of the correlation time lags. The V-band to 8 mm, 1 mm, and 0.87 mm LCCFs show the strongest correlation at positive time lags with $> 2\sigma$ significance. The relative time lags between the mm and sub-mm bands are consistent with the time lags discussed in section 5.2.1. The V-band to 21 mm correlation is not as significant ($< 2\sigma$) and the time delay does not match the relative cm to mm time lags exactly. But the 21 mm radiation is expected to come from a larger region than the V-band radiation and, consequentially, does not exhibit as strong flares as V-band, but stronger variability on longer time scales (c.f. fig. 4.17). Thus, the strength of correlation is expected to decrease towards longer wavelengths. Additionally, we find partial evidence for consistent time lags between the short term variability of V-band, X-rays, and 1 mm. This scenario implies that the optical emission region lies downstream of the VLBI mm and cm cores, beyond the BLR. Adopting the average Lorentz factor $\Gamma = 15.5$ and viewing angle $\theta = 2.1$ by Jorstad et al. (2005) with redshift $z = 0.5362$ (Marziani et al., 1996) the time lag of $\tau = 250$ days corresponds to a distance between the optical emission region and the 1 mm emission region of

$$d = \frac{\mathrm{c}\beta\tau}{(1+z)(1-\beta\cos\theta)} \approx 50\,\mathrm{pc}.$$

The time lag and distance imply that at the mm emission site the electron population is not energetic enough to produce optical synchrotron radiation. Slow acceleration of the particles (Böttcher et al., 2007), as it is indicated at the mm bands, cannot account for this time lag. The lag of 250 days corresponds to

$$\tau^{\mathrm{em}} = \frac{\tau^{\mathrm{obs}}}{1+z}\delta \approx 10\,\mathrm{years}$$

in the comoving frame of the emission region, adopting the same parameters as before. Assuming a magnetic field at the order of 1 Gauss (Hartman et al., 2001), a particle velocity at the order of $\gamma \sim 10^6$ for the optical synchrotron emission, and correction factor $k \sim 1$, the radiative cooling time scale is (e.g. Böttcher et al., 2007)

$$\begin{aligned} t_{\mathrm{cool}} &\approx 7.7 \cdot 10^7 B_G^{-1}\gamma^{-1}(1+k)^{-1}\,\mathrm{s} \\ &\approx 40\,s. \end{aligned}$$

Even with a low magnetic field strength at the order of μG the cooling time at the order of 1 year is significantly shorter than the time of motion between the two emission regions. The particles producing the optical synchrotron radiation have to be accelerated in situ. One possible pool of energy is the bulk motion. Once the bulk flow hits a shock the kinetic energy can be re-distributed and the particles get accelerated by the Fermi mechanism. These particles then lose their energy through synchrotron radiation or IC scattering. The observed long time lag between cm, mm, X-rays and V-band can be explained if an injected population of particles successively hits two shocks. The first shock accelerates the particles sufficiently to produce synchrotron radiation up to mm wavelength and IC scattered X-rays, the second shock accelerates particles to higher energies and the synchrotron radiation ranges up to optical and ultraviolet, implying that the particle acceleration is more efficient in the second shock region. Re-energization of the particles requires that also synchrotron emission at lower frequencies is emitted from the second shock region with probably different time lags. A quantitative test of this hypothesis requires to model two successive emission regions to properly disentangle the superposition of both regions in the light curves including all internal and relativistic time delays.

The third scenario suggests that the time lag between V-band and X-rays changes with time as indicated in fig. 5.19. Chatterjee et al. (2008) showed that the correlation time lag between optical and X-rays changes with time, with occasionally X-rays leading, occasionally optical leading. They explained these changes with the varying orientation of the jet, changing the relativistic time delay. But these time lags reported ranged from -50 to +25 days, significantly shorter than the potential delay observed here. Occasional close to zero time lags and long time lags are consistent with the two emission zone model discussed in the second scenario. Close to zero time lags are expected whenever particles are accelerated enough to produce optical synchrotron radiation. The long time lag may occur between two successive shocks. Simulations have to show if the long time lag correlation can dominate over the close to zero time lag correlation which is expected from the second emission region.

Gamma-ray correlations

Figure 5.20 shows the correlation between the adaptively binned (25 % unc.) γ-ray light curve and the V-band light curve using a 1 day binning of the LCCF. The correlation function peaks at -7^{+53}_{-30} days with a significance 0.74. In fig. 5.21 we show the correlation function after de-trending the light curves with a window width of 300 days. The short term variability is correlated with a significance 0.98. Before JD 2455150 the two light curves show a clear correspondence consistent with zero time lag. Every short term sub-flare has a counterpart in the other light curve. After JD 2455500 the light curves do not show a clear correlation. Especially after JD 2455800 the optical flares have no γ-ray counter part.

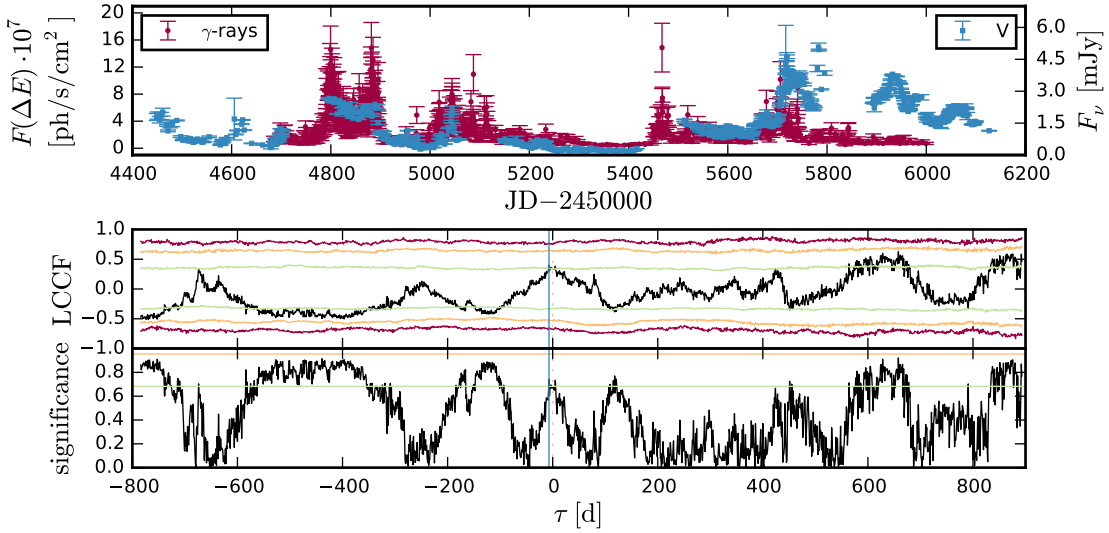

Figure 5.20: Correlation of γ-rays and V-band. Upper panel: γ-ray light curve (red) and V-band light curve (blue). Mid panel: cross-correlation function (black) and significance levels 1σ (green), 2σ (orange), 3σ (red). Lower panel: significance of the correlation coefficients. The vertical, blue line marks the strongest correlation peak.

We perform the cross-correlation analysis on two parts of the light curves individually to test whether the time lag changes with time. Before JD 2455500 the light curves are correlated with significance 0.99 at $+1^{+21}_{-16}$ days time lag. Hayashida et al. (2012) find γ-rays lagging by 10.7 ± 0.7 days behind R-band. Within the uncertainty we cannot discriminate between a positive, negative or zero time lag. The strong correlation and short, if any, time lag suggests that optical and γ ray radiation is produced by the same particle population of roughly the same energies in the same emission region.

Between JD 2455070 and JD 2455850 the light curves correlate at -18^{+20}_{-15} days time lag with significance 0.95. This correlation result matches the two strongest flares in each light curve in the time interval and is probably affected by the observation gaps. In fig. 5.22, mid panel we suggest a longer time delay of -45 days, γ-rays leading the optical light curve. The upper panel shows the observed light curves, in the lower panel the V-band light curve is shifted. We mark all flare peaks in the γ-ray light curve by vertical, grey lines. With a shift of -45 days all peaks in the γ-ray light curve have a counterpart in the optical light curve. We have included the quiescent period between JD 2455070 and JD 2455500 in both tested intervals. As fig. 5.22 shows the variation of V-band does not exactly correspond to the γ-rays variation, neither with zero time lag nor with -45 days time lag.

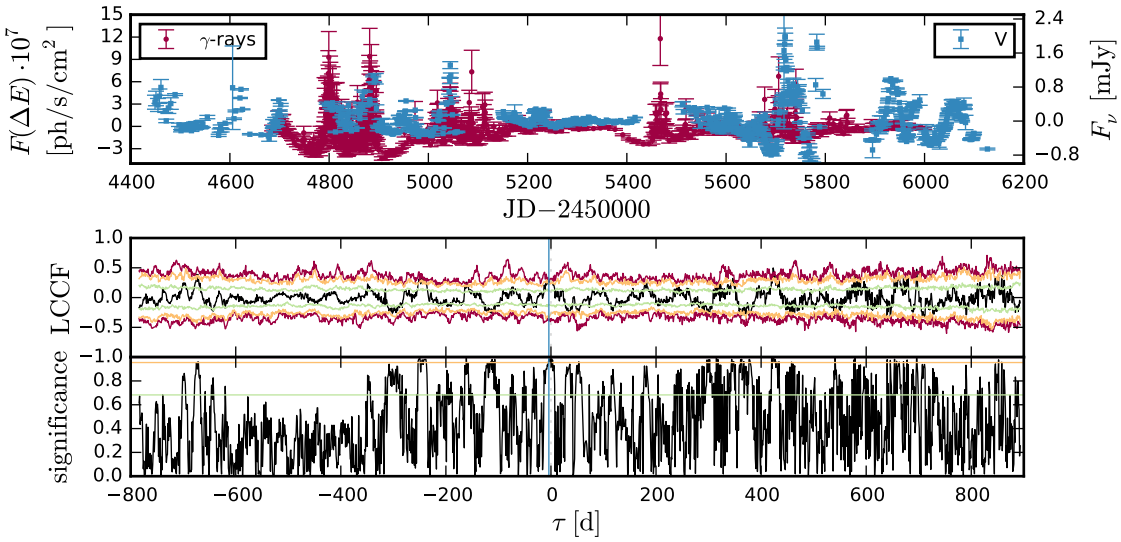

Figure 5.21: Correlation of the de-trended γ-rays and V-band. Upper panel: γ-ray light curve (red) and V-band light curve (blue) de-trended with a window size $\Delta t_{\rm sm} = 300$ d. Mid panel: cross-correlation function (black) and significance levels 1σ (green), 2σ (orange), 3σ (red). Lower panel: significance of the correlation coefficients. The vertical, blue line marks the strongest correlation peak.

Additionally, we shift the V-band data by the time lag of 250 days, which we observed between V-band and X-rays. This is shown in the lower panel of fig. 5.22. We find correspondence between several but not all peaks. The most compelling fact in this scenario is that it generally matches flaring periods in both bands, whereas the other time lags imply an optical flaring period which is not accompanied by a γ-ray flare.The LCCF of the γ-ray light curve at JD 2455200 − 6150 and the V-band light curve at JD 2455500 − 6150 peaks at time lag -251^{+16}_{-17} days with significance 0.89.

In fig. 5.23 we show various potential correlations between the γ-ray, X-ray, and V-band light curves. Red and grey data point show the measured light curve, open red points are time shifted. The open red points in the mid panel show the shifted light curve, correcting for the potential time lag of -250 days as discussed in the previous section. The red, open points in the bottom panel are shifted by +45 days regarding to the shifted V-band light curve, thus, shifted by -205 days regarding to the x-rays light curve. Vertical lines mark peaks in the light curves. The strongest correspondence of peaks is seen in the original γ-rays, the original X-rays and the shifted V-band light curves. In the leptonic model context (SSC, EC), it is unclear how γ-rays could be produced without contemporaneous optical synchrotron radiation, since both are expected to be produced by electrons of roughly the same energies. The zero time lag correspondence of flare peaks in the γ-ray and the X-ray light curves is not reflected in a strong correlation. The LCCF of γ-rays and X-rays has a minor peak at zero time lag with significance 0.41. As previously discussed, the observation gaps in the light curves may miss different prominent flares in the three bands, lowering the correlation coefficients. Given these data we highlight different possibilities of time lags, which currently cannot be validated nor excluded.

The three light curves show corresponding flares with zero time lag before JD 2455100. The most critical point is the strong X-ray flare at JD 2454950, which

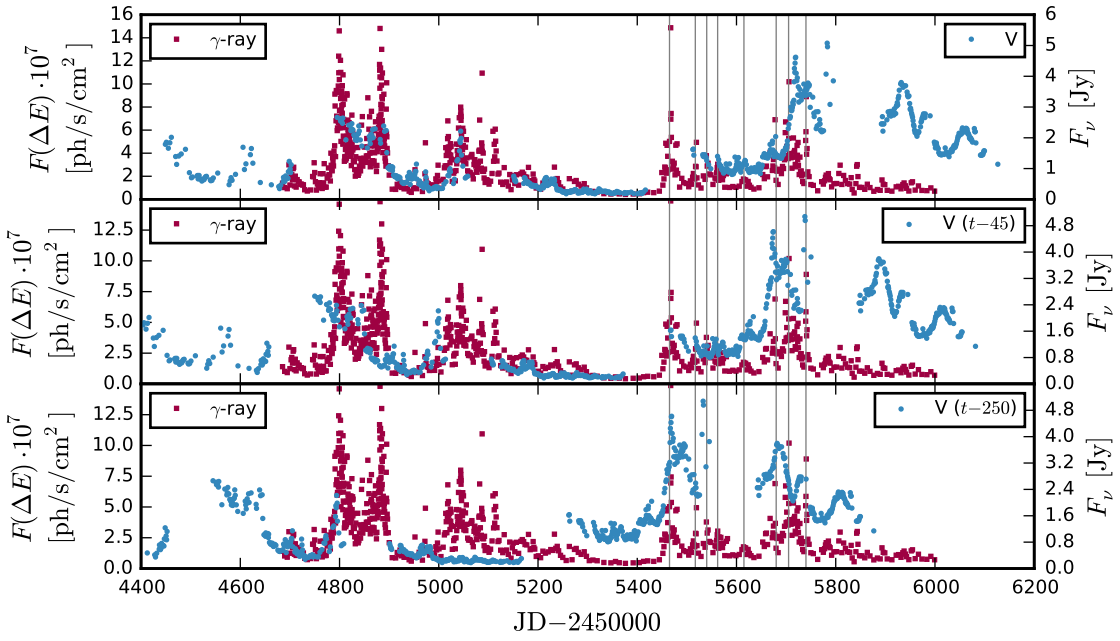

Figure 5.22: γ-ray (red) and V-band (blue) light curve. Upper panel: actual light curves. Mid panel: V-band shifted by -45 days. Lower panel: V-band shifted by -250 days.

is accompanied only by a minor flux density increase in the V-band. Interestingly, the two γ-ray flares at JD 2454800 and JD 2454880 are separated by roughly the same time as the two X-ray flares at JD 2454950 and JD 2455045. The time lag between each potential pair of γ-ray and X-ray flare is $\sim 150-165$ days. Hayashida et al. (2012) make the same observation and point out they "cannot currently envision any situation where the two would be causally connected". We note, though, that the potential lag of V-band behind X-rays and γ-rays in the later light curve is even longer.

At the current point we note, that the correlation of γ-rays, X-rays and optical bands exhibit complex behaviour. Correlation time lags and the strength of correlation certainly changes over time. We observe potentially extreme time lags at the order of several hundred days, which corresponds to distances at the order of one parsec. If these time lags indicate a physical connection between very distant emission regions this poses problems to any current model. Otherwise very similar patterns in the variability at different bands may hint to stationary patterns in the jet flow, which affect the variability in a characteristic way. In this context it has to be evaluated how occasionally only optical synchrotron radiation, occasionally X-rays and γ-rays without optical counterpart can be produced in this region. Further studies are needed to understand the complex behaviour pointed out here. Especially the analysis of SEDs, estimating the spectral indices at optical frequencies, X-rays and γ-rays may help to further investigate the potential time lags and physical connection of the different bands.

5.3 Summary of the correlation analysis

We have tested the light curves of the Quasar Movie Project for correlations and time lags between the 26 different frequency bands. Not all light curves are sampled well enough to obtain viable information from the 650 cross-correlation

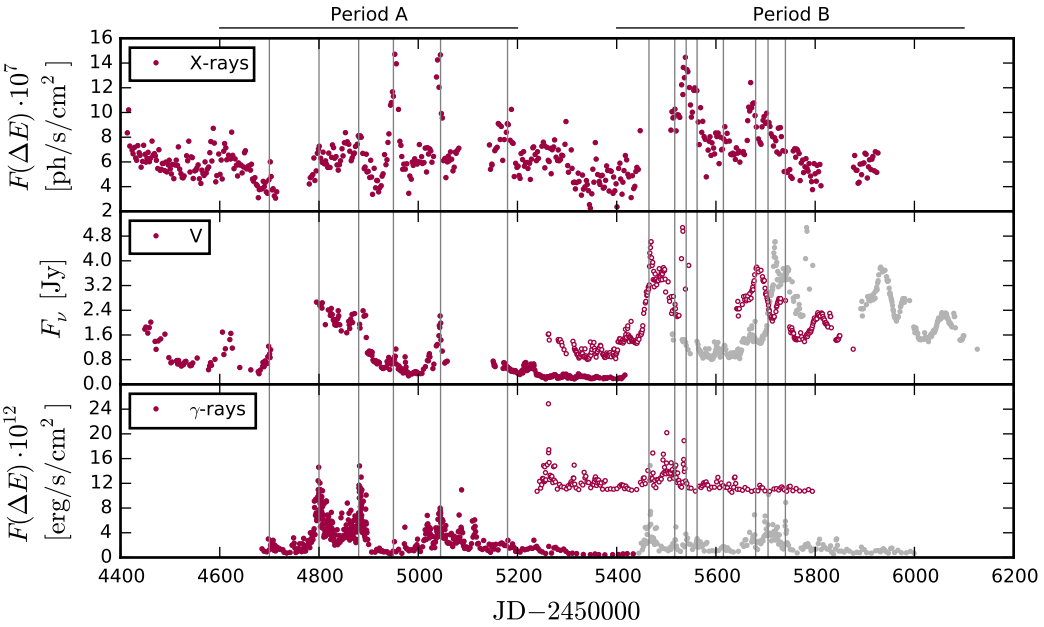

Figure 5.23: X-ray (top panel), V-band (mid panel), and γ-ray (bottom panel) light curve. Red and grey data point show the measured light curve, open red points are time shifted. V-band is partially shifted by -250 days, γ-rays by -205 days. The shifted γ-rays light curve is additionally shifted along the y-axis for clarity.

functions. Therefore, we concentrated on specific pairs of light curves. At the cm, mm, and sub-mm bands we find relative time lags consistent with the opacity effect of a synchrotron self-absorbed conical jet in equipartition. An inversion of the time lag at mm frequencies is indicated but not significant and could be explained by the gradual acceleration of particles. Infrared, optical, and ultraviolet bands are correlated. Within the uncertainties the time lags are consistent with zero. We do not find a frequency dependent relative lag.

The most outstanding result is the zero time lag correlation of the short term variability at 1 mm and X-rays. To our knowledge, no such strong correlation has been observed between X-rays and mm bands so far. It implies that these X-rays are produced through IC scattering by the same electron population which produces the mm synchrotron radiation. In section 4.5 we have argued that the mm synchrotron photons and the CMB photons are potentially serving as seed photons. We note, though, that this result applies only to the short term variable, low-level x-rays. The strong X-ray flare at JD 2455045 has no counterpart in the de-trended 1 mm band.

The correlation between γ-rays, X-rays, and V-band is complex. For the time we have marked as period A in fig. 5.23, the three bands show contemporaneous flares, indicating that the optical synchrotron radiation and the X-rays and γ-rays originate from the same emission region. The zero time lag correlation between the X-rays and 1 mm then implies that the common emission site is located at the mm VLBI core. The ratio of the flare peaks between the three bands varies drastically, though, throughout the period of zero time lag, including on prominent X-ray flare without γ-ray counterpart and only a minor V-band flare. On the other hand, a double flare at γ-rays and X-rays with comparable temporal separation could also indicate a time lag between x- and γ-rays.

In the later light curves, period B, there is certainly no zero time lag correlation

between V-band and x- and γ-rays. Estimating the exact time lag is difficult due to severe gaps in the light curves. We have discussed different potential time lags, which are suggested by comparable patterns of variability peaks. The most significant time lags, consistent with the opacity effect at radio frequencies, imply V-band to lag behind mm frequencies and X-rays by 250 days, corresponding to a distance at the order of one parsec. If the γ-rays are also delayed after the X-rays or contemporaneous with X-rays is not clear. Zero or close to zero time lag between V-band and γ-rays, locates the γ-ray emission site far beyond the BLR. In that case only synchrotron, dust torus, NLR or CMB photons can serve as seed photons for the IC scattering. In section 4.5, we have argued that CMB photons are not energetic enough to be up-scattered to GeV energy. The best candidate of a seed photon field is infrared radiation from the dust torus. On the other hand, zero time lag between X- and γ-rays with optical frequencies lagging hundreds of days behind, requires to explain how γ-rays can be produced without optical synchrotron radiation occurring roughly at the same time. Similar patterns in the variability at different bands and different times could also indicate a stationary structure in the jet flow that relates to characteristic variability in the light curves, when fed with new particles. Disentangling the various correlation patterns requires more detailed analysis of the cross-correlation functions, including the measurement and correlation analysis of spectral indices at radio, optical, X- and γ-rays.

Chapter 6

Polarization

In this chapter we introduce the polarization data of the Quasar Movie Project. We address in detail the problem of the 180 °-ambiguity of the polarization angle and introduce a method to estimate the reliability of solving the ambiguity. Furthermore we introduce a method to quantify the smoothness of an Electric Vector Position Angle (EVPA) curve. We apply these methods to our data and characterize the variation of the polarization fraction and polarization angle.

6.1 Introduction to polarization and polarimetry

An electro-magnetic wave moving along z-direction consists of an electric field component $\mathbf{E}(t, z)$ and a magnetic field component $\mathbf{B}(t, z)$, both perpendicular to one another, both oscillating in the x-y-plane at any z. The polarization of a single electro-magnetic wave is characterized by the orientation of the electric vector, which can be written component-wise at an arbitrary z as:

$$E_x(t) = E_x(0)\cos(\omega t - \phi_1) \tag{6.1}$$
$$E_y(t) = E_y(0)\cos(\omega t - \phi_2), \tag{6.2}$$

where ω is the angular frequency and $\phi_{1,2}$ are two phases. The electro-magnetic wave is called *linearly polarized* when $\phi_1 = \phi_2$. It is called *circular polarized* when $\phi_2 = \phi_1 \pm \pi/2$ and $E_x(0) = E_y(0)$; for a positive sign it is *right-hand circular* polarized, for a negative sign *left-hand circular* polarized. The general case is called *elliptical polarization*. A single photon is necessarily polarized. Only in high-energy astronomy (x-rays, γ-rays and higher energies) single photons can be observed[1], at lower energies radiation is observed which is a superposition of electro-magnetic waves. The polarization of a left-hand and a right-hand circular polarized wave with same amplitudes cancels out, so does the polarization of two linear polarized waves with same amplitudes and perpendicular polarization. Consequentially, when the polarization of the superposing waves is not uniform, only a fraction of the radiation is polarized. Therefore, the description of the polarization of radiation consists of two pieces of information: (a) the orientation (linear, left-hand circular, right-hand circular, elliptical) and (b) the amount of polarization usually expressed as the fraction of light which is polarized.

[1]The technical potential of measuring the polarization of photons at x-rays and higher frequencies is currently evolving.

One formalism to express the polarization state is the *Stokes vector* **S** consisting of the four components, the *Stokes parameters*:

$$I = \left\langle E_x^2(t) \right\rangle + \left\langle E_y^2(t) \right\rangle \tag{6.3}$$
$$Q = \left\langle E_x^2(t) \right\rangle - \left\langle E_y^2(t) \right\rangle \tag{6.4}$$
$$U = 2 \left\langle E_x(t) E_y(t) \cos\delta \right\rangle \tag{6.5}$$
$$V = 2 \left\langle E_x(t) E_y(t) \sin\delta \right\rangle, \tag{6.6}$$

where $\delta = \phi_2 - \phi_1$ and $\langle \cdot \rangle$ denotes time averages. I is the total intensity, Q and U describe the linear polarization and V the circular polarization.

The linear polarization can be described in polar coordinates which can be expressed through the Stokes parameters I, Q, and U

$$m_l = \frac{\sqrt{Q^2 + U^2}}{I} \qquad \in [0, 1] \tag{6.7}$$
$$\chi = \frac{1}{2} \arctan\left(\frac{U}{Q}\right) \qquad \in [0, \pi) \tag{6.8}$$

where m_l is the linear polarization fraction and χ is the EVPA, the orientation of the linear polarization[2]. The circular polarization fraction can be expressed as:

$$m_c = \frac{V}{I} \in [-1, 1]. \tag{6.9}$$

In the following study we consider only the linear polarization and use the terms *linear polarization fraction*, *polarization fraction* and *fractional polarization* interchangeably.

Radio telescopes, which typically have two orthogonally polarized antennae are polarimeters by design. Amplitude and phase information can be recorded and the auto-correlated and cross-correlated signals of the two feads can be converted directly into the Stokes parameters. The incoming signals can be expressed in linear, Cartesian components x, y or left-hand, right-hand components L, R. Accordingly, the receiving system can be designed in two ways with different technical advantages and better sensitivity regarding to either linear or circular polarization. Both systems can be converted into one another.

In optical observations only intensity information but no phase information is obtained. To measure the Stokes parameters, intensities $I(\theta)$ are measured after filtering out all light but that linearly polarized under a certain angle θ. The intensity is measured for different angles ($\theta = 0\,^\circ, 90\,^\circ, 45\,^\circ, 135\,^\circ$) subsequently or simultaneously[3]. The Stokes parameters Q and U result as the difference of the two perpendicular pairs of measurements, I is the sum of either pair. Two systems are used as polarization filters: either wire-grid polarizers which transmit only light polarized perpendicularly to the grid or Wollaston-prisms which split the light into two perpendicularly polarized components. A half-wave plate may be used to turn the plane of linear polarization instead of rotating the grid of

[2]The EVPA is usually measured from North to East.

[3]Simultaneous measurements of polarized intensities requires to split the incoming light, lowering the sensitivity. This approach is preferred when the polarization is expected to vary between subsequent exposures.

prism. Theses systems allow only to measure linear polarization. A quarter-wave plate transforms circular polarized light to linear polarized light and vice versa. After this transformation circular polarization can be measured using the same techniques as for linear polarization measurements.[4]

6.2 Polarimetry data

The Quasar Movie Projecthas acquired polarization data of 3C 279 at various bands. The observatories contributing these data are listed in table 6.1.

Table 6.1: Observatories contributing polarization data to the Quasar Movie Project.

Observatory/Observer	Tel. diam.	Filters
	optical	
Calar Alto, Spain	2.2 m	R
CrAO, Ukraine	0.7 m	R
Kanata, Japan	1.5 m	V
KVA, La Palma	0.6 m	white light
Liverpool Telescope, La Palma	2 m	V+R
Perkins, USA	1.83 m	R
OAN-SPM, Mexico	0.84 m	R
St. Petersburg, Russia	0.4 m	R
Steward Obs., USA	1.52 m	V
	2.3 m	5000-7000 Å
	mm, cm	
IRAM	30 m	86, 229 GHz
UMRAO	26 m	5, 8, 15 GH

The Boston University Blazar Research Group[5] provided R-band polarization data from Calar Alto, CrAO, Perkins, and St. Petersburg. As part of the Monitoring AGN with Polarimetry at the Calar Alto Telescopes (MAPCAT)[6] project (Jorstad et al., 2010) 3C 279 was observed at the 2.2 m of the Calar Alto Astronomical Observatory in Spain between July 2007 and February 2012 (Jorstad et al., 2010). From the 70 cm telescope operated by the Crimean Astrophysical Observatory (CrAO) in the Ukraine and the 40 cm telescope of the St. Petersburg State University we have obtained data between June 2005 to June 2012 and January 2007 and May 2012, respectively (Larionov et al., 2008; Jorstad et al., 2010). The data observed with the 1.8 m Perkins telescope of Lowell Observatory in Arizona, USA ranges from April 2011 to June 2012, and R-band (Jorstad et al., 2010).

Calar Alto and CrAO are also participating in the WEBT-collaboration[7] (e.g. Böttcher et al., 2007; Larionov et al., 2008). Additional WEBT-data comes from the Observatorio Astronómico Nacional - San Pedro Mártir (OAN-SPM)

[4]This introduction is based on the review article by Trippe (2014).

[5]`https://www.bu.edu/blazars/`

[6]`http://www.iaa.es/~iagudo/_iagudo/MAPCAT.html`

[7]`http://www.oato.inaf.it/blazars/webt/`

observed with the 84 cm telescope between January 2011 and April 2012 (Sorcia et al., 2013).

Further data was observed with the KVA 60 cm telescope and the robotic 2 m Liverpool telescope both sighted at the Observatorio del Roque de los Muchachos of the Instituto de Astrofísica de Canarias on the Canary island La Palma, Spain. The KVA observed at white light, without any filters. The data ranges from December 2010 to June 2011 (Aleksić et al., 2014). The former RINGO2 instrument used up to October 2012 at the Liverpool Telescope was equipped with a hybrid V+R filter. The data ranges from November 2010 to March 2012 (Aleksić et al., 2014).

The Higashi-Hiroshima Observatory provided polarimetry data observed at V-band with the 1.5 m Kanata telescope between December 2009 and June 2011. Observations before February 2010 were performed with the TRISPEC instrument (Watanabe et al., 2005), later observations with HOWPol (Kawabata et al., 2008; Hayashida et al., 2015).

Additionally we use the open access data provided by the Steward Observatory spectropolarimetric monitoring project of the University of Arizona[8]. Polarization data was observed between November 2008 and July 2012 at V-band and 5000-7000 Å with the Bok 2.3 m telescope located on Kitt Peak in Arizona, USA and the 1.54 m Kuiper telescope located on Mt. Bigelow in Arizona, USA (Smith et al., 2009).

Polarimetry data at 86 GHz and 229 GHz between April 2010 and January 2012 is provided through an polarimetric AGN survey performed at the IRAM 30 m telescope (Agudo et al., 2010, 2014). Polarimetry data at 5, 8, and 15 GHz observed between November 2011 and February 2012 is contributed by the University of Michigan Radio Astronomy Observatory (UMRAO) observed with the 26 m telescope (Aller et al., 1985).

The fractional linear polarization is biased. Uncertainties in the Stokes parameters Q and U always contribute positively and sum up due to the squares in eq. (6.7). The uncertainties are Rice-distributed, if the errors in Q and U are Gaussian. We de-bias the fractional linear polarization m_l with uncertainty σ_{m_l} following Pavlidou et al. (2014):

$$m_{l,\mathrm{debiased}} = \begin{cases} \sqrt{m_l^2 - \sigma_{m_l}^2} & \text{for } m_l/\sigma_{m_l} \geq \sqrt{2} \\ 0 & \text{otherwise} \end{cases} \tag{6.10}$$

The frequency-dependence of the polarization fraction and the EVPA in optical are relatively weak. Therefore we combine all optical polarization curves. We remove one data point in the KVA data with a $>60\,^\circ$ offset from the combined EVPA curve and four data points in the SPM polarimetry identified as outliers based on the simultaneous EVPA curves of 3C 279 and 3C 273.

We average data points within time intervals of 0.5 days. At time scales shorter than half a day the variation of the polarization fraction and the EVPA is at the same order as the uncertainties. The averaging thus reduces the noise without removing significant real variation. We use the algorithm introduced in section 2.1.2 to identify averaging intervals. The polarization fraction and the EVPA are averaged using the error weighted mean. For the EVPA we consider

[8] `http://james.as.arizona.edu/~psmith/Fermi/`

the 180 °-modulus in the following manner: for N data points χ_i, $i = 1 \ldots N$ in an averaging interval we calculate the error weighted mean of χ_i' with

$$\chi_i' = \begin{cases} \chi_i + 180\,^\circ & \text{for } \max_i(\chi_i) - \chi_i > 90\,^\circ \\ \chi_i & \text{otherwise} \end{cases} . \tag{6.11}$$

As final averaged value we take 180 °-modulus of the weighted mean.

Calculating the mean of the polarization fraction and the EVPA directly is only an approximation. The correct approach would be to calculate the mean of the Stokes parameters I, Q, U and transform the averages into the polar description. For most of the data we do not have the Stokes parameters and the back-transformation is not unambiguously possible. Therefore, we use this approximation.

Table 6.2: Polarisation data sampling. The columns show the observing band, observation time interval, total length of the light curve, median time step, maximum time gap, and number of data points.

Band	JD−2 450 000	T [d]	$\widetilde{\Delta t}$ [d]	$\max \Delta t$ [d]	N
opt	3529-6127	2598	1	238	501
1 mm	5321-5958	637	2	246	13
3 mm	5305-5958	653	3	92	30
21 mm	5509-5973	464	17	52	67
37 mm	5547-5981	434	27	58	51
62 mm	5532-5939	407	1	89	45

Table 6.2 lists details on the data sampling of the combined optical and the mm and cm polarization curves.

6.3 EVPA ambiguity

The EVPA χ is defined within a 180 °-interval[9], c.f. eq. (6.8). The measurement of χ is ambiguous due to the 180 °-modulus. This problem is often referred to as the 180 °-*ambiguity* or $n\pi$-*ambiguity* (e.g. Marscher et al., 2008; Larionov et al., 2008; Abdo et al., 2010a). The ambiguity is problematic when the variation of the EVPA is to be characterized because the difference $\Delta\chi = \chi_2 - \chi_1 \pm n \cdot 180\,^\circ$ is ambiguous, too. This relation shows that even the direction of the rotation is unclear: a rotation of $20\,^\circ/t$, where t is an arbitrary time step, cannot be discriminated from a rotation of $-160\,^\circ/t$. Without a known physical limitation on the rotation rate this problem could only be resolved by observing at infinitely short time steps, or if there were such a limit $(\mathrm{d}\chi/\mathrm{d}t)_{\max}$ at time steps short enough $\Delta t < 90\,^\circ \cdot (\mathrm{d}\chi/\mathrm{d}t)_{\max}^{-1}$. With sufficiently short time sampling continuous EVPA-rotations that extend beyond the 180 °-interval appear with a sharp jump of $|\Delta\chi| = |\chi_i - \chi_{i-1}| > 90\,^\circ$ in the otherwise smooth varying curve. Under the assumption of minimal variation between two data points, the measured EVPA-curve can be adjusted to visualize large continuous rotations.

[9]The choice of the EVPAinterval-limits is arbitrary. Usual limits are $0\,^\circ \leq \chi < 180\,^\circ$ or $-90\,^\circ \leq \chi < 90\,^\circ$. We use the former.

One scheme of adjusting the EVPA curve reported in the literature (e.g Sasada et al., 2011; Sorcia et al., 2013) is to shift data a data point χ_i by $\pm n \cdot 180\,^\circ$ if it the deviation from the previous data point is significantly larger than $90\,^\circ$. The noise reduced difference is:

$$\begin{aligned}\Delta\chi_{\mathrm{red}} &= |\Delta\chi| - \sqrt{\sigma^2_{\chi_i} + \sigma^2_{\chi_{i-1}}} \\ &= |\chi_i - \chi_{i-1}| - \sqrt{\sigma^2_{\chi_i} + \sigma^2_{\chi_{i-1}}} \qquad (6.12)\\ & \qquad (6.13)\end{aligned}$$

where σ_{χ_i} and $\sigma_{\chi_{i-1}}$ are the uncertainties of the current and the preceding EVPA data point. Only if $\Delta\chi_{\mathrm{red}} > 90\,^\circ$ the data point χ_i is shifted by $n \cdot 180\,^\circ$ with $n \in \mathbb{N}_\pm$ selected such that the difference between two adjacent data points is minimized:

$$\chi_{i,\mathrm{shift}} = \chi_i + n \cdot 180\,^\circ \qquad (6.14)$$

$$n = \mathrm{round}\left(\frac{\chi_i - \chi_{i-1}}{180\,^\circ}\right), \qquad (6.15)$$

where round$(\cdot)$ denotes rounding to an integer.

This scheme is problematic for two reasons. First, the concept is to shift a data point only if there is a significant deviation of $90\,^\circ$. But the uncertainties of both data points imply that the difference is either overestimated or underestimated, arguing either for or against shifting the data point. Second, this method is not consistent. The resulting EVPA curve may depend on choice of the initial two quadrants it is measured in, as we show in the following example.

We consider two data points χ_1 and χ_2 with corresponding uncertainties σ_{χ_1} and σ_{χ_2} and choose two initial intervals:

Interval: $[0, 180\,^\circ)$

$\chi_1 = 40\,^\circ$ $\quad \sigma_{\chi_1} = 10\,^\circ$

$\chi_2 = 140\,^\circ$ $\quad \sigma_{\chi_1} = 10\,^\circ$

$\Delta\chi_{\mathrm{red}} = 85.9\,^\circ \;\rightarrow$ do not shift

$\chi_1' = 40\,^\circ$

$\chi_2' = 140\,^\circ$

Interval: $[-90, 90\,^\circ)$

$\chi_1 = 40\,^\circ$ $\quad \sigma_{\chi_1} = 10\,^\circ$

$\chi_2 = -40\,^\circ$ $\quad \sigma_{\chi_1} = 10\,^\circ$

$\Delta\chi_{\mathrm{red}} = 65.9\,^\circ \;\rightarrow$ do not shift

$\chi_1' = 40\,^\circ$

$\chi_2' = -40\,^\circ$

The value of the second adjusted data point χ_2' depends on the initial interval. The method is not consistent, but produces arbitrary results for arbitrary choices of the initial interval. We recommend not to use the uncertainty-considering method.

If the uncertainties are not considered in the decision of whether or not to shift a data point, but all data points χ_i are adjusted according to eqs. (6.14)

to (6.15) the resulting shape of the adjusted curve is independent of the initial interval[10].Continuing the example:

$\Delta\chi = 100\,^\circ \;\rightarrow$ shift

$\chi'_1 = 40\,^\circ$
$\chi'_2 = -40\,^\circ$

$\Delta\chi = 80\,^\circ \;\rightarrow$ do not shift

$\chi'_1 = 40\,^\circ$
$\chi'_2 = -40\,^\circ$

We suggest a generalization of this method, which considers more than just one preceding data point as reference. For N data points χ_i with $i{=}2 \ldots N$ we iteratively calculate the median $\{\cdot\}$ of the $N_{\rm ref}$ preceding data points[11]

$$\chi_{i,\rm ref} = \left\{[\chi_{i-1-N_{\rm ref}}, \ldots, \chi_{i-1}]\right\}, \tag{6.16}$$

and shift each data point by $n \cdot 180\,^\circ$ with $n \in \mathbb{N}_\pm$ selected such that the difference between the current data point and the median reference is minimized:

$$\chi_{i,\rm shift} = \chi_i + n \cdot 180\,^\circ \tag{6.17}$$

$$n = \text{round}\left(\frac{\chi_i - \chi_{i,\rm ref}}{180\,^\circ}\right). \tag{6.18}$$

For $N_{\rm ref}{=}1$ the method is identical to the second one. For $N_{\rm ref}{\geq}3$ the generalized method is less susceptible to measurement errors. With increasing $N_{\rm ref}$ the impact of outliers is reduced but the method is more likely to obscure real variation if the data is not well sampled.

In the following section we test the reliability of our generalized method (eqs. (6.16) to (6.18)) for various $N_{\rm ref}$.

6.3.1 Reliability of the EVPA adjustment

Under the assumption of minimal variation between adjacent data points the EVPA adjustment method described by eqs. (6.16) to (6.18) aims to reconstruct the intrinsic EVPA curve $\chi_{\rm intr}$ from the measured one $\chi_{\rm obs}$, which is the $180\,^\circ$ modulo of the intrinsic curve.

We define the reliability of the method as the probability of correct reconstruction, i.e. the probability $P(\chi_{\rm adj} = \chi_{\rm intr})$ that the shape[12] of the adjusted EVPA curve $\chi_{\rm adj}$ is identical to the shape of the intrinsic curve $\chi_{\rm intr}$. We want to test the reliability under various conditions.

In the optimal case of no observational errors $\sigma_\chi = 0$ and constant time sampling Δt the reliability is either zero or one, depending on the variation rate of the EVPA. If we assume a constant variation rate $\mathrm{d}\chi/\mathrm{d}t$ the sampled rotation (between each

[10]The difference between all data points is the same. The entire curves might be set off by $\pm n \cdot 180\,^\circ$.

[11]For $i{=}2 \ldots N_{\rm ref}$ we use the median of all preceding data points.

[12]The difference between all data points is the same. The entire curves might be set off by $\pm n \cdot 180\,^\circ$.

two data points) is $\Delta\chi = \Delta t \cdot \mathrm{d}\chi/\mathrm{d}t$. At data point χ_i the value of the first and last reference point are given by:

$$\begin{aligned}\chi_{i-N_{\mathrm{ref}}} &= \chi_i - N_{\mathrm{ref}} \cdot \Delta\chi \\ \chi_{i-1} &= \chi_i - \Delta\chi.\end{aligned}$$

For the constant variation rate the reference value $\chi_{i,\mathrm{ref}}$ (eq. (6.14)) can be expressed as the average of the first and last reference point:

$$\begin{aligned}\chi_{i,\mathrm{ref}} &= \frac{1}{2}\left(\chi_{i-N_{\mathrm{ref}}} + \chi_{i-1}\right) \\ &= \chi_i - \frac{1}{2}(N_{\mathrm{ref}}+1)\Delta\chi.\end{aligned}$$

The EVPA curve will be correctly reconstructed if

$$\begin{aligned}\chi_i - \chi_{i,\mathrm{ref}} &= \frac{1}{2}(N_{\mathrm{ref}}+1)\Delta\chi < 90\,^\circ \\ \Leftrightarrow \Delta\chi &< \frac{180\,^\circ}{N_{\mathrm{ref}}+1}.\end{aligned}$$

Here, considering just one reference point is the best option as it allows for the largest sampled rotation. Higher N_{ref} require better sampling.

For sampled rotations $\Delta\chi < 60\,^\circ$ the adjustment with $N_{\mathrm{ref}} = 1$ and with $N_{\mathrm{ref}} = 2$ or higher may result in the same EVPA curve. We define the consistency level N_{cons} as the highest number of reference points for which all adjusted curves with $N_{\mathrm{ref}} \leq N_{\mathrm{cons}}$ are identical:

$$N_{\mathrm{const}} = \max\{N \in \mathbb{N}_{\geq 1} : \chi_{\mathrm{adj},(N_{\mathrm{ref}}=1)} = \chi_{\mathrm{adj},(N_{\mathrm{ref}}=i)}\ \forall\ i \leq N\}. \tag{6.19}$$

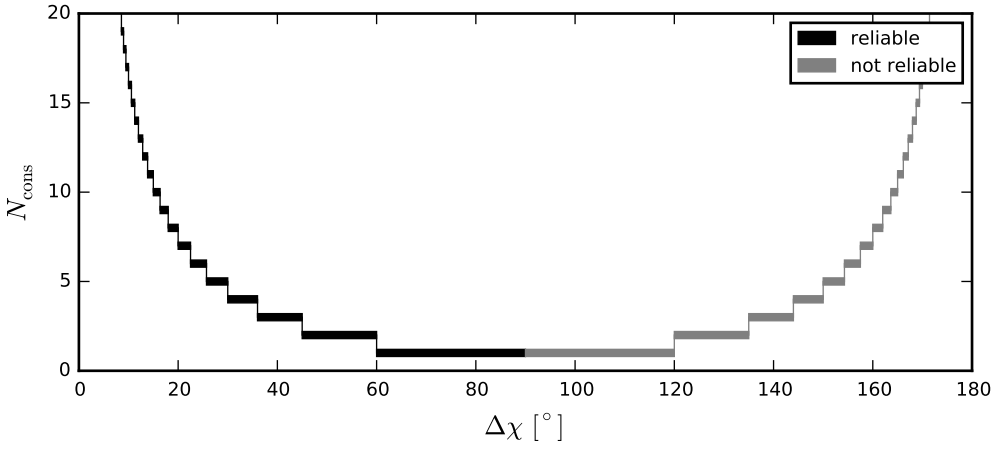

Figure 6.1: Consistency level of the EVPA adjustment depending on the sampled rotation for constant time sampling an no observational errors.

Figure 6.1 shows the consistency level depending on the sampled rotation rate $\Delta\chi = \mathrm{d}\chi/\mathrm{d}t \cdot \Delta t$ with a constant rotation rate $\mathrm{d}\chi/\mathrm{d}t$, constant time steps Δt and

no observational errors. We note that consistency between curves adjusted with different numbers of reference points does not imply correctness of the reconstruction. For instance an intrinsic rotation of $+10\,^\circ\,\mathrm{d}^{-1}$ observed at time steps $\Delta t = 10\,\mathrm{d}$, corresponding to a sampled rotation of $\Delta\chi = 100\,^\circ$ would appear as a sampled rotation of $\Delta\chi = 100\,^\circ - 180\,^\circ = -20\,^\circ$ or $-2\,^\circ\,\mathrm{d}^{-1}$. Therefore, no intrinsic rotation that is sampled at $\Delta\chi \geq 90\,^\circ$ can be correctly reconstructed. We expect the consistency level shown in fig. 6.1 to be lower when the EVPA curve is affected by observational errors. In the following we test the influence of observational errors on the reliability and the consistency level.

We simulate a linear increasing EVPA curve $\chi(t_i)$ with slope $\mathrm{d}\chi/\mathrm{d}t = 3.6\,^\circ\,\mathrm{d}^{-1}$ over a total time $T = 100\,\mathrm{d}$ with three different, but constant sampling rates $\Delta t = 1, 5, 10\,\mathrm{d}$. To each data point Gaussian noise $\mathcal{N}(0, \sigma)$ is added where σ is the noise scale. The resulting curve $\chi_{\mathrm{intr}}(t_i)$ is reduced to the observed $180\,^\circ$ interval $\chi_{\mathrm{obs}}(t_i)$ and then adjusted attempting to reconstruct the intrinsic curve. Figure 6.2 shows the probability of correct EVPA reconstruction $P(\chi_{\mathrm{adj}} = \chi_{\mathrm{intr}})$ depending on the noise level for the three sampling rates and different number of reference points N_{ref} for the adjustment.

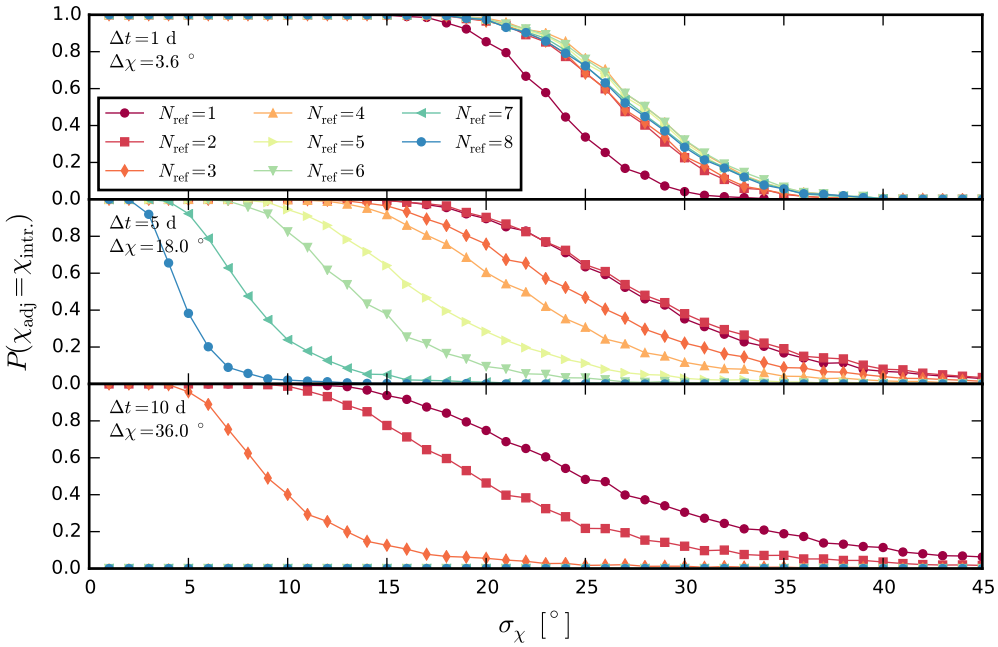

Figure 6.2: Probability of the correct EVPA reconstruction for differently sampled rotations $\Delta\chi$ (top to bottom panel) over the Gaussian noise level σ_χ using different numbers of reference points N_{ref}.

At the best time sampling $\Delta t = 1\,\mathrm{d}$ the intrinsic variation between two data points is $\Delta\chi = 3.6\,^\circ$. At error scales $\sigma_\chi \geq 15\,^\circ$ the variation is clearly noise dominated and the reliability drops. The reliability is higher for more reference points up to $N_{\mathrm{ref}} \leq 7$, but decreases again for $N_{\mathrm{ref}} > 7$. This threshold depends on the intrinsic underlying rotation rate.

At the $5\,\mathrm{d}$ and $10\,\mathrm{d}$ sampling rates the sampled rotation is $18\,^\circ$ and $36\,^\circ$, respectively. With degrading sampling the reliability begins to drop at lower noise levels and thus is generally lower than with better sampling. For the $5\,\mathrm{d}$ sampling the adjustment with one and with two reference points performs roughly equally well. With more reference points the reliability decreases. For worsening sampling

the adjustment based on a single data point performs best and drastically decreases when more reference points are considered.

The best choice for N_{ref} depends on the situation. For very well sampled data under the influence of strong observational errors a higher number of reference points may help to increase the reliability of the EVPA adjustment, decreasing the impact of the noise contribution. On the other hand, for less well sampled data - beyond a threshold that depends on the usually a priori unknown intrinsic variation rate - considering only one preceding reference data point is the best option. Generally the reliability drops with decreasing sampling rates and increasing noise contribution.

We extend the previous test to the grid of sampled rotation rates $\Delta\chi$ and the error scale σ_χ both sampled from 2 to 40 degrees at a step of 2 degrees. At each grid point we run 1 000 simulations. We simulate a linear EVPA increase of 360 degrees with a constant time sampling set by the rotation sampling. Gaussian noise with zero mean and the standard deviation given by the error scale is added to each data point. The simulated curve is reduced to the 180 °-interval and then adjusted. We test the reliability of the adjustment with $N_{\mathrm{ref}} = 1$ and the consistency level.

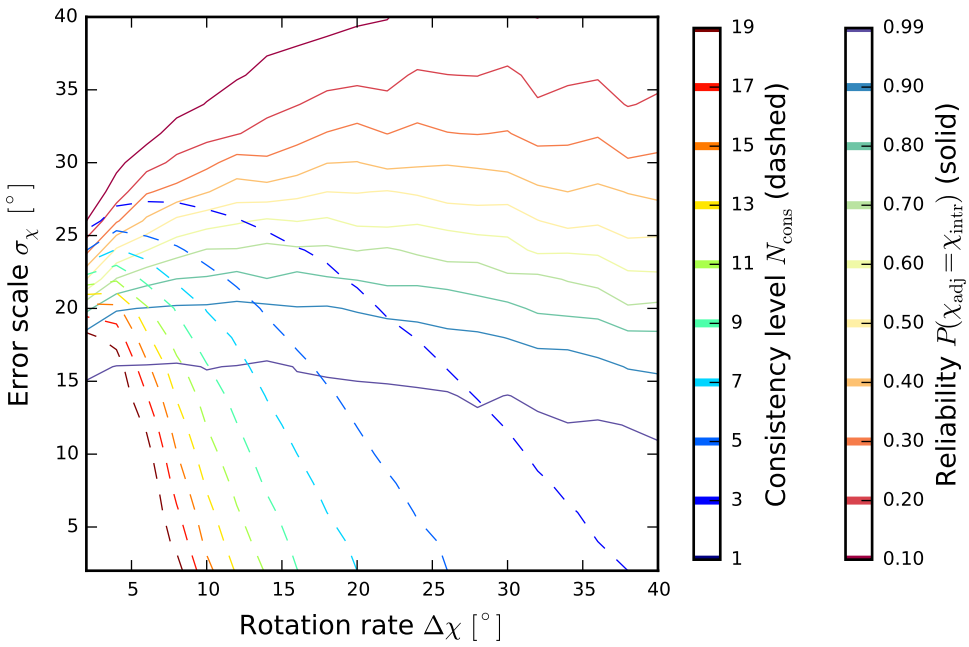

Figure 6.3: Limits on the consistency level (dashed lines) and the reliability (solid lines) depending on the sampled rotation rate and the error scale.

Limits on the $N_{\mathrm{ref}} = 1$-reliability and the consistency level N_{cons} are shown in fig. 6.3. The consistency level and the reliability do not show a direct correspondence. High consistency $N_{\mathrm{cons}} \geq 19$ indicates good sampling of the measured rotation rate $\Delta\chi < 8\,^\circ\,\mathrm{d}^{-1}$, limit the error scale $\sigma_\chi < 18\,^\circ$ and imply a reliability of $> 90\,\%$, but lower consistency levels overlap a wide range of the reliability.

So far we have tested the optimal case of even sampling and homoscedastic errors. In the following we want to test the reliability of reconstructing an EVPA curve given the data sampling and the amount of observational errors of our observed data. The observation time steps follow roughly a power-law. We simulate these time steps by drawing random samples from a truncated power-law distribution

$$P(x) = \frac{\alpha + 1}{x_{\mathrm{max}}^{\alpha+1} - x_{\mathrm{min}}^{\alpha+1}} x^{\alpha}, \tag{6.20}$$

with a minimum time step of 0.5 d, a maximum time step of 21 d and a power-law index of -1.7. For various intrinsic rotation rates of $\mathrm{d}\chi/\mathrm{d}t = 1 \ldots 20\,^{\circ}/\mathrm{d}$ we simulate a linear increasing EVPA curve of a total amplitude of $360\,^{\circ}$, adjusting the total time T according to the rotation rate. Thus, each simulated curve is influenced by the $180\,^{\circ}$ ambiguity once between two data points. Gaussian noise $\mathcal{N}(0, \sigma)$ is added to each data point. The noise scale σ is drawn from a log-normal distribution $\mathcal{LN}(\mu_{\mathrm{err}}, \sigma_{\mathrm{err}})$ to simulate heteroscedastic errors. We estimate the distribution parameters from our measured EVPA uncertainties $e_{\mathrm{EVPA},i}$ through the mean and standard deviation of $\ln(e_{\mathrm{EVPA},i}/^{\circ})$ as: $\hat{\mu}_{\mathrm{err}} = 0.4$, $\hat{\sigma}_{\mathrm{err}} = 1.2$. The resulting curve is reduced to the $180\,^{\circ}$ interval and then adjusted trying to reconstruct the intrinsic variation. The top panel of fig. 6.4 shows the probability of correct reconstruction over various rotation rates for different numbers of reference points. Given the time sampling and uncertainty scales of our observed data, the adjustment considering only one reference data point $N_{\mathrm{ref}} = 1$ is the most reliable for intrinsic rotation rates $\geq 3\,^{\circ}/\mathrm{d}$. The highest reliability at $\leq 3\,^{\circ}/\mathrm{d}$ is 98 %. For higher rotation rates the reliability drops and it decreases faster for higher N_{ref}. We further test the consistency of the adjustment with different N_{ref}.

We show the average consistency level in the lower panel of fig. 6.4. Error bars indicate the corresponding standard deviation. We have tested the consistency level up to $N_{\mathrm{ref}} = 20$ which is reached and possibly exceeded at the lowest intrinsic rotation rate. A high consistency rate $N_{\mathrm{cons}} \gtrsim 10$ indicates low intrinsic variation and a high probability of correct curve reconstruction. For rotation rates $\geq 5\,^{\circ}/\mathrm{d}$ the consistency decreases slowly from initially 5 ± 4 corresponding to a wide range of reliability, as shown previously for constant time sampling and homoscedastic errors in fig. 6.3.

We conclude, that for our data sampling and observational errors the best choice for the number of reference points considered in the EVPA adjustment is $N_{\mathrm{ref}} = 1$, except for very slow intrinsic rotations of less than three degrees per day. Considering more reference points is likely to obscure real variation. The consistency level ≥ 10 indicates good sampling of the intrinsic variation given the observational noise level and allows to estimate the reliability. We point out, that this threshold depends on the sampling rate and the observational noise. It is tested for the very sampling and estimated errors of our data and may require new simulations for different data sets.

6.4 Optical EVPA variation of 3C 279

We show the optical EVPA data sets in the upper panel of fig. 6.5. The lower panel shows the combined and averaged, optical, adjusted EVPA curve. The full data set is split into four epochs (I, II, III, IV) by three, annual observation gaps marked by dashed lines. We further sub-divide epochs II-IV based on the general trend of the curve. Those divisions are indicated by dotted lines. The time ranges of the epochs are given in table 6.3. For each epoch we measure the adjustment consistency level N_{cons} (c.f. section 6.3.1), the total rotation amplitude $|\Delta\chi| = \max \chi(t_i) - \min \chi(t_i)$ and the duration of the largest rotation $\Delta t = |\mathrm{argmax}\, \chi(t_i) - \mathrm{argmin}\, \chi(t_i)|$. The results are summarized in table 6.3.

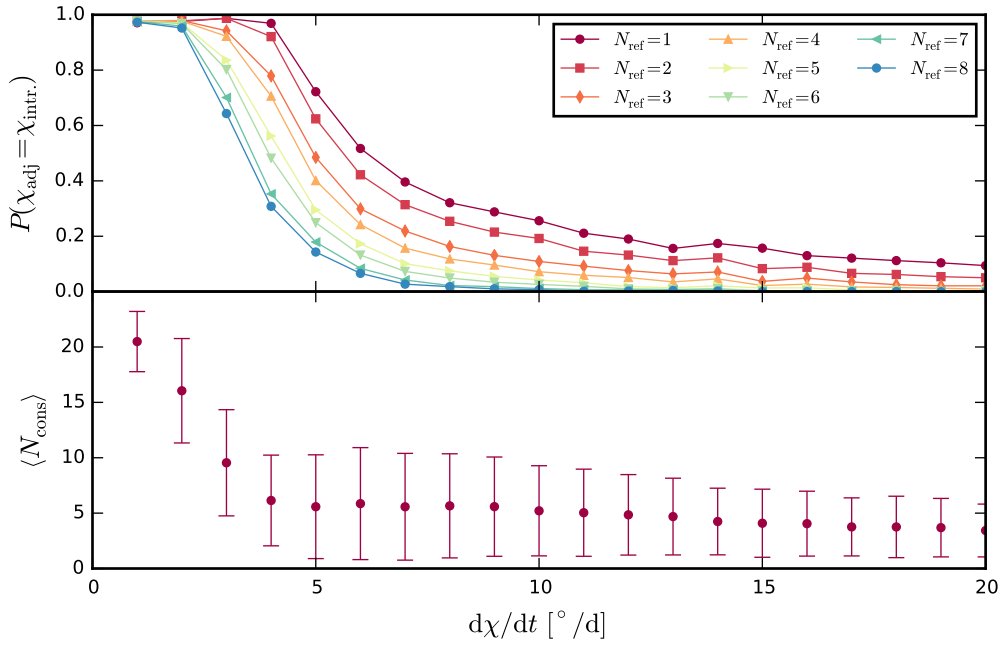

Figure 6.4: Probability of the correct EVPA reconstruction using different numbers of reference points $N_{\rm ref}$ (upper panel) and average consistency levels (lower panel) over different rotation rates dχ/dt.

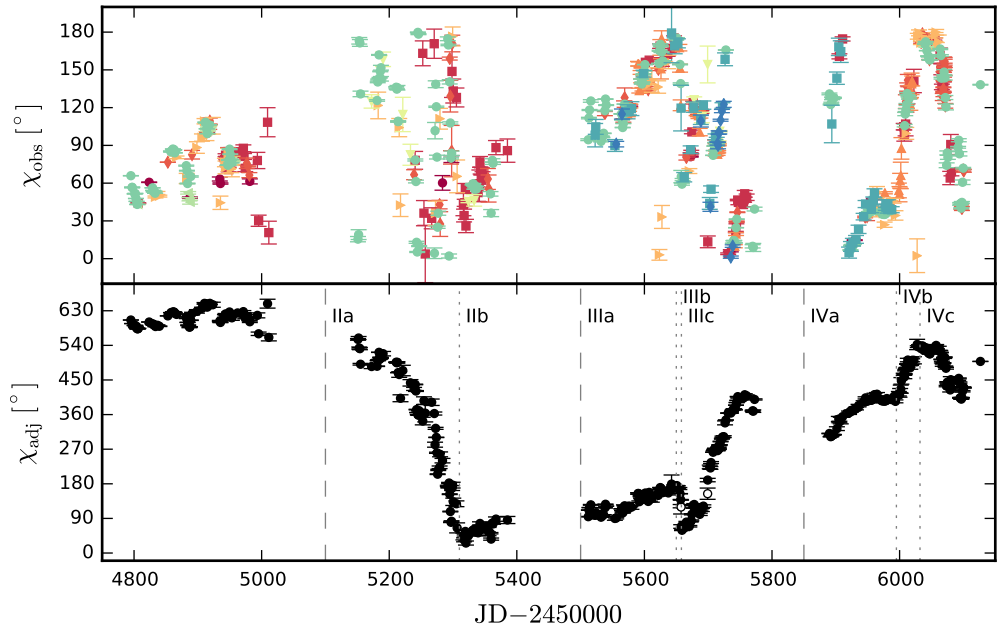

Figure 6.5: Measured (top panel) and combined, adjusted (bottom panel) optical electric vector position angle (EVPA) of 3C 279. Red circles: Calar Alto (R), Red squares: CrAO-70cm (R), red diamonds: Perkins (R), orange up-sided triangles: SPM (R), orange right-sided triangles: St. Petersburg (R), green down-sided triangles: Kanata (V), green left-sided triangles: Steward Obs. (V), blue circles: Steward Obs. (spec.), blue squares: Liverpool (V+R), blue diamonds: KVA (white light). Open symbols are added from the non-averaged EVPA curve.

Epoch I exhibits only little variation $|\Delta\chi| < 90\,^\circ$. Thus the consistency is infinite. We point out, that period I contains the apparent $\sim 180\,^\circ$ rotation at

Table 6.3: Optical EVPA variation of 3C 279 for different periods (col. 1): period time range (col. 2, 3), EVPA adjustment consistency level based on the averaged data (col. 4) and the non-averaged data (col. 5 if differing), maximum EVPA difference (col. 6), and duration of the maximum variation (col. 7).

Period	JD−2450000	$N_{\rm cons}$		$\Delta\chi$ [°]	Δt [d]
I	4750-5100	∞		< 90	
II	5100-5500	1			
III	5500-5800	2	(4)		
IV	5800-6150	6	(8)		
IIa	5100-5310	1		-494	154
IIb	5310-5500	∞		62	47
IIIa	5500-5650	∞	(78)	89	89
IIIb	5650-5658	3	(8)	-106	7
IIIc	5658-5850	2	(4)	352	98
IVa	5850-5995	51	(65)	110	73
IVb	5995-6032	23	(30)	131	28
IVc	6032-6150	6	(8)	-140	39

JD 2454880 − 900 described by Abdo et al. (2010a). Given our data the EVPA variation does not exceed 90 ° and the fast rotation is not sampled well enough to be visible.

Epoch II starts with a long, overall clock-wise trend (epoch IIa) with an amplitude of $\geq 494\,^\circ$. This trend possibly started in epoch I and is probably even larger than observed. The average rotation rate is $\Delta\chi/\Delta t = -3.2\,^\circ$/d. This steep EVPA decrease is not sampled well, indicated by no adjustment consistency $N_{\rm cons} = 1$. The consistency is lower than expected by our simulations (c.f. fig. 6.4). The reason is, that the observed variation strongly diverges from a plain linear trend but appears to be much more erratic. Therefore we cannot estimate the probability that the adjusted curve is a correct reconstruction of the intrinsic variation. Epoch IIb shows an overall clockwise rotation trend which is possibly continued in epoch IIIa.

Epoch IIIb contains a very sharp counter-clockwise rotation of $-106\,^\circ$ in a few days with an average rotation rate of $-15\,^\circ$/d. This rotation is sampled by only six data points with a large gap of 70 degrees. The averaging at an interval of 0.5 days probably removed intrinsic variation in this epoch. We show two data points from the non-averaged data as open circles in fig. 6.5 filling this gap partially. The non-averaged data has a consistency level of 8, much higher than the averaged data with a consistency of 3, whereas both adjusted curves give an identical total amplitude. We therefore conclude that this counter-rotation is not an artefact due to bad sampling but is a real event.

This sharp rotation is followed by general counter-clockwise trend over almost 360 degrees within 98 days at an average rotation rate of 3.3 °/d (epoch IIIc). This rotation is fully covered by the observation. The beginning of a clockwise rotation is clearly visible at the end of epoch IIIc. The average rotation rate 3.3 °/d estimated from the total amplitude and the median rotation rate 3.9 °/d estimated from each pair of adjacent data points suggest a high probability of $\approx 98\,\%$ that the adjusted EVPA curve correctly represents the intrinsic shape of the curve (c.f. fig. 6.4). The low consistency level of 2 on the other hand is below the expectation value

at this intrinsic rotation rate (c.f. fig. 6.4) and implies a lower reliability of the curve adjustment. This low consistency is due to a large gap of 68 degrees. As for epoch IIIb the averaging possibly removed intrinsic variation in this epoch. In fig. 6.5 we show one data point of the non-averaged data as an open circle in the data gap. Based on the non-averaged data the consistency level is 4, consistent with the expectation at the observed average rotation rate. And both the averaged and non-averaged data yield the same shape of the adjusted curve. We thus conclude that the adjusted EVPA curve during epoch IIIc represents the intrinsic variation correctly with a probability of $\approx 98\,\%$. This large rotation was partially observed by Aleksić et al. (2014), who see only a $140\,^\circ$ rotation.

Epochs IVa and IVb show again an overall counter-clockwise trend with changing rotation rates, followed by a clockwise trend during epoch IVc. The high consistency (53, ∞, and 6, respectively), the low rotation amplitudes and rates suggests well sampling of the variation and a high probability that the adjusted curve represents the intrinsic variation correctly.

6.5 mm and cm EVPA variation of 3C 279

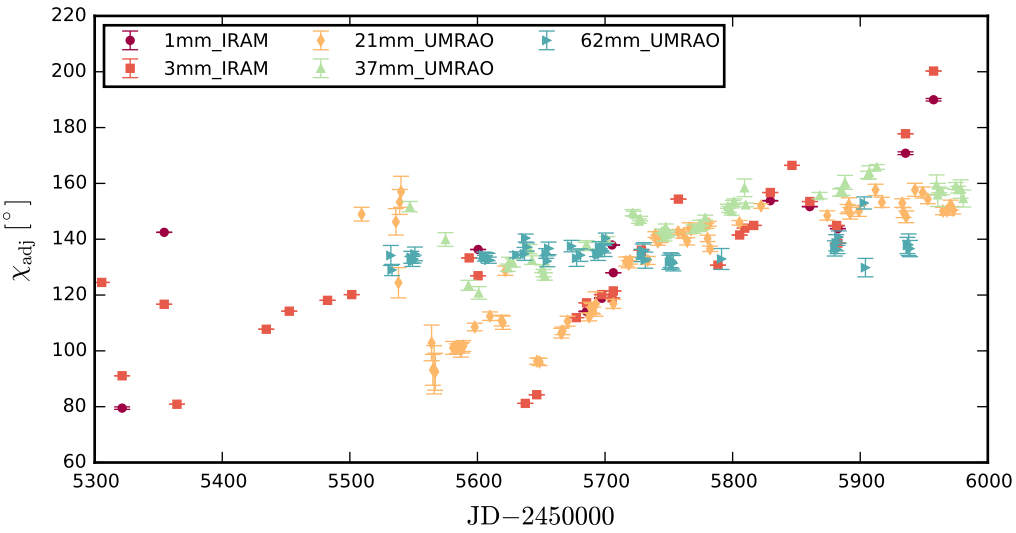

Figure 6.6: Electric vector position angle (EVPA) of 3C 279 at cm and mm wavelength.

Figure 6.6 shows the mm and cm adjusted EVPA curves. The 1 mm to 37 mm curves all show a counter-clockwise rotation trend starting roughly with the beginning of the optical $\sim 360\,^\circ$/d-rotation in epoch IIIc, consistent with the overall optical rotation trend. The rotation rate is decreasing with frequency down to an almost constant EVPA at 62 mm. With a mean time sampling between 7 days to 53 days the reliable reconstruction of the intrinsic variation is uncertain.

In fig. 6.7 we show the mm EVPA curves and the combined optical curve. Optical and mm EVPA roughly match until JD 2455710. The adjusted mm curves suggest a much slower rotation rate than in the optical after JD 2455710. On the other hand we show in fig. 6.7 (open symbols) that the mm curve can be adjusted manually to roughly match the optical EVPA curve. The overlapping data points in the mm curves and the optical combined curve are too few to justify this manual adjustment. But this case illustrates the importance of good time sampling to measure the intrinsic variation reliably given the $180\,^\circ$-ambiguity. The cm curves

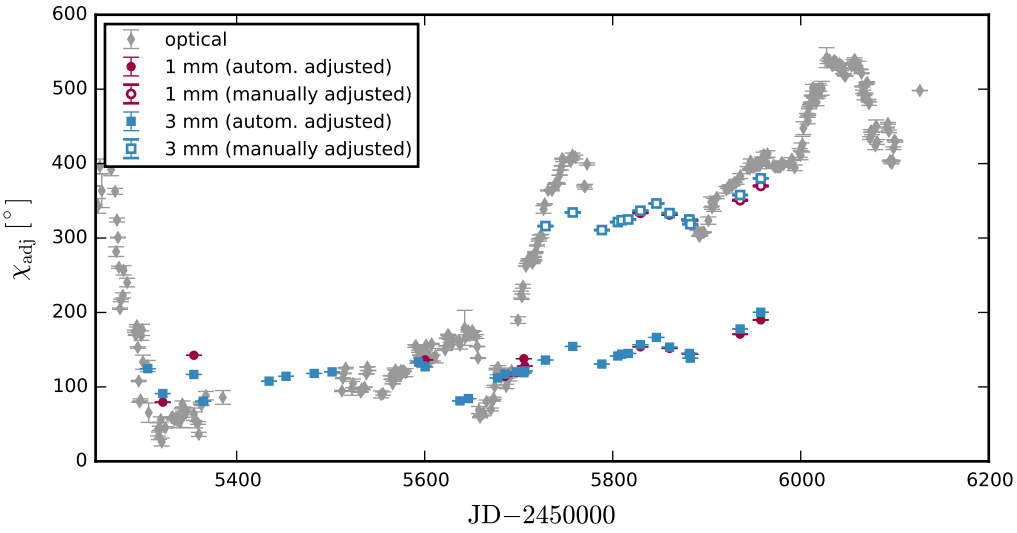

Figure 6.7: Automatically adjusted (filled symbols) and manually adjusted (open symbols) mm EVPA curves overlying the combined, adjusted optical curve.

cannot be adjusted to match the optical EVPA variation and the continuous trend with decreasing rate over the frequency range suggests that the measured curves correctly represent the intrinsic variation. The intrinsic mm variation is uncertain, it may (a) follow the optical variation or (b) continue the trend of increasing rotation rates with increasing frequency from cm to optical.

6.6 EVPA variation estimator

Inspecting the adjusted optical EVPA curve (fig. 6.5), some parts of the curve show a smoother variation (e.g., the 360 °-rotation in period IIIc and following) than other parts (e.g., the $> 500\,°$ rotation in period IIa). The apparent smoothness of an EVPA curve is used in the literature (e.g., Marscher et al., 2008) to argue against the stochastic origin of the EVPA rotation which is expected to produce more erratic variation of the polarization angle. In the following we introduce a quantitative measure of the smoothness of a curve. This measure is an essential part in our effort to discriminate stochastic from non-stochastic variation, which is discussed in chapter 7.

For an EVPA curve $\chi_i = \chi(t_i)$ we define the *relative point-to-point variation* in units of degrees per time unit:

$$\left(\frac{\Delta\chi}{\Delta t}\right)_i = \frac{\chi_i - \chi_{i-1}}{t_i - t_{i-1}}. \tag{6.21}$$

The mean of the point-to-point variation indicates a secular trend of the data:

$$\overline{\chi}_t = \langle(\Delta\chi/\Delta t)\rangle \tag{6.22}$$

The point-wise deviation of the point-to-point variation from the secular trend is calculated as:

$$s_i = \left(\frac{\Delta\chi}{\Delta t}\right)_i - \left\langle\left(\frac{\Delta\chi}{\Delta t}\right)\right\rangle . \tag{6.23}$$

Point-to-point variation at the order of the trend, $s_i \sim 0$, indicates smooth variation. Deviation of the point-to-point variation from the trend, $\pm s_i > 0$, indicates erratic variation, i.e. the curve is more jagged. We define the *variation estimator* as the absolute mean over s_i:

$$s = \langle |s_i| \rangle = \left\langle \left| \left(\frac{\Delta\chi}{\Delta t}\right)_i - \left\langle\left(\frac{\Delta\chi}{\Delta t}\right)\right\rangle \right| \right\rangle . \tag{6.24}$$

The variation estimator s is the *mean absolute deviation over the mean* of the *relative point-to-point variation* (eq. (6.21)). We use s as an estimator for the smoothness of a curve with respect to a potential linear trend. An EVPA curve with s_1 is considered *smoother* than a second curve with $s_2 > s_1$. The measured variation estimator is biased by measurement errors and curvature of the smooth EVPA variation. We discuss both biases in the following.

We point out that in our combined optical EVPA curve we have adjacent data points at very short time spacing down to 10 seconds due to the combination of multiple data sets with differences at the order of the error bars. These data point combinations may yield very high relative point-to-point variation and may artificially increase the variation estimator. Averaging out this variation (c.f. section 6.2) is therefore mandatory.

6.6.1 Error bias of the variation estimator

Measurement errors are not averaged out due to the absolute mean in eq. (6.24). The top panel of fig. 6.8 shows the variation estimator over the noise scale relative to the time sampling Δt. Each data point is averaged over 5 000 simulations, error bars indicate the standard deviation. Each simulation follows an intrinsic linear increase of the EVPA of arbitrary slope[13] over 100 data points sampled at $\Delta t = 1\,\mathrm{d}$. Gaussian noise of zero mean and the standard deviation given by the error scale σ_χ is added to each data point.

The average variation estimator s depends on the error scale σ_χ and the time sampling Δt through: $s = (1.13 \pm 0.1) \cdot \sigma_\chi / \Delta t$, estimated by a linear fit. This relation is shown by as a dashed line in fig. 6.8. The scattering around this mean value increases for larger relative error scales, indicated by the two dotted lines in fig. 6.8 following the upper and lower limit of the previous relation. The variation estimator inversely depends on the time sampling, because the point-to-point variation affected by measurement errors is calculated relative to the time step. Therefore the noise contribution is scaled up by shorter time steps. The lower panel of fig. 6.8 shows the distributions of the variation estimator at some of the tested noise scales for daily sampling. There is no dependency on the underlying rotation rate. Assuming homoscedastic errors σ_χ and even sampling Δt the error bias of the variation estimator can be estimated though:

$$s_{\mathrm{bias}} = (1.13 \pm 0.1) \cdot \frac{\sigma_\chi}{\Delta t} \tag{6.25}$$

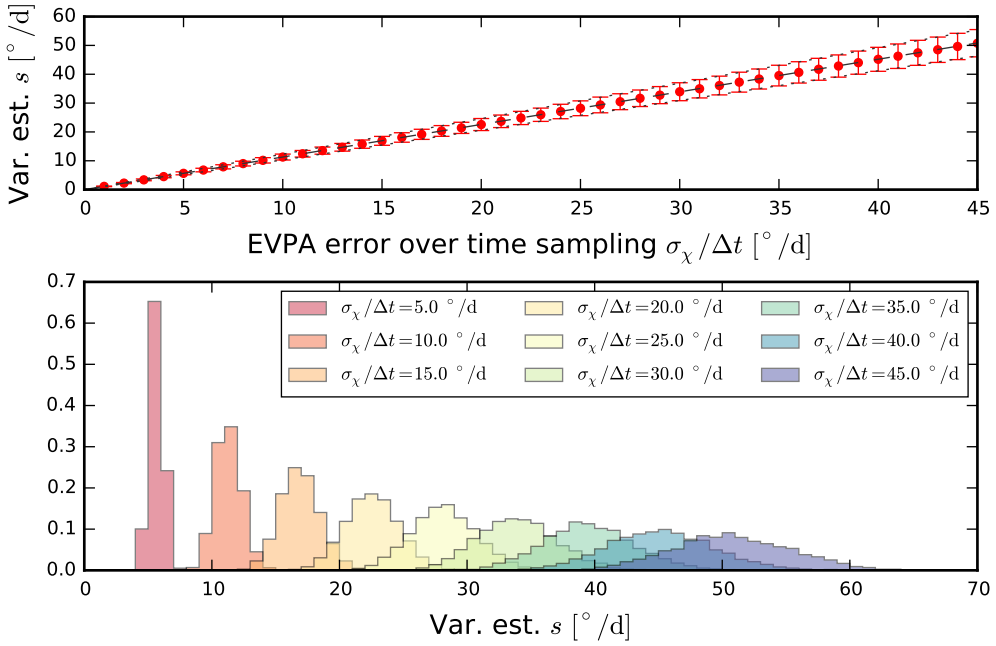

Figure 6.8: The upper panel shows the variation estimator bias over the error scale. Error bars indicate the standard deviation. Each data point is based on 5 000 simulations. The lower panel shows the distribution of the variation estimator for some of the tested error scales.

Assuming intrinsic erratic variation of the EVPA additionally to observational errors the total, observed variation estimator follows:

$$s_{\mathrm{tot}} = \sqrt{s_{\mathrm{intr}}^2 + s_{\mathrm{bias}}^2}, \tag{6.26}$$

where s_{intr} describes the erratic behaviour due to intrinsic variation and s_{bias} describes the observational noise bias which can be estimate through eq. (6.25) for homoscedastic errors. The de-biased variation estimator is an estimator of s_{intr}, s_{obs} is the variation estimator calculated from observed data:

$$s_{\mathrm{debiased}} = \sqrt{s_{\mathrm{obs}}^2 - s_{\mathrm{bias}}^2} \quad \text{for} \quad s_{\mathrm{obs}} > s_{\mathrm{bias}} \tag{6.27}$$

We test if de-biasing is also possible for heteroscedastic uncertainties and uneven sampling. We model the distribution of the uncertainties of the optical EVPA curve as a log-normal distribution $\mathcal{LN}(\mu_{\mathrm{unc}}, \sigma_{\mathrm{unc}})$ with $\mu_{\mathrm{unc}} = 0.4$ and $\sigma_{\mathrm{unc}} = 1.2$. The time steps are drawn from a truncated power-law distribution (eq. (6.20)) with minimum time step 0.5 d, maximum time step 21 d and power-law index -1.7. We simulate observational Gaussian noise $\mathcal{N}(0, \sigma_{\mathrm{err}})$ where σ_{err} is drawn from the log-normal distribution. We measure the secular trend and the variation estimator in 100 000 simulations. The results are shown in fig. 6.9. The trend is measured unbiased with a standard deviation of 0.2 $^\circ$/d. The mean variation estimator bias is:

$$s_{\mathrm{bias}} = 3.7 \pm 0.6\,^\circ/\mathrm{d}. \tag{6.28}$$

[13] Here we do not consider the 180 $^\circ$-ambiguity.

The uncertainty of the variation estimator bias is affected by the variance of the noise scale and the variance of the time steps. We notice that the distribution of the variation estimator is slightly right-tailed and de-biasing with the average bias may not remove the full effect of the observational noise on the variation estimator.

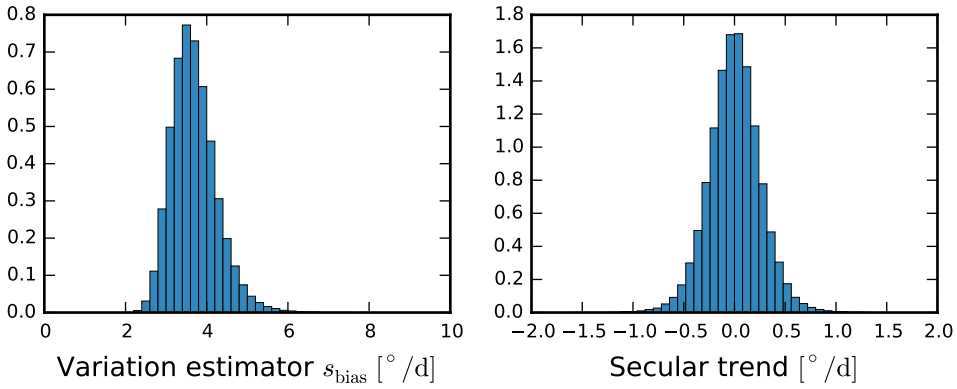

Figure 6.9: Variation estimator bias based on the observational error distribution of estimation (right panel).

To test if de-biasing is possible, we simulate intrinsic variation following a Gaussian distribution $\mathcal{N}(0, \sigma_{\mathrm{intr}})$ with the noise scale σ_{intr} drawn from a uniform distribution between 0 degrees and 45 degrees and add observational Gaussian noise as previously with the noise scales $\sigma_{i,\mathrm{err}}$ drawn from a log-normal distribution $\mathcal{LN}(\mu_{\mathrm{unc}}{=}0.4, \sigma_{\mathrm{unc}}{=}1.2)$:

$$\begin{aligned} \chi_{\mathrm{intr}}(t_i) &= \mathcal{N}(0, \sigma_{\mathrm{intr}}) \\ \chi_{\mathrm{obs}}(t_i) &= \chi_{\mathrm{intr}}(t_i) + \mathcal{N}(0, \sigma_{i,\mathrm{err}}). \end{aligned}$$

The time steps are randomly drawn from the same truncated power-law distribution as used to estimate the bias. We calculate again the variation estimator of the intrinsic and the observed variation curves, we use the estimated observational noise contribution of eq. (6.28) to de-bias. The results of 100 000 simulations are shown in fig. 6.10. Panel (b) shows that the variation estimator is not strongly affected by the observational noise contribution when the intrinsic variation estimator is $s_{\mathrm{intr}} \gtrsim 10\,^\circ/\mathrm{d}$. The observational noise contributes significantly when the intrinsic variation is smaller. This contribution can be removed with de-biasing although the scatter of the de-biased variation estimator remains slightly larger at $s_{\mathrm{intr}} \gtrsim 5\,^\circ/\mathrm{d}$ than at larger intrinsic variation as panel (c) in fig. 6.10 shows. The histogram of the difference between the intrinsic and the de-biased variation estimator peaks at $-0.4\,^\circ/\mathrm{d}$ and is slightly left-tailed, indicating that the de-biased variation estimator on average is still larger than the intrinsic one, as expected for a Ricean bias. De-biasing improves the accuracy of estimating the intrinsic variation estimator, but it does not fully remove the error bias in the case of uneven sampling and heteroscedastic uncertainties. The distribution standard deviation is $0.6\,^\circ/\mathrm{d}$ equal to the uncertainty of the bias (c.f. eq. (6.28)). We point out that the derived bias is valid only for the uncertainty distribution of our observed, optical EVPA curve and the corresponding sampling. It has to be estimated anew for different uncertainty and time step distributions.

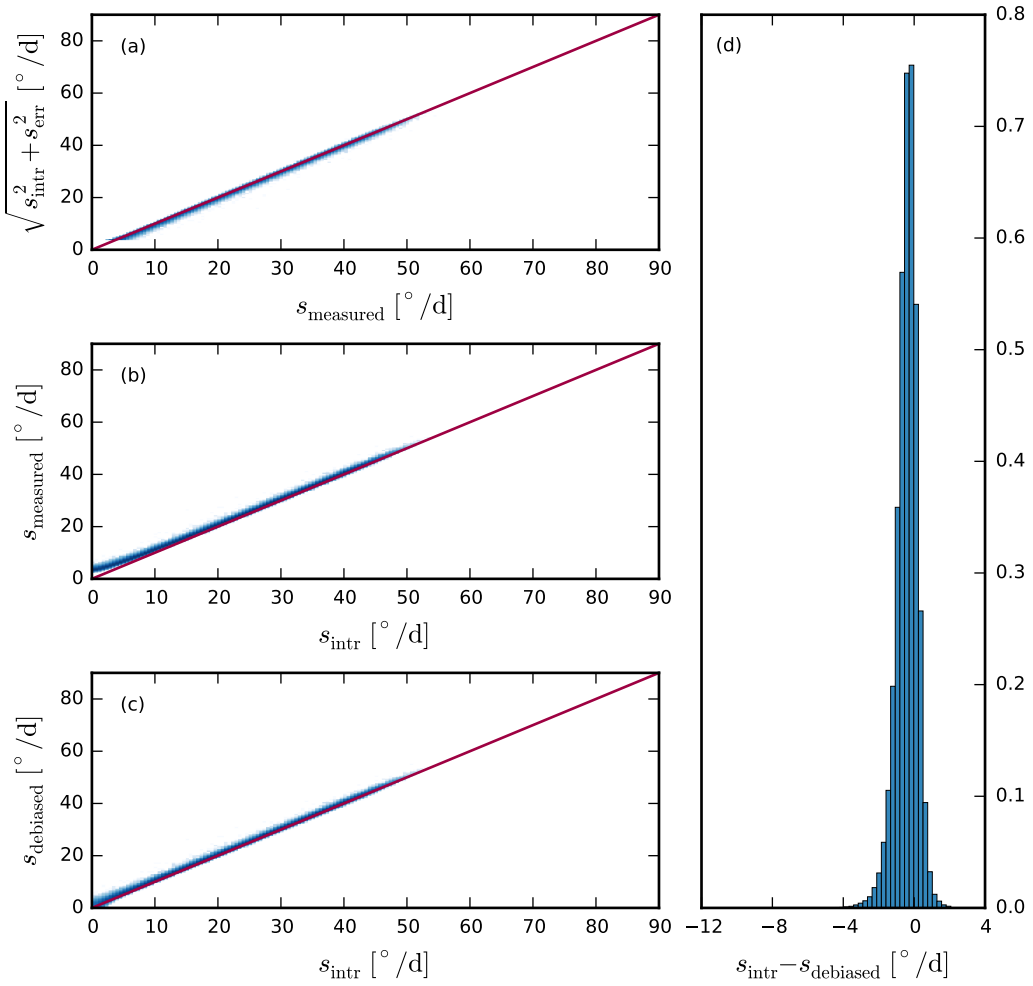

Figure 6.10: Panels (a)-(c) show 2d-histograms of various combinations of the intrinsic, observed and de-biased variation estimator based on simulations with heteroscedastic errors. Solid red lines mark the diagonal. Panel (d) shows the distribution of the difference between the intrinsic and the de-biased variation estimator.

6.6.2 Curvature bias of the variation estimator

The point-to-point variation is corrected for first order rotations, i.e. constant rotation rates (c.f. eqs. (6.21) and (6.23)). The secular trend $\bar{\chi}_t$, i.e the mean of the point-to-point variation estimates the constant rotation rate. This trend is considered intrinsic, non-erratic variation and subtracted from the point-to-point variation. Following this definition the variation estimator is zero for constant rotation rates. For higher order (i.e. curved) rotation curves the variation estimator is biased. To test the dependency of the bias on the curvature we simulate EVPA curves that follow a power-law over time without observational or intrinsic noise contribution:

$$\chi(t_i) = \chi_{\rm max}\left(\frac{t}{T}\right)^{\alpha}. \tag{6.29}$$

with power-law index $\alpha \geq 1$. The EVPA value $\chi_{\rm max}$ at time $t_i = T$ equals the total rotation amplitude $\Delta\chi = \chi(T) - \chi(0)$ over the full time interval T. Example curves for $\alpha = 1, 2, \cdots, 10$ are shown in the upper panel of fig. 6.11.

We define the total rotation rate as $\delta\chi \cdot T^{-1}$ and estimate it through the trend:

$$\frac{\Delta\chi}{T} = \frac{\chi_{\max}}{T} \approx \overline{\chi}_t \tag{6.30}$$

The curvature bias of the variation estimator is given by the product of the curvature factor f_s and the total rotation rate:

$$s_{\text{bias}} = f_s \cdot \frac{\Delta\chi}{T} \approx f_s \cdot \overline{\chi}_t. \tag{6.31}$$

The curvature factor f_s is derived from simulations and plotted in the lower panel of fig. 6.11. For instance a 360 degrees rotation over 100 days following a quadratic increase introduces a curvature bias of 1.8 degrees per day. To correct the variation estimator for higher order variation fitting the EVPA curve and subtracting the fit from the point-to-point variation is necessary. The a priori set highest order of the fitting function represents a threshold to the order of variation which is considered smooth and which is considered erratic variation. To avoid a subjective and arbitrary choice we use the lowest order, considering a linear trend as smooth variation. Any deviation from that trend contributes to the variation estimator.

One possible improvement would be to measure the variation estimator for sequential time intervals treating curved variation as a sequence of (approximately) linear variation at the time scale of the data chunks but with changing rates at larger time scales. This approach requires, first, sufficient sampling of the time chunks and, second, the definition of a time scale threshold. Variation on time scales larger than this threshold would be considered smooth variation, variation on smaller time scales erratic variation. Comparable to the choice of the order of a fitting function the a priori selection of this threshold is arbitrary.

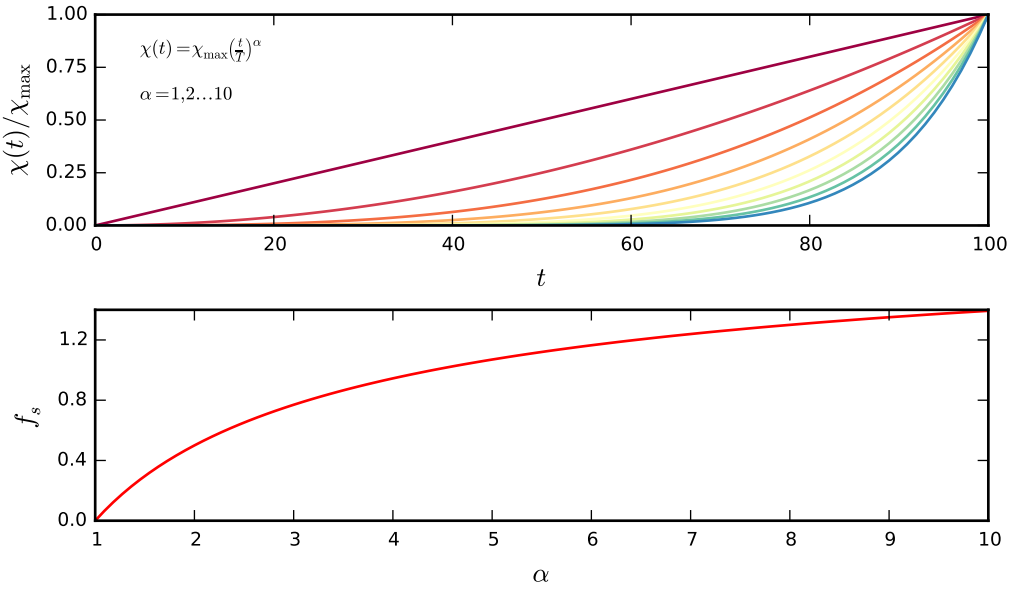

Figure 6.11: The upper panel shows exemplary power-law curves with increasing curvature, i.e. power-law index α from 1 (red) to 10 (blue). The lower panel shows the curvature factor (see text for description).

The variation estimator is applied to our polarization data in section 6.8.

6.7 EVPA rotation identification

The optical EVPA curve of 3C 279 exhibits variation with changing rates over time, including variation of the sign of rotation, i.e. the direction of the rotation. To characterize the continuous variation over larger time scales and multiple data point, we need a formal definition of a *rotation*[14]. Continuous rotations reported in the literature are usually identified on the loose criterion of following an overall trend (e.g. Larionov et al., 2008; Abdo et al., 2010a; Hayashida et al., 2012). This trend may be restricted by the rotation direction or a limited range of the rotation rate. Whereas we have subdivided our optical polarization data into different periods in section 6.4 based loosely on the overall EVPA trend, too, here we are going to introduce a distinct definition of a *rotation* and implement a set of distinct rules to identify parts of the EVPA curves which agree with our definition.

We define an EVPA rotation as a *continuous, significant variation of the EVPA with consistent direction.* This definition implies that a rotation ends when the direction changes. In the following section we define an algorithm to identify rotation events base on this definition incorporating the uncertainties of the data.

6.7.1 Rotation identification algorithm

The algorithm identifies significant rotations by iterating point-wise through the data. The difference of the current iteration step is $\Delta\chi_{\mathrm{curr}} = \chi_i - \chi_{i-1}$. The difference is considered significant, if

$$|\Delta\chi_{\mathrm{curr}}| > \varsigma \cdot \sqrt{\sigma^2_{\chi_i} + \sigma^2_{\chi_{i-1}}}, \tag{6.32}$$

where σ_{χ_i}, $\sigma_{\chi_{i-1}}$ are the corresponding uncertainties and ς is a factor that characterizes the significance level at which the difference is considered significant. For a subset of data points $[\chi_j, \ldots, \chi_{j+N}]$ identified as rotation the *amplitude* is given by the difference of the two (local) extrema (χ_{min}, χ_{max}). Accordingly, the amplitude is considered significant if

$$|\Delta\chi_{\mathrm{rot}}| > \varsigma \cdot \sqrt{\sigma^2_{\chi_{\mathrm{min}}} + \sigma^2_{\chi_{\mathrm{max}}}}, \tag{6.33}$$

where $\sigma_{\chi_{\mathrm{min}}}$, $\sigma_{\chi_{\mathrm{max}}}$ are the uncertainties of the two (local) extrema.

Table 6.4 gives an overview of the different states that can occur at each iteration step and the corresponding operations. A *storage* is set up that contains all found, significant EVPA rotations. This storage contains both the amplitudes and the first and last data point index for all found rotations. Operations on this storage are described in table 6.4, col. 6. The *current rotation* is an interval of data points starting at the end of the last significant rotation and ending at the data point previous to the current. Information about the current rotation consists of the rotation amplitude and direction, which are determined from the minimum and maximum in this interval, and the significance. Operations on the current rotation are described in table 6.4, col. 7, operations on the significance in table 6.4, col. 8.

The operations depend on the states of the current rotation and the *new rotation.* The new rotation is the change of the EVPA between the data point of the current

[14]The terms *(EVPA) rotation (event)*, *EVPA swing* or *polarization swing* are common in the literature and we use them synonymously.

iteration step and the previous data point. The state is defined by the significance of the current rotation (table 6.4, col. 1), the significance of the new rotation (table 6.4, col. 2) and whether the current rotation direction is continued or changes (table 6.4, col. 4). In the case of a current insignificant rotation an additional state description is needed, which describes whether or not the current rotation interval with the new data point added becomes significant (table 6.4, col. 3) and if so how this rotation is oriented with regard to the previous significant rotation that was stored (table 6.4, col. 5). In table 6.4 significance and insignificance are denoted by "Y" or "N". A continued rotation is denoted by "+" and change of the rotation direction is denoted by "-". Ten different states may occur during the iteration through the data. Those are described in the following.

State 1: YY+ A currently significant rotation is continued with a significant rotation. *Operation:* The new data point is added to the current interval.

State 2: YY- A currently significant rotation is followed by a significant rotation with changed direction. *Operation:* The current rotation is stored. The new rotation is set as the current rotation.

State 3: YN+ A currently significant rotation is continued by an insignificant rotation. *Operation:* The new data point is added to the current interval.

State 4: YN- A currently significant rotation is followed by an insignificant rotation with changed direction. *Operation:* The current rotation is stored. The new rotation is set as the current rotation. The significance of the current rotation is set to "N".

State 5: NNN+/- The currently insignificant rotation is followed by an insignificant rotation with either the same or opposite direction. The combined rotation is not significant. *Operation:* The new data point is added to the current interval.

State 6: NNY+ The currently insignificant rotation is followed by an insignificant rotation. The combined rotation is significant and has the same direction as the latest, stored rotation. *Operation:* The latest, stored rotation is taken from the storage. The current rotation interval is set to the combination of the previously stored rotation and the now significant current rotation including the new data point. The amplitude and direction is derived from the extrema of this newly set current rotation interval. The current rotation significance is set to "Y".

State 7: NNY- The currently insignificant rotation is followed by an insignificant rotation. The combined rotation is significant and has changed the direction with respect to the previously stored rotation. *Operation:* If the previously stored rotation had a positive sign the data points up the maximum of the current rotation interval are added to the stored rotation. The current rotation is set to start at the same maximum and to end at the new data point. If the previously stored rotation had a positive sign the same procedure is used with the minimum instead of the maximum. The current rotation significance is set to "Y".

State 8: NY++ The currently insignificant rotation is followed by a significant rotation. The previously stored, the current and the new rotation all have

the same direction. *Operation:* The latest, stored rotation is taken from the storage. The current rotation interval is set to start with the previously stored rotation up to the new data point. The current rotation significance is set to "Y".

State 9: NY− The currently insignificant rotation is followed by a significant rotation. The previously stored and the new rotation have the same direction, while the current, insignificant rotation in between had the opposite direction. *Note:* The insignificant counter-rotation in between is not considered a break of the total rotation starting with the previously stored rotation and continued with the new rotation. This total rotation is evaluated as a continuous rotation. The duration of the insignificant interval in between is not considered. This might be a critical part in the algorithm. *Operation:* The same as for state 8.

State 10: NY+-/-+ The currently insignificant rotation is followed by a significant rotation. The direction has changed during the insignificant rotation interval. *Operation:* The same as for state 7.

This scheme identifies the local maxima and minima in an EVPA curve at a user-defined significance-level. All data in between two adjacent extrema are considered a continuous rotation. Insignificant rotation intervals may be part of an identified significant rotation and may even lead or end the rotation. Saddle points are not identified by this scheme (c.f. state 9).

6.7.2 Testing the rotation identification

We test the rotation identification algorithm on an arbitrary curve with multiple local extrema. The intrinsic curve is shown as a solid line in fig. 6.12, with two colours marking the ranges between the local extrema. The curve contains 11 rotations. We sample the intrinsic curve at random points $y_i(x_i)$ and add random Gaussian noise $\mathcal{N}(0, \sigma_i)$ to each data point with σ_i drawn from a log-normal distribution $\mathcal{LN}(0.4, 1.2)$, yielding heteroscedastic uncertainties. The sampled, error affected curve is shown by grey data points with corresponding error bars. We identify rotations at three different significance levels $\varsigma = 1, 2, 3$. At the three significance levels 29, 14 and 10 rotations are identified, respectively. Each identified rotation is shown in fig. 6.12 in either green or red data points.

The identification strongly depends on the choice of the significance level ς. With higher ς smaller variation is considered significant and fewer rotations are identified. Setting ς too low will over-estimate the number of intrinsic rotations, setting it too high will under-estimate the number of rotations. The optimal choice of ς depends on the intrinsic variation rate and the noise scale. Too subtle intrinsic variation is not considered significant, strongly outlying data points (possibly with under-estimated uncertainties) wrongly introduce significant variation. We suggest either to determine an optimal significance level from simulations or to use various significance levels for comparison. Even if the data does not allow to identify the intrinsic rotations the algorithm presented here allows to study the distribution of rotations (e.g. the number, duration or amplitude of rotations) as it identifies rotations on strict criteria considering only the data and the corresponding uncertainties without any model assumptions.

We apply the rotation identification to our polarization data in section 6.8.

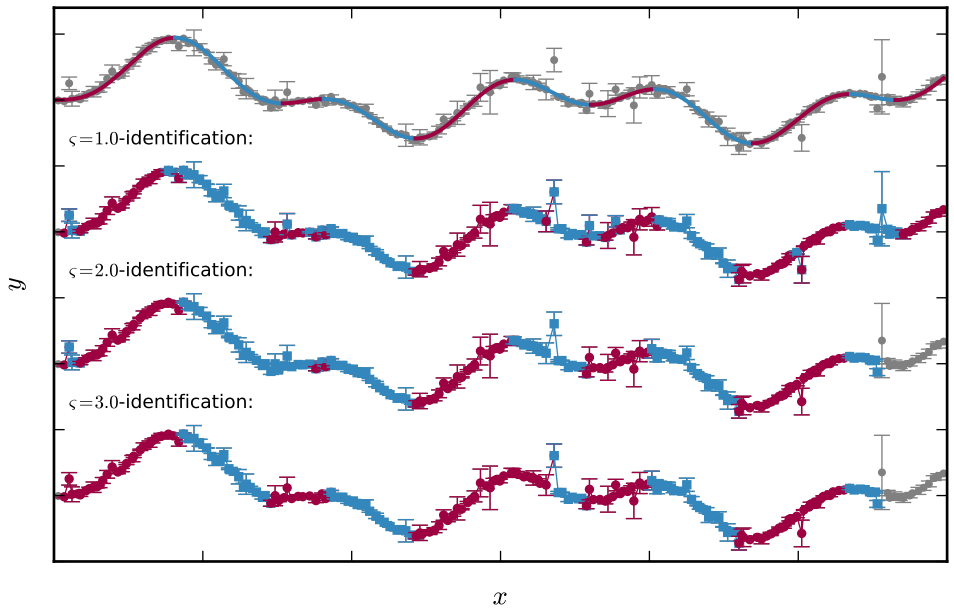

Figure 6.12: The solid two-coloured line shows an arbitrary curve. The two colours mark the ranges between local extrema. Gray data points follow the intrinsic solid curve with additional heteroscedastic Gaussian noise. The three lower curves show the identification of significant rotations (marked in two colours) at different significance levels. The curves are set off for clarity.

6.8 Polarization properties of 3C 279

We characterize the optical polarization and the variation of the polarization of 3C 279 in the time of JD 2454700 − 2455150 measuring the mean and standard deviation of the polarization fraction, the total amplitudes and durations of general EVPA rotation trends and the EVPA variation estimator (c.f. section 6.6) for the full data, the individual observation periods (I, II, III, IV) and the sub-periods identified in section 6.4 based on the general rotation trends. The results are summarized in table 6.5. We point out that period IIIb consists of only 6 data points. The actual uncertainties due to the low number statistics for any parameter estimation may not be correctly represented by the error bars. Especially the variation estimator is highly over-estimated due to the sparse, uneven sampling of the fast rotation. Therefore, we do not include period IIIb in the following discussion. The period selection, optical polarization fraction, combined measured and adjusted EVPA and the EVPA point-to-point variation (c.f. eq. (6.21)) are shown in fig. 6.13.

The mean optical polarization fraction is $11.7 \pm 0.3\,\%$. Between the different periods it varies from 5 % to 18 %. The standard deviation of the optical polarization fraction varies from 3 % to 10 %, lying at $7.9 \pm 0.2\,\%$ for the full data. All measurements are based on the de-biased polarization fraction. The uncertainties are estimated with a bootstrap method. For N data points we randomly draw N integers uniformly from $\mathcal{U}_{\mathrm{int}}(1, N)$ and remove the duplicates. We select the corresponding data points, leaving approximately $1 - \mathrm{e}^{-1} \approx 0.63\,\%$ of the data, and measure the wanted property. After 10 000 iterations the standard deviation of the parameter distribution is used as estimate of the uncertainty.

We measure the EVPA variation estimator, introduced in section 6.6, for all periods and the full data set. The full data set and the observation periods (I, II,

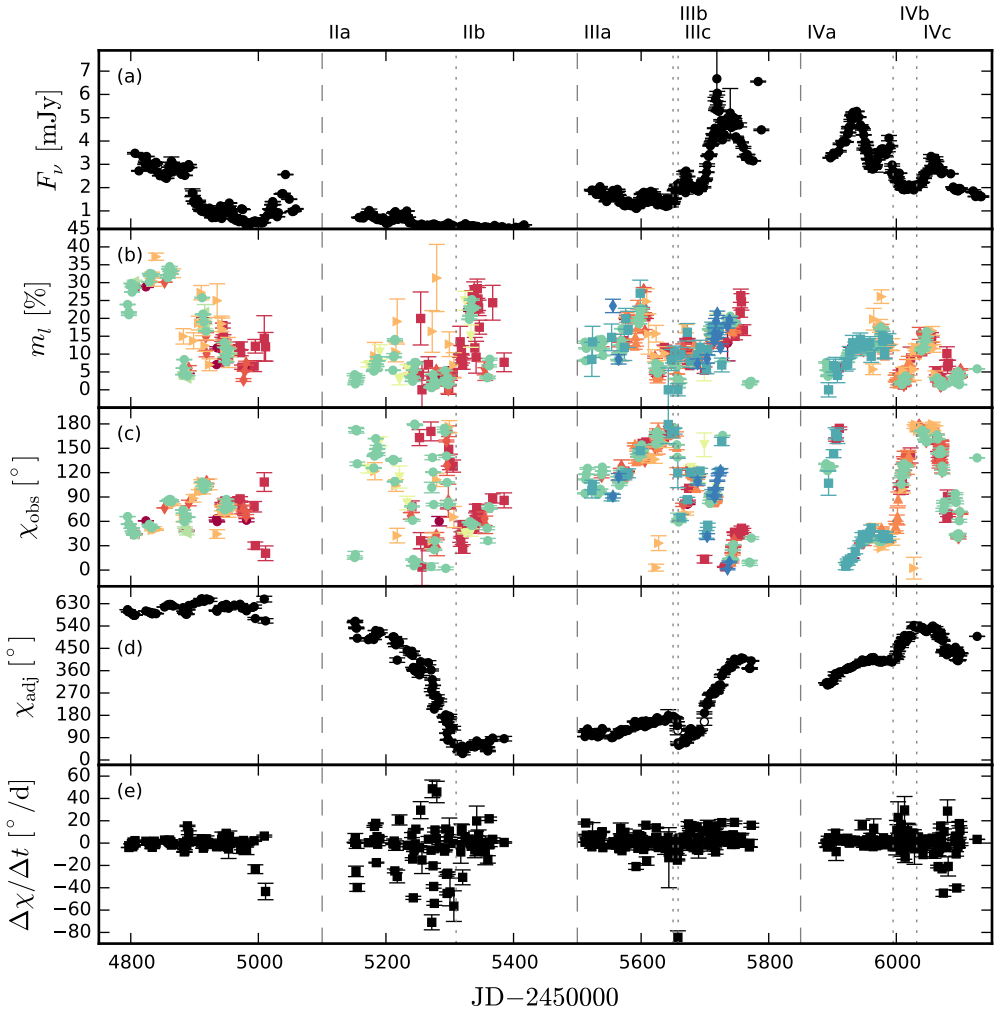

Figure 6.13: Optical flux and polarization of 3C 279. Combined R-band light curve (panel a); combined optical de-biased polarization fraction (panel b) and measured EVPA (panel c), red circles: Calar Alto (R), Red squares: CrAO-70cm (R), red diamonds: Perkins (R), orange up-sided triangles: SPM (R), orange right-sided triangles: St. Petersburg (R), green down-sided triangles: Kanata (V), green left-sided triangles: Steward Obs. (V), blue circles: Steward Obs. (spec.), blue squares: Liverpool (V+R), blue diamonds: KVA (white light); combined, adjusted EVPA (panel d), and EVPA point-to-point variation (panel e).

III, IV) all contain two or more sub-periods with a different general rotation trend and direction. Thus, the global average trend (eq. (6.22)), which the variation estimator is corrected for, does not represent the local trends. Therefore, the variation estimator is increased by the curvature bias (c.f. section 6.6.2). A better estimate is given by the variation estimators of the sub-periods (IIa to IVc). Those periods are chosen based on a general trend and reasonably minimize the curvature bias. We correct all variation estimators for the error bias following eq. (6.27). The error bias is estimated following the method used to attain eq. (6.28). We estimate the bias for each observation period individually to account for different time sampling and different uncertainty distributions.

Estimating the error bias from simulations requires to model the time sampling and the EVPA uncertainties. The distribution of the time steps $\Delta t_i = t_i - t_{i-1}$ is modelled as a truncated power-law (c.f. eq. (6.20)). The model parameters are shown

in table 6.6 for each observation period. The distribution of the EVPA uncertainties is bimodal with a sharp peak at $\approx 0.14\,^\circ$, whereas all higher uncertainties can be described by a log-normal distribution. The low uncertainties all correspond to the spectropolarimetry data observed at Steward Observatory and are probably underestimated. We estimate the log-normal distribution parameters from the observed distribution ignoring all uncertainties below $0.14\,^\circ$ and model the uncertainties as a plain log-normal distribution with the attained parameters. Thus a fraction of the observed very low uncertainties is not included in the simulation. The log-normal distribution parameters are listed in table 6.7.

We do not estimate the bias for each sub-period as those contain too few data points to reliably estimate the time sampling and the EVPA uncertainty distribution parameters. We de-bias the variation estimator of each sub-period with the bias derived for the corresponding observation period.

The de-biased variation estimator ranges from variation at the order of the error bias (period IVa), indicating a smoothly in- or decreasing curve with little or no intrinsic erratic behaviour, up to $18.3 \pm 1.3\,^\circ$/d (period IIa). Differences in the variation estimator of various periods are consistent with the impression that some periods show more erratic variation (e.g., period IIa) and others exhibit very smooth curves (e.g., period IIIc). The variation estimator successfully quantifies the smoothness of the EVPA curve. The highly erratic variation during period IIa regarding to the other periods becomes especially obvious in the plot of the relativ point-to-point variation of the EVPA curve (c.f. eq. (6.21)) in fig. 6.13, panel (e). The scatter, which is measured by the variation estimator, is the highest in period IIa.

The variation of both, the polarization fraction and the polarization angle, changes over time. In fig. 6.14 we plot the EVPA variation estimator of all sub-periods over the mean polarization fraction $\langle m_l \rangle$ (left panel), the polarization fraction standard deviation $\sigma(m_l)$ (mid panel) and the ratio of standard deviation and mean $\sigma(m_l)/\langle m_l \rangle$ (right panel). There is no correlation between the variation estimator and the mean or standard deviation of the polarization fraction, but an increase in the polarization fraction variation relative to the mean polarization fraction coincides with an increase of the erratic EVPA variability with a correlation coefficient of 0.8.

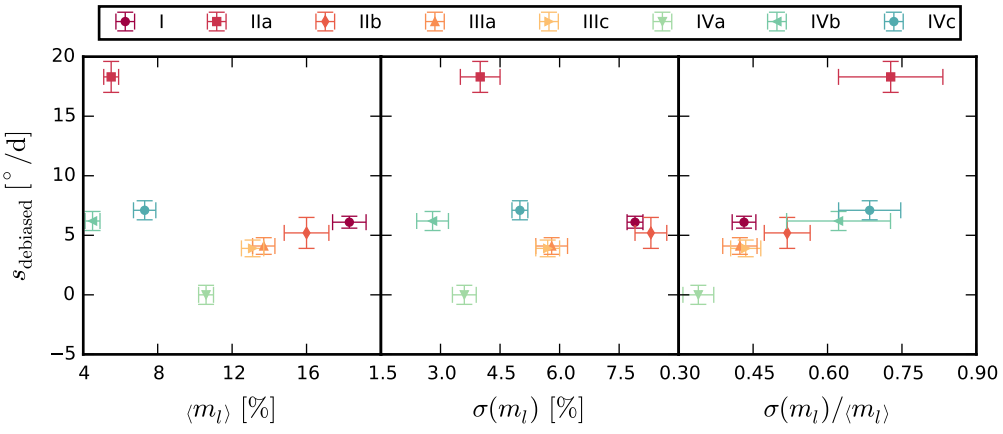

Figure 6.14: The EVPA variation estimator plotted over the polarization fraction mean (left panel), standard deviation (mid panel) and the ratio of standard deviation to mean polarization fraction (right panel).

We identify EVPA rotations, following the definition in section 6.7, in the combined optical curve using the algorithm introduced in section 6.7.1. In fig. 6.15 we show the rotations identified at a 3σ significance level ($\varsigma = 3$). Continuous rotations are shown in one colour, with a colour change when a new rotation with opposite rotation direction starts. Only in the periods IIIb and IVb a single rotation is identified. Otherwise multiple rotations are found. We calculate the relative number of rotations per 100 days for each period and plot it over the EVPA variation estimator in fig. 6.16. There is no correlation between the EVPA variation estimator and the relative number of rotations. Therefore, we cannot identify periods of more erratic variation based on the relative number of identified rotations.

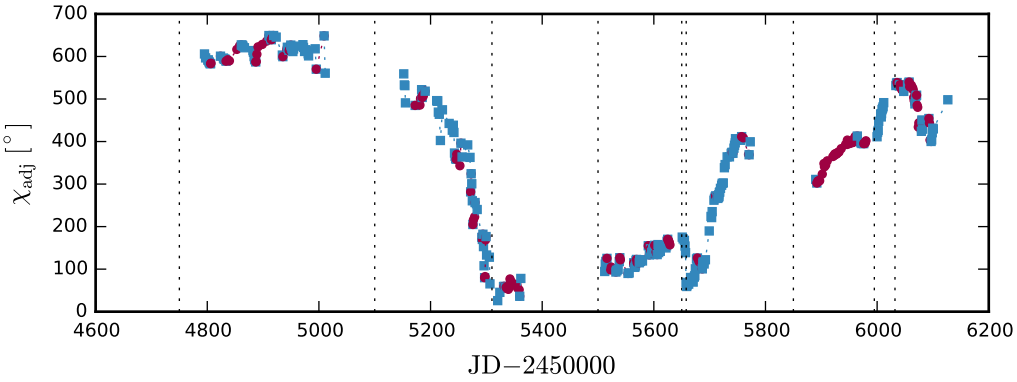

Figure 6.15: Combined optical EVPA curve of 3C 279. The two colours mark continuous rotations identified at a 3σ significance level. A change of the colour marks a significant change of the rotation direction.

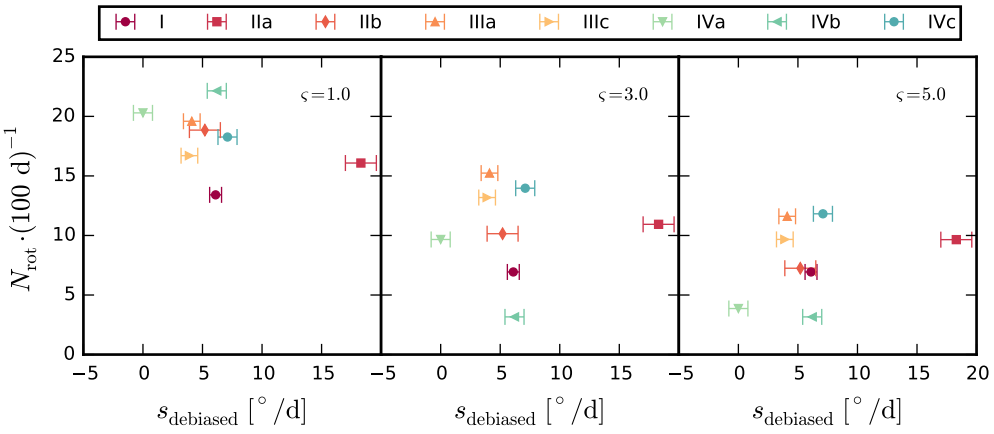

Figure 6.16: Relative number of continuous rotations per 100 days identified at three different significance levels (left panel: 1σ, mid panel: 2σ, right panel: 3σ) plotted over the de-biased EVPA variation estimator.

The mean and standard deviation of the polarization fraction at the combined optical, mm and cm frequency ranges from JD 2455500 to JD 2455995 are listed in table 6.8. The variation decreases with decreasing frequency, consistent with the flattening of the total EVPA variation observed over this frequency range. The average polarization fraction decreases from optical over the mm range to 2.1 cm wavelength and gradually increases again for larger wavelengths. The increase of

the polarization fraction from 21 mm to 62 mm could imply that we start to observe the optically thin emission of the radio jet at these wavelengths but the dependency of the polarization fraction on the wavelength at radio frequencies would require a more thorough study to draw conclusive results.

In chapter 7 we introduce a class of stochastic processes which are capable of producing EVPA variation and test whether the large rotation trends in the optical EVPA curve during period IIa and period IIIc can be explained by those processes.

Table 6.4: Description of the occurring states and the corresponding operations for the EVPA rotation identification.

	State					Do		
	Current rotation significance	New rotation significance	Insign. rotation becoming significant	Rotation direction current/ new	Rotation direction stored/ current	Store rotation	Set current rotation	Set current rotation significance
1.	Y	Y		+			current+new	Y
2.	Y	Y		-		current	new	Y
3.	Y	N		+			current+new	Y
4.	Y	N		-		current	new	N
5.	N	N	N	+/-			current+new	N
6.	N	N	Y		+	delete last entry	stored+min/max (current+new)	Y
7.	N	N	Y		-	stored+min/max (current)	min/max (current)+new	Y
8.	N	Y		+	+	delete last entry	stored+current +new	Y
9.	N	Y		-	-	delete last entry	stored+current +new	Y
10.	N	Y		+/-	-/+	stored+min/max (current)	min/max (current)+new	Y

Table 6.5: Optical polarization characteristics of 3C 279 for different periods (col. 1): mean and standard deviation of the polarization fraction (col. 2, 3), rotation amplitude over rotation duration (col. 4), total (col. 5) and debiased (col. 6) EVPA variation estimator, and variation estimator bias (col. 7).

Period	$\langle m_l \rangle$ [%]	$\sigma(m_l)$ [%]	$\Delta\chi/\Delta t$ [°/d]	s [°/d]	s_{debiased} [°/d]	s_{bias} [°/d]
tot	11.7 ± 0.3	7.9 ± 0.2		7.1	6.1 ± 0.5	3.7 ± 0.5
I	18.3 ± 0.9	10.4 ± 0.4		3.7	2.6 ± 1.0	2.7 ± 1.0
II	9.1 ± 0.6	7.7 ± 0.5		14.6	14.0 ± 1.3	4.0 ± 1.3
III	13.1 ± 0.4	5.9 ± 0.2		5.8	5.0 ± 0.7	2.8 ± 0.7
IV	8.1 ± 0.3	4.7 ± 0.2		5.5	4.2 ± 0.8	3.5 ± 0.8
IIa	5.5 ± 0.4	4.0 ± 0.5	$-494/154$	18.7	18.3 ± 1.3	4.0 ± 1.3
IIb	16.0 ± 1.2	8.3 ± 0.4	$62/47$	6.6	5.2 ± 1.3	4.0 ± 1.3
IIIa	13.7 ± 0.6	5.8 ± 0.4	$89/89$	5.0	4.1 ± 0.7	2.8 ± 0.7
IIIb	6.0 ± 1.1	3.2 ± 0.8	$-106/7$	24.6	24.5 ± 0.7	2.8 ± 0.7
IIIc	13.1 ± 0.6	5.7 ± 0.3	$352/98$	4.8	3.9 ± 0.7	2.8 ± 0.7
IVa	10.6 ± 0.4	3.46 ± 0.3	$110/73$	2.4	≈ 0	3.5 ± 0.8
IVb	4.5 ± 0.4	2.8 ± 0.4	$131/28$	7.1	6.2 ± 0.8	3.5 ± 0.8
IVc	7.3 ± 0.6	5.0 ± 0.2	$-140/39$	8.0	7.1 ± 0.8	3.5 ± 0.8

Table 6.6: Truncated power-law distribution parameters modeling the random time steps.

Period	α_t	Δt_{min} [d]	Δt_{max} [d]
tot	-1.7	0.5	21.0
I	-1.6	0.5	18.0
II	-1.9	0.7	21.0
III	-1.8	0.5	14.0
IV	-1.8	0.5	11.0

Table 6.7: Log-normal distribution parameters modelling the random EVPA uncertainties.

Period	μ_{unc}	σ_{unc}
tot	0.4	1.2
I	0.1	1.2
II	0.7	1.2
III	0.2	1.1
IV	0.4	1.1

Table 6.8: Polarization fraction mean (col. 2) and standard deviation (col. 3) of 3C 279 between JD2455500 and JD2455995.

Frequency	$\langle m_l \rangle$	$\sigma(m_l)$
Opt	12.3 ± 0.3	5.4 ± 0.2
1 mm	5.5 ± 0.6	2.3 ± 0.6
3 mm	4.6 ± 0.3	1.5 ± 0.2
21 mm	2.9 ± 0.1	1.2 ± 0.1
37 mm	4.0 ± 0.1	1.1 ± 0.1
62 mm	5.3 ± 0.1	0.6 ± 0.1

Chapter 7

Random walk polarization model

Stochastic processes as origin for polarization angle swings have been discussed since the 1980s. Jones et al. (1985) introduced the concept of an Electric Vector Position Angle (EVPA) random walk, which was discussed in the context of various observed EVPA swings (e.g. D'Arcangelo et al., 2007; Marscher et al., 2010). More recently, models like the Turbulent, Extreme Multi-Zone Model (TEMZ) (Marscher, 2014) build upon the same idea of a jet containing of multiple cells which vary due to a stochastic process.

In this chapter we introduce three random walk processes based on Jones et al. (1985). In section 7.2 we discuss the possible and most likely realizations of observable parameters for these models, how these observables depend on the model input parameters and on one another. Expectation values for the polarization fraction mean and standard deviation are presented in section 7.3. We test the models against the two major EVPA rotation events in our data and present the results in section 7.4. We summarize and interpret the results in section 7.6.

7.1 Definition of the random walk models

To simulate the stochastic variation of the polarization parameters, EVPA and linear polarization fraction, we perform random walks in the Stokes parameters I, Q, and U. The model consists of N_{cells} cells. The *variation rate* n_{var} sets the number of cells that change their properties per unit time step. We randomize the time sampling of the simulations to match the sampling of our observed data and include the simulation of EVPA measurement uncertainties. We define several random walk processes that differ in the properties of the cells and in how one selects the cells which are to be changed.

7.1.1 Randomized time sampling

The simulation time steps $\Delta t_i = t_i - t_{i-1}$ are drawn from a truncated power-law distribution (eq. (6.20)) with power-law index $\alpha_t < -1$, minimum time step Δt_{min} and maximum time step Δt_{max}. The parameters are derived from the observed data and described in table 6.6. The simulation times

$$t_i = t_0 + \sum_{j=1}^{i} \Delta t_j \tag{7.1}$$

for $i \geq 1$ are produced iteratively until the total simulation time T is reached after $N-1$ time steps with N data points such that $t_N - t_0 \leq T$ and $t_{N+1} - t_0 > T$. t_0 is generally set to zero.

7.1.2 Simple Q, U random walk process

The simple Q, U random walk process (siQU) models random polarization variation in a turbulent medium. The model consists of N_{cells} initial cells. All cells have uniform intensity I_i and each cell has a uniform but randomly oriented magnetic field, i.e. randomly oriented EVPA. The uniform magnetic field implies that each cell is maximally polarized. The polarization fraction $m_{l,\max}$ of synchrotron radiation in a uniform magnetic field is determined by the power-law index of the electron energy distribution p (Longair, 2011, p. 217):

$$m_{l,\max} = \frac{p-1}{p-\frac{7}{3}}. \tag{7.2}$$

For $p = 2.5$ (Longair, 2011, p. 217) the maximum polarization is $m_{l,\max} \approx 72\,\%$. For each cell $i = 1 \ldots N_{\text{cells}}$ the initial random variables q_i and u_i are drawn from a Gaussian distribution and normalized to obtain the Stokes parameters Q_i, U_i:

$$q_i = \mathcal{N}(0,1) \tag{7.3}$$
$$u_i = \mathcal{N}(0,1) \tag{7.4}$$
$$I_i = \frac{I}{N_{\text{cells}}} = \text{const} \tag{7.5}$$
$$Q_i = \frac{q_i}{\sqrt{q_i^2 + u_i^2}} \cdot I_i \cdot m_{l,\max} \tag{7.6}$$
$$U_i = \frac{u_i}{\sqrt{q_i^2 + u_i^2}} \cdot I_i \cdot m_{l,\max}. \tag{7.7}$$

The uniform intensities of the cells are set such that the total intensity is I. The total intensity does not affect the polarization fraction and angle and is set to $I = 1$. The normalization in eqs. (7.6) and (7.7) yields the uniform intensity and the maximum polarization for each cell. As illustrated in fig. 7.1 the normalization moves all pairs of q, u random draws onto a circle of radius $I \cdot m_{l,\max}$ in the Q-U-plane. The normalization removes any dependence on the standard deviation of the Gaussian distribution the initial q and u are drawn from. In section 7.1.7 we discuss the choice of the Gaussian prior distribution for q and u.

The total number of cells changed at time t since the beginning of the simulation $t_0 = 0$ is given by:

$$N_{\text{var}}(t) = \text{int}\,(n_{\text{var}} t) \tag{7.8}$$

where $\text{int}(x)$ denotes rounding to an integer.

Consequentially the number of cells changed between two time steps t_1 and t_2 is given by:

$$N_{\text{var}}(t_1, t_2) = \text{int}\,(n_{\text{var}} t_2) - \text{int}\,(n_{\text{var}} t_1) \tag{7.9}$$

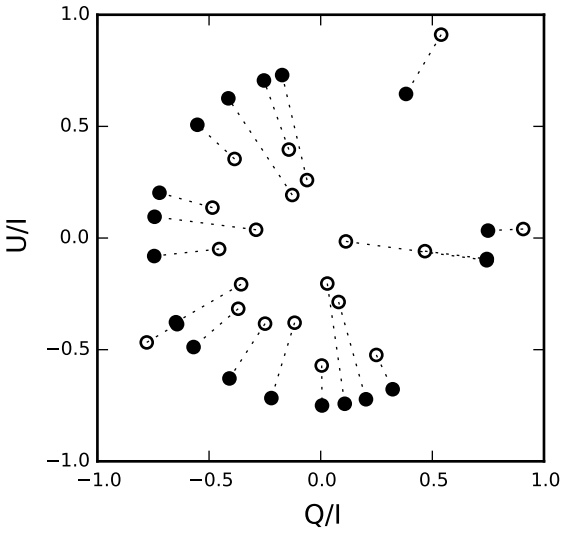

Figure 7.1: Open points illustrate random draws of q and u which are radially moved by the normalization to positions on a circle of radius $I \cdot m_{l,\max}$ indicated by filled points.

In the simple random walk process the cells changing at any time step are selected randomly. The cell properties of those selected cells are newly set following eqs. (7.3) to (7.7).

7.1.3 Shock Q, U random walk process, I uniform

The shock random walk process models a shock passing through a turbulent medium. The initial cells for the shock Q, U random walk process with uniform I (shQUc) are created exactly as in the siQU process. All cells have uniform and constant flux, are maximally polarized, and have a random magnetic field orientation, i.e. EVPA. The selection of the cells which change each time step differs from the simple random walk. The shock cells are numbered and ordered. Assuming at time t n_t cells change, all cell properties are shifted by n_t cells. The last n_t cell properties are lost as the shock does not highlight this part of the medium any more, the first n_t cell properties representing the first cells behind the shock front are set with new, random properties. In contrast to the siQU process selecting the changing cells randomly the shQUc process is less randomized. Only the first cells change, which implies that the cells changed within the last time step cannot be changed again until they move out of the shock region.

7.1.4 Shock Q, U random walk process, I decreasing

With the shock Q, U random walk process with decreasing I (shQUd) we model a shock passing through a turbulent medium where the shock front has the highest intensity with a degrading afterglow behind the shock front. We scale the cell intensities linearly from the highest intensity at the shock front (the first model cell) to zero intensity at the $N_{\text{cells}} + 1$th cell.

$$I_i = \hat{I}(N_{\text{cells}} - i) \quad \text{for} \quad i = 0 \ldots N_{\text{cells}} - 1 \tag{7.10}$$

We determine $\hat{I}$ such that the total intensity is I:

$$
\begin{aligned}
I = \sum_i I_i &= \hat{I} \sum_{i=0}^{N_{\text{cells}}-1} N_{\text{cells}} - i \\
&= \hat{I} \left(N_{\text{cells}}^2 - \frac{(N_{\text{cells}}-1)^2}{2} - \frac{N_{\text{cells}}-1}{2} \right) \\
&= \hat{I} \left(\frac{N_{\text{cells}}^2}{2} - \frac{N_{\text{cells}}}{2} \right) \qquad (7.11) \\
\Leftrightarrow \hat{I} &= \frac{2I}{N_{\text{cells}}^2 + N_{\text{cells}}} \\
\Rightarrow I_i &= \frac{2I}{N_{\text{cells}}^2 + N_{\text{cells}}} (N_{\text{cells}} - i) \qquad (7.12)
\end{aligned}
$$

The cells Stokes Q and U are set as in the other processes (eqs. (7.3) to (7.7)) with normalization by the scaled intensities. The scheme of changing the cell properties is the same as in the shQUc process.

7.1.5 Integrated polarization

At each time step t_i after changing $N_{\text{var}}(t_i, t_{i-1})$ (eq. (7.9)) according to one of the processes described above, the Stokes vector

$$
\begin{pmatrix} I \\ Q \\ U \end{pmatrix} = \mathbf{S} = \sum_{i=1}^{N_{\text{cells}}} \mathbf{S}_i = \sum_{i=1}^{N_{\text{cells}}} \begin{pmatrix} I_i \\ Q_i \\ U_i \end{pmatrix} \qquad (7.13)
$$

integrated over all cells is calculated. From the integrated Stokes vector we calculate the linear polarization fraction m_l eq. (6.7) and the EVPA χ (eq. (6.8)).

7.1.6 Simulated EVPA errors

We include simulated EVPA "measurement" errors in the random walk simulations such that the distribution of the simulated errors reflects the distribution of the errors in our data set. For each data point $\chi_{\text{rw},i} = \chi_{\text{rw}}(t_i)$ simulated by one of the random walk processes we draw a random-number σ_{χ_i} from a log-normal $\mathcal{LN}(\mu_{\text{err}}, \sigma_{\text{err}})$ distribution representing the *error scale* of that data point with the distribution parameters μ_{err} and σ_{err} determined from our data (c.f. section 6.8, table 6.7). The error scale represents the "measurement error".

For each data point the error is simulated by adding a random number $\chi_{\text{err},i}$ drawn from a Gaussian distribution $\mathcal{N}(0, \sigma_{\chi_i})$ with mean zero and standard deviation σ_{χ_i} given by the corresponding error scale to the random walk data point:

$$
\chi_{\text{sim},i} = \chi_{\text{rw},i} + \chi_{\text{err},i}. \qquad (7.14)
$$

We point out, that the optimal way to simulate errors would be to define error distributions for the Stokes parameters I, Q and U and propagate those errors through to the polarization parameters. Our data set does not contain the Stokes parameters, but the polarization parameters, m_l and χ, only. Thus, we have no means to determine the underlying distributions. We have further investigated the

distribution of EVPA errors for dependencies on the total and the polarized flux. The polarized flux puts an upper limit on the EVPA error distribution. The higher the polarized flux, the lower are the maximal EVPA errors.

We do not include any dependence of the EVPA errors on the polarized flux in our random walks as none of the processes includes the simulation of flux variation, but they all set a constant Stokes I.

With our simplified error simulation scheme all error scales are independent. The flaring behaviour of real Stokes I curves and the partial dependence of the EVPA errors on the polarized flux cancels the complete independence of errors. During flares EVPA errors are generally lower than during low-brightness states. This behaviour cannot be captured by our model.

7.1.7 Prior distribution selection

The models siQU, shQUc and shQUd are defined such that every cell has a specific intensity, is maximally polarized and has a random magnetic field orientation. With the choice of Gaussian prior distributions for the initial q and u (eqs. (7.3) and (7.4)) the orientation and accordingly the EVPA are uniformly distributed. With the normalization (eqs. (7.6) and (7.7)) this approach is equivalent to Jones et al. (1985) drawing a unit vector with random phase. Jones et al. (1985) note that their results of investigating random walk EVPA rotations were almost identical when choosing a uniform prior distribution $\mathcal{U}(-1, 1)$ for Q and U.

We point out that with uniform prior distributions the EVPA is not uniformly distributed. In the right panel of fig. 7.2 we show the distribution of the EVPA χ based on random draws of q and u pairs from a uniform distribution and from a Gaussian distribution. Each normalized histogram is based on 1 000 000 simulations. With (identical) Gaussian prior distributions for q and u the EVPA is uniformly distributed. With (identical) uniform prior distributions for q and u the EVPA distribution peaks at $22.5\,^\circ \pm n \cdot 45\,^\circ$ and has minima at $\pm n \cdot 45\,^\circ$. The reason is that more points lie on the diagonals of the uniformly filled q-u-plane than in any other direction and the diagonals correspond to an EVPA of $\chi = 22.5\,^\circ \pm n \cdot 45\,^\circ$ where the χ-distribution peaks. Accordingly the least points lie on the horizontal and vertical axis of the q-u-plane corresponding to the χ-distribution minima. Consequentially, the selection of a uniform distribution introduces a higher ordering of the magnetic field orientation of multiple cells as some orientations are preferred over others.

The integrated polarization fraction and the integrated EVPA of multiple cell models are not affected by this preferred orientation. The χ-distribution is symmetric around zero and identical every 45 degrees. Therefore the probability of producing two cells with perpendicular magnetic field orientation is as probable as producing two cells with parallel field orientation. Although internally the cells are more ordered preferring orientations close to $22.5\,^\circ \pm n \cdot 45\,^\circ$ neither the integrated polarization fraction is increased nor has the integrated polarization angle a preferred orientation. Figure 7.3 shows that the distributions of the integrated polarization fraction and angle are identical for both choices of prior distributions, uniform and Gaussian, in the case of a few cells ($N_{\text{cells}} = 10$, left plots) and many cells ($N_{\text{cells}} = 100$, right plots). Therefore, consistent with the note of Jones et al. (1985) the results of the random walk simulations will not depend on the choice of the prior distribution.

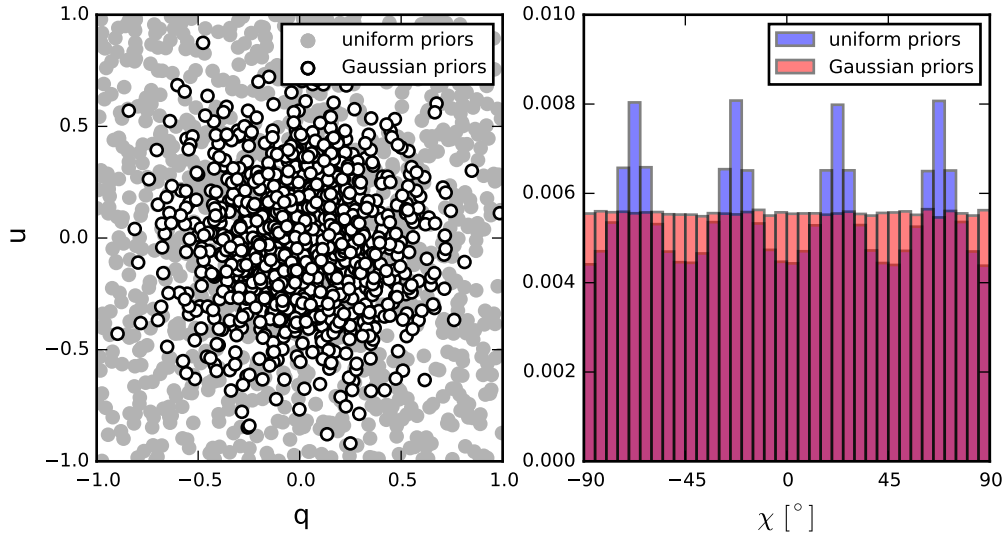

Figure 7.2: Left panel: 1 000 exemplary random draws in the Q-U-plane from a uniform distribution (gray circles) and a Gaussian distribution (open circles). Right panel: Normalized histogram of the EVPA based on 1 000 000 random q, u draws from a uniform or a Gaussian distribution.

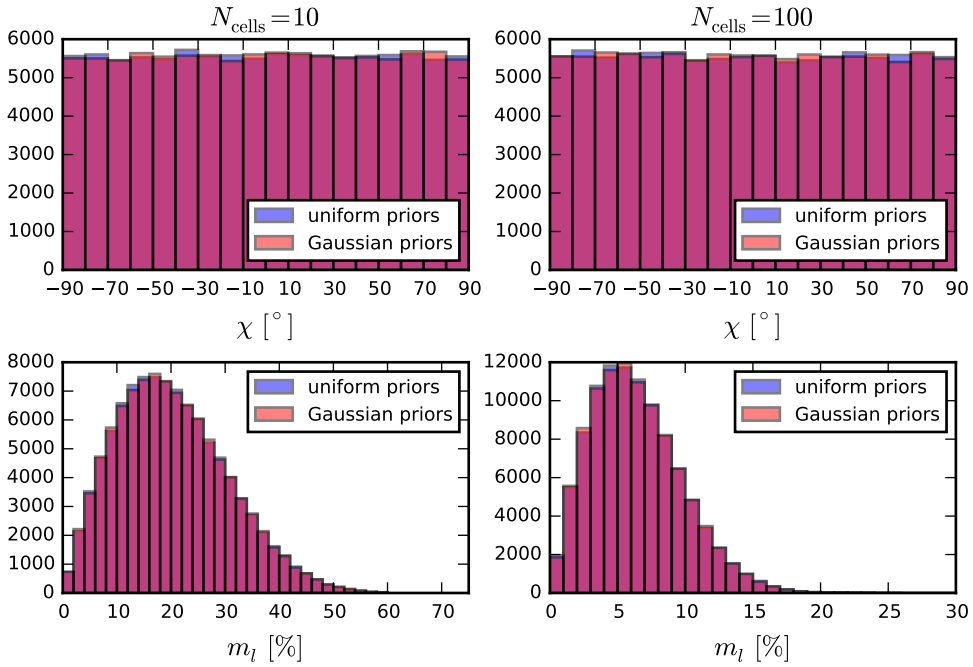

Figure 7.3: Distributions of the integrated EVPA χ (upper plots) and the integrated linear polarization fraction m_l (lower plots) for a 10-cell model (left column) and a 100-cell model (right column) with the initial Stokes parameters drawn either from a uniform distribution (blue) or a Gaussian distribution (red). Each histogram is based on 100 000 simulations.

7.2 Model analysis

Before we test the random walk models against the observed data we discuss the general model behaviour in the following sections. In section 7.2.1 we discuss how the measured parameters we used in section 6.8 to characterize the variation of the

polarization fraction and angle depend on the two main model input parameters. In section 7.2.2 we discuss dependencies between the measured parameters and in section 7.2.3 we compare the siQU, shQUc, and shQUd model.

7.2.1 Dependency on input parameters

All random walk processes introduced in section 7.1 have two primary input parameters: the number of $N_{\rm cells}$ and the cell variation rate $n_{\rm var}$. Secondary input parameters describe the distribution of the time sampling steps (α_t, $\Delta t_{\rm min}$, $\Delta t_{\rm max}$) and the distribution of the EVPA uncertainties ($\mu_{\rm unc}$, $\sigma_{\rm unc}$). In this section we keep the secondary parameters fixed to the values derived from the full observed data set (c.f. tables 6.6 and 6.7, first row, Period: tot).

In chapter 6 we have used the polarization fraction mean $\langle m_l \rangle$ and standard deviation $\sigma(m_l)$, the EVPA rotation amplitude $\Delta\chi$, rotation time T_χ, and variation estimator s_χ, the number of identified rotation $N_{\rm rot}$, and the EVPA adjustment consistency $N_{\rm cons}$ to characterize the observed polarization variation. In this section we discuss the dependency of these measured parameters on the primary input parameters of the random walk polarization models. Here, we limit the discussion on the siQU model. A model comparison is presented in section 7.2.3.

To test the parameter dependency we run 2 000 000 simulations of the siQU process, the cell number uniformly drawn from $N_{\rm cells} \in [2, 600]$ and the cell rotation rate uniformly drawn from $n_{\rm var} \in [0.1\,{\rm d}^{-1}, 100\,{\rm d}^{-1}]$. The total time of the simulated polarization curves is $T \approx 260\,{\rm days}$, roughly[1] the duration of our observation periods (I, II, III, IV). After the simulations we grid the input parameters space $N_{\rm cells}$-$n_{\rm var}$ into 50×50 cells, corresponding to a step size of $\Delta N_{\rm cells} \approx 12$ and $\Delta n_{\rm var} = 2\,{\rm d}^{-1}$. For each grid cell we calculate the mean and the standard deviation of the measured parameters over all the corresponding simulations. We show the results for all measured parameters in figs. 7.4 to 7.10. In all figures coloured lines mark the contours of the average parameter, the grey scale background illustrates the parameter standard deviation.

Polarization fraction mean: $\langle m_l \rangle$. The integrated polarization fraction encodes the uniformity of the magnetic field. The more cells are aligned, i.e. have (close to) parallel EVPA, the higher is the polarization fraction. For only two cells perfect alignment (maximum polarization fraction) is as likely as perfect anti-alignment (zero polarization fraction) and any other difference between the two cells. Therefore the average and variance of the polarization fraction is highest for this configuration. With an increasing number of cells the perfect alignment of all cells becomes less likely and thus the average and variance of the polarization fraction decrease. Figure 7.4 shows the average polarization fraction mean is independent of the cell variation rate, only the variance is slightly increased for low cell variation rates.

Polarization fraction standard deviation: $\sigma(m_l)$. The polarization fraction standard deviation depends on both the number of cells and the cell variation rate. Generally, the average value and the variance increase for a decreasing number of cells for the same reasons that explain the increase of the mean polarization fraction. Increasing the cell variation rate increases the variation of the polarization fraction

[1] The exact simulation time differs every simulation as the time steps are drawn randomly. The total time ranges between $T - \Delta t_{\rm max}$ and T, where $\Delta t_{\rm max}$ is the longest allowed time step.

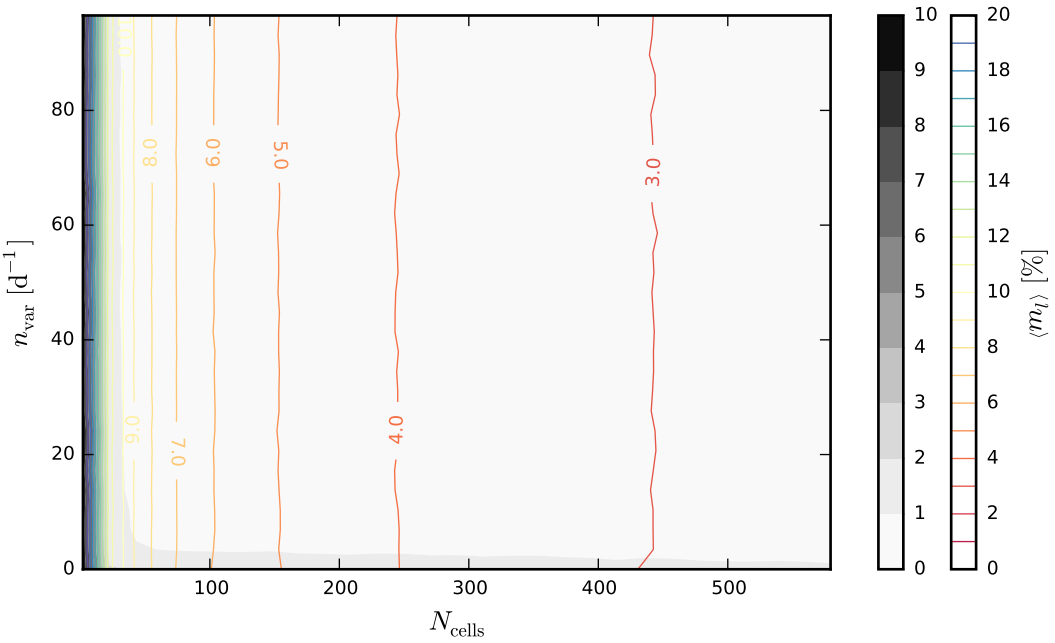

Figure 7.4: Average (colour contours) and variance (grey scale background) of the polarization fraction mean $\langle m_l \rangle$ depending on the number of cells N_{cells} and the cell variation rate n_{var} based on siQU simulations.

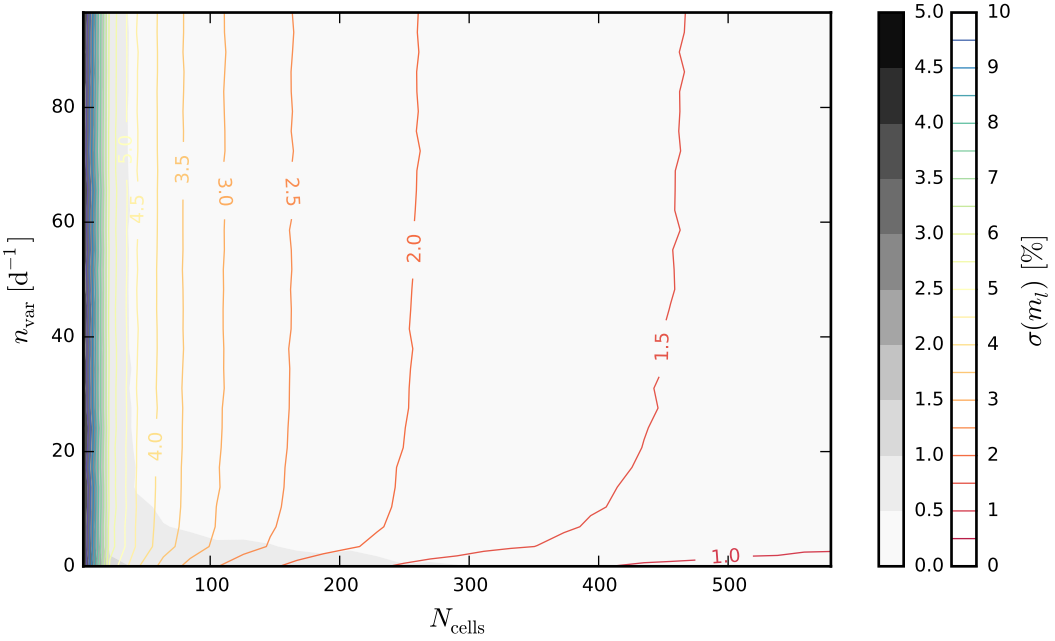

Figure 7.5: Average (colour contours) and variance (grey scale background) of the polarization fraction standard deviation $\sigma(m_l)$ depending on the number of cells N_{cells} and the cell variation rate n_{var} based on siQU simulations.

up to an asymptotic value which is approximately half the mean polarization fraction for the corresponding number of cells. The variance of the polarization fraction standard deviation is slightly higher at low cell variation rates as shown in fig. 7.5.

EVPA amplitude: $\Delta\chi$. The EVPA amplitude $\Delta\chi$ is the difference between the minimum and maximum EVPA occurring during the 260 days-simulation. This value does not imply that the variation leading to this total amplitude comes from a single, continuous rotation, according to our definition (c.f. section 6.7). Figure 7.6 shows that higher cell variation rates increase the average EVPA amplitude and the variance. Increasing the number of cells lowers the average and variance of the amplitude. The higher the relative number of changing cells $n_{\mathrm{var}}/N_{\mathrm{cells}}$ the stronger can the change between to time steps be and thus the average and the variance of the amplitude is increased. We note, that at a fixed sampling rate Δt, for example one day, increasing the cell variation rate beyond $n_{\mathrm{var}} > N_{\mathrm{cells}}/\Delta t$ is not changing the distribution of the EVPA amplitude or any of the following measured parameter. All cells are changed at every time step and the variation cannot be further increased. Since we simulate random time steps, the N_{cells}-n_{var} parameter space for which the measured parameter distribution will not change is not distinctively defined.

EVPA rotation time: T_χ. The EVPA rotation time T_χ is the time difference between the minimum and the maximum of the simulated polarization curves. In our simulations we have found rotation times from 0.5 days, the minimum time step, to 260 days, the total simulation time, ranging around an average of 151 ± 61 days. Our simulations do not show a distinct connection between the input parameters and the rotation time. Instead, we show the rotation rate Δ_χ/T_χ in fig. 7.7. The average rotation rate increases for fewer cells and higher cell variation rates, consistent with the average rotation amplitudes, which show the same dependency.

EVPA variation estimator: s_χ. Figure 7.8 shows that the variation estimator follows the same dependency on the input parameters as the EVPA amplitude. The same behaviour which leads to potentially longer rotations – fewer cells and higher cell variation rates – increases the variation estimator, which is an indicator for more erratic, less smooth EVPA variation.

Number of identified EVPA rotations: N_{rot}. We identify rotations, according to our definition in section 6.7, at a significance level $\varsigma = 3$. The number of identified rotations as shown in fig. 7.9 again follows the same parameter dependency as the EVPA rotation amplitudes and the variation estimator. An increase of the erratic variation indicated by a higher variation estimator implies that the continuation of a rotation becomes less likely. Instead changes of the rotation sign occur more often. With increasing variation rates, variation on short time scales becomes more likely to be seen as significant, thus increasing the number of identified rotations.

EVPA adjustment consistency: N_{cons}. When the total EVPA amplitudes and the amount of erratic variation decreases for more cells and lower variation

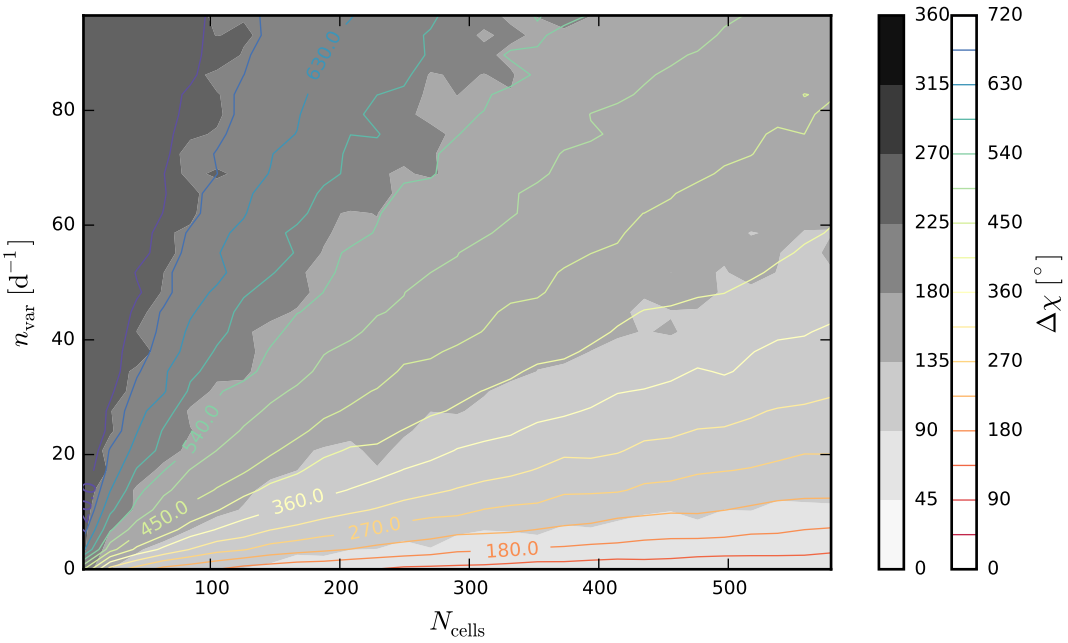

Figure 7.6: Average (colour contours) and variance (grey scale background) of the EVPA amplitude $\Delta\chi$ depending on the number of cells N_{cells} and the cell variation rate n_{var} based on siQU simulations.

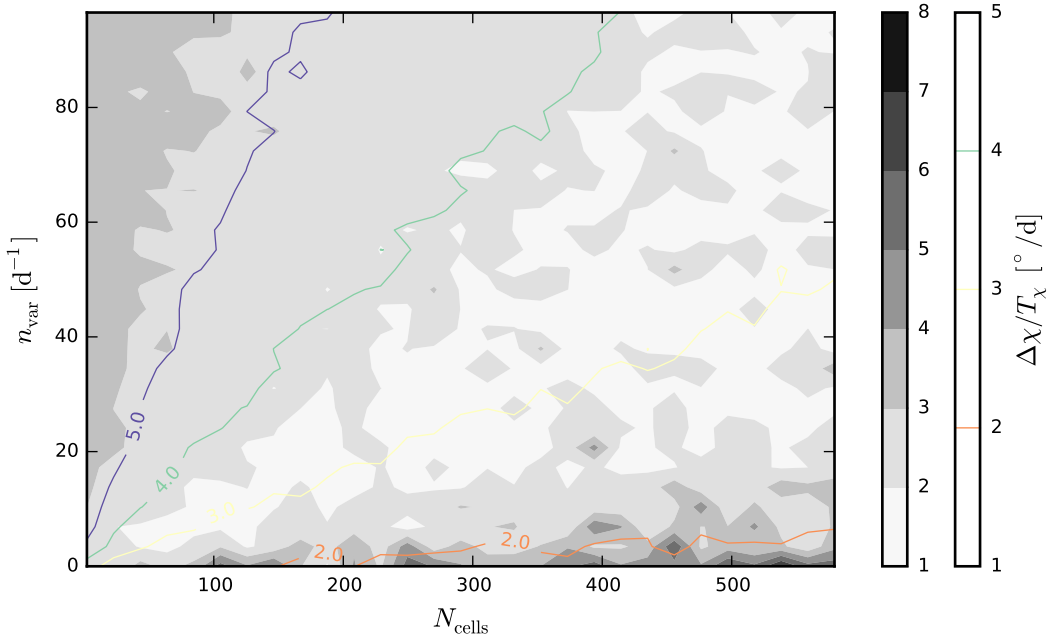

Figure 7.7: Average (colour contours) and variance (grey scale background) of the EVPA rotation rate Δ_χ/T_χ depending on the number of cells N_{cells} and the cell variation rate n_{var} based on siQU simulations.

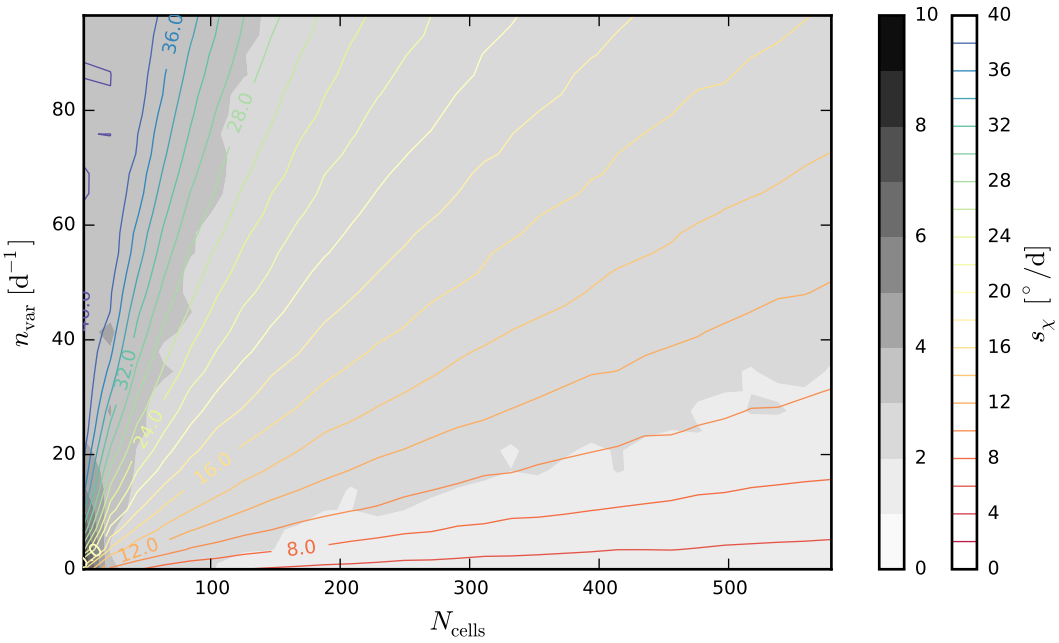

Figure 7.8: Average (colour contours) and variance (grey scale background) of the EVPA variation estimator s_χ depending on the number of cells N_{cells} and the cell variation rate n_{var} based on siQU simulations.

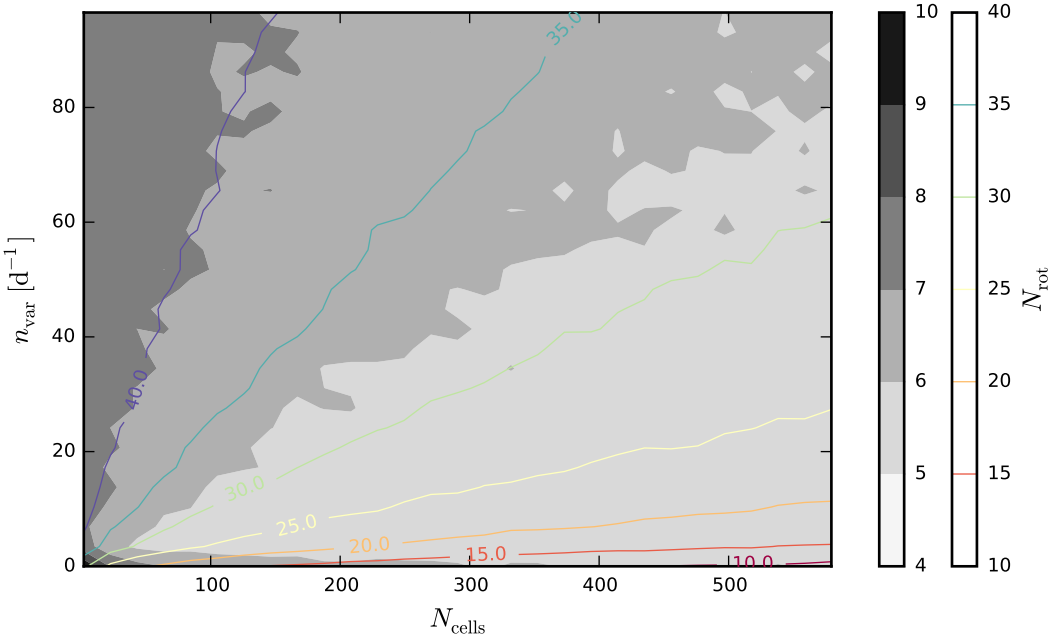

Figure 7.9: Average (colour contours) and variance (grey scale background) of the number of EVPA rotations N_{rot} identified at 3σ-significance depending on the number of cells N_{cells} and the cell variation rate n_{var} based on siQU simulations.

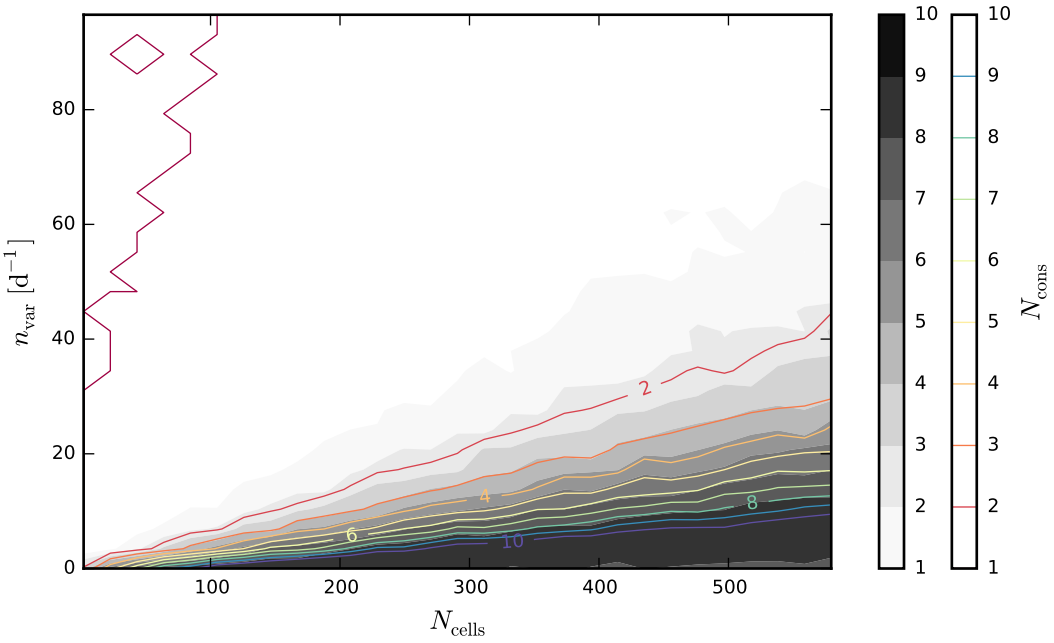

Figure 7.10: Average (colour contours) and variance (grey scale background) of the EVPA adjustment consistency N_{cons} depending on the number of cells N_{cells} and the cell variation rate n_{var} based on siQU simulations.

rates the consistency of the EVPA adjustment increases, consequently. But the consistency average is the same as the variance at all parameter combinations. Therefore, low adjustment consistency does not carry much information in the context of random walk polarization variation as it may occur at all parameter combinations, whereas high consistency indicates relatively low variation, i.e. low amplitudes and low variation estimators.

7.2.2 Dependencies between measured parameters

The similar dependencies of the EVPA amplitude, variation estimator, and number of identified rotations on the model input parameters imply some amount of correlation between those parameters. In the following we discuss the dependencies between the measured parameters based on the 2 000 000 siQU simulations. Figure 7.11 shows 2d-histograms of the EVPA variation estimator s_χ, the rotation time T_χ, the number of identified rotations N_{rot} and the EVPA adjustment consistency N_{cons} over the rotation amplitude $\Delta\chi$.

The upper panels of fig. 7.11 show some correlation between the EVPA amplitude, variation estimator, and the number of identified rotations, consistent with our interpretation and explanation in section 7.2.1. But the scatter of the dependency between the two parameter combinations is large, especially towards higher values, thus allowing for a large range of observed parameter combinations. Generally, larger rotations are more erratic, consistent with higher variation estimators and more identified rotations. Also, the consistency drops for larger rotations, which is expected when the sampled rotations between adjacent data points increase. Furthermore, we plot the rotation time T_χ over the amplitude in the lower left panel of section 7.2.1. Whereas short rotations $< 180\,^\circ$ may happen within a few up to hundreds of days, much larger rotations can only happen over longer time scales as the largest variation between to adjacent EVPA data points observable is

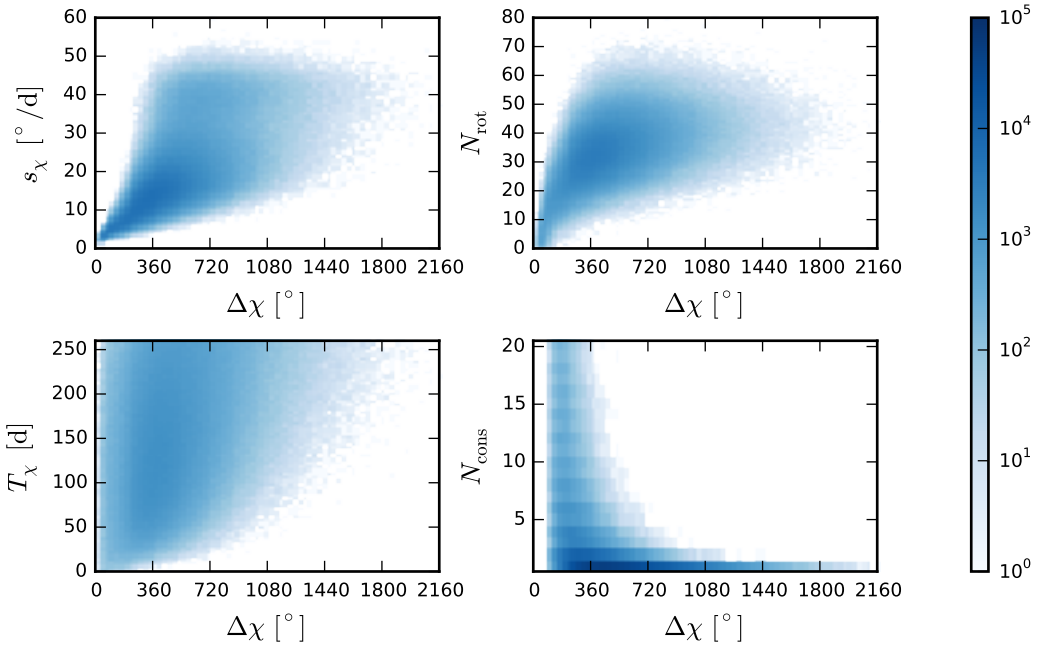

Figure 7.11: Dependencies between the EVPA amplitude $\Delta\chi$ and other observational parameters based on 2 000 000 simulations of the siQU model. Upper left panel: EVPA variation estimator, upper right panel: number of identified rotations, lower left panel: duration of maximum rotation, lower right panel: EVPA adjustment consistency.

90 °.

We point out, that the exact shapes of the shown 2d-distributions depend on the choice of the input parameter ranges. Extending the range for the cell variation rate will increase the number of simulations with large rotations and more erratic EVPA variation at high cell numbers. Furthermore, the EVPA amplitudes, rotation times, and number of identified rotations depend on the simulation time T and will increase for longer rotations.

7.2.3 Model comparison

In the previous two sections we have discussed the dependencies of the measured parameters on the model parameters and on one another based on the siQU model. The behaviour discussed for the siQU model is qualitatively the same for the shQUc and the shQUd model, but the absolute numbers may differ. In this section we compare all three models and discuss differences in the distributions of the measured parameters.

We run 2 000 000 simulations for each model with the same secondary parameters and primary parameter ranges as in section 7.2.1. In figs. 7.12 to 7.20 we show the distributions of the measured parameters for each random walk model.

Polarization fraction mean: $\langle m_l \rangle$. Figure 7.12 shows the distribution of the mean polarization fraction including the full range of cell numbers and cell variation rates. In fig. 7.13 we show the same distribution for shQUd simulations with specific numbers of cells. The siQU and shQUc models qualitatively show the same behaviour. The highest polarization fractions are produced by the 2-cell-models. The distribution gradually shifts to lower polarization fractions for more cells, the difference between the distribution peaks is decreasing and the distributions

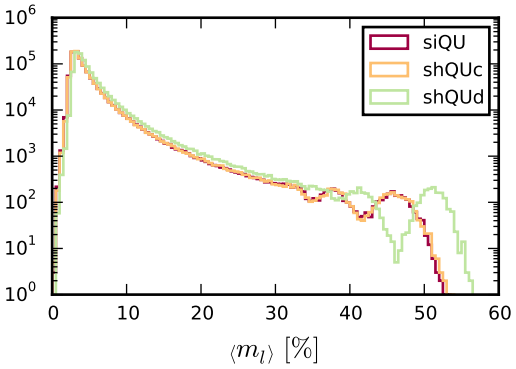

Figure 7.12: Distribution of the mean polarization fraction based on three different polarization random walk models.

become narrower. This explains the shape of the full distribution including a large range of cell numbers in fig. 7.12. There are distinct minima in the distribution between the 2-cell-model and the 3-cell model contribution as well as between the 3-cell-model and the 4-cell model contribution. For lower cell numbers the individual contributions overlap more and the overall distribution becomes a smooth continuum. Below $< 3\,\%$ the distribution drops towards lower polarization fractions. This drop is due to the upper limit of 600 cells for the simulations.

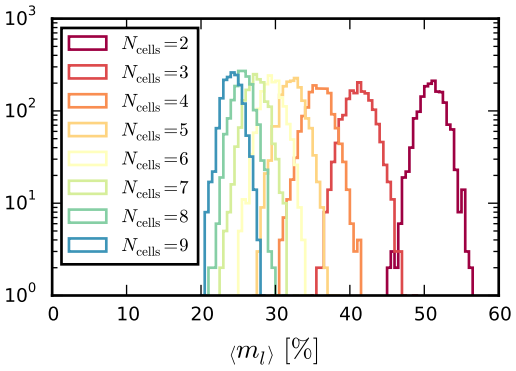

Figure 7.13: Distribution of the mean polarization fraction based on the shQUd model with various numbers of cells.

The siQU and the shQUc model produce distributions of the mean polarization fraction ranging from $0.4 \pm 0.1\,\%$ to $53.2 \pm 0.3\,\%$ (siQU) and $53.6 \pm 0.5\,\%$ (shQUc), indistinguishable within the uncertainties[2] The shQUd model generally produces a higher polarization fraction up to a maximum of $56.0 \pm 0.2\,\%$. This is expected as the linear fading of the cell flux reduces the impact of the cells, further away from the shock front, on the integrated polarization; therefore the shQUd effectively behaves like a shQUc model with fewer cells.

Polarization fraction standard deviation: $\sigma(m_l)$. The distribution of the polarization fraction standard deviation is shown in fig. 7.14. As for the mean polarization fraction distribution the decrease towards lower values below $< 2\,\%$ is du to the upper limit of the cell number in the simulations. The gradual decrease for higher values originates from the model contributions with decreasing cell numbers, similar to the distributions shown in fig. 7.13. The distributions of the siQU and the shQUc model are indistinguishable, the shQUd generally shows a higher variability of the polarization fraction up to $20\,\%$. Beyond $20\,\%$, the siQU and the shQUc model show an additional peak produced by the corresponding 2-cell-model. This

[2]The uncertainties are estimated with a bootstrap method as described in section 6.8, randomly selecting only $\sim 63\,\%$ of the simulations for several iterations.

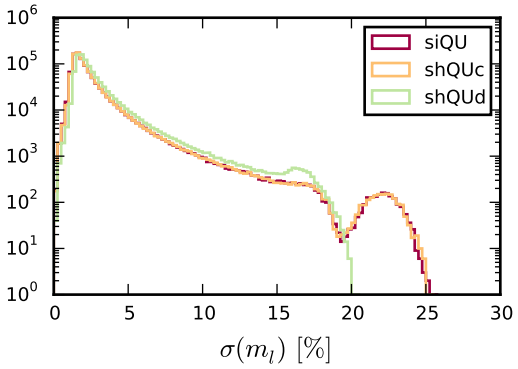

Figure 7.14: Distribution of the polarization fraction standard deviation based on three different polarization random walk models.

peak does not occur in the shQUd model. The flux decrease over the cells, reduces the 2-cell-model de facto to a 1.5-cell-model. Whereas two equally bright, fully polarized cells may vary between zero and maximum polarization, for one and a half cells the polarization fraction is at least one third of the maximum polarization, reducing the variance of the polarization fraction. The standard deviation ranges up to $25.5 \pm 0.3\,\%$ for the siQU model, up to $25.2 \pm 0.2\,\%$ for the shQUc model, and up to $20.2 \pm 0.2\,\%$ for the shQUd model, defining an upper limit for the polarization variance which can be produced by these random walk processes.

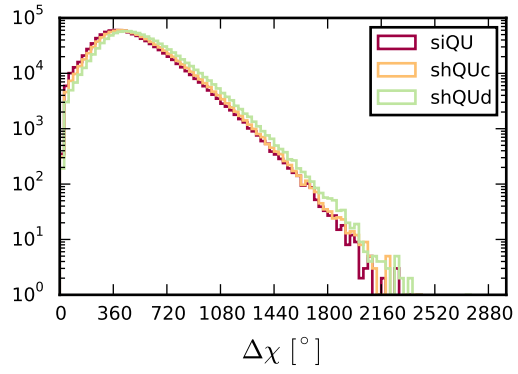

Figure 7.15: Distribution of the EVPA amplitude based on three different polarization random walk models.

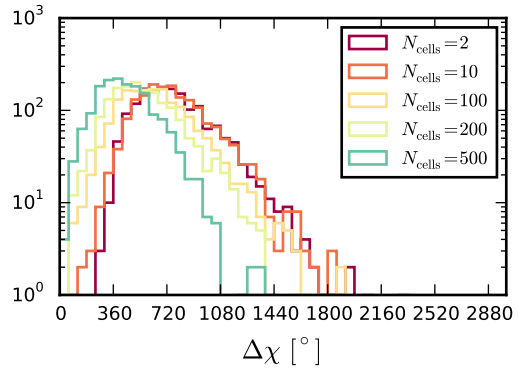

Figure 7.16: Distribution of theEVPA amplitude based on the shQUd model with various numbers of cells.

EVPA amplitude: $\Delta\chi$. Figure 7.15 shows the distribution of the EVPA amplitude for all three random walk models, the contribution of selected cell numbers is shown in fig. 7.16 for the shQUd model. For all cell numbers the distribution has a lower limit (asymptotically going to zero for higher cell numbers), showing that a constant EVPA is unlikely to arise from stochastic processes with a few

cells. The distribution shifts to lower amplitudes for more cells. Nevertheless, the range of potential rotation amplitudes from $16 \pm 1\,^\circ$ to $2600 \pm 180\,^\circ$ is large for all tested cell numbers. Maximum amplitudes are $2380 \pm 50\,^\circ$ (siQU), $2390 \pm 50\,^\circ$ (shQUc), and $2600 \pm 180\,^\circ$ (shQUd). The shQUc model produces slightly larger amplitudes than the siQU model and the shQUd produces the largest amplitudes. The absolute values describing the distribution position depend on the simulation time T. Choosing a longer time interval increases the amplitudes.

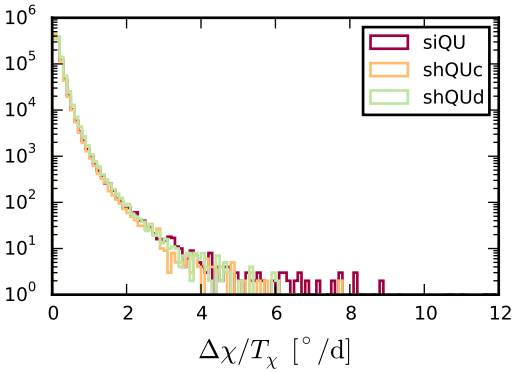

Figure 7.17: Distribution of the EVPA rotation rate based on three different polarization random walk models.

EVPA rotation rate: $\Delta\chi/T_\chi$. The rotation rates generated by the random walk models range from $\sim 0\,^\circ$/d to $11 \pm 1\,^\circ$/d. The probability of higher rotation rates gradually decreases. The three random walk processes do not show distinct differences in fig. 7.17.

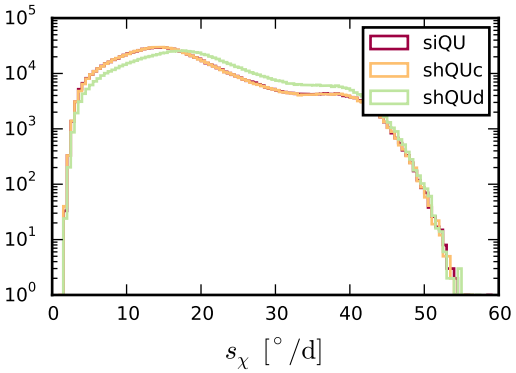

Figure 7.18: Distribution of the EVPA variation estimator based on three different polarization random walk models.

EVPA variation estimator: s_χ. The distributions of the EVPA variation estimator shown in fig. 7.18 have a two peak structure. High values correspond to models with a few cells, whereas low values are mostly produced by models with high cell numbers. The exact distribution shape is affected by the limited ranges of the cell number and the cell variation rate. Higher cell numbers would increase the distribution low end, higher cell variation rates would increase the high end of the distribution. The comparison of the models shows no distinct difference between the siQU and the shQUc model. The shQUd distribution tends to higher variation estimators, indicating more erratic EVPA variation, but the upper limit on the variation estimator of $56 \pm 0.5\,^\circ$/d is consistent for all models within the uncertainties.

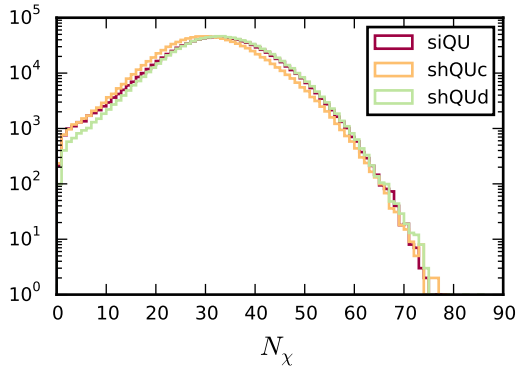

Figure 7.19: Distribution of the number of EVPA rotations identified at 3σ significance level based on three different polarization random walk models.

Number of identified EVPA rotations: N_{rot}. The number of identifiedEVPA rotation ranges from zero, indicating that the total amplitude is below the 3σ noise, to 77 ± 1 for the siQU and the shQUc model and 83 ± 3 for the shQUd model. The distribution mode increases from the shQUc over the siQU to the shQUd model as indicated in fig. 7.19. A higher number of rotations for the shQUd model is consistent with the generally higher EVPA variation estimator. Both indicate more erratic variation of the EVPA. The slight difference between the siQU model and the shQUc model is unclear as the variation estimator distributions are indistinguishable.

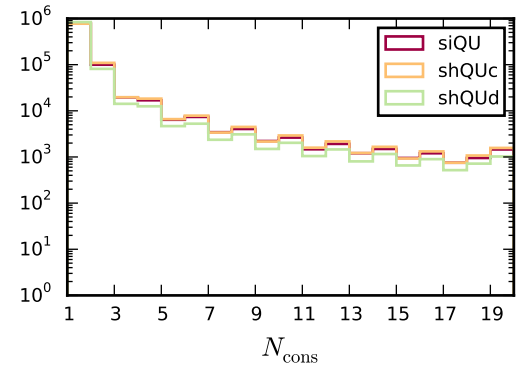

Figure 7.20: Distribution of the EVPA adjustment consistency based on three different polarization random walk models.

EVPA adjustment consistency: N_{cons}. The consistency level is generally lower for the shQUd model. This is consistent with the more erratic EVPA variation indicated by the variation estimator and the rotation number distributions. The siQU model and the shQUc model are indistinguishable. The consistency distribution generally decreases as expected, but shows that even numbers are more likely to occur than odd numbers. This is a technicality of the EVPA adjustment (c.f. section 6.3), which uses the median of the reference points as reference number. The median of an even number of data points is the arithmetic mean of the two mid-points. Using this average apparently increases the likelihood that an even number of reference points produces a consistent adjusted EVPA curve over the enclosing odd numbers.

The three polarization random walk models compared and discussed in this section differ in the selection of the changing cells (simple model vs. shock model) and the intensity distribution of the cells (constant vs. decreasing). Technically, the simple model is more randomized than the shock models, as the changing cells are not predetermined but randomly selected. However, the polarization variation may

be smaller for the simple model. Whereas the in the shock model different cells are changed every time step, the simple model in principle allows to change the same cells over again keeping a fraction of the cells constant for some time, although with an increasing number of cells it is less likely to happen. The parameter distributions discussed previously do not show any significant differences between the simple and the shock model with constant cell intensity. The shock model with decreasing cell intensity differs from the other two models. The polarization fraction is generally higher and more variable, the EVPA variation stronger leading to higher amplitudes and higher variation estimators. As argued before the reason is, that the decreasing flux reduces the impact of the cells on the integrated polarization, such that the model behaves similar to a shock model with constant cell flux but fewer cells.

7.3 Expectation values of the fractional polarization

Figures 7.4 and 7.5 imply that each combination of model input parameters N_{cells}, n_{var} produce a distribution of realizations for the polarization fraction mean $\langle m_l \rangle$ and standard deviation $\sigma(m_l)$ instead of sharp values. Whereas we have averaged over a range of input parameters in these figures, now, we want to determine the distributions of $\langle m_l \rangle$ and $\sigma(m_l)$ for explicit values of N_{cells} and n_{var}. Therefore, we run 1 000 simulations for each combination of cell numbers in the range $N_{\mathrm{cells}} = 10, 20, \ldots, 100, 200, \ldots, 600$ and cell variation rates in the range $n_{\mathrm{var}} = 0.1, 0.2, \ldots, 1.0, 2.0, \ldots, 10.0\,\mathrm{d}^{-1}$. Secondary other model parameters are taken from tables 6.6 and 6.7 (first row, Period: tot).

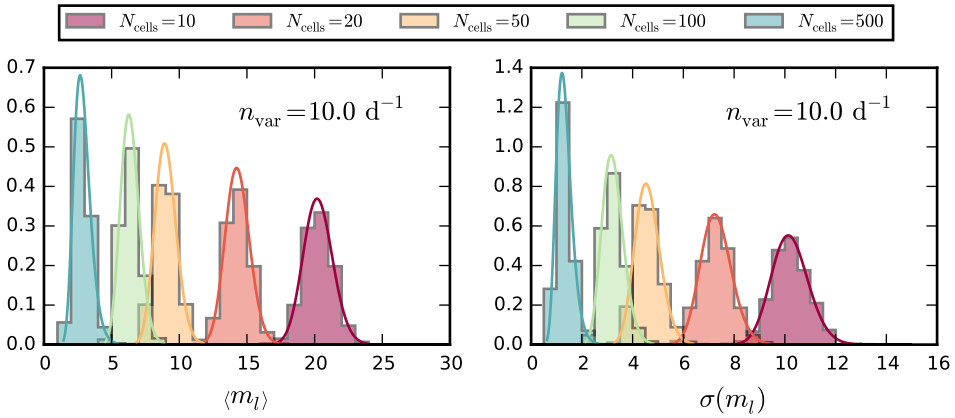

Figure 7.21: Distributions of the polarization fraction mean (left panel) and standard deviation (right panel) each based on 1 000 siQU model simulations for a fixed cell variation rate and different numbers of cells. Solid coloured lines show the corresponding log-normal distribution with parameters estimated from the simulations.

In fig. 7.21 we show some example distributions of $\langle m_l \rangle$ (left panel) and $\sigma(m_l)$ (right panel) for a fixed cell variation rate and various numbers of cells. Both parameters are well described by a log-normal distribution. The corresponding distributions, based on distribution parameter estimated from the simulations, are shown as solid, coloured lines. In fig. 7.22 similar distributions are shown for a fixed number of cells and different variation rates. In fig. 7.23 we show the expectation values of $\langle m_l \rangle$ (upper panel) and $\sigma(m_l)$ (lower panel) depending on

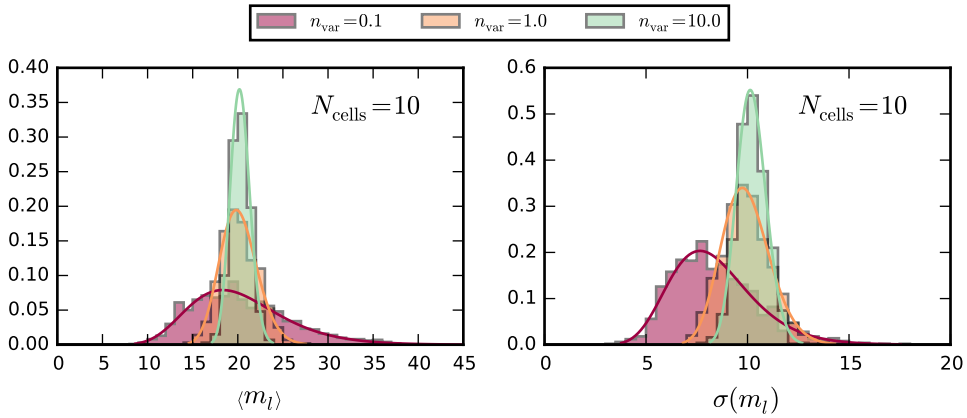

Figure 7.22: Distributions of the polarization fraction mean (left panel) and standard deviation (right panel) each based on 1 000 siQU model simulations for a fixed number of cells and different cell variation rates. Solid coloured lines show the corresponding log-normal distribution with parameters estimated from the simulations.

the cell variation rate for various cell numbers. Error bars indicate the distribution standard deviation. Each data point is based on 1 000 simulations.

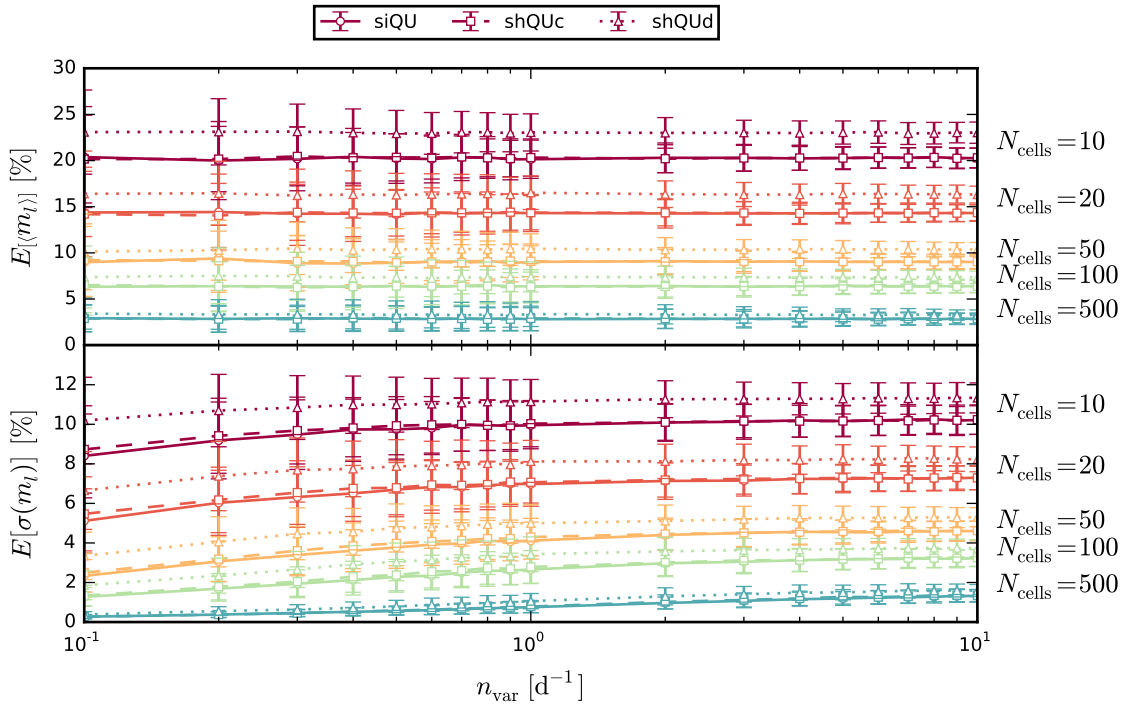

Figure 7.23: Expectation values of the polarization fraction mean (upper panel) and standard deviation (lower panel) for different numbers of cells depending on the cell variation rate. Each data point is based on 1 000 simulations. Solid lines and circles correspond to the siQU model, dashed lines and squares to the shQUc model, and dotted lines and triangles to the shQUd model.

The expectation value of $\langle m_l \rangle$ increases with decreasing cell number following the relation

$$E\left[\langle m_l \rangle\right] \propto \frac{1}{\sqrt{N_{\mathrm{cells}}}}. \tag{7.15}$$

The expectation value is independent of the cell variation rate, but the distribution spread increases with decreasing variation rates. The distribution of $\sigma(m_l)$ is more complex. The expectation value increases with decreasing cell numbers and with increasing cell variation rates. The expectation value ratio of the polarization fraction standard deviation and mean asymptotically reaches 0.5 for high cell variation rates, when (nearly) all cells are changed every time step:

$$\frac{E\left[\sigma(m_l)\right]}{E\left[\langle m_l \rangle\right]} \xrightarrow{n_{\mathrm{var}} \to N_{\mathrm{cells}}/\Delta t} 0.5. \tag{7.16}$$

This relation holds for all cell numbers. Consequentially, the expectation value of $\sigma(m_l)$ is lower than half the expectation value of the mean polarization fraction and the ratio decreases for lower cell variation rates. The distribution spread of the polarization fraction standard deviation increases with lower cell variation rates.

As discussed in section 7.2.3 the shQUd model produces a generally higher polarization fraction mean and variation than the siQU and the shQUc model. The siQU and the shQUc process do not show a significant difference.

Since the polarization fraction mean and standard deviation both show a broad distribution for each model input parameter combination, especially for low cell variation rates, it is not recommendable to fix the model parameters, when testing the stochastic models against observed data. For instance, D'Arcangelo et al. (2007) fix the cell number based on the observed polarization fraction using a relation like eq. (7.15). First, $\langle m_l \rangle$ and $\sigma(m_l)$ are log-normal distributed and thus right-tailed, the expectation value does not represent the most likely value, the distribution mode. Second, whereas the fixed parameters may be the optimal choice to produce the observed polarization fraction variation, a different parameter combination may have a higher probability of producing the observed variation in the polarization fraction and the EVPA. Therefore, we recommend to run simulation over a large enough parameter space to identify the most probable parameter region producing the observed polarization variation. We apply this scheme in the following section.

7.4 Test random walk polarization models against observations

We run simulations of the three random walk polarization models to test whether these processes can produce the observed variation of the polarization fraction and angle. We focus on the two strongest rotation events in our data, period IIa and period IIIc, which exhibit the largest rotation amplitudes.

7.4.1 Period IIa: parameter distributions

We run 2 000 000 simulations for each random walk process, drawing the cell number and the cell variation rate randomly from uniform distributions in the ranges $N_{\mathrm{cells}} \in [2, 600]$ and $n_{\mathrm{var}} \in [0.1, 100]\,\mathrm{d}^{-1}$. The simulation total time equals the duration of period IIa $T = 154\,\mathrm{d}$. The parameters defining the time sampling

distribution are given in table 6.6 and the parameters of the EVPA uncertainties distribution are listed in table 6.7.

For all simulations we measure the polarization fraction mean $\langle m_l \rangle$ and standard deviation $\sigma(m_l)$ the absolute EVPA amplitude $\Delta\chi = \max(\chi(t)) - \min(\chi(t))$ and the EVPA variation estimator s_χ. First, we test if the random walk processes can produce the observed polarization fraction variability. The observed polarization mean during period IIa is $\langle m_l \rangle = 5.5 \pm 0.4\,\%$ the standard deviation $4.0 \pm 0.5\,\%$ (c.f. section 6.8). To find the optimal model parameters we grid the input parameter space N_{cells}-n_{var} in bins of 10 cells and 2 cells per day. For each grid bin the total number of simulations N_{sim} is counted and the number of simulations N_{cond} which fulfil the conditions:

$$\text{Pol. fraction condition 1: } 5.1\,\% \leq \langle m_l \rangle < 5.9\,\%,$$
$$\text{Pol. fraction condition 2: } 4.5\,\% \leq \sigma(m_l) < 4.5\,\%.$$

We note, that the choice of the condition ranges is arbitrary and affects the number of identified simulations, the larger the range the more simulations fulfill the condition. We use the 1σ uncertainties of the observed values to set the ranges.

We show the distribution of $N_{\mathrm{cond}}/N_{\mathrm{sim}}$ over the input parameter space for the mean polarization fraction condition in fig. 7.24, for the polarization fraction variation in fig. 7.25, and fulfilling both conditions in fig. 7.26. Each figure shows the distribution for each random walk model in different panels. We point out, that the relative simulation counts $N_{\mathrm{cond}}/N_{\mathrm{sim}}$ are not probabilities of fulfilling the condition, i.e. producing the observed characteristic. The normalizing number of simulations N_{sim} depends on the binning of the input parameter space. Therefore, the bin sizes strongly affect the relative counts presented in all following figures showing the distribution of $N_{\mathrm{cond}}/N_{\mathrm{sim}}$.

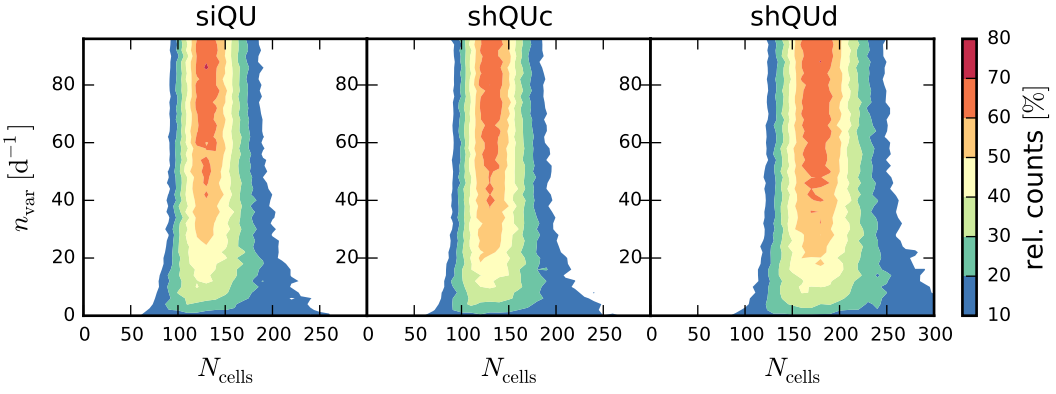

Figure 7.24: Distribution of the relative count of simulations consistent with the observed mean polarization fraction during period IIa (pol. fraction condition 1) over the number of cells N_{cells} and the cell variation rate n_{var} based on the three different random walk processes.

The observed polarization fraction mean is common ($\sim 70\,\%$ of the simulations) in the siQU and shQUc model around 135 ± 5 cells and in the shQUd model around 175 ± 5 cells at cell variation rates $> 40\,\mathrm{d}^{-1}$. The observed polarization fraction variation is common ($\sim 80\,\%$ of the simulations) at fewer cells: 65 ± 5 for the siQU and shQUc model, 95 ± 5 for the shQUd model. Consequentially, the observed mean and variation of the polarization fraction occurs only rarely ($\sim 2.4\,\%$ of the

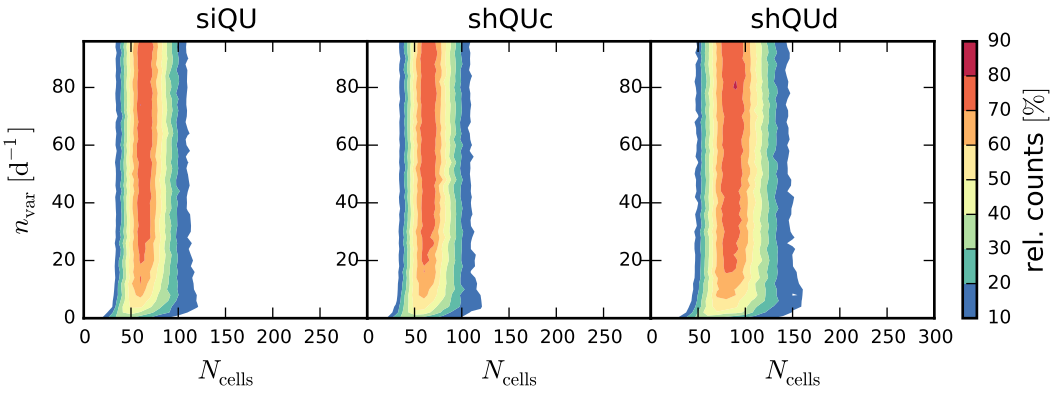

Figure 7.25: Distribution of the relative count of simulations consistent with the observed polarization fraction standard deviation during period IIa (pol. fraction condition 2) over the number of cells N_{cells} and the cell variation rate n_{var} based on the three different random walk processes.

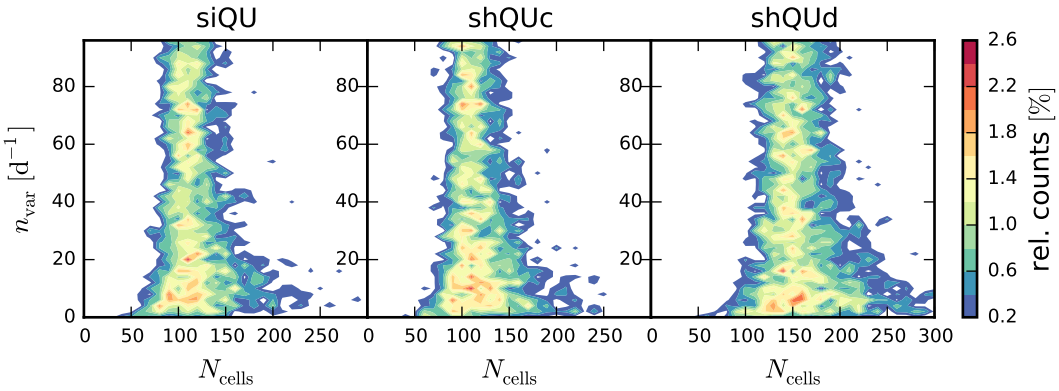

Figure 7.26: Distribution of the relative count of simulations consistent with the observed polarization fraction during period IIa (pol. fraction condition 1+2) over the number of cells N_{cells} and the cell variation rate n_{var} based on the three different random walk processes.

simulations) for 115 ± 5 cells (siQU and shQUc) and 145 ± 5 cells (shQUd) and low variation rates $16 \pm 6\,\mathrm{d}^{-1}$ and less frequently for other cell numbers and variation rates.

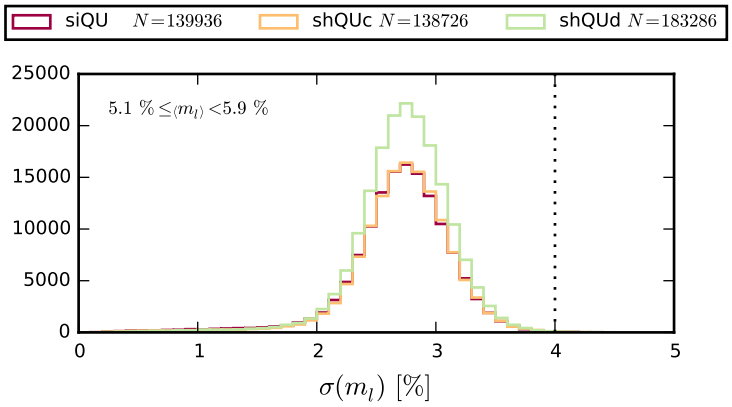

Figure 7.27: Distribution of the polarization fraction standard deviation for all simulations with a mean polarization fraction consistent with the observed value during period IIa. The observed polarization standard deviation value is indicated by the black dotted line.

As discussed in section 7.3 the polarization fraction standard deviation, when produced by one of the random walk processes, is typically distributed around half the polarization fraction mean or lower. The observed ratio of $\sigma(m_l)/\langle m_l \rangle \approx 0.7$ is atypically high under the assumption of a random walk process. We show the distribution of $\sigma(m_l)$ for all simulations that have the observed polarization fraction mean (pol. fraction condition 1) in fig. 7.27. The dotted black line marks the observed standard deviation. Given the observed polarization fraction mean, it is unlikely to observe a standard deviation as high as in the data when produced by a random walk process.

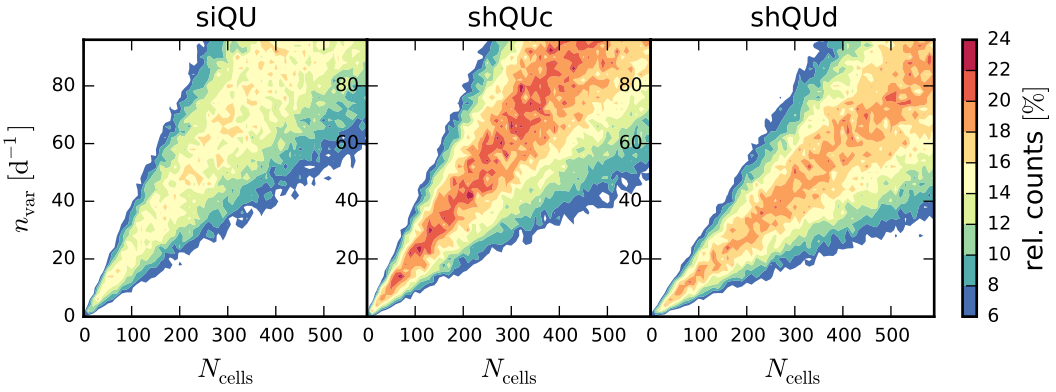

Figure 7.28: Distribution of the relative count of simulations consistent with higher EVPA amplitudes and smoother EVPA variation than observed during period IIa (pol. angle condition 1+2) over the number of cells N_{cells} and the cell variation rate n_{var} based on the three different random walk processes.

The observed EVPA amplitude during period IIa is $\Delta\chi = 494\,^\circ$ and the EVPA variation estimator $s_\chi = 18.7 \pm 1.3\,^\circ/\mathrm{d}$ (including the error bias which also affects the simulated polarization curves). In sections 7.2.1 and 7.2.2 we have shown that the EVPA amplitude and the variation estimator are contrary parameters, where the probability of high smoothness (low variation estimator) on average decreases with higher amplitudes and vice versa. Therefore, we set the conditions on the EVPA, which we are searching for in the simulations, to:

$$\text{Pol. angle condition 1: } \Delta\chi \geq 494\,^\circ,$$
$$\text{Pol. angle condition 2: } s_\chi \leq 18.7\,^\circ/\mathrm{d}.$$

In fig. 7.28 we show the distribution of the relative simulation count fulfilling both conditions on the EVPA variation over the model parameter space. Longer and smoother rotations occur most likely in a diagonal cone in the N_{cells}-n_{var} parameter space. Models with more cells require higher cell variation rates to produce the desired rotations. The shQUc model is most likely to produce the observed variation with $N_{\mathrm{cond}}/N_{\mathrm{sim}} \approx 25\,\%$ at the peak, the shQUd model has a peak of $N_{\mathrm{cond}}/N_{\mathrm{sim}} \approx 22\,\%$, and the siQU model less likely produces the observed EVPA variation than the two shock processes.

In fig. 7.29 the distribution of the EVPA amplitude is shown based on all simulations with the observed polarization mean (pol. fraction condition 1). Given the observed polarization fraction mean, EVPA amplitudes equal or larger than observed are a likely event under the assumption of a stochastic process.

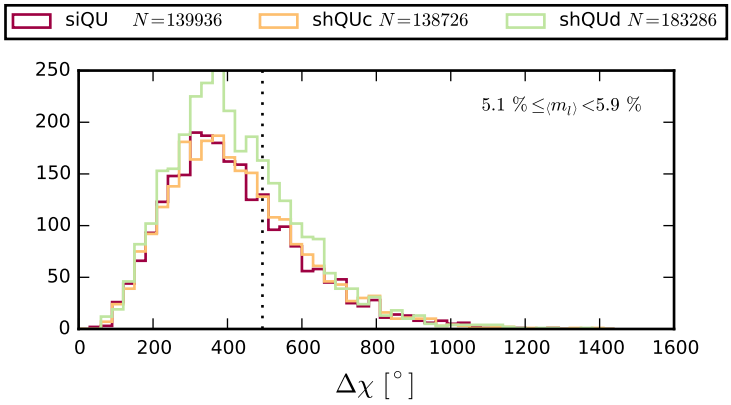

Figure 7.29: Distribution of the polarization angle amplitude for all simulations with a mean polarization fraction consistent with the observed value during period IIa. The observed amplitude is indicated by the black dotted line.

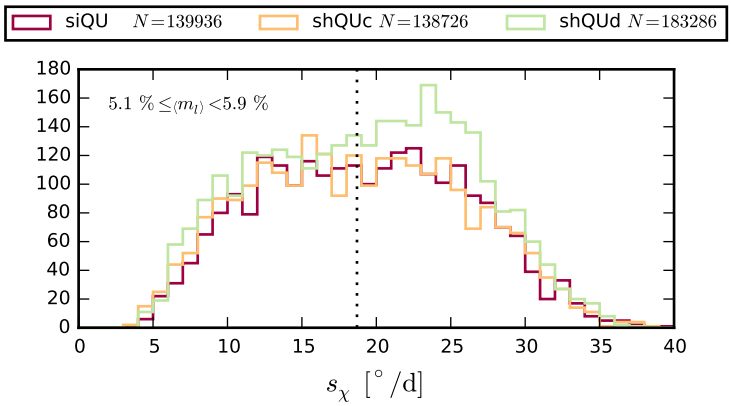

Figure 7.30: Distribution of the EVPA variation estimator for all simulations with a mean polarization fraction consistent with the observed value during period IIa. The observed variation estimator is indicated by the black dotted line.

In fig. 7.30 we show the distribution of the EVPA variation estimator for those simulations which fulfil polarization fraction condition 1. The observed EVPA variation is close to the distribution mean. Under the assumption of a stochastic processes, given the observed polarization fraction mean, the observed value of EVPA variation estimator is the most likely to occur.

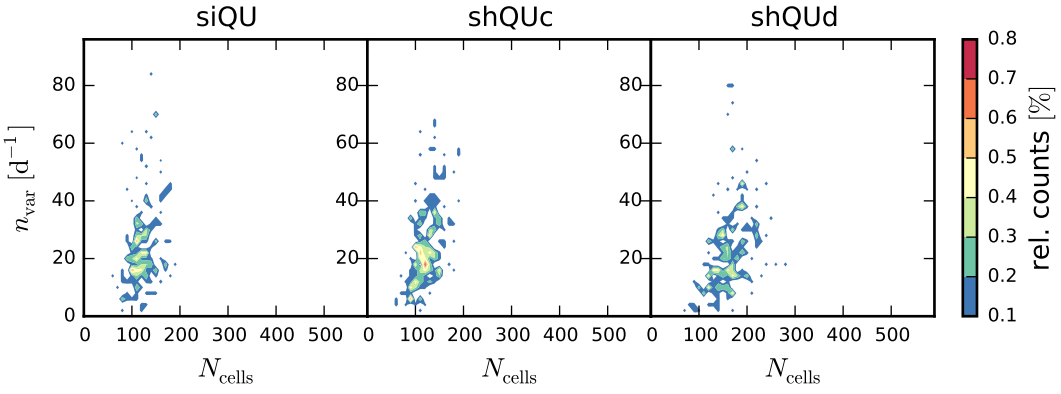

Figure 7.31: Distribution of the relative count of simulations consistent with the observed polarization fraction and angle variation during period IIa (pol. fraction condition 1+2 and pol. angle condition 1+2) over the number of cells N_{cells} and the cell variation rate n_{var} based on the three different random walk processes.

Figure 7.31 shows the distribution of the relative count of simulations, fulfilling

all observational conditions (pol. fraction condition 1+2 and pol. angle condition 1+2), over the model parameter space. The observed polarization variation occurs only rarely in the random walk model simulations ($< 1\,\%$ of the simulations at the distribution peak). Whereas the EVPA variation is consistent with the random walk processes, the high polarization fraction variation cannot be explained by theses processes. Therefore, the likelihood to fulfil all observational conditions is low. In fig. 7.32 we drop the second polarization fraction condition. Up to $15\,\%$ of the simulations show the observed mean polarization fraction and the observed (or more extreme) EVPA variation. The distributions of the polarization fraction standard deviation for this sub-selection of simulations looks exactly like the distributions shown in fig. 7.27.

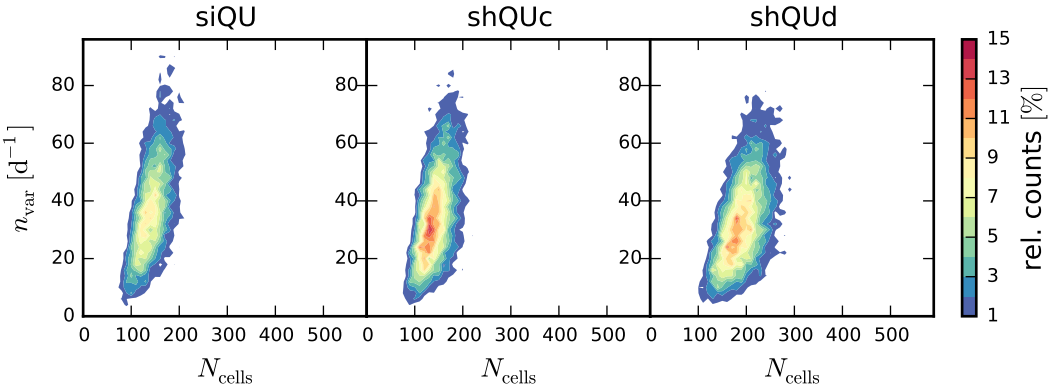

Figure 7.32: Distribution of the relative count of simulations consistent with the mean polarization fraction (pol. fraction condition 1) and angle variation (pol. angle condition 1+2) observed during period IIa over the number of cells N_{cells} and the cell variation rate n_{var} based on the three different random walk processes.

We point out, that the polarization fraction during period IIa contains several data points with large uncertainties, which show a severely higher polarization fraction than the rest of the data points, with average uncertainties. Those data points are possibly outliers, which lead to overestimate the standard deviation of the polarization fraction. Once we remove the three data points with uncertainties larger than $5\,\%$ in the combined, averaged polarization fraction curve the polarization fraction mean is lowered from $5.5 \pm 0.4\,\%$ to $5\,\%$ and the standard deviation is lowered from $4.0 \pm 0.5\,\%$ to $3.0\,\%$. This lower standard deviation is much closer to the distribution peak shown in fig. 7.27 and even with the slightly lowered mean of $5\,\%$ the standard deviation does not differ severely from the expected value $0.5 \cdot 5\,\% = 2.5\,\%$ (c.f. eq. (7.16)). We conclude, that the measured polarization fraction standard deviation is probably overestimated due to a few uncertain, possibly largely overestimated data points and that the observed polarization variation seen in both the polarization fraction and the polarization angle is probably consistent with a stochastic process. We determine the probability of producing the observed variation with one of the random walk models in the following section.

7.4.2 Period IIa: probability

To calculate the probability that one of the random walk processes produces the polarization fraction variation (pol. fraction condition 1+2) and the polarization

angle variation (pol. angle condition 1+2) observed during period IIa we run simulations at specific cell numbers and cell variation rates. We select the most probable parameter range based on the results of the previous section:

$$N_{\text{cells},i} \in [80, 90, \ldots, 220],$$
$$n_{\text{var},j} \in [4, 8, \ldots, 40]\,\text{d}^{-1}$$

For each combination of input parameters i, j we run $N_{\text{sim}} = 10\,000$ simulations and count the number of simulations $N_{i,j,\text{cond}}$ which fulfil the observational conditions. The probability that a random walk process produces a polarization curve fulfilling the conditions at each i, j is given through

$$P_{i,j}(\text{cond}) = \frac{N_{i,j,\text{cond}}}{N_{\text{sim}}}. \tag{7.17}$$

The highest probability is

$$P_{\text{max}}(\text{cond}) = \max_{i,j} P_{i,j}(\text{cond}) \tag{7.18}$$

occurring at the optimal model parameters $N_{\text{cells}}^{\text{opt}}$, $n_{\text{var}}^{\text{opt}}$. The simulation results are shown in fig. 7.33. The highest probabilities and the optimal model parameters are listed in table 7.1. As discussed before, the probability is very low ($< 1\,\%$) due to the high polarization fraction variation. We also determine the probability a slightly different conditions on the polarization fraction:

$$\text{Pol. fraction condition 1b: } 4.6\,\% \leq \langle m_l \rangle < 5.4\,\%,$$
$$\text{Pol. fraction condition 2b: } 2.5\,\% \leq \sigma(m_l) < 3.5\,\%.$$

Table 7.1: Probability (col. 2) of producing the polarization variation observed during period IIa with the optimal number of cells (col. 3) and the optimal cell variation rate (col. 4) based on the three different random walk processes (col. 1).

Model	P_{max}	$N_{\text{cells}}^{\text{opt}}$	$n_{\text{var}}^{\text{opt}}$
siQU	$0.2\,\%$	120 ± 5	$24 \pm 2\,\text{d}^{-1}$
shQUc	$0.3\,\%$	120 ± 5	$16 \pm 2\,\text{d}^{-1}$
shQUd	$0.4\,\%$	150 ± 5	$16 \pm 2\,\text{d}^{-1}$

Here, we use the values for the polarization fraction mean and standard deviation measured after removing the potentially overestimated outliers with very high uncertainties.The probability distribution for this lower mean and variance of the polarization fraction is shown in fig. 7.34. The corresponding highest probabilities and optimal model parameters are listed in table 7.2. Assuming the removed data points are overestimated and the measured polarization fraction mean and standard deviation – after removing the these outliers – are the correct representation of the polarization fraction variation, then the random walk polarization models can produce the observed variation with a probability up to $P_{\text{max}} = 7\,\%$.

Table 7.2: Probability (col. 2) of producing the polarization variation observed during period IIa (after removing data points with high uncertainty) with the optimal number of cells (col. 3) and the optimal cell variation rate (col. 4) based on the three different random walk processes (col. 1).

Model	$P_{\max}$	$N_{\text{cells}}^{\text{opt}}$	$n_{\text{var}}^{\text{opt}}$
siQU	5 %	160 ± 5	$32 \pm 2\,\text{d}^{-1}$
shQUc	7 %	160 ± 5	$36 \pm 2\,\text{d}^{-1}$
shQUd	6 %	210 ± 5	$32 \pm 2\,\text{d}^{-1}$

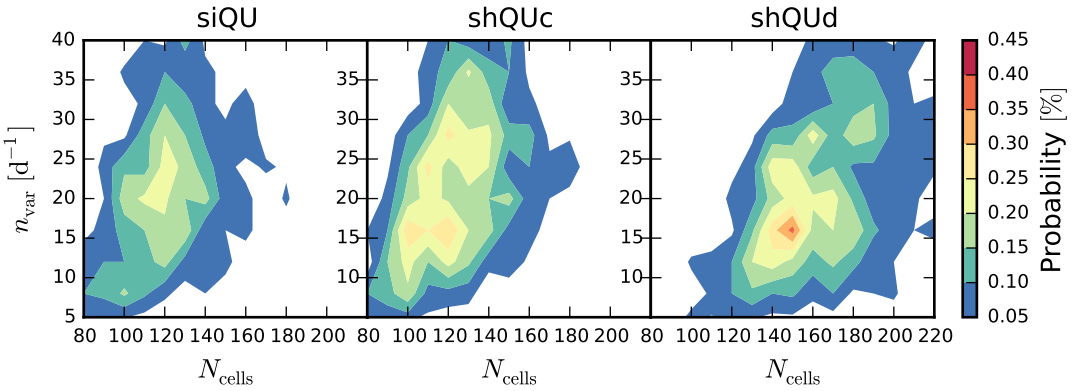

Figure 7.33: Probability of the random walk processes producing the polarization variation (pol. fraction condition 1+2 and pol. angle condition 1+2) observed during period IIa over the number of cells N_{cells} and the cell variation rate n_{var}.

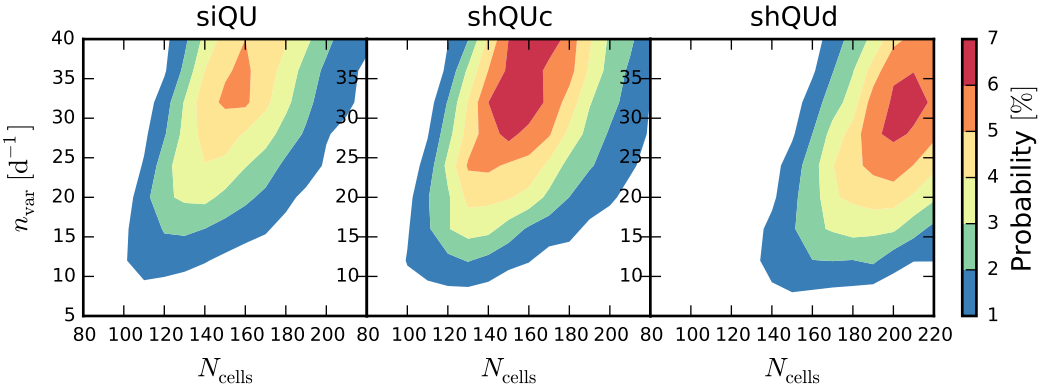

Figure 7.34: Probability of the random walk processes producing the polarization variation (pol. fraction condition 1b+2b and pol. angle condition 1+2) observed during period IIa (after removing data points with high uncertainty)over the number of cells N_{cells} and the cell variation rate n_{var}.

7.4.3 Period IIIc: parameter distributions

To test the random walk polarization models against the period IIIc data we run 2 000 000 simulations with $N_{\text{cells}} \in [2, 600]$ and $n_{\text{var}} \in [0.1, 100]\,\text{d}^{-1}$ drawn randomly from uniform distributions. The simulation total time equals the duration of period IIIc $T = 98\,\text{d}$. The parameters defining the time sampling distribution are given in table 6.6 and the parameters of the EVPA uncertainties distribution are listed in table 6.7.

We test the simulation results for four observational conditions:

Pol. fraction condition 1: $12.5\,\% \leq \langle m_l \rangle < 13.7\,\%$,
Pol. fraction condition 2: $5.4\,\% \leq \sigma(m_l) < 6.0\,\%$,
Pol. angle condition 1: $\Delta\chi \geq 352\,^\circ$,
Pol. angle condition 2: $s_\chi \leq 4.8\,^\circ/\mathrm{d}$.

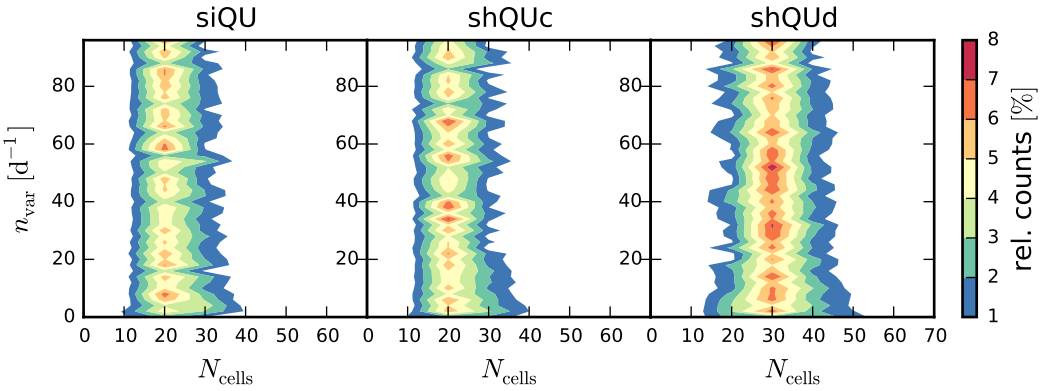

Figure 7.35: Distribution of the relative count of simulations consistent with the observed polarization fraction during period IIIc (pol. fraction condition 1+2) over the number of cells N_{cells} and the cell variation rate n_{var} based on the three different random walk processes.

In fig. 7.35 we show the distribution of the relative count of simulations, which are consistent with the observed polarization fraction variation (pol. fraction condition 1+2). The high observed mean polarization fraction requires a small number of cells: 25 ± 5 for the siQU and the shQUc model, 35 ± 5 for the shQUd model.

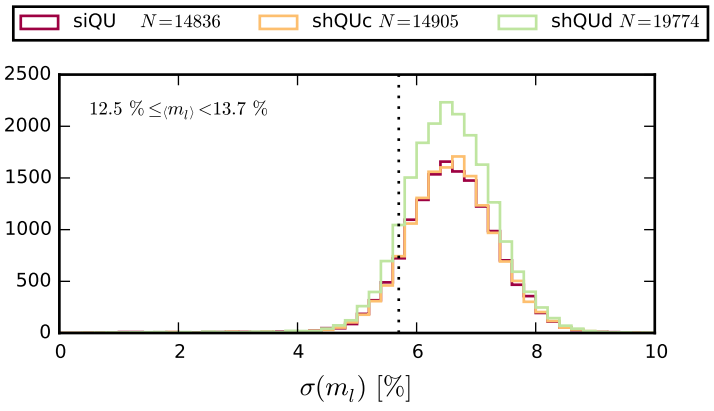

Figure 7.36: Distribution of the polarization fraction standard deviation for all simulations with a mean polarization fraction consistent with the observed value during period IIIc. The observed polarization standard deviation value is indicated by the black dotted line.

In fig. 7.36 the distribution of the polarization fraction standard deviation is shown based on those simulations which produced the observed mean polarization fraction. Under the assumption of a random walk process the observed standard deviation is lower than the expectation value but a probable realization.

The according distributions of the EVPA amplitude and the variation estimator are shown in figs. 7.37 and 7.38. The observed amplitude is a typical event for random walks with the observed mean polarization fraction. The observed value is

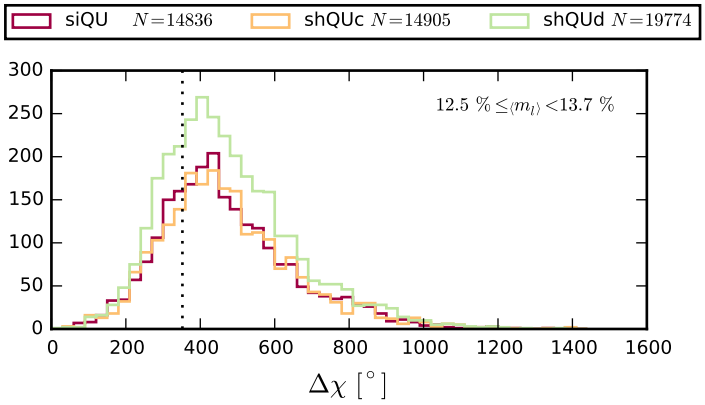

Figure 7.37: Distribution of the polarization angle amplitude for all simulations with a mean polarization fraction consistent with the observed value during period IIIc. The observed amplitude is indicated by the black dotted line.

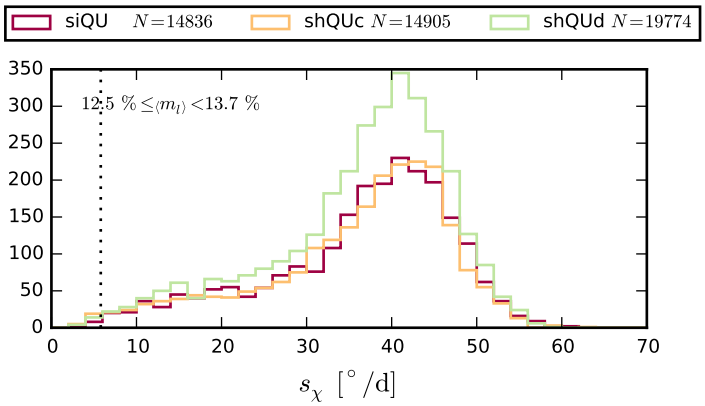

Figure 7.38: Distribution of the EVPA variation estimator for all simulations with a mean polarization fraction consistent with the observed value during period IIIc. The observed variation estimator is indicated by the black dotted line.

close to the distribution mode for each model. On the other hand, the low EVPA variation observed is unlikely to occur from a random walk process when the mean polarization fraction is as high as during period IIIc. The measured variation estimator is at the very low end of the distributions.

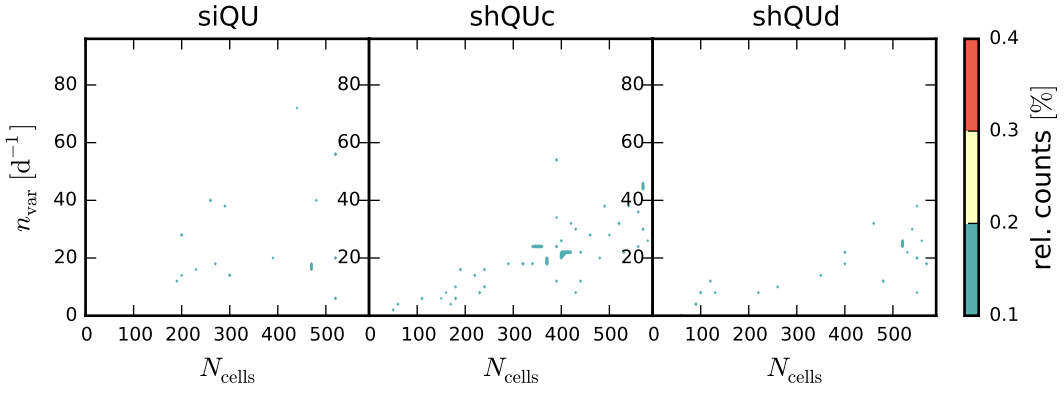

Figure 7.39: Distribution of the relative count of simulations consistent with higher EVPA amplitudes and smoother EVPA variation than observed during period IIIc (pol. angle condition 1+2) over the number of cells N_{cells} and the cell variation rate n_{var} based on the three different random walk processes.

Independently of the polarization fraction, EVPA rotation events as long and smooth as during period IIIc occur only rarely in the random walk simulations.

Figure 7.39 marks the parameter space where single event fulfilling the polarization angle conditions 1+2 were found. These instances occur preferably at low ratios of $n_{\mathrm{var}}/N_{\mathrm{cells}}$. Only low cell variation rates can produce smooth EVPA variation whereas a minimum of variation is necessary to result in a large rotation amplitude. None of the 2 000 000 simulations did fulfil all four conditions observed during period IIIc.

7.4.4 Period IIIc: probability

To derive probabilities we probe the parameter space which showed a few rotation events in fig. 7.39 consistent with the observed amplitude and smoothness:

$$N_{\mathrm{cells},i} \in [5, 10, \ldots, 50],$$
$$n_{\mathrm{var},j} \in [0.1, 0.2, \ldots, 1.0, 2.0, \ldots, 20.0]\,\mathrm{d}^{-1}$$

At each parameter combination we run 10 000 simulations. In fig. 7.40 we show the probability of producing a smooth EVPA rotation (pol. angle condition 1+2) as observed during period IIIc. With a probability $P \leq 0.1\,\%$ preferentially at 7 cells with a variation rate of < 0.4 cells per day a few events occur. No simulations are consistent with the polarization fraction and angle variation (pol. fraction condition 1+2 and pol. angle condition 1+2). The number of simulations $N_{\mathrm{sim}} = 10\,000$ at each tested parameter combination puts an upper limit on the probability $P \leq N_{\mathrm{sim}}^{-1}$. Under the assumption of a random walk process, the probability that the polarization variation observed during period IIIc occurs is less than 0.0001. We conclude, that the observed rotation event cannot be described by one of the three random walk processes.

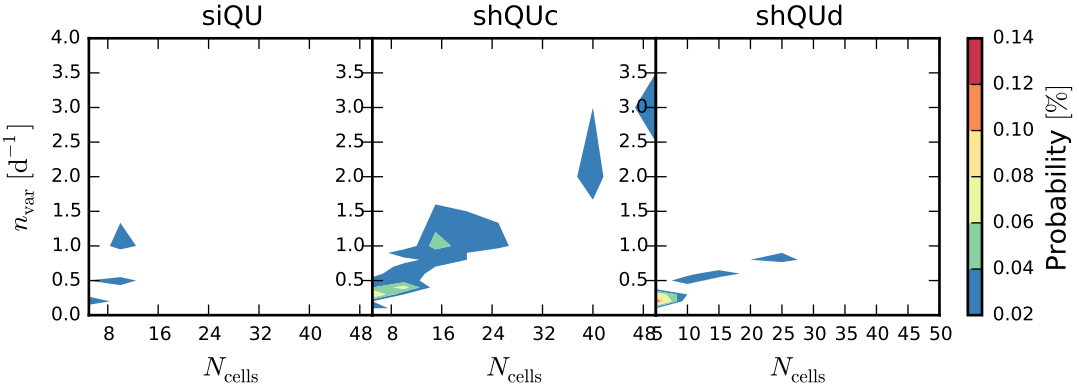

Figure 7.40: Probability of the random walk processes producing the polarization angle variation (pol. angle condition 1+2) observed during period IIIc over the number of cells N_{cells} and the cell variation rate n_{var}.

7.5 Distribution of rotation amplitudes

In the total optical EVPA curve we identify 111 rotations with amplitudes ranging between 1° and 170° using the algorithm introduced in section 6.7 at a 3σ-significance level, $\varsigma = 3$. Observational gaps are not counted as significant rotation. The distribution of the absolute rotation amplitudes is shown in fig. 7.41. We point

out, that here we use the strict definition of a rotation as given in section 6.7. The identified rotations are not the same as those previously identified by eye.

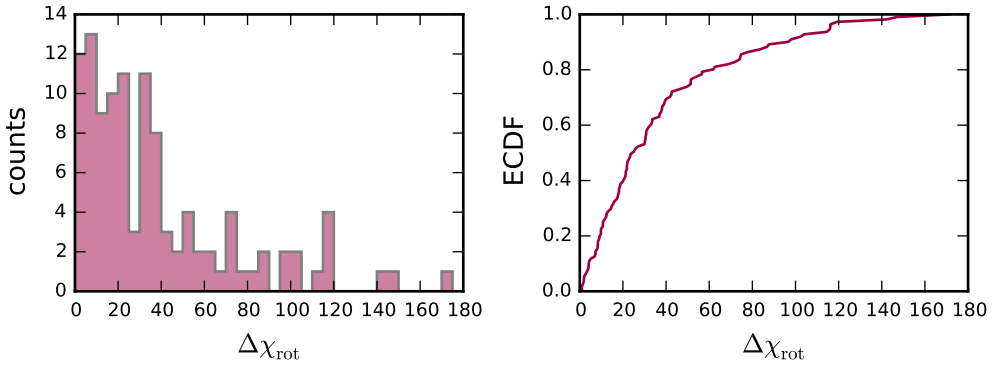

Figure 7.41: Distribution of the absolute amplitudes $|\Delta\chi_{\rm rot}|$ of rotations in the full optical EVPA curve of 3C 279 identified at 3σ-significance.

In the following we test whether this distribution is consistent with a random walk process. Therefore we run single random walk simulations with a total time of $T = 100\,000\,\mathrm{d}$, all other secondary model parameters as given in tables 6.6 and 6.7 for each model and each combination of the two main model parameters in the ranges:

$$N_{\rm cells} \in [10, 20, \ldots, 300]$$
$$n_{\rm var} \in [4, 8, \ldots, 40]\mathrm{d}^{-1}$$

The simulated EVPA curves are adjusted with eqs. (6.14) and (6.15) and rotations are identified at a significance level ς=3. Figure 7.42 exemplary shows the amplitude distribution of identified EVPA rotations for four siQU simulations with different $N_{\rm cells}$ and $n_{\rm var}$. The full distribution (orange filled range) consists of two populations of identified rotations: rotations containing only (a) two and rotations including (b) more than two data points. The corresponding distributions are shown as red (two-point-rotations) and blue (multiple-point-rotations) lines. For small cell variation rates (left panels) both population distributions show a gradual decrease over the largest range of amplitudes. The two data point population distribution is cut off at $\sim 90\,^\circ$ due to the $180\,^\circ$-ambiguity. EVPA errors allow for slightly larger two point rotations. The distribution tail at the smallest rotations is affected by the smallest simulation time step and the cell number and variation rate. For higher variation rates the EVPA variation becomes more erratic and two point rotations are more likely to be identified as significant, consequentially the two point rotations become more prominent. The multiple point population shifts to higher amplitudes as the cell variation rate increases. The distribution tail at low amplitudes decreases as higher amplitudes and two point rotations become more likely. The distribution further depends on the identification significance level ς. Increasing ς decreases the contribution of the two point population as those rotations are less likely to be identified as significant.

We perform a two-sample KS test comparing the absolute rotation amplitudes identified in the observed EVPA curve and in the simulated curves for all model parameter combinations given above. We show the test p-values over the parameter space in fig. 7.43. Solid lines mark the contours of 1σ, 2σ and 3σ rejection. The

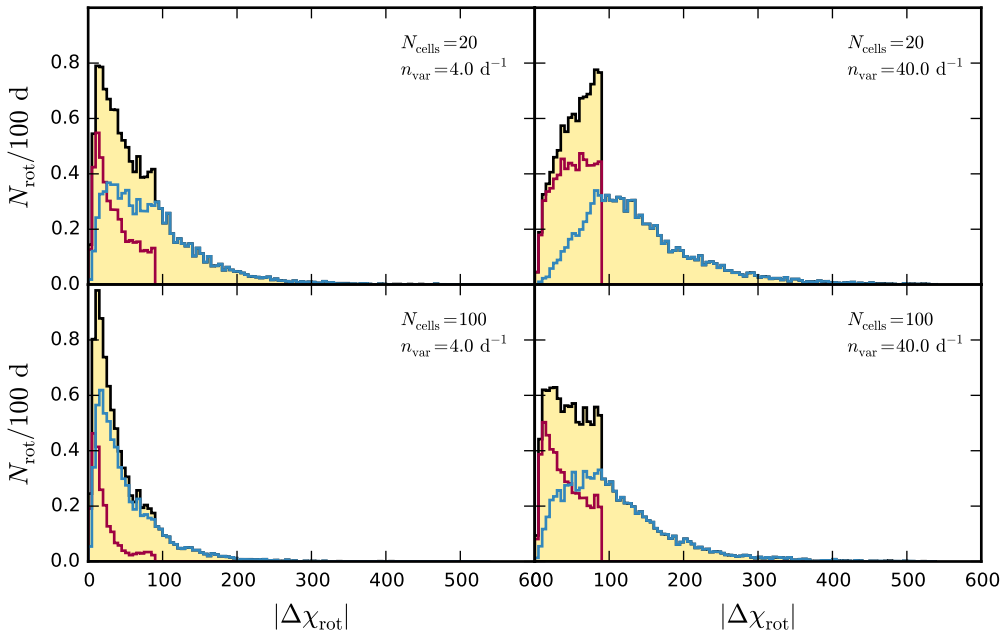

Figure 7.42: Distribution of the absolute amplitudes $|\Delta\chi_{\rm rot}|$ of rotations identified at 3σ-significance in siQU model simulations with different cell numbers and cell variation rates. Red line: distribution of two-data-point rotations, blue line: distribution of multiple-data-point rotations, orange filled region: distribution of all rotations.

model cannot be rejected with 2σ significance at high cell numbers $N_{\rm cells} \gtrsim 60$ and low cell variation rates. In this parameter range the random walk processes can produce longer rotations up to the observed $\sim 170\,°$. For lower cell numbers or higher variation rates the resulting EVPA curve is too erratic, resulting in shorter rotation. As shown in fig. 7.35 low cell numbers $N_{\rm cells} \lesssim 50$ are needed to produce the observed high polarization fraction. In this parameter range we reject the hypothesis that the rotation distribution is produced by a random walk process at 3σ significance.

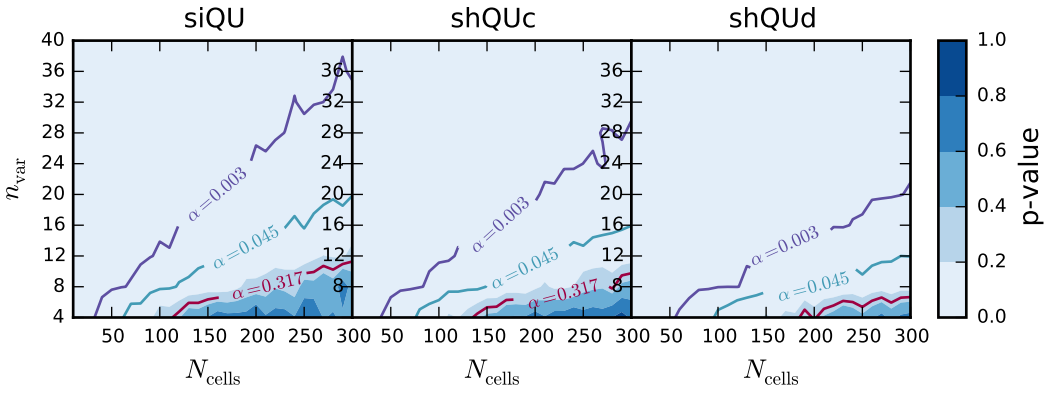

Figure 7.43: P-values of the KS-test, testing the observed against simulated rotation amplitude distributions based on the three random walk processes.

We conclude that the overall distribution of rotations identified in the observed data is not produced by a random walk process. The selected periods are too short to get reliable estimates of the rotation amplitude distribution. Therefore, we do not test single periods against the simulations.

7.6 Conclusion: two classes of processes

We have tested the random walk polarization models, introduced in sections 7.1.2 to 7.1.4 against the optical polarization data, especially focussing on the two major rotation events happening during period IIa and period IIIc. In section 7.5 we have argued that the distribution of the identified, significant rotations in the full data set is not compatible with a random walk process. This is consistent with the result for period IIIc. The random walk models are rejected for the smooth EVPA rotation during that period. A random walk process would either produce a smooth variation of lower amplitude or a much more erratic variation of comparable amplitude. Producing the observed smooth rotation of 352 degrees is generally unlikely ($< 0.1\,\%$). Given the high polarization fraction, which indicates very few cells for a random walk model, the probability is even lower ($< 0.0001\,\%$).

On the other hand, we have pointed out in sections 7.4.1 and 7.4.2 that the EVPA variation during period IIa shows the typical behaviour of a random walk process. The erratic variation and the total amplitude are consistent with the observed mean polarization fraction. However, the probability of producing the variation observed in both the polarization fraction and the EVPA as described in section 6.8 is generally low. The reason is, that the standard deviation of the polarization fraction is incompatible with the mean value, if the data were based on a random walk process. Yet, we could argue that the standard deviation and the mean are probably overestimated due to a few highly uncertain, outlying data points in the polarization fraction data. With those data points removed the polarization data is a possible realization of a random walk process, which occurs with a probability of up to $7\,\%$. All the three random walk processes can be an origin of the observed variation during period IIa.

In the two periods IIa and IIIc we observe very different behavior. During period 2a the (optical) jet is in a low-brightness state (c.f. fig. 6.13), the polarization fraction mean is significantly lower than averaged over the full data set (table 6.5), the EVPA variation is very erratic indicated by a variation estimator significantly higher than during any other period (excluding IIIb) and the whole polarization variation is probably consistent with a random walk process. During period IIIc the jet is flaring throughout the entire spectrum, the mean polarization fraction is slightly higher than averaged over the full data set, the EVPA variation is very smooth compared to period IIa, and the total polarization variation cannot be explained by a random walk.

We come to the conclusion that we observe two different processes during the low-brightness state and the flaring state of the jet. The significantly lower polarization fraction during the low-brightness state is compatible with a larger emission region consistent with a high number of cells (> 100). The turbulent medium of the quiescent optical jet may produce the observed polarization variation, as modelled by the siQU process. For simplification we have fixed the intensity of each cell. Additional variation of the total intensity of each cell may increase the polarization variation further. This interpretation does not require the entire jet magnetic field structure to be turbulent on all scales. The large scale structure could be well structured. For instance the integrated polarization of a large scale helical magnetic field would partially cancel out when emission from all parts of the structure reaches the observer. Small scale turbulence at the order of the cell size would be sufficient to produce a stochastic polarization variation. We suggest that this stochastic part of the polarization variation is always present but only

clearly observable during a quiescent state.

During the flaring state the jet emission is highly polarized implying a significantly smaller emission region. This small bright region dominates the overall polarization variation. The variation during the flaring period cannot be explained by one of the random walk processes tested here. We suggest that the polarization variation during the flaring period is due to a different process, possibly a geometric effect as a small emission region on a helical path passing through a helical magnetic field (Marscher et al., 2008). However, we cannot dismiss stochastic models in general.

We have focused on the two major rotation events and neglected discussing the other periods so far. Periods IVa,b,c occur during the continuous flaring state. Although not explicitly tested and despite the lower EVPA amplitudes we suspect these rotations cannot be explained by the random walk processes, since the EVPA variation is still very smooth. Towards the end of period IV, when the total flux decreases in IVc the EVPA variation becomes more erratic again. In the two-processes-interpretations this part could indicate the stochastic variation of the quiescent jet to become gradually predominant again. Periods IIIa, preceding the prominent flaring epochs, happens during a higher flux state though not strongly flaring. The polarization fraction is comparable to period IIIc and the EVPA variation is comparably smooth and this period is probably part of the same event as period IIIc. Figure 7.37 implies that the observed $\sim 90\,^\circ$ rotation is unlikely due to a random walk. The random walk processes at this high polarization fraction tend to result in much larger rotations. Period IIIb is sampled with too few data points to draw any reliable conclusions. But since we expect periods IIIa and IIIc to be related to the same event, the sharp EVPA drop during period IIIb has to be explained by the same mechanism.

Period IIb is much more polarized than period IIa though even lower in total intensity. since the observation gap after JD 2455400 does not allow to track the following polarization and total flux variation, we cannot draw any justified conclusions whether the drastic increase of the polarization fraction in period IIb marks the beginning of the following flaring period or if it is still a continuation of the low-brightness stochastic variation.

Period I captures the end of a flare prior to our data set. The total flux fades into a low though not fully quiescent state. The polarization fraction is exceptionally high in the beginning. Nevertheless, the polarization angle shows little variation and thus an exceptionally smooth curve, both during the end of the flare and the low-brightness part. Thus, period I does neither show consistent behaviour with the other flaring periods, which exhibit strong EVPA rotations, nor with the low-brightness state, which shows extremely erratic EVPA variation.

In conclusion we point out, that the polarization variability of 3C 279 shows complex behaviour which most likely cannot be explained by a single physical process.

Chapter 8

Deterministic polarization variation models

In chapter 7 we have shown that the continuous EVPA rotation during epoch IIIc and probably the following rotations cannot be explained by a stochastic process. In this chapter we discuss several deterministic models which produce smooth variations of the EVPA.

Holmes et al. (1984) discussed polarization swings due to the superposition of two polarized components. In fig. 8.1 we show examples of such swings. We have two components equally polarized with 73 % but with different polarization angles. During the total time T the flux of the second component rises from zero to twice the constant flux of the first component. We show the characteristic changes of the integrated polarization fraction and EVPA for different angles $\Delta\chi$ between the EVPAs of the two components.

A change of the polarization fraction and angle can be produced by a change of the relative flux or polarization fraction (or angle) of the two components. The amplitude of the EVPA swing is limited to the relative angle between the two components. Thus, rotations produced by two components always smaller than 90 °. Multiple components could, in principle, subsequently evolve to produce any kind of EVPA swing, but aligning at least four components accordingly to produce a $\sim 360\,^\circ$-rotation as observed during epoch IIIc is unlikely. Therefore, we dismiss this model as possible explanation for the observed long EVPA swings.

Nalewajko (2010) discusses polarization swings due to curved trajectories of the emission region. This model assumes a magnetic field axially symmetric with respect to the bending flow direction and a small emission region moving within this flow. The EVPA is either parallel or perpendicular to the projected velocity direction. Thus, changes of the flow direction correspond directly to changes of the EVPA and both are affected by relativistic aberration. Given a relativistic velocity, a small change of the angle between the jet flow and the line of sight appears a much larger angle and, thus, can produce EVPA swings up to 180 °.

This model has been used by Nalewajko (2010) and Abdo et al. (2010a) to explain the apparent $\sim 180\,^\circ$ swing in 3C 279 at JD 2454880 − 900. While this epoch is contained in our data, the EVPA variation does not exceed 90 ° given our polarization data.

Aleksić et al. (2014) observe only a part of the epoch IIIc rotation with an amplitude of $\sim 140\,^\circ$ and use the bending jet model to explain this rotation. We can clearly reject the bending jet hypothesis for this EVPA rotations as it largely exceeds 180 °. The model presented by Zhang et al. (2014) also cannot explain

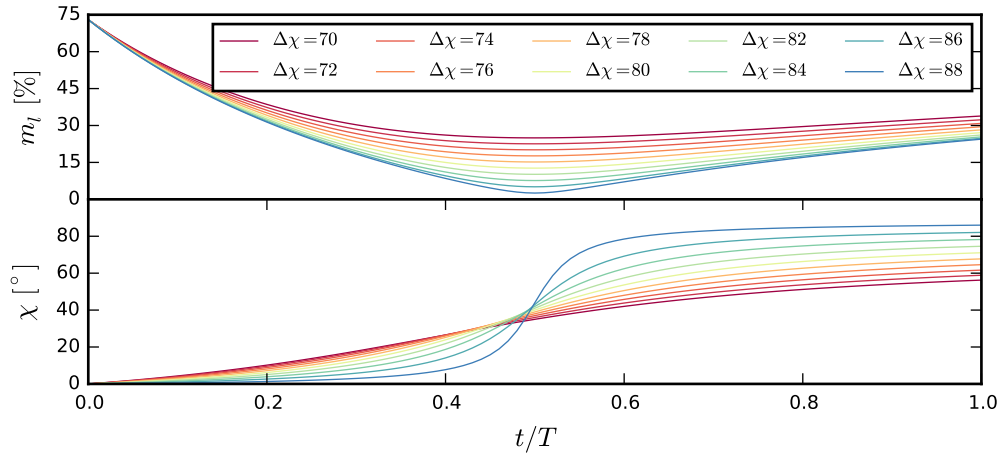

Figure 8.1: Polarization fraction and angle variation due to the linear flux increase of a second polarized component with a relative polarization angle $\Delta\chi$ between the two components.

rotations larger than 180 °, unless multiple shocks are involved.

Currently the most favourable model is that of an emission region on a helical path in a helical magnetic field. This model assumes that the polarization variability is dominated by a small emission region, which does not fill the cross-section of the jet. This emission region moves on a helical trajectory, gradually tracing different parts of the jet. If the magnetic field is toroidal or helical the emission site gradually moves through parts of the magnetic field with different orientation of the magnetic field lines. Since the EVPA is perpendicular to the magnetic field projected on the sky, the EVPA gradually changes. The rotation of the EVPA is connected to the physical rotation of an emission region within the cross-section of the jet as it is moving down the jet. Since this rotation is in principle not limited, this model can produce arbitrary large EVPA rotations.

The initial angular momentum of the emission region, resulting in the helical motion, may be directly connected to the jet launching mechanism: either to the ergosphere of the rotating black hole Blandford and Znajek (1977) or the rotating accretion disc Blandford and Payne (1982).

The model of a helical motion in a helical magnetic field has been applied to several EVPA rotations reported in the literature. Kikuchi et al. (1988) explain a series of EVPA swings in OJ 287 by a shock traversing a helical magnetic field. Marscher et al. (2008) phenomenologically introduce the model of a helical motion in a helical magnetic field to explain a $\sim 190\,^\circ$ rotation in BL Lac. This model has further been applied to a 720 ° rotation in PKS 1510−089 by Marscher et al. (2010) and Larionov et al. (2008) explain the $\sim 300\,^\circ$ rotation of the optical and 43 GHz EVPA in 3C 279 in 2006-2007 with this model.

We currently work on our own implementation of this model. Changes of the EVPA-rotation direction pose a critical point to the model of a physical rotation of an emission region within the jet as this rotation cannot change the direction. We point out again, that we interpret the EVPA-rotation during period IIa to originate from a different, a stochastic process. This clockwise rotation does not conflict with the counter-clockwise rotation during period IIIc. But even the rotation during period IIIc shows several significant changes of the rotation direction. As a preliminary result, we point out, that our model is capable of producing such changes, which is a projection effect. Additionally, the superposition of a

small rotating emission region and a constant or stochastically changing, polarized background introduces further variation of the EVPA, which may lead to temporary changes of the general rotation direction. Once this has been thoroughly tested, we will try to fit the observed 360 ° rotation with it. Consistency with such a model would be a strong indication for a predominantly helical magnetic field structure.

Chapter 9

Summary and outlook

The origin of the γ-ray emission and the structure of the magnetic field pose two of the main questions in blazar astrophysics. A large fraction of the energy output of a blazar is in the high frequency component of the spectrum ranging from keV to GeV and occasionally even TeV energy. The question for the origin of this radiation regards to the physical process and the location where this process takes place. Currently, the two main classes of emission models – leptonic models on the on hand, hadronic models on the other hand – cannot be discriminated. And even for leptonic models, which are based on Inverse Compton scattering, it is not clear, where the seed photons participating in the IC process come from, the jet itself, other parts of the AGN or the CMB. Thus, locating the emission site can give an indication to the underlying process.

No matter which process, highly relativistic particles are required to produce radiation at GeV and TeV energies. Magnetic fields are expected to play a major role in the acceleration of the particles: on the one hand acceleration of the bulk flow up to Lorentz factors at the order of $\Gamma \sim 10$, on the other hand the acceleration of individual particles to Lorentz factors at the order of $\gamma \sim 10^5$ or even higher. Whether the magnetic field structure is predominantly ordered, e.g. helical, or tangled is debated.

This thesis addresses both questions. First, we try to understand the connection between the physical processes responsible for the low energy component (radio to ultraviolet) and the high energy component (x-rays and γ-rays) through the analysis of multi-frequency photometry data of 3C 279. Secondly, we use densely sampled polarimetry data to infer information about the magnetic field of 3C 279. The archetypical blazar 3C 279 is one of the best monitored blazars. The data used in this thesis are provided by the Quasar Movie Project.

Processing the individual light and polarization curves into concisely combined data sets was an essential part of this project. We have developed new algorithms for the cross-calibration and averaging of light curves and recommend to use these algorithms for similar studies. With the combination of more than hundred light and polarization curves we have obtained a data set, exceptionally well sampled in the time and frequency domain. The light curves include multiple flaring events over the whole frequency range, some of which have previously been discussed in the literature.

On the origin of the high energy radiation. We have discussed in detail the methodology of the Power Spectral Density estimation and the cross-correlation analysis and proposed several advancements over the methods reported in the

literature. We have thoroughly tested and discussed the effects of red noise leakage, aliasing, and observational noise on the estimation of the power spectrum. We have presented a method to estimate the power spectrum of an unevenly sampled light curve, including a way of estimating the uncertainties due to light curve re-sampling. We note that it is inevitable to de-trend light curves in order to discriminate the power spectral indices of intrinsically steep spectra. Furthermore, we have introduced methods to estimate the confidence interval of the power spectral index, the model p-value, the rate of false model rejections, and a reliability test of the method itself.

In the context of the PSD estimation and the correlation analysis we have discussed various approaches of simulating light curves. Whereas we note that the Timmer and Koenig (1995) algorithm is currently the best way to simulate light curves for the PSD estimation, we point out that Gaussian light curves do not correctly represent the variability of the observed light curves. We have discussed the algorithm of Emmanoulopoulos et al. (2013) and point out that the significance estimation of the cross-correlation function depends on the choice of the algorithm used to simulate light curves. Correlations are potentially overestimated using simulated Gaussian light curves.

Applying our method of the PSD estimation to the photometry data set, we have determined the PSDs of contemporaneous light curves at 26 different bands. We find that throughout the entire frequency range the power spectrum is consistent with a red noise process. At cm and mm bands we find a gradual steepening of the power spectral index towards lower frequencies. This result is consistent with an increasing emission region size towards lower frequencies, which can be explained either by the cooling time dependence on the particle energy or by an opacity effect in an expanding flow region. Accordingly, we see a gradual time delay between the radio light curves with higher frequencies leading lower frequencies. We have tested the delays against the opacity model and find them consistent with Synchrotron Self-Absorption in a conical jet in equipartition.

The mm power spectra are comparable to the PSDs in the infrared, optical, and ultraviolet frequency range, implying that the radiation at these bands is produced, probably cospatially, by the same population of particles, only at different ranges of the energy distribution. Correlation time lags consistent with zero between all infrared, optical, and ultraviolet bands and between the long term variability of the 1 mm and V-band light curve support this hypothesis. On the other hand the short term variability shows V-band lagging behind 1 mm, indicating a more complex situation. A similar power spectrum between sub-mm bands and X-rays is indicated. This result is consistent with a SSC process where X-rays are produced by the same electron population which emits synchrotron radiation at sub-mm bands. This hypothesis is strengthened by the significant cross-correlation of the short term variability of X-rays and the 1 mm band. The correlation time lag is zero within the uncertainties. Thus, X-rays, at least those contributing to the short term variability of the light curve, are produced at the same emission site as the mm synchrotron radiation, i.e. the mm VLBI core. The mm VLBI core typically is assumed to be located outside of the BLR, implying that the seed photons scattered to keV energies do not originate in the AGN disc or BLR. Instead, we have argued that mm synchrotron photons and CMB photons serve as potential candidates for seed photons. We point out that, to our knowledge, such strong correlation between X-rays and mm bands has not been reported and the analysis of the short term variability through de-trending of the light curve is only possible due to the high

sampling rates achieved by combining several light curves of different instruments.

The optical to ultraviolet frequency range indicates a gradual flattening of the variability power spectrum. This trend is not significant given the uncertainties, but could indicate a power spectral index at far-ultraviolet bands similar to the γ-ray power spectrum. This could imply that the same particle population produces the radiation at the far-ultraviolet through synchrotron radiation and γ-rays through IC scattering. We have found strong correlations between all infrared, optical and ultraviolet bands consistent with zero time lag. Therefore, we conclude that the emission in those bands is produced at one emission site. Assuming far-ultraviolet and γ-rays are produced by the same particle population, this further implies that the γ-rays are produced at the same site as the infrared to ultraviolet radiation.

This hypothesis is supported by the zero time lag correlation of V-band and γ-rays before approximately JD 2455400. In this part of the light curves all flares occur during a general flux decrease in the radio bands. With the exception of the X-ray flare at JD 2454950, which is not accompanied by strong γ-ray variability and only a minor flare in optical bands, flaring activity occurs throughout all bands. And we have identified flare peaks consistent with zero time lag. During the radio decreasing period flaring activity throughout the whole spectral range from infrared to γ-rays probably originates from the same emission region. We have located one X-ray emission site, responsible for the short term varibility, at the mm VLBI core. Coinciding X-ray and γ-ray flares may also imply that the γ-ray emission originates at the mm core. We have identified two potential seed photon fields for the γ-ray in a leptonic process: either SSC scattering with seed photons at infrared frequencies or the infrared photons could originate in the dust torus of the AGN. SSC-scattering is improbable for a high Compton dominance source as 3C 279. Thus, the dust torus is the most likely source of seed photons for IC-scattering to γ-rays.

Flaring activity after approximately JD 2455400 happens during a gradual flux increase throughout all radio bands. The continuous rise of radio flux implies one or multiple new injections of particles into the jet. This should be further investigated with radio interferometry data. In this part of the data, we have found ambiguous correlation results between radio frequencies, optical frequencies, X-rays, and γ-rays. The most significant correlation between V-band and X-rays suggests V-band lagging by 250 days. This result is consistent with the time lags between V-band and radio frequencies. This long time lag corresponds to a distance of approximately 1.8 parsec, posing a severe problem of maintaining a physical connection over such a large distance. We propose that an injected population of particles traverses two subsequent shock regions. The first shock accelerates the particles such that radio and mm synchrotron radiation is emitted, the second shock re-accelerates the particles to higher energies such that synchrotron radiation up to ultraviolet frequencies is emitted. Alternatively, a constant structure in the emission flow could produce similar patterns in the variability. Multiple injections of particles with different initial energies could produce the observed variability. These multiple injections could further explain the gradual increase of the radio flux. The particle population at lower energies has longer cooling times as higher energies and multiple injections can overlap in the radio bands. A third option is the continuous acceleration in a moving shock traversing through a gradually changing environment, i.e. changing magnetic field strength or changing ambient photon field or both. Thus, the ratio of power emitted through synchrotron radiation and through IC-scattering would change over time.

The γ-ray correlation with V-band and X-rays is uncertain after JD 2455400. The time dependent changes of the correlation time lags between the different frequencies could imply that we observe flares from various emission regions with different local conditions. This complicates the interpretation of the cross-correlation functions. As future studies we plan to analyse SEDs, to estimate the spectral indices at radio bands, optical bands, X-rays, and γ-rays in order to find correlations between the spectral indices and the light curves. These studies may indicate how to proceed with the interpretation of the current results, showing a complex and time-dependent behaviour of flaring activity at all bands.

On the magnetic field structure. We have introduced various new methods for the analysis of polarization data. The $180\,^\circ$ ambiguity of the Electric Vector Position Angle is a critical point in the interpretation of polarization data. We have discussed different methods of reconstructing the intrinsic variation of the EVPA and introduced a method which allows to estimate the reliability of the reconstruction. The interpretation of EVPA rotations is commonly based on arguments about the apparent smoothness of the rotation. With the *variation estimator* we have introduced a quantitative measure of the smoothness of a curve. Furthermore, we have presented an algorithm to identify continuous, significant EVPA rotations based on a clear definition of a rotation. The concise identification of rotations is especially important in statistical studies of rotation events and we recommend to use a clear definition of a rotation event and the corresponding implementation like ours in such studies.

With the combination of data from various instruments we have obtained an unprecedentedly well sampled optical polarization curve. The data shows rotations of the EVPA in both directions of various rotation rates and amplitudes. We have focused our studies on the two largest rotation events: a $\sim 500\,^\circ$ clockwise rotation at JD $2455100 - 5310$ during a general low brightness state of the jet and a $\sim 360\,^\circ$ counter-clockwise rotation at JD $2455658 - 5850$ coinciding with strong flaring activity throughout all bands. While the former rotation has a larger amplitude, the latter shows a significantly smoother variation.

We have described three stochastic processes, implemented as a random walk through Stokes Q-U space, as toy models of (a) a turbulent plasma and (b) a shock moving through a turbulent plasma in two slightly different configurations. We have tested whether the two largest observed rotations can be produced by these processes. Here, we have considered the mean and standard deviation of the polarization fraction and the amplitude and smoothness of the EVPA as observational parameters to be reproduced by the models. We have pointed out that it is recommended to test a large parameter space, instead of fixing model parameters based on the polarization fraction as it is usually practised in comparable studies. We have noticed that the random walk processes discussed in this thesis can, in principle, produce arbitrarily large rotations and very smooth rotations, depending on the model parameters and the simulation time. But increasingly large rotations are less likely to be smooth and vice versa. Therefore, it is not sufficient to test, whether a model can produce an observed rotation amplitude. Instead, we have tested if the processes can produce a rotation of comparable amplitude and smoothness. In this context we emphasize again the importance of a quantitative measure of smoothness as introduced in this thesis.

Based on a large set of simulations we have shown that the $\sim 500\,^\circ$ rotation is consistent with the erratic EVPA variability of a random walk process. On

the other hand the smooth $\sim 360\,^\circ$ rotation is highly unlikely to occur from a random walk process. We suggest that we observe two different processes during the low brightness state and the flaring state. The polarization variability follows a stochastic process during the low brightness state, probably due to turbulence in the optical jet. A higher polarization fraction during the flaring state implies that the polarization variation is dominated by a significantly smaller emission region. The variability during the flaring state does not follow a stochastic process.

We have discussed different deterministic processes which can explain smooth gradual changes of the polarization angle. We can with certainty reject the bending jet scenario, since we observe a rotation of $\sim 360°$, significantly larger than $180\,^\circ$. Thus, we contradict Aleksić et al. (2014) who observed only a part of this rotation event. Currently, the most favourable model is that of an emission feature on a helical path in a helical magnetic field. An implementation of this model is currently in progress. Once, we have tested this model against the observed data, a good fit would be a strong argument for a predominantly helical magnetic field at the optical emission site.

Future prospects. So far, we have focused our studies on (a) the photometry data, estimating the variability power spectra of the light curves and estimating correlation time lags between the light curves, in order to locate the emission region of the high energy radiation, and (b) on the polarimetry data, especially testing different stochastic models against the data, to understand the structure of the magnetic field. We have already noted that an implementation of the helical motion in a helical magnetic field model is in progress to test it against the smooth $\sim 360\,^\circ$ EVPA rotation.

We have restricted the PSD analysis to a simple power-law model, limiting the model test to a one dimensional problem of estimating the power spectral index. The RXTE X-ray data and the V-band data are long enough and sampled well enough to test other spectral models against these data. A break in the variability power spectrum would indicate a characteristic time scale. Complementary to the PSD estimation the structure function analysis allows to estimate characteristic time scales of the variability. Modelling the flares to estimate the typical flaring time scales and to better cross-identify flare peaks throughout the spectrum may increase the accuracy of the time lag estimation. Additionally, including the variability of the spectral indices at various frequency ranges will help to clarify our understanding of the emission processes.

The time and frequency sampling of the Quasar Movie Project data set allows to produce a time series of SEDs posing a great opportunity to test various stationary and time dependent blazar models against the data.

Furthermore, the VLBI data, the most essential part of the Quasar Movie Project observation campaign, has not been incorporated into the analysis yet. These data allow to observe changes of the jet structure, orientation, flow and polarization at six frequencies, and changes of the spectral index at roughly 20 days cadence over more than a year. Combining these data with the photometry and polarimetry data analysed in this thesis provides the most complete, observationally possible picture of a blazar.

Bibliography

A. A. Abdo, et al., *A change in the optical polarization associated with a γ-ray flare in the blazar 3C279*, Nature, 463:pp. 919–923 [2010a].

A. A. Abdo, et al., *Gamma-ray Light Curves and Variability of Bright Fermi-detected Blazars*, ApJ, 722:pp. 520–542 [2010b].

A. A. Abdo, et al., *The Spectral Energy Distribution of Fermi Bright Blazars*, ApJ, 716:pp. 30–70 [2010c].

A. A. Abdo, et al., *The First Fermi Multifrequency Campaign on BL Lacertae: Characterizing the Low-activity State of the Eponymous Blazar*, ApJ, 730:101 [2011].

I. Agudo, C. Thum, J. L. Gómez, and H. Wiesemeyer, *A simultaneous 3.5 and 1.3 mm polarimetric survey of active galactic nuclei in the northern sky*, A&A, 566:A59 [2014].

I. Agudo, C. Thum, H. Wiesemeyer, and T. P. Krichbaum, *A 3.5 mm Polarimetric Survey of Radio-loud Active Galactic Nuclei*, ApJS, 189:pp. 1–14 [2010].

I. Agudo, et al., *Mapcat: Monitoring AGN with Polarimetry at the Calar Alto Telescopes*, International Journal of Modern Physics Conference Series, 8:pp. 299–302 [2012].

J. Aleksić, et al., *MAGIC observations and multifrequency properties of the flat spectrum radio quasar 3C 279 in 2011*, A&A, 567:A41 [2014].

H. D. Aller, M. F. Aller, G. E. Latimer, and P. E. Hodge, *Spectra and linear polarizations of extragalactic variable sources at centimeter wavelengths*, ApJS, 59:pp. 513–768 [1985].

E. Angelakis, et al., *Radio jet emission from GeV-emitting narrow-line Seyfert 1 galaxies*, A&A, 575:A55 [2015].

R. R. J. Antonucci and J. S. Miller, *Spectropolarimetry and the nature of NGC 1068*, ApJ, 297:pp. 621–632 [1985].

W. B. Atwood, et al., *The Large Area Telescope on the Fermi Gamma-Ray Space Telescope Mission*, ApJ, 697:pp. 1071–1102 [2009].

W. Baade and R. Minkowski, *Identification of the Radio Sources in Cassiopeia, Cygnus A, and Puppis A.*, ApJ, 119:p. 206 [1954].

A. J. Beasley and J. E. Conway, *VLBI Phase-Referencing*, in J. A. Zensus, P. J. Diamond, and P. J. Napier (Eds.), *Very Long Baseline Interferometry and the VLBA*, vol. 82 of *Astronomical Society of the Pacific Conference Series*, p. 327 [1995].

M. S. Bessell, *UBVRI photometry. II - The Cousins VRI system, its temperature and absolute flux calibration, and relevance for two-dimensional photometry*, PASP, 91:pp. 589–607 [1979].

J. A. Biretta, W. B. Sparks, and F. Macchetto, *Hubble Space Telescope Observations of Superluminal Motion in the M87 Jet*, ApJ, 520:pp. 621–626 [1999].

R. D. Blandford and D. G. Payne, *Hydromagnetic flows from accretion discs and the production of radio jets*, MNRAS, 199:pp. 883–903 [1982].

R. D. Blandford and R. L. Znajek, *Electromagnetic extraction of energy from Kerr black holes*, MNRAS, 179:pp. 433–456 [1977].

S. D. Bloom, C. M. Fromm, and E. Ros, *The Accelerating Jet of 3C 279*, AJ, 145:12 [2013].

E. Bonning, et al., *SMARTS Optical and Infrared Monitoring of 12 Gamma-Ray Bright Blazars*, ApJ, 756:13 [2012].

M. Böttcher, *Modeling the Spectral Energy Distributions and Variability of Blazars*, ArXiv e-prints 1205.0539 [2012].

M. Böttcher, D. E. Harris, and H. Krawczynski (Eds.), *Relativistic Jets from Active Galactic Nuclei*, 1st ed., Wiley-VCH [2012].

M. Böttcher, A. Reimer, K. Sweeney, and A. Prakash, *Leptonic and Hadronic Modeling of Fermi-detected Blazars*, ApJ, 768:54 [2013].

M. Böttcher, et al., *The WEBT Campaign on the Blazar 3C 279 in 2006*, ApJ, 670:pp. 968–977 [2007].

D. N. Burrows, et al., *The Swift X-Ray Telescope*, in K. A. Flanagan and O. H. W. Siegmund (Eds.), *X-Ray and Gamma-Ray Instrumentation for Astronomy XIII*, vol. 5165 of *Society of Photo-Optical Instrumentation Engineers (SPIE) Conference Series*, pp. 201–216 [2004].

H. Campins, G. H. Rieke, and M. J. Lebofsky, *Absolute calibration of photometry at 1 through 5 microns*, AJ, 90:pp. 896–899 [1985].

J. A. Cardelli, G. C. Clayton, and J. S. Mathis, *The relationship between infrared, optical, and ultraviolet extinction*, ApJ, 345:pp. 245–256 [1989].

A. Carraminana, L. Carrasco, A. Porras, and E. Recillas, *Extensive near infrared monitoring of millimeter-wave / gamma-ray bright blazars*, ArXiv e-prints 1001.0204 [2010].

R. Chatterjee, et al., *Correlated Multi-Wave Band Variability in the Blazar 3C 279 from 1996 to 2007*, ApJ, 689:pp. 79–94 [2008].

R. Chatterjee, et al., *Similarity of the Optical-Infrared and γ-Ray Time Variability of Fermi Blazars*, ApJ, 749:191 [2012].

M. Cohen, W. A. Wheaton, and S. T. Megeath, *Spectral Irradiance Calibration in the Infrared. XIV. The Absolute Calibration of 2MASS*, AJ, 126:pp. 1090–1096 [2003].

W. D. Cotton, et al., *3C 279 - The case for 'superluminal' expansion*, ApJ, 229:pp. L115–L117 [1979].

A. W. J. Cousins, *Standard Stars for VRI Photometry with S25 Response Photocathodes*, Monthly Notes of the Astronomical Society of Southern Africa, 35:p. 70 [1976].

F. D. D'Arcangelo, et al., *Rapid Multiwaveband Polarization Variability in the Quasar PKS 0420-014: Optical Emission from the Compact Radio Jet*, ApJ, 659:pp. L107–L110 [2007].

A. Dolcini, et al., *Multiband photometry of the blazar PKS 0537-441: a major active state in December 2004-March 2005*, A&A, 443:pp. L33–L36 [2005].

V. T. Doroshenko, et al., *BVRI CCD-Photometry of Comparison Stars in the Neighborhoods of Galaxies with Active Nuclei. I*, Astrophysics, 48:pp. 156–178 [2005].

R. A. Edelson and J. H. Krolik, *The discrete correlation function - A new method for analyzing unevenly sampled variability data*, ApJ, 333:pp. 646–659 [1988].

D. Emmanoulopoulos, I. M. McHardy, and I. E. Papadakis, *Generating artificial light curves: revisited and updated*, MNRAS, 433:pp. 907–927 [2013].

M. Errando, et al., *Discovery of very high energy gamma-rays from the flat spectrum radio quasar 3C 279 with the MAGIC telescope*, in F. A. Aharonian, W. Hofmann, and F. Rieger (Eds.), *American Institute of Physics Conference Series*, vol. 1085 of *American Institute of Physics Conference Series*, pp. 423–426 [2008].

B. L. Fanaroff and J. M. Riley, *The morphology of extragalactic radio sources of high and low luminosity*, MNRAS, 167:pp. 31P–36P [1974].

E. A. Fath, *The spectra of some spiral nebulae and globular star clusters*, Lick Observatory Bulletin, 5:pp. 71–77 [1909].

E. Fermi, *On the Origin of the Cosmic Radiation*, Physical Review, 75:pp. 1169–1174 [1949].

L. Fuhrmann, et al., *Detection of significant cm to sub-mm band radio and γ-ray correlated variability in Fermi bright blazars*, MNRAS, 441:pp. 1899–1909 [2014].

D. C. Gabuzda, É. Murray, and P. Cronin, *Helical magnetic fields associated with the relativistic jets of four BL Lac objects*, MNRAS, 351:pp. L89–L93 [2004].

N. Gehrels, *The Swift Gamma-Ray Burst Mission*, in *American Astronomical Society Meeting Abstracts*, vol. 36 of *Bulletin of the American Astronomical Society*, p. 116.01 [2004].

C. A. Glasser, C. E. Odell, and S. E. Seufert, *The proportional counter array (PCA) instrument for the X-ray timing explorer satellite (XTE)*, IEEE Transactions on Nuclear Science, 41:pp. 1343–1348 [1994].

J. N. González-Pérez, M. R. Kidger, and F. Martín-Luis, *Optical and Near-Infrared Calibration of AGN Field Stars: An All-Sky Network of Faint Stars Calibrated on the Landolt System*, AJ, 122:pp. 2055–2098 [2001].

J. Gubbay, et al., *Variations of Small Quasar Components at 2,300 MHz*, Nature, 224:pp. 1094–1095 [1969].

A. C. Gupta, J. H. Fan, J. M. Bai, and S. J. Wagner, *Optical Intra-Day Variability in Blazars*, AJ, 135:pp. 1384–1394 [2008].

M. A. Gurwell, A. B. Peck, S. R. Hostler, M. R. Darrah, and C. A. Katz, *Monitoring Phase Calibrators at Submillimeter Wavelengths*, in A. J. Baker, J. Glenn, A. I. Harris, J. G. Mangum, and M. S. Yun (Eds.), *From Z-Machines to ALMA: (Sub)Millimeter Spectroscopy of Galaxies*, vol. 375 of *Astronomical Society of the Pacific Conference Series*, p. 234 [2007].

R. C. Hartman, et al., *Detection of high-energy gamma radiation from quasar 3C 279 by the EGRET telescope on the Compton Gamma Ray Observatory*, ApJ, 385:pp. L1–L4 [1992].

R. C. Hartman, et al., *Multiepoch Multiwavelength Spectra and Models for Blazar 3C 279*, ApJ, 553:pp. 683–694 [2001].

M. Hayashida, et al., *The Structure and Emission Model of the Relativistic Jet in the Quasar 3C 279 Inferred from Radio to High-energy γ-Ray Observations in 2008-2010*, ApJ, 754:114 [2012].

M. Hayashida, et al., *Rapid Variability of Blazar 3C 279 during Flaring States in 2013-2014 with Joint Fermi-LAT, NuSTAR, Swift, and Ground-Based Multi-wavelength Observations*, ArXiv e-prints 1502.04699 [2015].

S. E. Healey, et al., *CRATES: An All-Sky Survey of Flat-Spectrum Radio Sources*, ApJS, 171:pp. 61–71 [2007].

P. A. Holmes, et al., *A polarization flare in OJ 287*, MNRAS, 211:pp. 497–506 [1984].

D. C. Homan, M. L. Lister, H. D. Aller, M. F. Aller, and J. F. C. Wardle, *Full Polarization Spectra of 3C 279*, ApJ, 696:pp. 328–347 [2009].

T. W. Jones, et al., *Magnetic field structures in active compact radio sources*, ApJ, 290:pp. 627–636 [1985].

S. G. Jorstad, et al., *Polarimetric Observations of 15 Active Galactic Nuclei at High Frequencies: Jet Kinematics from Bimonthly Monitoring with the Very Long Baseline Array*, AJ, 130:pp. 1418–1465 [2005].

S. G. Jorstad, et al., *Flaring Behavior of the Quasar 3C 454.3 Across the Electromagnetic Spectrum*, ApJ, 715:pp. 362–384 [2010].

K. S. Kawabata, et al., *Wide-field one-shot optical polarimeter: HOWPol*, in *Society of Photo-Optical Instrumentation Engineers (SPIE) Conference Series*, vol. 7014 of *Society of Photo-Optical Instrumentation Engineers (SPIE) Conference Series* [2008].

K. I. Kellermann, R. Sramek, M. Schmidt, D. B. Shaffer, and R. Green, *VLA observations of objects in the Palomar Bright Quasar Survey*, AJ, 98:pp. 1195–1207 [1989].

S. Kikuchi, Y. Mikami, M. Inoue, H. Tabara, and T. Kato, *A synchronous variation of polarization angle in OJ 287 in the optical and radio regions*, A&A, 190:pp. L8–L10 [1988].

T. D. Kinman, *Optical Polarization Measures of Five Radio Sources*, ApJ, 148:p. L53 [1967].

A. Konigl, *Relativistic jets as X-ray and gamma-ray sources*, ApJ, 243:pp. 700–709 [1981].

O. M. Kurtanidze and M. G. Nikolashvili, , Proc. of the OJ-94 Annual Meeting 1999, Blazar Monitoring toward the Third Millennium, p. 25 [1999].

O. M. Kurtanidze and M. G. Nikolashvili, , Blazar Astrophysics with BeppoSAX and Other Observatories, ASI Special Publication, pp. 189–196 [2002].

R. A. Laing, *A model for the magnetic-field structure in extended radio sources*, MNRAS, 193:pp. 439–449 [1980].

V. M. Larionov, et al., *Results of WEBT, VLBA and RXTE monitoring of 3C 279 during 2006-2007*, A&A, 492:pp. 389–400 [2008].

S. Larsson, et al., *APEX sub-mm monitoring of gamma-ray blazars*, ArXiv e-prints 1206.3799 [2012].

A. M. Levine, et al., *First Results from the All-Sky Monitor on the Rossi X-Ray Timing Explorer*, ApJ, 469:p. L33 [1996].

M. L. Lister, et al., *MOJAVE: Monitoring of Jets in Active Galactic Nuclei with VLBA Experiments. VI. Kinematics Analysis of a Complete Sample of Blazar Jets*, AJ, 138:pp. 1874–1892 [2009].

A. P. Lobanov, *Ultracompact jets in active galactic nuclei*, A&A, 330:pp. 79–89 [1998].

M. S. Longair, *High Energy Astrophysics*, 3rd ed., Cambridge University Press [2011].

B. Lott, L. Escande, S. Larsson, and J. Ballet, *An adaptive-binning method for generating constant-uncertainty/constant-significance light curves with Fermi-LAT data*, A&A, 544:A6 [2012].

R.-S. Lu, et al., *Fine-scale Structure of the Quasar 3C 279 Measured with 1.3 mm Very Long Baseline Interferometry*, ApJ, 772:13 [2013].

A. P. Marscher, *Jets in Active Galactic Nuclei*, ArXiv e-prints 0909.2576 [2009].

A. P. Marscher, *Turbulent, Extreme Multi-zone Model for Simulating Flux and Polarization Variability in Blazars*, ApJ, 780:87 [2014].

A. P. Marscher, *Time-variable linear polarization as a probe of the physical conditions in the compact jets of blazars*, in F. Massaro, C. C. Cheung, E. Lopez, and A. Siemiginowska (Eds.), *IAU Symposium*, vol. 313 of *IAU Symposium*, pp. 122–127 [2015].

A. P. Marscher and W. K. Gear, *Models for high-frequency radio outbursts in extragalactic sources, with application to the early 1983 millimeter-to-infrared flare of 3C 273*, ApJ, 298:pp. 114–127 [1985].

A. P. Marscher, et al., *The inner jet of an active galactic nucleus as revealed by a radio-to-γ-ray outburst*, Nature, 452:pp. 966–969 [2008].

A. P. Marscher, et al., *Probing the Inner Jet of the Quasar PKS 1510-089 with Multi-Waveband Monitoring During Strong Gamma-Ray Activity*, ApJ, 710:pp. L126–L131 [2010].

P. Marziani, J. W. Sulentic, D. Dultzin-Hacyan, M. Calvani, and M. Moles, *Comparative Analysis of the High- and Low-Ionization Lines in the Broad-Line Region of Active Galactic Nuclei*, ApJS, 104:p. 37 [1996].

T. A. Matthews and A. R. Sandage, *Optical Identification of 3c 48, 3c 196, and 3c 286 with Stellar Objects.*, ApJ, 138:p. 30 [1963].

W. Max-Moerbeck, et al., *A method for the estimation of the significance of cross-correlations in unevenly sampled red-noise time series*, MNRAS, 445:pp. 437–459 [2014a].

W. Max-Moerbeck, et al., *Time correlation between the radio and gamma-ray activity in blazars and the production site of the gamma-ray emission*, MNRAS, 445:pp. 428–436 [2014b].

K. Nalewajko, *Polarization Swings from Curved Trajectories of the Emitting Regions*, International Journal of Modern Physics D, 19:pp. 701–706 [2010].

K. Nalewajko, D. Giannios, M. C. Begelman, D. A. Uzdensky, and M. Sikora, *Radiative properties of reconnection-powered minijets in blazars*, MNRAS, 413:pp. 333–346 [2011].

K. Nilsson, T. Pursimo, C. Villforth, E. Lindfors, and L. O. Takalo, *The host galaxy of 3C 279*, A&A, 505:pp. 601–604 [2009].

J. A. Nousek, *Status of Swift Operations and Instruments*, in *American Astronomical Society Meeting Abstracts*, vol. 36 of *Bulletin of the American Astronomical Society*, p. 116.02 [2004].

I. E. Papadakis and A. Lawrence, *Improved Methods for Power Spectrum Modelling of Red Noise*, MNRAS, 261:p. 612 [1993].

J.-H. Park and S. Trippe, *Radio Variability and Random Walk Noise Properties of Four Blazars*, ApJ, 785:76 [2014].

V. Patiño-Álvarez, et al., *Multiwavelength variability analysis of the FSRQ 3C 279*, in F. Massaro, C. C. Cheung, E. Lopez, and A. Siemiginowska (Eds.), *IAU Symposium*, vol. 313 of *IAU Symposium*, pp. 89–90 [2015].

V. Pavlidou, et al., *The RoboPol optical polarization survey of gamma-ray-loud blazars*, MNRAS, 442:pp. 1693–1705 [2014].

T. J. Pearson, et al., *Superluminal expansion of quasar 3C273*, Nature, 290:pp. 365–368 [1981].

B. M. Peterson, et al., *On Uncertainties in Cross-Correlation Lags and the Reality of Wavelength-dependent Continuum Lags in Active Galactic Nuclei*, PASP, 110:pp. 660–670 [1998].

T. S. Poole, et al., *Photometric calibration of the Swift ultraviolet/optical telescope*, MNRAS, 383:pp. 627–645 [2008].

R. Porcas, *Superluminal motions - Astronomers still puzzled*, Nature, 302:p. 753 [1983].

M. Punch, et al., *Detection of TeV photons from the active galaxy Markarian 421*, Nature, 358:p. 477 [1992].

B. Rani, et al., *Jet outflow and gamma-ray emission correlations in S5 0716+714*, A&A, 571:L2 [2014].

J. L. Richards, et al., *Blazars in the Fermi Era: The OVRO 40 m Telescope Monitoring Program*, ApJS, 194:29 [2011].

P. W. A. Roming, et al., *The Swift Ultra-Violet/Optical Telescope*, Space Sci. Rev., 120:pp. 95–142 [2005].

R. E. Rothschild, et al., *In-Flight Performance of the High-Energy X-Ray Timing Experiment on the Rossi X-Ray Timing Explorer*, ApJ, 496:pp. 538–549 [1998].

M. Sasada, et al., *Prominent Polarized Flares of the Blazars AO 0235+164 and PKS 1510-089*, PASJ, 63:pp. 489– [2011].

J. D. Scargle, *Studies in astronomical time series analysis. II - Statistical aspects of spectral analysis of unevenly spaced data*, ApJ, 263:pp. 835–853 [1982].

F. K. Schinzel, et al., *Identification of γ-ray emission from 3C 345 and NRAO 512*, A&A, 532:A150 [2011].

D. J. Schlegel, D. P. Finkbeiner, and M. Davis, *Maps of Dust Infrared Emission for Use in Estimation of Reddening and Cosmic Microwave Background Radiation Foregrounds*, ApJ, 500:p. 525 [1998].

M. Schmidt, *3C 273 : A Star-Like Object with Large Red-Shift*, Nature, 197:p. 1040 [1963].

C. K. Seyfert, *Nuclear Emission in Spiral Nebulae.*, ApJ, 97:p. 28 [1943].

P. S. Smith, et al., *Coordinated Fermi/Optical Monitoring of Blazars and the Great 2009 September Gamma-ray Flare of 3C 454.3*, ArXiv e-prints 0912.3621 [2009].

K. V. Sokolovsky, *Three New Eclipsing Binaries Near the Galactic Center*, Peremennye Zvezdy Prilozhenie, 9:p. 9 [2009].

M. Sorcia, et al., *Long-term Optical Polarization Variability of the TeV Blazar 1ES 1959+650*, ApJS, 206:11 [2013].

H. C. Spruit, *Theory of Magnetically Powered Jets*, in T. Belloni (Ed.), *Lecture Notes in Physics, Berlin Springer Verlag*, vol. 794 of *Lecture Notes in Physics, Berlin Springer Verlag*, p. 233 [2010].

H. Teräsranta, et al., *Fifteen years monitoring of extragalactic radio sources at 22, 37 and 87 GHz*, A&AS, 132:pp. 305–331 [1998].

H. Teräsranta, et al., *Twenty years monitoring of extragalactic sources at 22, 37 and 87 GHz*, A&A, 427:pp. 769–771 [2004].

J. Timmer and M. Koenig, *On generating power law noise.*, A&A, 300:p. 707 [1995].

S. Trippe, *[Review] Polarization and Polarimetry*, Journal of the Korean Astronomical Society, 47:pp. 15–39 [2014].

C. M. Urry and P. Padovani, *Unified Schemes for Radio-Loud Active Galactic Nuclei*, PASP, 107:p. 803 [1995].

P. Uttley, I. M. McHardy, and I. E. Papadakis, *Measuring the broad-band power spectra of active galactic nuclei with RXTE*, MNRAS, 332:pp. 231–250 [2002].

C. von Montigny, et al., *High-Energy Gamma-Ray Emission from Active Galaxies: EGRET Observations and Their Implications*, ApJ, 440:p. 525 [1995].

J. F. C. Wardle, D. C. Homan, R. Ojha, and D. H. Roberts, *Electron-positron jets associated with the quasar 3C279*, Nature, 395:pp. 457–461 [1998].

M. Watanabe, et al., *TRISPEC: A Simultaneous Optical and Near-Infrared Imager, Spectrograph, and Polarimeter*, PASP, 117:pp. 870–884 [2005].

J. R. Webb, et al., *The 1987-1990 optical outburst of the OVV quasar 3C 279*, AJ, 100:pp. 1452–1456 [1990].

A. E. Wehrle, et al., *Multiwavelength Observations of a Dramatic High-Energy Flare in the Blazar 3C 279*, ApJ, 497:pp. 178–187 [1998].

W. F. Welsh, *On the Reliability of Cross-Correlation Function Lag Determinations in Active Galactic Nuclei*, PASP, 111:pp. 1347–1366 [1999].

A. R. Whitney, et al., *Quasars Revisited: Rapid Time Variations Observed Via Very-Long-Baseline Interferometry*, Science, 173:pp. 225–230 [1971].

H. Zhang, X. Chen, M. Boettcher, F. Guo, and H. Li, *Polarization Swings Reveal Magnetic Energy Dissipation in Blazars*, ArXiv e-prints 1502.07825 [2015].

H. Zhang, X. Chen, and M. Böttcher, *Synchrotron Polarization in Blazars*, ApJ, 789:66 [2014].

Acronyms

AGN Active Galactic Nucleus

BLR Broad Line Region

CCPD Cross-Correlation Peak Distribution

CDF Cumulative Distribution Function

CMB Cosmic Microwave Background

DCF Discrete Correlation Function

DFT Discrete Fourier Transform

iDFT inverse Discrete Fourier Transform

ECDF Empirical Cumulative Distribution Function

EVPA Electric Vector Position Angle

EC External Compton

FFT Fast Fourier Transform

FSRQ Flat Spectrum Radio Quasar

IC Inverse Compton

KS test Kolmogorov–Smirnov test

LCCF Local Cross-Correlation Function

LSP Lomb-Scargle periodogram

NLR Narrow Line Region

OVV Optically Violently Variable

PDF Probability Density Function

PSD Power Spectral Density

QMP Quasar Movie Project

QSO Quasi-Stellar Object

SED Spectral Energy Distribution

shQUc shock Q, U random walk process with uniform I

shQUd shock Q, U random walk process with decreasing I

siQU simple Q, U random walk process

SMBH Super-massive Black Hole

SSA Synchrotron Self-Absorption

SSC Synchrotron Self-Compton

VLBI Very Long Baseline Interferometry

Acknowledgements

I would like to express my deepest and sincere gratitude to my thesis advisor, Dr. Tuomas Savolainen, for countless hours of thriving discussion, his support and guidance, and keen interest in this work. My sincere appreciation is extended to my thesis advisory committee, consisting of Prof. Dr. J. A. Zensus, Prof. Dr. A. Eckart, Dr. T. Savolainen, and Dr. A. Lobanov for valuable suggestions regarding the scientific progression and time management of my PhD project. My highest gratitude goes to Prof. Dr. J. A. Zensus, the Max-Planck-Institut für Radioastronomie (MPIfR), the International Max-Planck Research School (IMPRS) for Astronomy and Astrophysics, and the Max-Planck Gesellschaft for supporting this work with a stipend. I express my highest appreciation to Dr. Tuomas Savolainen and Dr. Emmanouil Angelakis for supporting my early scientific career.

My sincere appreciation goes to the Quasar Movie Project collaboration for providing me with this incredibly interesting data set. I would like to thank especially Dr. Kirill Sokolovsky, Dr. Frank Schinzel, and Dr. Svetlana Jorstad for the support and discussion on numerous occasions. Furthermore, my deepest gratitude goes to all the observers, spending days and nights with observations, data reduction and writing proposals.

I would like to thank the people in the VLBI group for a hospitable environment and numerous fruitful discussions. Special thanks go to Manolis Angelakis, Simone Pott, and the various IMPRS representatives for the organization of numerous seminars, presentations, field trips and retreats, making the participation in the IMPRS scientifically fruitful and highly enjoyable.

Heartfelt greetings go to my office fellows and neighbours Ioannis, Vassilis, Bia, Bindu, Jeff, Florent, Moritz, and Eric for largely fun and occasionally scientific discussions.

Most of all I would like to express my deepest gratitude to my family, my sister Katharina, my grandparents Christel, Irene and Günther, my grandaunt and -uncle Liesel and Hans, and especially my parents Marina and Peter, for all their endless support and affection in every aspect of my entire life. Vor allem möchte ich meiner Familie meinen tiefsten Dank ausdrücken, meiner Schwester Katharina, meinen Großeltern Christel, Irene and Günther, meiner Großtante und meinem Großonkel Liesel und Hans, und ganz besonders meinen Eltern Marina und Peter, für ihre endlose Zuneigung und Unterstützung in allen Aspekten meines Lebens. And I wholeheartedly express my profound gratitude to my life companion Ines . . . bis die ganze Zeit über!

This work made use of Python 2.7 and Python packages numpy, scipy, matplotlib, pytables, statsmodels, ipython, contained in the Anaconda distribution freely provided by Continuum Analytics `http://continuum.io/downloads`.

All plots are produced by Sebastian Kiehlmann with python/matplotlib.

Figure 1.1 is produced by Sebastian Kiehlmann with Adobe Illustrator as reproduction of fig. 1 in Urry and Padovani (1995).

Erklärung

Ich versichere, dass ich die von mir vorgelegte Dissertation selbständig angefertigt, die benutzten Quellen und Hilfsmittel vollständig angegeben und die Stellen der Arbeit – einschließlich Tabellen, Karten und Abbildungen –, die anderen Werken im Wortlaut oder dem Sinn nach entnommen sind, in jedem Einzelfall als Entlehnung kenntlich gemacht habe; dass diese Dissertation noch keiner anderen Fakultät oder Universität zur Prüfung vorgelegen hat; dass sie – abgesehen von unten angegebenen Teilpublikationen – noch nicht veröffentlicht worden ist sowie, dass ich eine solche Veröffentlichung vor Abschluß des Promotionsverfahrens nicht vornehmen werde. Die Bestimmungen dieser Promotionsordnung sind mir bekannt. Die von mir vorgelegte Dissertation ist von Prof. hon. Dr. Zensus, J. A. betreut worden.

Ort, Datum

Unterzeichner

Teilpublikationen

Kiehlmann, S. et al. Analyzing polarization swings in 3C 279. The Innermost Regions of Relativistic Jets and Their Magnetic Fields, Granada, Spain, Edited by José L. Gómez; EPJ Web of Conferences, Volume 61, id.06003, December 2013.